

# JOURNAL OF SCIENCE

PART A: ENGINEERING AND INNOVATION



Year | Yıl: 2022

Volume | Cilt: 9

Issue | Sayı: 2

e-ISSN 2147-9542



## Owner | Sahibi

on behalf of Gazi University | Gazi Üniversitesi adına

Rector | Rektör

Prof. Dr. | Prof. Dr.

**Musa YILDIZ**

## Publishing Manager

Prof. Dr. | Prof. Dr.

**Cevriye GENCER**

Gazi University | Gazi Üniversitesi

## Chief Editor

Prof. Dr. | Prof. Dr.

**Sema Bilge OCAK**

Gazi University | Gazi Üniversitesi

## Managing Editors

Prof. Dr. | Prof. Dr.

**Mustafa Gürhan YALÇIN**

Akdeniz University | Akdeniz Üniversitesi

Prof. Dr. | Prof. Dr.

**Selim ACAR**

Gazi University | Gazi Üniversitesi

Assoc. Prof. Dr. | Doç. Dr.

**Uğur GÖKMEN**

Gazi University | Gazi Üniversitesi

Assoc. Prof. Dr. | Doç. Dr.

**Gürhan İÇÖZ**

Gazi University | Gazi Üniversitesi

## Associate Editors | Alan Editörleri

Prof. Dr.   Prof. Dr. <b>Adem TATAROĞLU</b>	Gazi University - Physics Gazi Üniversitesi - Fizik
Prof. Dr.   Prof. Dr. <b>Adnan SÖZEN</b>	Gazi University - Energy Systems Engineering Gazi Üniversitesi - Enerji Sistemleri Mühendisliği
Prof. Dr.   Prof. Dr. <b>Ali KESKİN</b>	Çukurova University - Automotive Engineering Çukurova Üniversitesi - Otomotiv Mühendisliği
Prof. Dr.   Prof. Dr. <b>Ali Osman SOLAK</b>	Ankara University - Chemistry Ankara Üniversitesi - Kimya
Prof. Dr.   Prof. Dr. <b>Alper BÜYÜKKARAGÖZ</b>	Gazi University - Civil Engineering Gazi Üniversitesi - İnşaat Mühendisliği
Prof. Dr.   Prof. Dr. <b>Atilla BIYIKOĞLU</b>	Gazi University - Mechanical Engineering Gazi Üniversitesi - Makine Mühendisliği
Prof. Dr.   Prof. Dr. <b>Çağlayan AÇIKGÖZ</b>	Bilecik Şeyh Edebali University - Chemical Engineering Bilecik Şeyh Edebali Üniversitesi - Kimya Mühendisliği
Prof. Dr.   Prof. Dr. <b>Demet CANSARAN DUMAN</b>	Ankara University - The Institute of Biotechnology Ankara Üniversitesi - Biyoteknoloji Enstitüsü
Prof. Dr.   Prof. Dr. <b>Elif ORHAN</b>	Gazi University - Physics Gazi Üniversitesi - Fizik
Prof. Dr.   Prof. Dr. <b>Erdal IRMAK</b>	Gazi University - Electrical-Electronic Engineering Gazi Üniversitesi - Elektrik-Elektronik Mühendisliği
Prof. Dr.   Prof. Dr. <b>Fatih ÖZ</b>	Atatürk University - Food Engineering Atatürk Üniversitesi - Gıda Mühendisliği
Prof. Dr.   Prof. Dr. <b>Hakan ATEŞ</b>	Gazi University - Metallurgical and Materials Engineering Gazi Üniversitesi - Metalurji ve Malzeme Mühendisliği
Prof. Dr.   Prof. Dr. <b>Hüseyin Serdar YÜCESU</b>	Gazi University - Automotive Engineering Gazi Üniversitesi - Otomotiv Mühendisliği
Prof. Dr.   Prof. Dr. <b>Meltem DOĞAN</b>	Gazi University - Chemical Engineering Gazi Üniversitesi - Kimya Mühendisliği
Prof. Dr.   Prof. Dr. <b>Metin GÜRÜ</b>	Gazi University - Chemical Engineering Gazi Üniversitesi - Kimya Mühendisliği
Prof. Dr.   Prof. Dr. <b>Murat KAYA</b>	Aksaray University - Biotechnology and Nanotechnology Aksaray Üniversitesi - Biyoteknoloji ve Nanoteknoloji

### Associate Editors | Alan Editörleri

- Prof. Dr. | Prof. Dr. Ege University - Chemical Engineering  
**Nalan KABAY** Ege Üniversitesi - Kimya Mühendisliği
- Prof. Dr. | Prof. Dr. Ankara Hacı Bayram Veli University - Chemistry  
**Nazife ASLAN** Ankara Hacı Bayram Veli Üniversitesi - Kimya
- Prof. Dr. | Prof. Dr. Eskişehir Technical University - Materials Science and Engineering  
**Nuran AY** Eskişehir Teknik Üniversitesi - Malzeme Bilimi ve Mühendisliği
- Prof. Dr. | Prof. Dr. Gazi University - Electrical-Electronic Engineering  
**Nursel AKÇAM** Gazi Üniversitesi - Elektrik-Elektronik Mühendisliği
- Prof. Dr. | Prof. Dr. İstanbul Technical University - Chemical Engineering  
**Ömer ŞAHİN** İstanbul Teknik Üniversitesi - Kimya Mühendisliği
- Prof. Dr. | Prof. Dr. Konya Technical University - Environmental Engineering  
**Şükrü DURSUN** Konya Teknik Üniversitesi - Çevre Mühendisliği
- Prof. Dr. | Prof. Dr. Ankara Yıldırım Beyazıt University - Mechanical Engineering  
**Veli ÇELİK** Ankara Yıldırım Beyazıt Üniversitesi - Makine Mühendisliği
- Prof. Dr. | Prof. Dr. TOBB University of Economics and Technology - Mechanical Engineering  
**Yücel ERCAN** TOBB Ekonomi ve Teknoloji Üniversitesi - Makine Mühendisliği
- Prof. Dr. | Prof. Dr. Middle East Technical University - Engineering Sciences  
**Zafer EVİS** Orta Doğu Teknik Üniversitesi - Mühendislik Bilimleri
- Assoc. Prof. Dr. | Doç. Dr. Hitit University - Chemical Engineering  
**Çetin ÇAKANYILDIRIM** Hitit Üniversitesi - Kimya Mühendisliği
- Assoc. Prof. Dr. | Doç. Dr. Ankara University - Physics  
**Defne AKAY** Ankara Üniversitesi - Fizik
- Assoc. Prof. Dr. | Doç. Dr. Gazi University - Computer Engineering  
**Hacer KARACAN** Gazi Üniversitesi - Bilgisayar Mühendisliği
- Assoc. Prof. Dr. | Doç. Dr. Gazi University - Biology  
**Mine TÜRKTAŞ** Gazi Üniversitesi - Biyoloji
- Assist. Prof. Dr. | Dr. Öğr. Üyesi Akdeniz University - Mathematics  
**Fusun YALÇIN** Akdeniz Üniversitesi - Matematik
- Assist. Prof. Dr. | Dr. Öğr. Üyesi Dr. Marmara University - Mechanical Engineering  
**Senai YALÇINKAYA** Marmara Üniversitesi - Makine Mühendisliği



## Foreign Editorial Advisory Board | Yabancı Yayın Danışma Kurulu

Prof. Dr.	Istituto Nazionale di Fisica Nucleare (INFN)
<b>Ali Behcet ALPAT</b>	Physics
Prof. Dr.	Université d'Évry Val d'Essonne
<b>Abdelmejid BAYAD</b>	Mathematics
Prof. Dr.	Miami University
<b>Burçin BAYRAM</b>	Physics
Prof. Dr.	The University of Sheffield
<b>Rob DWYER-JOYCE</b>	Mechanical Engineering
Prof. Dr.	Jeonbuk National University
<b>Daeyeoul KIM</b>	Mathematics
Prof. Dr.	Loughborough University
<b>Homer RAHNEJAT</b>	Electrical and Manufacturing Engineering
Prof. Dr.	Vijayanagara Sri Krishnadevaraya University
<b>Loksha VEERABHADRIAH</b>	Mathematics
Assist. Prof. Dr.	University Džemal Bijedić Mostar
<b>Toni NIKOLIC</b>	Geological Engineering

## English Language Editors | İngilizce Dil Editörleri

Lecturer   Okutman	Gazi University - School of Foreign Languages
<b>Gizem AÇELYA AYKAN</b>	Gazi Üniversitesi - Yabancı Diller Yüksekokulu
Lecturer   Okutman	Gazi University - School of Foreign Languages
<b>Tuğçe BÜYÜKBAYRAM</b>	Gazi Üniversitesi - Yabancı Diller Yüksekokulu

## Technical Editors | Teknik Editörler

Dr.	Akdeniz University
<b>Fatih UÇAR</b>	Akdeniz Üniversitesi
Dr.	Gazi University
<b>Silver GÜNEŞ</b>	Gazi Üniversitesi
Dr.	Gazi University
<b>Murat AKIN</b>	Gazi Üniversitesi



## Correspondence Address

Gazi University Graduate School of Natural and Applied Sciences  
Emniyet Neighborhood, Bandırma Avenue, No:6/20B, 06560, Yenimahalle - ANKARA  
B Block, Auxiliary Building

## Yazışma Adresi

Gazi Üniversitesi Fen Bilimleri Enstitüsü  
Emniyet Mahallesi, Bandırma Caddesi, No:6/20B, 06560, Yenimahalle - ANKARA  
B Blok, Ek Bina

**e-mail | e-posta**  
gujsa06@gmail.com

**web page | web sayfası**  
<https://dergipark.org.tr/tr/pub/gujsa>

**Gazi University Journal of Science Part A: Engineering and Innovation  
is a peer-reviewed journal.**

Gazi Üniversitesi Fen Bilimleri Dergisi Bölüm A: Mühendislik ve İnovasyon  
hakemli bir dergidir.

## INDEXING | DİZİNLENME

# TRDİZİN



# ASOS indeks



## ACCESSIBILITY | ERİŞİLEBİLİRLİK



# DergiPark AKADEMİK



This work are licensed under a Creative Commons Attribution-ShareAlike 4.0 International License.



Bu eser Creative Commons Atıf-AynıLisanslaPaylaş 4.0 Uluslararası Lisansı ile lisanslanmıştır.

## CONTENTS | İÇİNDEKİLER

Page   Sayfa	Articles   Makaleler
49-61	<b>Development and Performance Evaluation of a Variable-Pitch Tapered-Shaft Screw Press for Palm Oil Extraction</b> Kehinde Peter ALABI  Rasheed Amao BUSARI  Olawale Joel OLADIMEJI  Research Article Agricultural Engineering <a href="https://doi.org/10.54287/guj.1069996">10.54287/guj.1069996</a> Araştırma Makalesi Ziraat Mühendisliği
62-78	<b>An Approach on Developing a Dynamic Wind-Solar Map for Tracking Electricity Production Potential and Energy Harvest</b> Fırat SALMANOĞLU  Numan Sabit ÇETİN  Research Article Energy Systems Engineering <a href="https://doi.org/10.54287/guj.1085005">10.54287/guj.1085005</a> Araştırma Makalesi Enerji Sistemleri Mühendisliği
79-86	<b>Radiochemical Procedure for Measurement Specific Activities of Uranium Isotopes in Asphaltite Bioleaching Liquor by Alpha-Particle Spectrometry</b> Meryem SEFERİNOĞLU  Research Article Chemical Engineering <a href="https://doi.org/10.54287/guj.1117169">10.54287/guj.1117169</a> Araştırma Makalesi Kimya Mühendisliği
87-95	<b><i>Moringa oleifera</i> (Lam.) and <i>Momordica charantia</i> (Lam.-) as Potential Larvicides and Fumigants of <i>Culex Mosquitoes</i></b> Olajide Joseph AFOLABI  Akinbode Ayekooto OLONISAKIN  Research Article Biology <a href="https://doi.org/10.54287/guj.1079339">10.54287/guj.1079339</a> Araştırma Makalesi Biyoloji
96-103	<b>Investigation of Arsenic Content in Field Pesticides Using Inductively Coupled Plasma Optical Emission Spectroscopy (ICP-OES)</b> Şükrü KALAYCI  Research Article Chemical Engineering <a href="https://doi.org/10.54287/guj.1100870">10.54287/guj.1100870</a> Araştırma Makalesi Kimya Mühendisliği
104-111	<b>Computer Aided Simulation with Finite Element Analysis of the Effect of Face Mask Use Against COVID-19 and Other Infections</b> Canan İNAL  Kadir GÖK  H. Deniz ADA  Sermet İNAL  Arif GÖK  Research Article Biomedical Engineering <a href="https://doi.org/10.54287/guj.1083882">10.54287/guj.1083882</a> Araştırma Makalesi Biyomedikal Mühendisliği



## CONTENTS | İÇİNDEKİLER

Page   Sayfa	Articles   Makaleler	
112-119	<b>Amalgamated Rings with <math>n-UJ</math>-Properties</b> Esra MEMİŞOĞULLARINDAN  Tufan ÖZDİN  Research Article Mathematics <a href="https://doi.org/10.54287/gujisa.1106287">10.54287/gujisa.1106287</a>	Araştırma Makalesi Matematik
120-135	<b>Production and Characterization of Bilayer Tissue Scaffolds Prepared with Different Alginate-Salts and Fibroin</b> Özge ÇELİK  Salma A. Taher MOHAMED  Nuray EMİN  Research Article Biomedical Engineering <a href="https://doi.org/10.54287/gujisa.1107158">10.54287/gujisa.1107158</a>	Araştırma Makalesi Biyomedikal Mühendisliği
136-155	<b>Experimental and Modelling Comparison of the Effects of UV Energy on Liquefaction Efficiency in Coal Liquefaction Mechanism</b> Yelda ALTINSOY  Emir H. ŞİMŞEK  Research Article Chemical Engineering <a href="https://doi.org/10.54287/gujisa.1104126">10.54287/gujisa.1104126</a>	Araştırma Makalesi Kimya Mühendisliği
156-163	<b>Evaluation of Surface Dose for Intensity Modulated Radiotherapy of Head and Neck Cancer Using Thermoluminescent Dosimeters</b> Osman Vefa GUL  Nihal BUYUKCIZMECI  Hamit BASARAN  Research Article Physics <a href="https://doi.org/10.54287/gujisa.1109112">10.54287/gujisa.1109112</a>	Araştırma Makalesi Fizik
164-172	<b>Theoretical Evaluation of Angle-Dependent Optical Properties of a Thin Film Solar Cell Including One-Dimension Photonic Crystals</b> Çağlar ÇETİNKAYA  Research Article Physics <a href="https://doi.org/10.54287/gujisa.1129794">10.54287/gujisa.1129794</a>	Araştırma Makalesi Fizik
173-186	<b>On Approximation Properties of Stancu Type Post-Widder Operators Preserving Exponential Functions</b> Gülten TORUN  Research Article Mathematics <a href="https://doi.org/10.54287/gujisa.1113567">10.54287/gujisa.1113567</a>	Araştırma Makalesi Matematik



Gazi University

**Journal of Science**

PART A: ENGINEERING AND INNOVATION

<http://dergipark.org.tr/guj.1069996>

## Development and Performance Evaluation of a Variable-Pitch Tapered-Shaft Screw Press for Palm Oil Extraction

Kehinde Peter ALABI<sup>1</sup> , Rasheed Amao BUSARI<sup>1</sup> , Olawale Joel OLADIMEJI<sup>1</sup> <sup>1</sup>Department of Food and Agricultural Engineering, Kwara State University, Malete, P.M.B. 1530, Ilorin, Kwara State, Nigeria

Keywords	Abstract
Extraction Palm Fruit Oil Screw Press Efficiency Oil Industry	Palm fruit oil extraction is a difficult task to undertake. Screw press technology offers a solution to its extraction. However, most screw press available requires high power input for effective operation, thus affecting cost. Therefore, there is a need for improvement in order to limit cost and increase extraction efficiency. This work focuses on development of a variable-pitch tapered-shaft (VATS) screw press for enhancing palm fruit oil extraction efficiency. The VATS screw press machine consists of three main components including the hopper, the steamer, and the pressing unit, and was operated at temperature of 90, 110 and 130°C, shaft speed of 30, 45, and 60 rpm and heating time of 10, 15, 20 minutes. The performance evaluation carried on the machine includes oil yield, extraction efficiency and extraction loss. The results showed that the average oil yield, extraction efficiency and extraction loss were 83.72, 97.73 and 2.37% respectively. Whereas, a higher machine efficiency of 94.45% was obtained at a temperature of 130°C, shaft speed of 60 rpm, and heating time of 15 minutes. It is hoped that the information on the design concept for VATS screw press for palm fruit oil extraction will be useful for the vegetable oil industry.

### Cite

Alabi, K. P., Busari, R. A., & Joel, O. O. (2022). Development and Performance Evaluation of a Variable-Pitch Tapered-Shaft Screw Press for Palm Oil Extraction. *GU J Sci, Part A, 9(2)*, 49-61.

Author ID (ORCID Number)	Article Process	
K. P. Alabi, 0000-0002-8979-805x	<b>Submission Date</b>	08.02.2022
R. A. Busari, 0000-0001-8961-1729	<b>Revision Date</b>	28.03.2022
O. O. Joel, 0000-0001-5678-3057	<b>Accepted Date</b>	03.06.2022
	<b>Published Date</b>	06.06.2022

## 1. INTRODUCTION

Production of vegetable oil is generally determined by the extraction methods that are based on the four main principles *visa*: traditional wet rendering process, hydraulic press, solvent extraction, and screw press (Savoire et al., 2013; Amiolemhen & Esegibe, 2019; Alam et al., 2020; Chukwunwike & Ojmelukwe, 2021). Among all, a screw press is mostly used due to its simplicity and convenience. One major limitation of a screw press is pressure build up during operation, causing shaft rolling and operational failure. In the past decades, efforts have been made to improve the efficiency of a screw press. Typically, pressure modulation, and adjustable choke mechanism that allows the adjustment of back pressure have been developed and optimized (Adetola et al., 2014). However, factors such as applied pressure, rotational speed, temperature and moisture content considered in optimization process requires significant power input for effective operation (Tagoe et al., 2012; Aremu & Ogunlade, 2016; Atoyan et al., 2000, Amiolemhen & Esegibe, 2019). The most two important parameters *viz*: input power and throughput (efficiency) capacity, mostly considered in the design of a screw press for oil seeds, depend on the rate of energy consumption within the pressing zones. To obtain high efficiency, higher power is needed where the highest pressures arise in the material to be pressed (Okafor, 2015; Atoyan et al., 2000). For instance, a powered driven small-sized palm oil expeller with a uniform pitch shaft has extraction efficiency of 79.5%, with maximum extraction capacity of 532 kg/h, requires up to 5 hp electric motor (Adetola et al., 2014). Generally speaking, the available screw press requires higher power to operate. On the other hand, a screw press with uniform pitch shaft uses high speed/high power motor to effectively extract oil from oil-based seed materials, thus affecting cost (Olayanju

\*Corresponding Author, e-mail: [kehinde.alabi@kwasu.edu.ng](mailto:kehinde.alabi@kwasu.edu.ng) or [kennyp4all@yahoo.com](mailto:kennyp4all@yahoo.com)

et al., 2016). In the performance evaluation of some screw press, Firdaus et al. (2017) and Muhammad et al. (2021) reported ineffective press (in terms of high oil loss and nut breakage), and shaft failure, respectively.

Hence, there is a need to further improve extraction efficiency of a screw press for palm oil extraction. However, this work aim at development of a low torque and high efficiency palm fruit oil extraction machine using variable-pitch tampered-shaft (VATS) method that reduces time of cycle requires for screw press to complete a revolution.

## 2. MATERIALS AND METHOD

### 2.1. The Concept of the Machine and Working Principle

The VATS mechanism was proposed to achieve a higher extraction capacity and lower extraction loss than that of the uniform shaft. Figure 1 shows the typical diagram for the proposed concept and the prototype VATS, whereas Figure 2 shows the machine. The high-pitched shaft is extreme (up to 50 mm) in the extraction unit and began at 18 mm. When the oil seeds are fed through the hopper, the rotating shaft picks the materials at low pitch level and pushes them along the pitch until it reaches the extreme. Moreover, the whole extracting unit does not have to be oversized in other to cope with infrequent intensive extraction requirements, because the pressure required for extraction reaches its peak value in fewer revolutions and shorter time when compared with the same sized uniform pitch screw (Ndirika & Onwualu, 2016), thus making VATS screw press machine a novel extraction method.

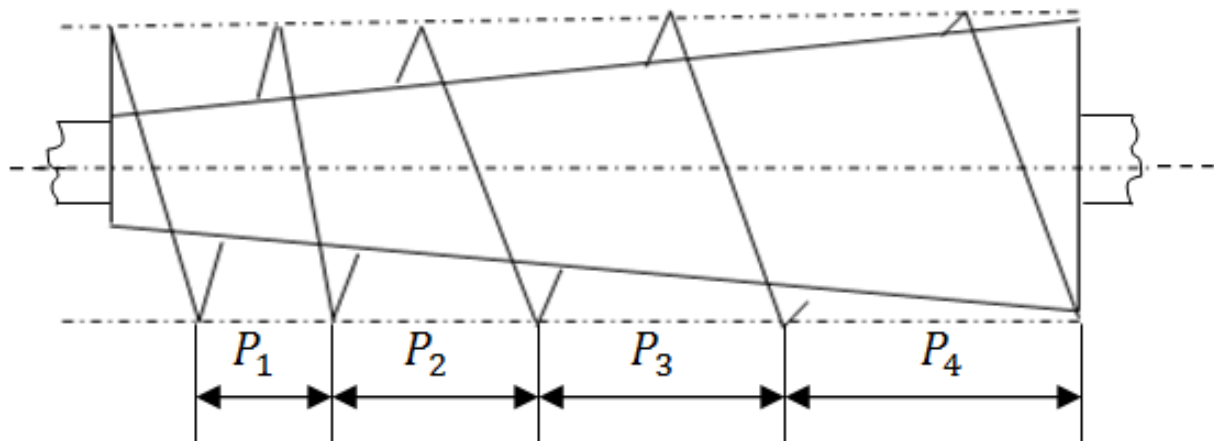


*Figure 1. Typical diagram for the proposed concept and the prototype VATS screw press*

### 2.2. Design Calculation

The exploded view showing the component parts and the pictorial view of the palm oil extraction machine were presented in Figure 2 and Figure 3 respectively. The machine designed with Autodesk Inventor software 2018 based on calculations. The design consists of five (5) different sections which are the steamer chamber, the hopper, the VATS pressing unit, capacity and power requirement of the machine (Figure 2). In addition, the functional parameters like motor speed, and machine torque were adequately considered.

#### 2.2.1. Design of the Steamer Chamber

The steamer is made up of a pulverized hole of 10 mm diameter and it is placed on top of a boiler with a controlled temperature in order to steam the palm fruit at a specified temperature. It has a gate of distance 98 mm. However, the steam chamber was designed according to Adetola et al. (2014).

Volume of the steamer ( $V_s$ )

$$V_s = \pi r^2 h \quad (1)$$

$$V_s = \pi \times 0.12^2 \times 0.05 = 0.00226 \text{ m}^3$$

The palm fruit has a configuration of length (0.025m), breath (0.015m) and width (0.015m). Therefore, the volume was determined using the Equation 2.

Volume of one palm fruit, ( $V_{pf}$ )

$$V_{pf} = lbh \quad (2)$$

$$V_{pf} = 0.025 \times .015 \times 0.015 = 5.6 \times 10^{-6} \text{ m}^3$$

The amount of palm fruit contained in one volume of steamer container ranges from 8 to 10 kg

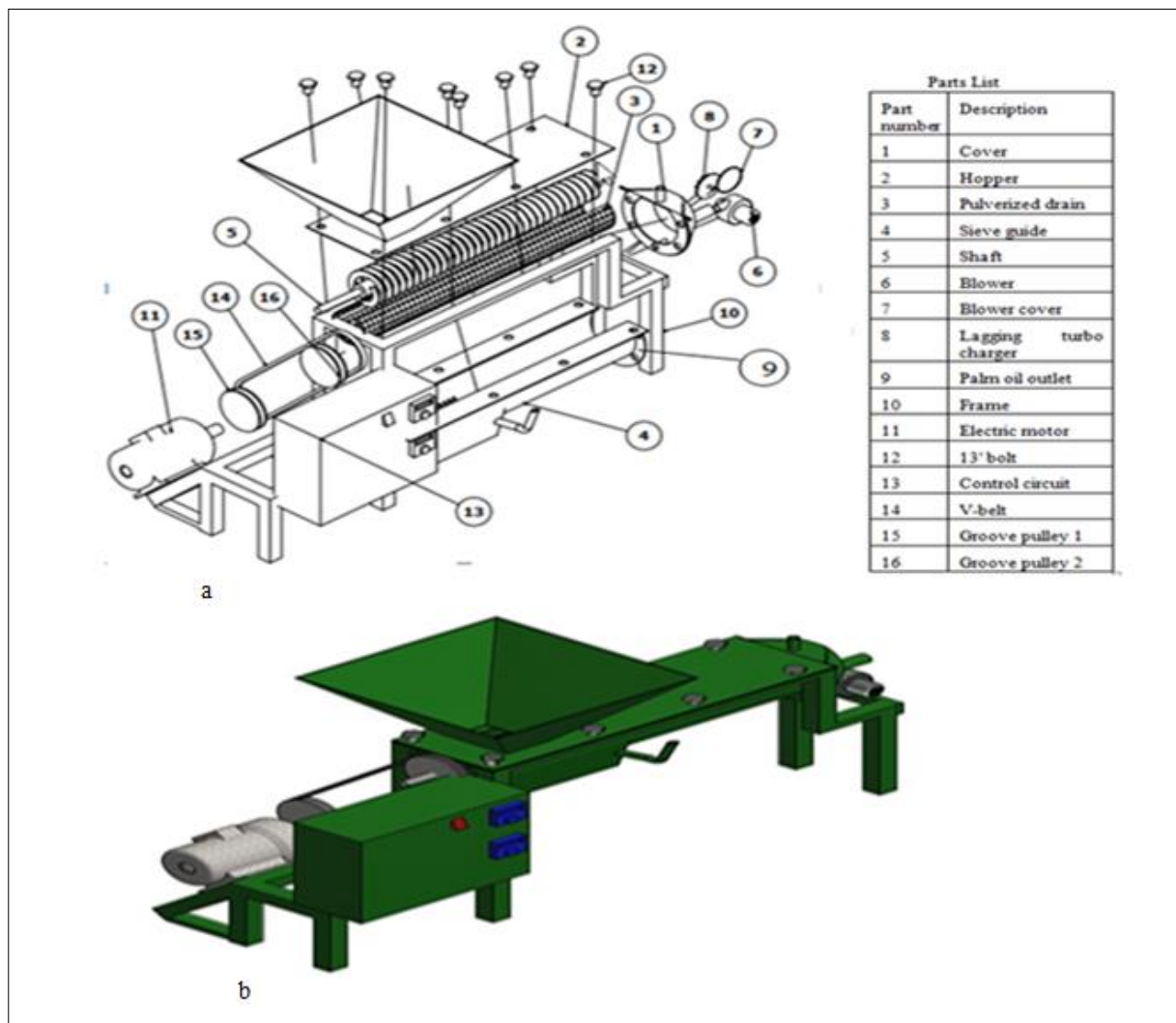


**Figure 2.** The machine showing components part; **a)** exploded view, **b)** 3D view



**Figure 3.** Pictorial view of the machine

### 2.2.2. Design of the Hopper

The hopper, as shown in Figure 4, has its volume ( $V_h$ ) designed to accommodate less volume of palm fruit as produced from steamer container in order to avoid bottle neck operation by using Equation 3.

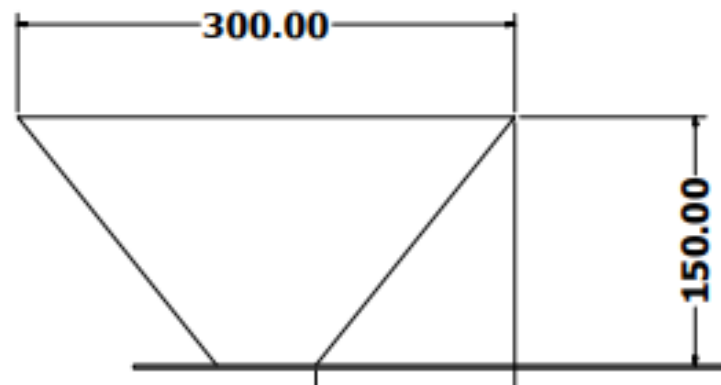


**Figure 4.** The hopper

$$V_h = \frac{1}{2}(a + b)hz \quad (3)$$

$$V_h = \frac{1}{2}(.3 + 0.05)0.15 \times .3 = 3.3 \times 10^{-5} \text{ m}^3$$

### 2.2.3. Design of the VATS Pressing Unit

By considering the most critical point of the palm fruit loading the hopper at full load, the volume of the pressing chamber  $V_{pc}$  is given as,

$$V_{pc} = \pi r^2 l \quad (4)$$

Density of steamed and bulk density of digested palm fruit is 373.47 and 1060  $kg/m^3$  respectively. The mass of steamed palm fruit ( $M_{sf}$ ) at full load = Density  $\times$  Volume.

$$M_{sf} = \rho_{sf} \times V_{sf} \quad (5)$$

$$V_{pc} = \pi \times 0.032^2 \times 0.537 = 0.001727 \text{ m}^3$$

$$M_{sf} = \rho_{sf} \times V_{sf}$$

$$M_{sf} = 1060 \times 0.001727 = 1.83 \text{ kg}$$

$$\text{Weight, } W = mg$$

$$W = 1.83 \times 9.81 = 17.96 \text{ N}$$

Figure 5 shows VATS pressing screw wounded around a shaft capable to withstand the torsional and bending stress. However, ASME code equation of shaft was used to compute the shaft diameter [Amiolemhen and Eseigbe \(2019\)](#).



**Figure 5.** The VATS pressing screw

$$d^3 = \frac{16}{\pi \tau_{all}} \sqrt{(K_b M_b)^2 + (K_t M_t)^2} \quad (6)$$

$$\tau_{all} = \frac{0.5\sigma_y}{sf} = 60 \text{ MN/m}^2$$

$\sigma_y$  is the yield strength for shaft material = 60  $MN/m^2$  (taking factor of safety to be 2)

where  $K_t$  is the combination of shock and fatigue factor applied under torsion moment,  $K_b$  is the combination of shock and fatigue factor applied under bending moment,  $M_t$  is the torque on shaft,  $M_b$  is the bending moment on shaft. The values for  $K_t$ ,  $K_b$ ,  $M_t$ , and  $M_b$  are 1.0, 1.5 98.01 Nm and 50.3 Nm respectively.

Circular rotational motion of the shaft,

$$v = \omega r \quad (7)$$

or

$$v = \frac{\pi N r}{30} \quad (8)$$

Base on the shaft analysis, the machine is considered to operate at low speed (i.e. 90 rpm)

$$v = \frac{\pi \times 90 \times 0.0275}{30} = 0,259 \text{ m/s}$$

Centrifugal force  $F_c$  pressing the palm fruit,

$$F_c = Ma = M\omega^2 r \quad (9)$$

And angular velocity is

$$\omega = \frac{2\pi N}{60} \quad (10)$$

Mass of shaft,

$$m_s = \rho \times V_s \quad (11)$$

$$m_s = 7850 \times 0.001449 = 11.37 \text{ kg}$$

Total mass at the compression chamber  $M_t$ ,

$M_t = \text{Mass of shaft} + \text{mass of palm fruit}$

$$M_t = 11.37 + 5 = 16.37 \text{ kg}$$

$$F_c = M \left( \frac{2\pi N}{60} \right)^2 r$$

$$F_c = 16.37 \left( \frac{2\pi \times 90}{60} \right)^2 \times 0.0275$$

Torque developed,

$$T = F_c r \quad (12)$$

$$T = 40 \times 0.0275 = 1.1 \text{ Nm}$$

### 2.2.4. Belt Design

The belt design is a crucial part that determines the operation of an entire drive system of the machine. Open belt, as shown in Figure 6, was considered because of its flexibility. Typically, the length of belt, power transmitted, angle of contact or lap, and load carried by the screw were designed according to Firdaus et al. (2017) and Muhammad et al. (2021) reported ineffective press (in terms of high oil loss and nut breakage), and shaft failure during testing of constant pitch screw press machine.

#### 2.2.4.1. Length of Belt

The length of the belt is given as thus:

In terms of pulley radii

$$L = \pi(r_1 + r_2) + 2x + \frac{(r_1 - r_2)^2}{x} \quad (13)$$

In terms of pulley diameter

$$L = \pi(d_1 + d_2) + 2x + \frac{(d_1 - d_2)^2}{4x} \quad (14)$$

where  $r_1$  and  $r_2$  is the radii of the larger and smaller pulleys, respectively,  $x$  is the distance between the centers of the two pulleys, and  $L$  is total length of belt.

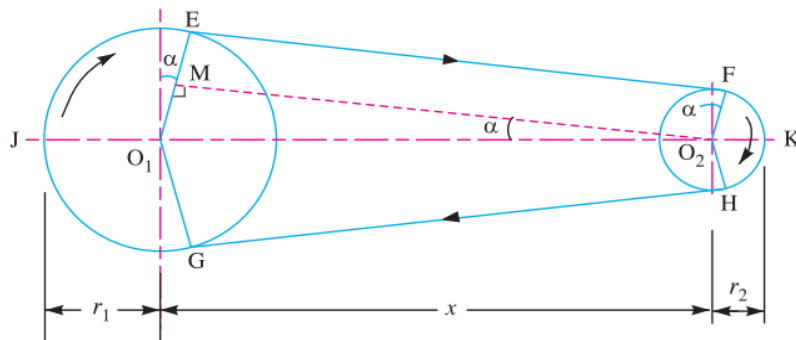


Figure 6. Schematic diagram of an open belt drive

#### 2.2.4.2. Power Transmitted by the Belt

Figure 7 illustrates the power transmitted through the belt driven by the two pulleys. Considering  $T_1$  and  $T_2$  (in Newton), and  $r_1$  and  $r_2$  (in metres) and  $v$  (m/s). The effective force to drive the pulleys is  $T_{Eff}$ .

$$T_{Eff} = T_1 - T_2 \quad (15)$$

The work done per second on the belt is given as:

$$W = T_{Eff}V \text{ (Nm/s)} \quad (16)$$

Power transmitted is

$$P = T_{Eff}W \text{ (Nm/s)} \quad (17)$$



However, torque exerted on the driving pulley is given as

$$T_{Eff}r_1 \tag{18}$$

and the torque exerted on the driven pulley is

$$T_{Eff}r_2 \tag{19}$$

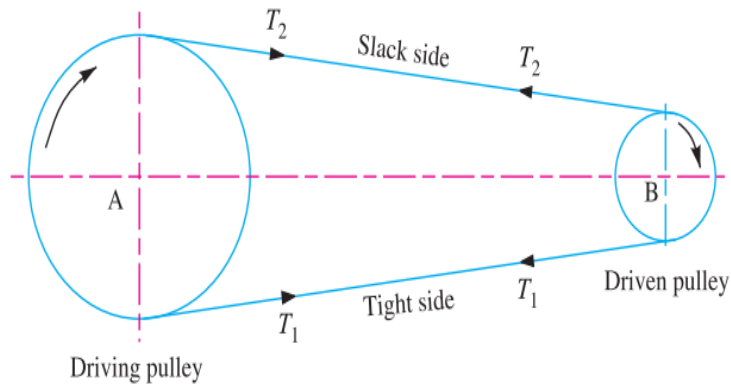


Figure 7. Power transmitted through the belt

**2.2.4.3. Angle of Contact or Lap**

For open belt, angle of contact is given as:

$$\frac{T_1}{T_2} = e^{\frac{\mu\theta}{\sin\beta}} \tag{20}$$

$$\sin\alpha = \frac{r_1 - r_2}{x}$$

where  $x$  is distance between the center of two pulleys,  $\alpha$  is angle of wrap,  $\mu$  is coefficient of friction between the belt and pulley,  $\theta$  is angle of contact between the belt and pulley,  $\beta$  is Half the wedge angle.

**2.2.5. Design of the Load to be Carried by the Screw**

The load on the screw ( $W_e$ ) was determined according to Adetola et al. (2014) as thus:

$$(W_e) = T \left( \frac{D_{m/2} \tan\theta + \mu / \cos\alpha}{1 - \mu \tan\theta \cos\alpha} \right) \tag{21}$$

$$\alpha = \tan^{-1}(\tan\theta_n \cos\alpha)$$

where  $T$  is the torque transmitted by the screw shaft,  $D_m$  is mean thread diameter,  $\mu$  is coefficient of friction,  $\theta_n$  is thread (lift) angle,  $\alpha$  = Helix angle.

$$\alpha = \tan^{-1}(\tan(45) \cos(20)) = 17.24^\circ$$

$$(W_e) = 1.11 \left( \frac{\frac{0.018}{2} \tan(45) + 0.3 / \cos(20)}{1 - 0.3 \tan(45) \cos(20)} \right) = 1.0340 \text{ kg}$$

### 2.2.6. Design of the Worm Shaft

The design of the worm shaft was according to [Adetola et al. \(2014\)](#) with slight modifications, as given below:

$$P_s = \pi \tan(\varphi) d_{wm} \quad (22)$$

where  $\varphi$  is lead angle,  $d_{wm}$  is mean shaft diameter and  $P_s$  value is  $P_s = \pi \tan(0.7) \times 0.018 = 0.0476$  m

### 2.2.7. Design of the Capacity of the Machine

The theoretical capacity of the expeller was determined using the modified form of the equation given by [Adetola et al. \(2014\)](#),

$$Q = 60 \times \frac{\pi}{4} \times (D^2 - d^2) P_s \rho N \phi \quad (23)$$

where  $Q$  is theoretical capacity,  $D$  is shaft diameter,  $d$  is screw diameter,  $\rho$  is density of palm kernel,  $P_s$  is screw pitch,  $N$  is shaft speed and  $\phi$  is filling factor.

$$Q = 60 \times \frac{\pi}{4} \times (0.05^2 - 0.018^2) 0.0476 \times 373.47 \times 90 \times 1 = 164.0609 \text{ m}^3/\text{min}$$

Theoretically,  $Q = 2.73 \text{ m}^3/\text{h}$

### 2.2.8. Design of the Pressure to be Developed by the Screw Thread

Pressure developed by the screw thread in oil expeller can be determined using the given equation;

$$P_r = \frac{W_e}{A_p} \quad (24)$$

$$A_p = \pi D_m n h$$

where  $A_p$  is the pressing area,  $n$  is the number of threaded turns subject to load,  $h$  is thread depth

$$A_p = \pi \times 0.018 \times 11 \times 0.001 = 6.2 \times 10^{-4} \text{ m}^2$$

### 2.2.9. Design of the Power Requirement of the Machine

The power required for oil extraction can be given as:

$$P = Q L_s \rho g F \quad (25)$$

where  $P$  is the power required for extraction,  $Q$  is the volumetric capacity,  $L_s$  is the length of screw shaft,  $\rho$  is the density of palm kernel,  $g$  is the acceleration due to gravity and  $F$  is material factor.

Substituting  $Q = 2.73 \text{ m}^3/\text{h}$ ,  $L_s = 0.61 \text{ m}$ ,  $\rho = 373.47 \text{ kg/m}^3$ ,  $g = 9.81 \text{ m/s}^2$ ,  $F = 0.3$  into Equation 25, Hence  $P = 1.5 \text{ kw}$

The power of the electric motor was determined according to (Adetola et al., 2014) as given below:

$$P_m = \frac{P_e}{\eta} \quad (26)$$

where  $P_m$  is the power of the electric motor, and  $\eta$  is the drive efficiency

Given the  $\eta = 75\%$  or  $0.75$ ,  $P_m = 2.0\text{hp}$ . Therefore, a 2hp three-phase electric motor was used to drive the machine.

### 2.3. Material Selection and Fabrication of Machine Components

The orthogonal view of the machine components are presented in Figure 8 in the appendix. The machine hopper was formed using 4 pieces of standard mild steel of dimension 300x150x200 mm. The shaft (of 18 mm base diameter) was fabricated from the mild steel rod of diameter 25 mm and length 210 mm. The screw thread was machined at a variable pitch from 50 mm to 18 mm to form a tapered screw conveyor of ten screw turns. A mild metal plate of 10 mm, 2 x 2 feet was cut, machined and used to form the barrel. However, small openings were made on the lower side of the barrel to allow the passage of the extracted oil. The frame was fabricated by using angle iron of dimension 40x40x30 mm. All the fabrication processes including marking out, machining, cutting, joining, drilling and fitting were performed at the farm power and machinery laboratory, Department of Food and Agricultural Engineering, Kwara State University, Malete, Nigeria. The workshop machines and equipments including grinding machine, lathe machine, welding machine, scribe, steel rule, and compass, centre punch, oxy-acetylene gas, saw frame and cutting blade were used. The specification of the materials used is presented in Table 1.

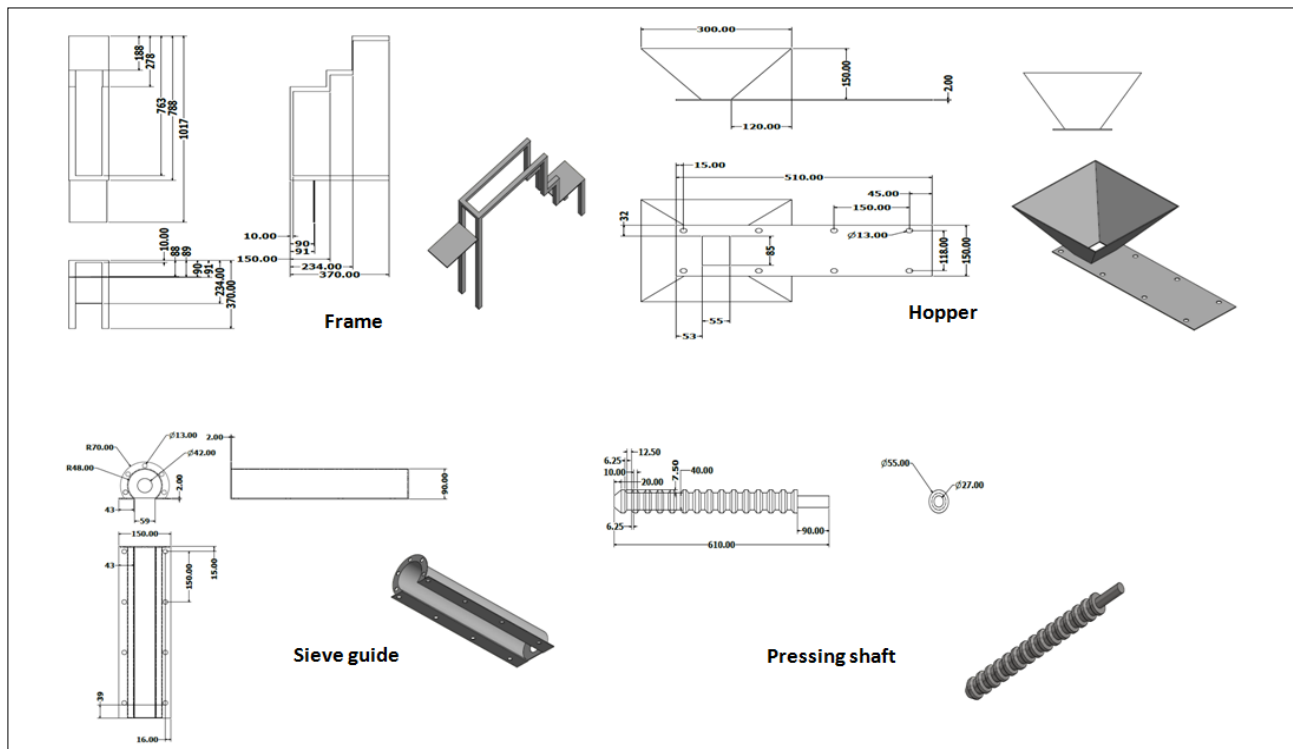


Figure 8. Orthogonal view of some component parts

### 2.4. Machine Operation and Testing

Palm fruit bunches were obtained from local farmers at Kwara State University Malete (Kwasu), Nigeria (51° 27' 49.144" N 19° 13' 4.303" E). The fresh palm fruits were taken to the Farm power and machinery laboratory, Department of Food and Agricultural Engineering, Kwasu, while dirt were removed and the fruits were weighed and prepared for oil extraction. The prepared palm fruits were charged into the machine

that was operated at temperatures of 90, 110, 130°C, heating time of 10, 15, 20 minutes, and shaft speed of 30, 45, and 60 rpm. The shaft of the machine was designed with two segments, with counter motion orientation to delay the palm fruit in the steaming chamber. In order to extract the oil, the steamed palm fruits were conveyed, squeezed and pressed by the variable-pitch tapered-shaft, while the collecting turbo impeller collect the oil from the pressed seeds and pushes it to the outlet chute. The variable-pitch tapered shaft rotates counter clockwise, pushing out the drained chaff and the kernel seed out of the outlet chute of the pressing chamber. The fresh palm fruits, the oil extracted, and the residual cake (kernel and fibre mixture) were collected and evaluated. The values evaluated are oil yield, machine extraction efficiency and extraction losses based on [Aremu and Ogunlade \(2016\)](#), as given below:

$$\text{Oil yield (\%)} = \frac{W_{OE}}{W_{TS}} \times 100 \quad (27)$$

$$\text{Extraction efficiency} = \frac{W_{OE}}{\alpha W_{TS}} \times 100 \quad (28)$$

$$\text{Extraction Loss (\%)} = \frac{W_{TS} - (W_{OE} + W_{CK})}{W_{TS}} \times 100 \quad (29)$$

where;

$\alpha$  : Oil content of the palm fruit

$W_{TS}$  : Total weight of sample (g)

$W_{OE}$  : Weight of oil extracted (g)

$W_{CK}$  : Weight of cake (g)

**Table 1.** Specification of construction material

s/n	Material	Description	Quantity
1	Metal plate	2 mm (0.08") mild steel	1 full sheet
2	Fly bar	3 mm (0.1") mild steel	1 full length
3	Motor	2 hp	1
4	Metal plate	8 mm (0.3")	2 x 2 feet
5	Ball bearing	Angular contact bearing	2
6	Fastener Bolt	13"	16 pieces
7	Motor speedcontroller	PWM (Pulse Width Modulation)	1
8	Temperatureregulator		1
9	Shaft	2.5 m (98") mild steel	2
10	Oil pump	Centrifugal pump	1
11	Pipes	1", 0.5" and 0.25"	
12	Pulleys		2
13	Belt		1

### 3. RESULTS AND DISCUSSION

Table 2 shows the average oil yield (%), extraction efficiency (%) and extraction loss (%) for different processing conditions. The average oil yield, extraction efficiency and extraction loss were 83.72, 97.73, and 2.37% respectively. The extraction efficiency (97.73%) is high when compared to the findings of [Adetola et al. \(2014\)](#) that has extraction efficiency value of 79.5%. The highest oil yield (84.90%) was obtained when the machine was operated at a temperature of 110°C, shaft speed of 45 rpm and 15 minutes heating time. The results obtained show that the machine operates smoothly without jamming and effectively extract the crude oil from the palm fruits.

**Table 2.** Average\* oil yield (%), extraction efficiency (%) and extraction loss (%) for different processing conditions

Temperature (°C)	Speed (rpm)	Heating Time (minutes)	Oil Yield (%)	ExtractionEfficiency (%)	ExtractionLoss (%)
<b>90</b>	30	10	82.51	97.23	2.48
		15	84.35	98.08	2.01
		20	84.01	98.01	2.82
<b>110</b>	45	10	83.45	97.54	2.23
		15	84.90	98.21	1.98
		20	83.52	98.00	2.53
<b>130</b>	60	10	83.06	97.25	2.45
		15	84.52	98.45	2.02
		20	83.19	96.78	2.78

\*Standard error = 0.21

### 4. CONCLUSION

In an attempt to improve the efficiency of a screw press extraction machine, a variable-pitch tampered-shaft (VATS) screw press was designed, constructed and evaluated for palm fruit oil extraction. The machine was simple in term of the design and easy to operate and maintained. Powered by 2hp three phase electric motor, the VATS screw press machine has average oil yield, extraction efficiency and extraction loss of 83.72, 97.73, and 2.37% respectively from the palm fruits. In conclusion, theVATS screw press machine allows higher efficiency with low extraction loss and can be applied for small and medium scale palm fruit oil extraction operation. Though, the technology can be further optimized to increase production rate of palm screw press extraction machine and providemore employment opportunitiesin the vegetable oil industry, future work should focus on the effect of extraction variables (such as time and temperature) on the quality of the extract oil.

### ACKNOWLEDGEMENT

The authors are grateful to the technical staff of the Farm Power and Machinery Laboratory, Department of Food and Agricultural Engineering, Kwara State University, Malete, Nigeria.

### CONFLICT OF INTEREST

There is no conflict of interest.

**REFERENCES**

- Adetola, O. A., Olajide, J. O., & Olalusi, A. P. (2014). Development of a Screw Press for Palm Oil Extraction. *International Journal of Scientific & Engineering Research*, 5(7), 1416-1422.
- Alam, M., Nandi, R., & Kabir, E. (2020). Development of a Manually Operated Palm Oil Extraction Machine. *Agricultural Engineering International: CIGR Journal*, 22(1), 213-218.
- Amiolemhen, P. A., & Eseigbe, J. A. (2019). Design and Fabrication of a Palm Kernel Oil Expeller Machine. *International Journal of Engineering and Technology*, 67(6), 39-46. doi:[10.14445/22315381/IJETT-V67I6P208](https://doi.org/10.14445/22315381/IJETT-V67I6P208)
- Aremu, A. K., & Ogunlade C. A. (2016). Effect of Operating Parameters on Mechanical Oil Expression from African Oil Bean Seed. *Global Journal of Science Frontier Research: Agriculture and Veterinary*, 16(1), 19-26.
- Atoyan, S. V., Generalov, M. B., & Trutnev, N. S. (2000). Input power required for compaction materials in screw presses. *Journal of Chemical and Petroleum Engineering*, 36(3), 31-32. doi:[10.1007/BF02463419](https://doi.org/10.1007/BF02463419)
- Chukwunwike, E., & Ojmelukwe, P. (2021). Processing Methods and Storage Period Affect the Quality of Palm Oil. *Carpathian Journal of Food Science and Technology*, 13(4), 192-210. doi:[10.34302/crpjfst/2021.13.4.15](https://doi.org/10.34302/crpjfst/2021.13.4.15)
- Firdaus, M., Salleh, S. M., Nawil, I., Ngali, Z., Siswanto, W. A., & Yusup, E. M. (2017). Preliminary Design on Screw Press Model of Palm Oil Extraction Machine. *IOP Conference Series: Materials Science and Engineering*, 165(1), 012029. doi:[10.1088/1757-899X/165/1/012029](https://doi.org/10.1088/1757-899X/165/1/012029)
- Muhammad, I. B., Husaini, Nurdin, A., Rauzatul, A., & Teuku, E. P. (2021). Failure Analysis of the Short Drive Shaft in a Screw Press Machine. *Key Engineering Materials*, 892, 74-80. doi:[10.4028/www.scientific.net/KEM.892.74](https://doi.org/10.4028/www.scientific.net/KEM.892.74)
- Ndirika, V. I. O., & Onwualu, A. P. (2016). *Design principles for post-harvest machines* (2nd Ed.). Naphtali Print, Nigeria.
- Okafor, B. E. (2015). Development of Palm Oil Extraction System. *International Journal of Engineering and Technology*, 5(2), 68-75.
- Olayanju, T. M. A., Akinoso, R., & Oresanya, M. O. (2006). Effect of Wormshaft Speed, Moisture Content and Variety on Oil Recovery from Expelled Beniseed. *Agricultural Engineering International: The CIGR Ejournal.*, 8, FP06 008.
- Savoire, R., Lanoisellé, J.-L., & Vorobiev, E. (2013). Mechanical Continuous Oil Expression from Oilseeds: A Review. *Food and Bioprocess Technology*, 6(1), 1-16. doi:[10.1007/s11947-012-0947-x](https://doi.org/10.1007/s11947-012-0947-x)
- Tagoe, S. M. A., Dickinson, M. J., & Apetorgbor, M. M. (2012). Factors influencing quality of palm oil produced at the cottage industry level in Ghana. *International Food Research Journal*, 19(1), 271-278.



Gazi University

**Journal of Science**

PART A: ENGINEERING AND INNOVATION

<http://dergipark.org.tr/gujisa>

## An Approach on Developing a Dynamic Wind-Solar Map for Tracking Electricity Production Potential and Energy Harvest

Fırat SALMANOĞLU<sup>1\*</sup> , Numan Sabit ÇETİN<sup>1</sup> <sup>1</sup>Ege University Solar Energy Institute Bornova İzmir

Keywords	Abstract
Renewable Energy Photovoltaic Wind Dynamic Map Optimization	Increasing energy demand brings in technical, environmental and economic problems as the production processes evolve. In this parallel, many countries are trying to satisfy the increasing energy demand using renewable energy sources. The scope of this study is to develop a mathematical model and data monitoring-evaluation software for wind and solar renewable energy sources, which can dynamically evaluate meteorological data measurements and make more precise energy harvest estimation with the data obtained. It is aimed to create a web based “Dynamic Wind-Sun Map of Turkey”. Through the developed software; instant data can be analyzed and instantaneous electrical energy values produced from wind and solar energy sources can be calculated. Thus, it can help create a system that allows regional management in energy production and is compatible. Within the scope of the study, a mathematical model expressing the problem was created by using some mathematical optimization methods. The created model was converted into a web-based software. PHP software development platform and MySQL database language were used during the software creation. The software developed within the scope of the study has analogues in the world literature. However, no study has been found in this context in Turkey. Especially since it can use real-time data and includes wind-photovoltaic calculations together, this software distinguishes it from its peers.

Cite
Salmanoğlu, F., & Çetin, N. S., (2022). An Approach on Developing a Dynamic Wind-Solar Map for Tracking Electricity Production Potential and Energy Harvest. <i>GU J Sci, Part A, 9(2)</i> , 62-78.

Author ID (ORCID Number)	Article Process
F. Salmanoğlu, 0000-0003-2975-9937	<b>Submission Date</b> 09.03.2022
N. S. Çetin, 0000-0002-4040-7097	<b>Revision Date</b> 02.06.2022
	<b>Accepted Date</b> 06.06.2022
	<b>Published Date</b> 07.06.2022

### 1. INTRODUCTION

With the technological change, the increase in energy demand shows itself day by day and this change naturally brings in technical, environmental and economic problems. According to International Energy Agency (IEA) data, global electrical energy demand decreased by about 1% in 2020 due to the effects of the Covid-19 pandemic. However, with the effect of the global economic recovery, the world electricity demand is expected to increase by 5% until the end of 2021 and by 4% in 2022. It is thought that almost half of this increase will come from fossil fuels, especially coal. This increase indicates that CO<sub>2</sub> emissions from the energy sector will reach record levels in 2022. 85% of this energy need in the world is expected to be met from fossil resources, also called limited resources (coal, oil, natural gas, etc.) (IEA, 2021).

Although the annual average growth in global energy consumption has slowed since 2020, it is predicted that the average annual growth in global energy consumption from 2010 to 2030 will be 1.7% (BP, 2011).

The Kyoto Protocol, which currently has 192 parties, was accepted on 11 December 1997, but entered into force on 16 February 2005 due to a complex ratification process. The Kyoto Protocol sets binding emission reduction targets for 37 industrialized countries and the European Union. Overall, the Protocol aims to contribute to an average of 5% emissions reductions compared to 1990 levels over the five-year period

\*Corresponding Author, e-mail: [firatsalmanoglu@gmail.com](mailto:firatsalmanoglu@gmail.com)

covering the first commitment period 2008-2012 ([UNFCCC, 2021](#)). Although this target has not been achieved yet, alternative ways of energy production are gaining more and more importance in order to respond to the increasing energy demand on the one hand and to reduce greenhouse gas emissions on the other. Renewable energy sources lead the way in these alternatives, and the most used energy sources in the world after fossil fuels are the Sun and Wind.

Within the scope of this study, a dynamic data source has been created to ensure reliable calculations and supply continuity, especially for wind and solar energy. The mathematical model and data monitoring and evaluation software developed here can dynamically process meteorological data measurements. The software analyzes instant data and optimizes the electrical energy values that can be produced instantly from wind and solar energy sources.

The increasing use of fossil fuels worldwide, especially after the industrial revolution, has caused many negative environmental effects and problems. Accordingly, research and development studies on the use of renewable energy sources have accelerated. One of the notable indicators of this is the recent increase in the funds allocated by developed countries for R&D studies for the use and expansion of clean energy resources.

Renewable energy sources do not emit greenhouse gases, which affect global climate conditions, within their energy conversion processes. Moreover, these resources are generally endless, inexhaustible and free, do not produce noise, allow electricity use in areas far from electricity networks and do not require much maintenance. The payback period for the initial investment costs is short and it is getting even shorter with the technological developments which both decreasing the initial costs and increasing the process efficiencies. Systems based on the Sun and wind, which are the most widely used renewable energy sources in the world today, also have an important role in creating regional employment.

As a result of the combustion of fossil fuels such as coal, petroleum derivatives and natural gas, various amounts of carbon dioxide (CO<sub>2</sub>) are emitted into the atmosphere depending on the amount of energy produced.

According to the International Energy Agency (IEA) data, although global CO<sub>2</sub> emissions decreased in 2020 due to the pandemic, they increased by about 5% in 2021, reaching the level of  $3.3 \times 10^{10}$  tons and approaching the 2018-2019 peak ([IEA, 2020](#)). Half of these greenhouse gas is released into the atmosphere, while the other half dissolves in the oceans and seas. This process introduces the concept of “Global warming” in parallel with the increase in the amount of greenhouse gases in the atmosphere. Accordingly, producing a decelerating solution to the global warming problem will only be possible using renewable energy sources.

Renewable energy sources are growing rapidly in the global market and are at the focus of attention for researchers and the industry. It is vital for investment and investor to determine the field to be invested in, and examine the field's characteristics in a multi-faceted manner, especially for wind and solar energy investments, since they are time dependent and intermittent. The largest obstacle in front of investments in renewable energy sources is the high initial investment costs. In this case, the first question that comes to the mind of the investor is how many years the system will pay itself back. For this reason, potential determination in the region where the implementation will be made is very important in terms of the payback period of the system. As a result of the literature review conducted within the scope of this study, it is seen that the studies on data monitoring and evaluation started in the 90s. However, it was seen that the studies on monitoring and potential determination in renewable energy systems intensified at the end of the 90s ([NREL, 2021](#)). In this study, a software has been developed that dynamically evaluates high-resolution data coming from data measurement stations located at specific measurement points and presents the outputs obtained as a dynamic evaluation map, unlike the theoretical studies we usually encounter.

In Turkey, there are static wind and solar energy maps, which are studied by the Renewable Energy Resources Branch Directorate of the Ministry of Energy and Natural Resources, and there is no study that includes dynamic and comprehensive calculations ([EİGM, 2022a, 2022b](#)).



When we take a look at the international literature, dynamic data for Wind, Solar, Biomass, Hydrogen and Geothermal energy sources developed by the Geographic Information System (GIS) team of “National Renewable Energy Laboratory – NREL”, one of the world's largest renewable energy laboratories in the United States. maps were created and these studies were seen to be a structure that has been started since 1986. NREL's Geographic Information Systems team presents high-resolution wind and solar data and analyzes for the evaluation of wind and solar resources in the United States, with the dynamic map developed similar to the software we developed in this study. The national wind and solar resource assessment studies initiated by NREL for the US Department of Energy in 1986 were published as the US Wind and Solar Energy Atlas in October of the same year (NREL, 2021).

The resulting software package aims to create a resource that can be a reference for scientific research and researchers, as well as institutions and organizations working in this field. The lack of a reliable database and source in this sector and the static nature of the available maps for Turkey, would underline the value of successful development of such dynamic wind-solar maps to be presented to the sector. The software developed within the scope of the study has analogues in the world literature. However, no study has been found in this context in Turkey. Especially since it can use real-time data and includes wind-photovoltaic calculations together, this software distinguishes it from its peers.

## 2. MATERIAL AND METHOD

Within the scope of the study, the following calculation methods were used.

### 2.1. Calculations for Photovoltaics

#### Sun Angles

Some of the sun angles taken into account in the calculations are given in (Honsberg & Bowden, 2019). (Figure 1)

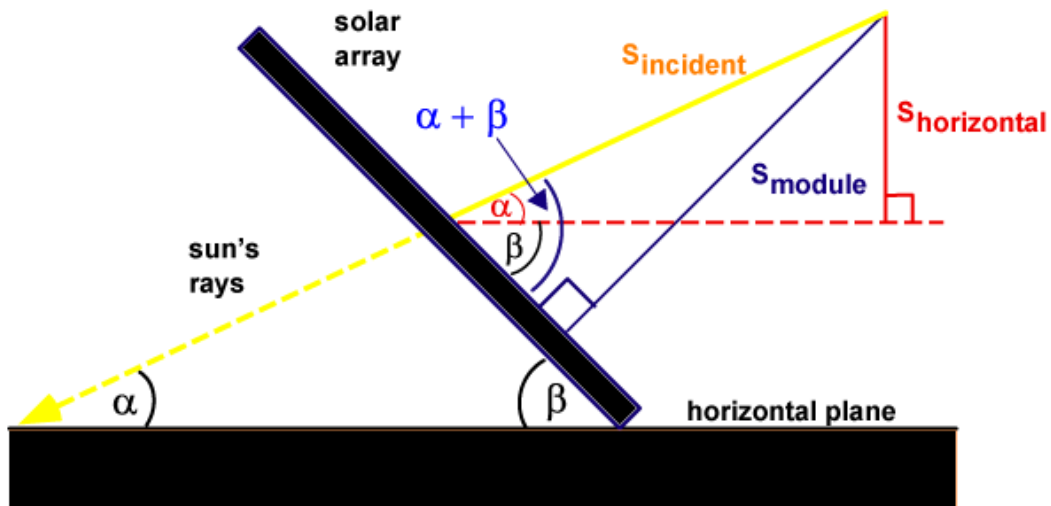
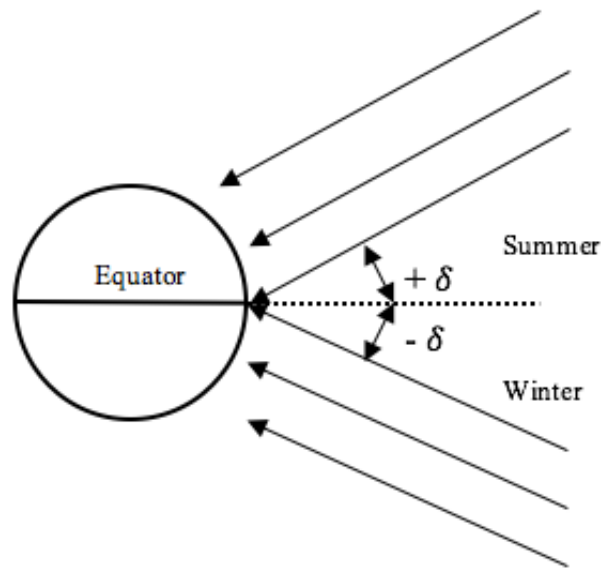


Figure 1. Sun angles (Honsberg & Bowden, 2019)

**Declination Angle,  $\delta$ :** It is the angle that the sun's rays make with the earth's equatorial plane. It can also be defined as the angle between the direction connecting the centers of Sun and Earth and its projection on the equatorial plane (Stanciu & Stanciu, 2014). (Figure 2)

The declination angle takes the extreme values of  $-23.45^\circ$  at the winter solstice on December 21<sup>st</sup> and  $+23.45^\circ$  at the summer solstice of June 21<sup>st</sup>. On March 21<sup>st</sup> at the spring equinox and September 21<sup>st</sup> at the autumn equinox, the declination angle becomes zero (Stanciu & Stanciu, 2014). (Figure 3)



**Figure 2.** Declination angle

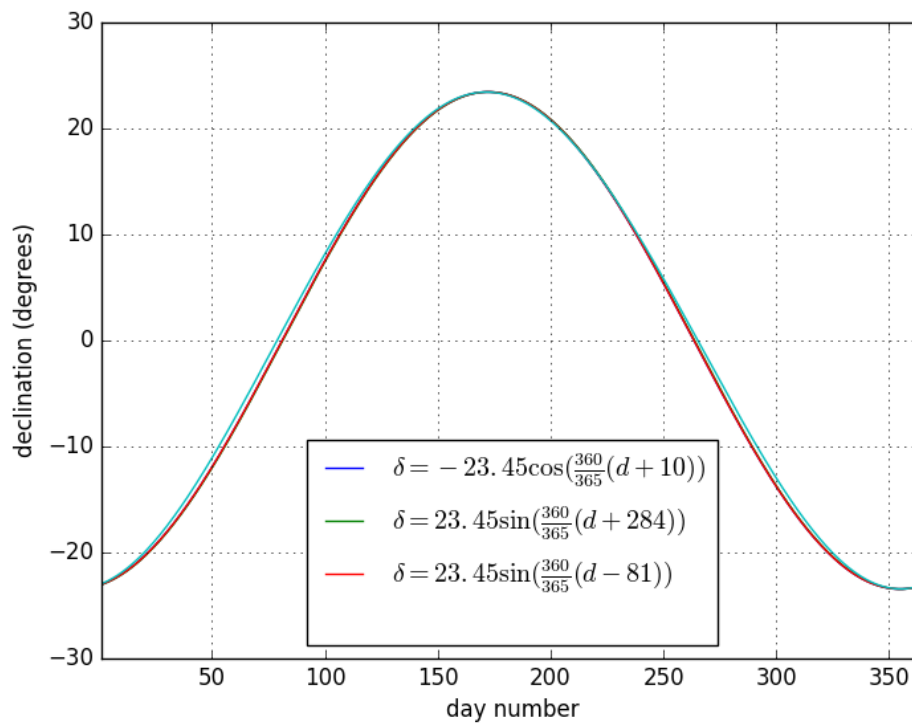


**Figure 3.** Variation of declination angle according to months

Declination Angle, with  $n$  number of days starting from January 1<sup>st</sup>, which is the first day of the year, with Equation 1;

$$\delta = 23,45 \times \sin (360 \times (284 + n) / 365) \quad (1)$$

is calculated as (Stanciu & Stanciu, 2014).

**Optimum Tilt Angle,  $\beta_{opt}$ :** It is the angle that the PV panel must make with the horizontal plane in order for the sun rays to fall vertically on the PV panel. It is calculated with Equation 2 (Sharma et al., 2021).

$$\beta_{opt} = \phi - \delta \quad (2)$$

### Calculation of Incoming Radiation Value to a Sloped and South Deflected Surface

In order to achieve maximum energy conversion in PV systems, the sun's rays must come to the PV panel at a right angle and the PV panels must be placed facing south. However, in some cases, it may not be possible to capture this environment. Therefore, if the standing angle ( $\beta$ ) of the PV panel on the plane and the angle of deviation from the south ( $\sigma$ ) are known, the solar radiation value ( $S_{module}$ ) on the PV panel at that moment can be calculated by the model expressed in Equation 3 (Honsberg & Bowden, 2019; Takilalte et al., 2020; Amiri et al., 2021).

$$S_{module} = S_{incident} \cdot (\cos \alpha \cdot \sin \beta \cdot \cos \sigma + \sin \alpha \cdot \cos \beta) \quad (3)$$

$$S_{incident} = S_{horizontal} / \sin \alpha \quad (4)$$

### System Efficiency

No system works with 100% efficiency. Every component, and therefore every system containing these components, has a conversion efficiency calculated accordingly. In PV systems, the system efficiency is calculated with Equation 5 (Salmanoğlu & Çetin, 2013).

$$\eta_{sys} = \eta_{PV} \times \eta_{inv} \times \eta_{bat} \times 0,9 \quad (5)$$

$\eta_{sys}$  : system efficiency,

$\eta_{PV}$  : PV panel efficiency,

$\eta_{inv}$  : inverter efficiency,

$\eta_{bat}$  : battery efficiency.

In this model, PV panel efficiency is an effective element when calculating system efficiency  $\eta_{sist}$ . The effect of temperature on  $\eta_{PV}$ , which is expressed as PV panel efficiency, is calculated with the model expressed in Equation 6 (Sultan et al., 2020).

$$\eta_{PV} = \eta_r [1 - \beta_T (T_c - T_r)] \quad (6)$$

$\eta_r$  : module efficiency expressed by the module manufacturer,

$\beta_T$  : string efficiency temperature coefficient,

$T_c$  : average monthly cell temperature,

$T_r$  : reference temperature given for cell efficiency.

### Calculation of the Annual Expected Energy Harvest Against the Determined PV Panel Installed Power

The model in Equation 7 is used when calculating the annual electrical energy production for the electrical energy produced by the photovoltaic method from solar energy (Salmanoğlu & Çetin, 2013).

$$G_{PV} = \sum_{k=1}^{8760} \eta_{sys} \cdot I_k \quad (7)$$

$I_k$  : total solar radiation on 1 m<sup>2</sup> area at the k hour of the year, kWh/m<sup>2</sup>,

$G_{PV}$  : annual energy harvest of 1 m<sup>2</sup> photovoltaic panel.

The mathematical model on which the software developed within the scope of this study was built, accepts readily available data provided by meteorological measurement stations as input and transform them into an adjusted and utilizable form. These data and derived results of the calculations are then presented dynamically to the user. The outputs are also rendered and shown on a map which is a powerful and comprehensive user interface choice.

## 2.2. The Calculation for Wind Power System

The primary parameter in calculating the electrical power obtained from the turbine is the wind speed and it is directly related to the height at which the measurement was made. For this reason, the measured wind speed values must be converted to the height at which the turbine is installed. Based on this conversion, it is possible to calculate the energy and power of the system or the site to be installed more reliably.

In the literature, the ‘‘Hellman Equation’’ expressed in Equation 8 is used in order to calculate the wind speed according to altitude mathematically (Salmanoğlu & Çetin, 2013). Wind speed data are obtained from the wind measurement station at a height of 30m, located within the Ege University Solar Energy Institute. The Hellman elevation equation is used to calculate the wind speed at tower height according to the wind turbine selected from the database.

$$V_r = V_{ref} \cdot (H/H_{ref})^\mu \quad (8)$$

$V_r$  : wind speed (m/s) to be obtained as a result of the calculation (wind speed value increased to tower height),

$V_{ref}$  : reference wind speed (m/s) used in the calculation,

$H$  : hub height (m),

$H_{ref}$  : reference height (m),

$\mu$  : friction coefficient (Table 1).

**Table 1.** Friction coefficient for a variety of landscapes (Suvire, 2011)

Landscape type	Friction coefficient
Lakes, ocean and smooth hard ground	0.10
Grasslands (ground level)	0.15
Tall crops, hedges and shrubs	0.20
Heavily forested land	0.25
Small town with some trees and shrubs	0.30
City areas with high rise buildings	0.40

The mathematical expression that can be used to obtain the power output characteristic of the wind turbine for the wind speed values derived for the desired heights with the Hellman equation is given in Equation 9. Wind speed measurements should be taken at two different heights at each measurement tower. Thus, the actual values of the roughness coefficient in the environment will be computable (Fotso et al., 2021).

$$P_W(V_r) = \begin{cases} 0, & V_r < V_{ci} \\ C_p \cdot \left(\frac{1}{2} \cdot \rho \cdot (\pi \cdot r^2) \cdot V^3\right), & V_{ci} < V_r < V_{rated} \\ P_r, & V_{rated} < V_r < V_{co} \\ 0, & V_r > V_{co} \end{cases} \quad (9)$$

$P_W(V_r)$  : power generation of wind turbine at  $V_r$  wind speed (W),

$P_r$  : rated power of wind turbine (W),

$V_r$  : wind speed at hub height (m/s),

$V_{ci}$  : cut-inn wind speed (m/s),

$V_{rated}$  : wind speed at the rated power of the wind turbine (m/s),

$V_{co}$  : cut-out wind speed (m/s).

Wind speed exhibits a fluctuating structure during the day. For this reason, wind blowing times should be known in the calculation of electrical energy obtained from wind energy. When this data is not present, it is essential to derive it using a proper mathematical approach. to synthetically derive it using a proper mathematical approach. Wind blowing times for the locations where no measurements are taken can be calculated from the meteorological data obtained from surrounding locations. For this calculation, “Rayleigh Distribution Function” and “Weibull Function”, which are continuous probability distributions, are frequently used in probability theory and statistical sciences. The hourly blowing times of the wind speed are calculated with the help of the “Rayleigh Distribution Function” as in Equation 10 (Serban et al., 2020).

$$h_r = 1 \cdot \frac{\pi}{2} \cdot (V_i / V_{ave}^2) \cdot e^{-\frac{\pi}{4} (V_i / V_{ave})^2} \quad (10)$$

Here;

$V_i$  : wind speed to be calculated (m/s),

$V_{ave}$  : average wind speed (m/s),

$h_r$  : daily blowing time (h).

As a result of these calculations, the hourly electrical energy value obtained from the wind turbine planned to be used in a wind power system can be calculated with the model in Equation 11.

$$G_W = \sum_{i=1}^{8760} \sum_{j=1}^{25} h_{r,i,j} \cdot C_p \cdot \left(\frac{1}{2} \cdot \rho (\pi r^2) \cdot V^3\right) / 1000 \quad (11)$$

Here,

$h_{r,i,j}$  : wind blowing time at  $i$  m/s wind speed at  $j$  hour of the year,

$C_p$  : wind turbine power coefficient.

### 2.3. Database Design

The software developed here was designed in a modular structure. The modules of the software are;

- Dynamic Data Monitoring Module,
- System Design Module
- Calculation Module,
- Carbon Footprint and Depreciation Calculation Module
- Reporting Module

System design and carbon footprint modules are hosted on the local server and the relevant data is stored in its own database. The Calculation and Reporting modules requires a valid password provided by the user. Access control is performed with a password to be determined and controlled via an application programming interface (API) running on the user side. The developer server hosts the password and license validity information in its database and answers the requests within license coverage. The general structure of the system can be seen in Figure 4.

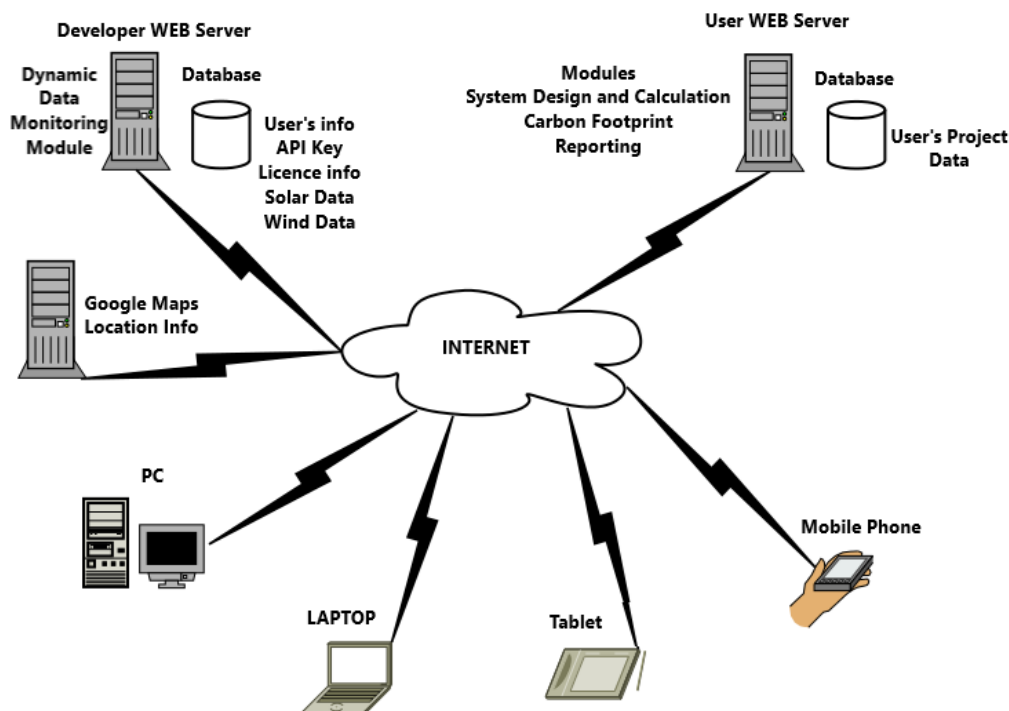


**Figure 4.** Working of the software over the internet

The software is developed with PHP programming language and user information is stored in MySQL database. The reasons for choosing this duo are that they provide all software needs, are open source and have low licensing costs.

Calculation and Reporting modules are hosted on the developer server and users with software licenses can benefit from these modules via WEB Service. The user requests account results, reports and analyzes from the WEB Service software on the developer servers. If the password (API password) transmitted with the request is valid, the modules fulfill the requests and send the results in JSON format to the user server. The flow diagram, which algorithmically expresses the working stages required to create a dynamic wind-solar map, is given in Figure 5.

The database developed in the MySQL environment generally contains user and project information, dynamic meteorological information and tables containing the definitions of the components used in the system and the relationship between these tables. Some examples of tables in the database are shown in Figures 6-9.

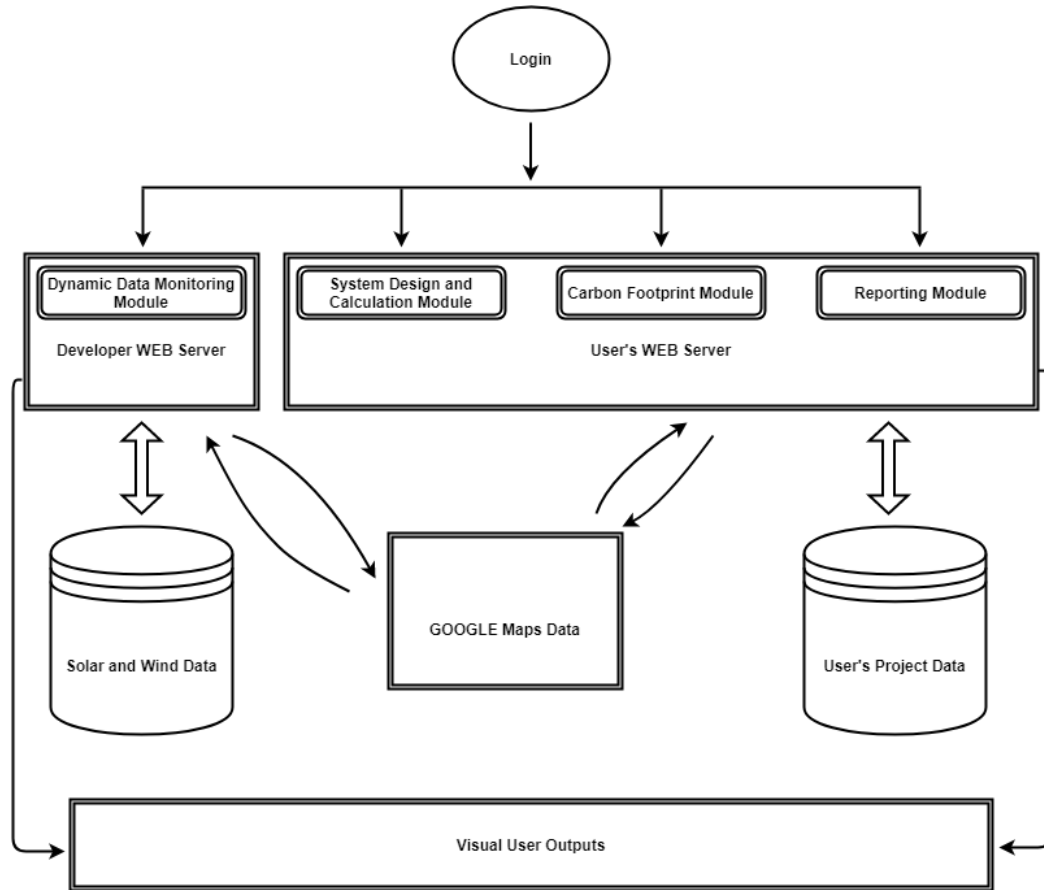


Figure 5. General working principle of the designed system

Sunucu: localhost » Veritabanı: ralenpro » Tablo:

Gözet Yapı SQL Ara Ekle

Tablo yapısı İlişki görünümü

#	Adı	Türü	Karşılaştırma	Öznitelik
<input type="checkbox"/>	1 id	int(11)		
<input type="checkbox"/>	2 textid	varchar(100)	utf8_turkish_ci	
<input type="checkbox"/>	3 username	varchar(100)	utf8_turkish_ci	
<input type="checkbox"/>	4 uname	varchar(100)	utf8_turkish_ci	
<input type="checkbox"/>	5 email	varchar(100)	utf8_turkish_ci	
<input type="checkbox"/>	6 password	varchar(64)	utf8_turkish_ci	
<input type="checkbox"/>	7 status	int(1)		
<input type="checkbox"/>	8 created	timestamp		
<input type="checkbox"/>	9 level	int(1)		

↑  Tümünü işaretle Seçilileri: Gözet

Merkezi sütunlardan kaldır

Figure 6. Table containing user information in the designed database

The screenshot shows a database management interface with the following table structure for 'projects':

#	Adı	Türü	Karşılaştırma	Öznitelikler
1	id	int(11)		
2	project_name	varchar(100)	utf8_turkish_ci	
3	description	varchar(255)	utf8_turkish_ci	
4	project_type	int(1)		
5	pid	int(11)		
6	uid	varchar(64)	utf8_turkish_ci	
7	created	timestamp		on update CURRENT_TIMESTAMP
8	status	int(1)		

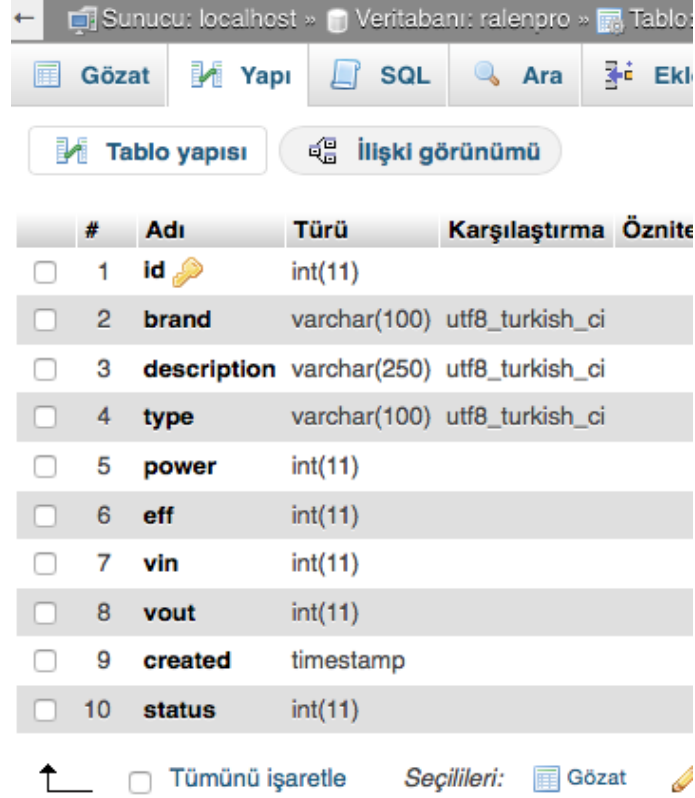
Figure 7. Table for project information in the designed database

The screenshot shows a database management interface with the following table structure for 'pv':

#	Adı	Türü	Karşılaştırma	Öznitelikle
1	id	int(11)		
2	type	varchar(50)	utf8_turkish_ci	
3	power	int(11)		
4	eff	double		
5	height	int(11)		
6	width	int(11)		
7	created	timestamp		
8	status	int(11)		

Figure 8. Table for PV panel information in the designed database





#	Adı	Türü	Karşılaştırma	Öznite
<input type="checkbox"/>	1 id	int(11)		
<input type="checkbox"/>	2 brand	varchar(100)	utf8_turkish_ci	
<input type="checkbox"/>	3 description	varchar(250)	utf8_turkish_ci	
<input type="checkbox"/>	4 type	varchar(100)	utf8_turkish_ci	
<input type="checkbox"/>	5 power	int(11)		
<input type="checkbox"/>	6 eff	int(11)		
<input type="checkbox"/>	7 vin	int(11)		
<input type="checkbox"/>	8 vout	int(11)		
<input type="checkbox"/>	9 created	timestamp		
<input type="checkbox"/>	10 status	int(11)		

**Figure 9.** Table for inverter information in the designed database

### 3. RESULTS AND DISCUSSION

Since the number of data providing stations was limited during the tests of the study, a data generator was developed to generate random data to be used in the software. The random data produced in certain ranges and properties, were used to input dynamic evaluation and modeling software. It has been proven that the mathematical model and the developed software structure work smoothly with virtual data.

Software is able to read and process the parametric values like wind speed and direction, temperature, pressure, humidity, and solar irradiation within one-minute resolution.

The software and the mathematical model it contains can calculate and report;

- Optimum angle for PV panel placement,
- Hourly, daily, monthly, annual energy harvest according to the selected PV panel and wind turbine characteristics,
- Avoided carbon emissions,
- Southward deviation energy losses in PV systems,
- Energy losses in PV systems deviating from the optimum angle,
- Optimum system design according to the energy consumption specified by the user.

Screenshots of the developed software and the function of each software module are explained below.

#### Developed Software

When the user accesses the system website over the internet, the “User Login Screen” appears in Figure 10, which requests user information and queries whether the user has permission to access the system.

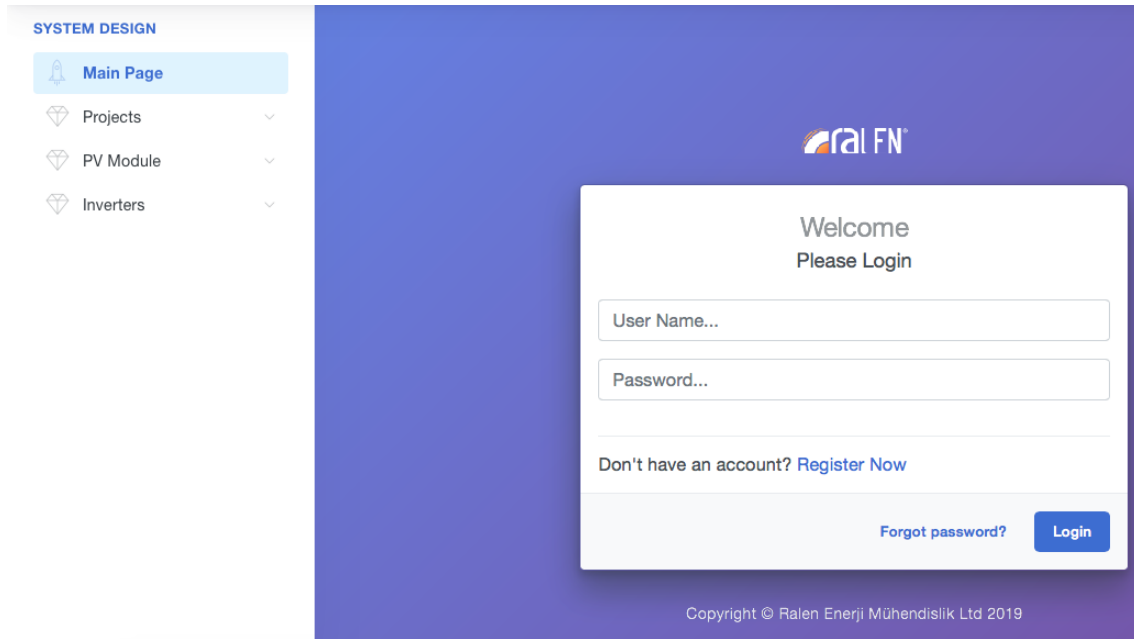


**Figure 10.** User login

The user can sign in to the system with the valid “User Name” and “Password” pair assigned to him/her, and if he/she does not have a User Name and Password, they can sign up to the system via this screen.

Once the user provides this information and the connection to the system is established, the “Module Selection Screen” shown in Figure 11 is shown.

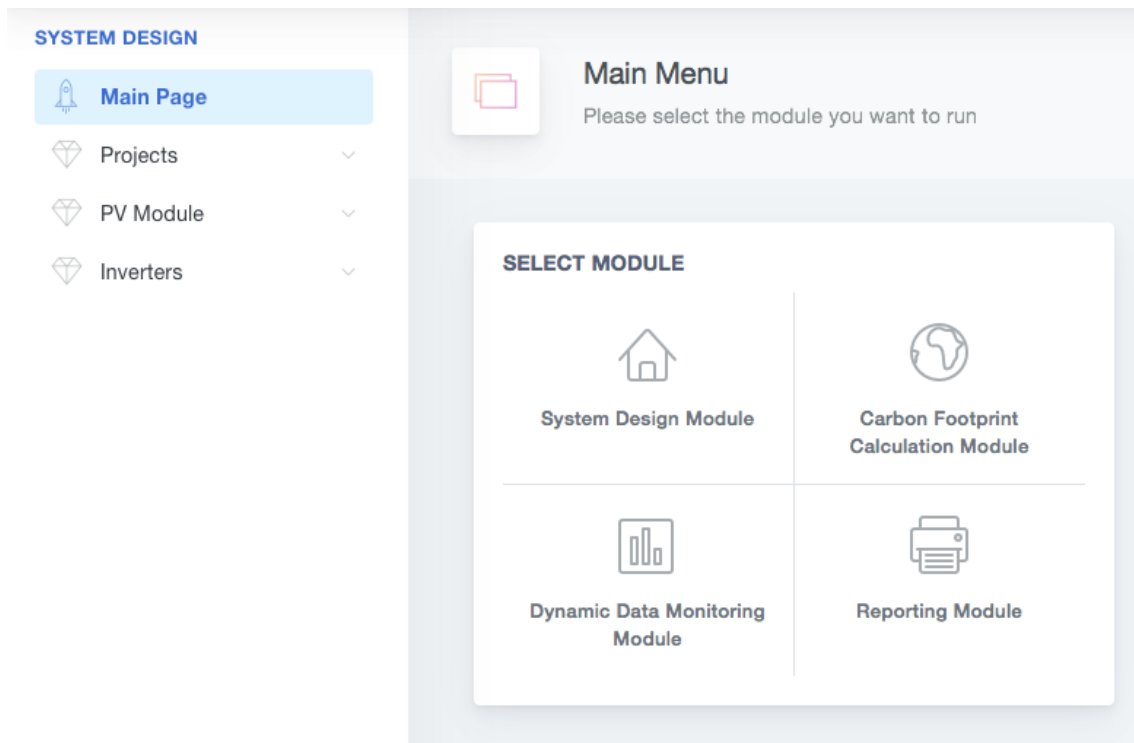


**Figure 11.** Module selection

The user can choose among the four main modules on this screen.

When the “System Design” module is clicked, firstly, basic information like the “Project Name” and “Project Type” of the project is requested to be entered in the screen shown in Figure 12.



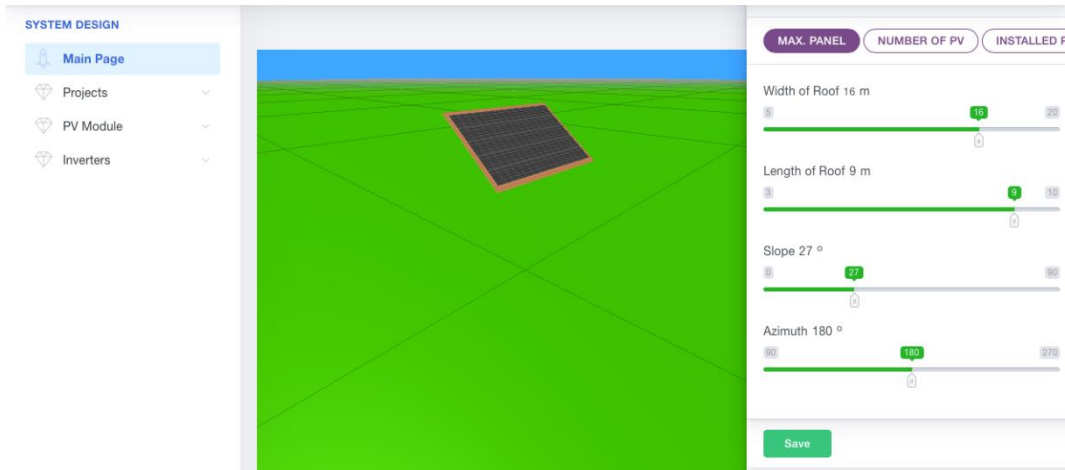


**Figure 14.** System design module system properties determination screen

When the “Dynamic Data Monitoring Module” is clicked by the user via the Module Selection Screen, the change of wind-sun and other meteorological data for the previously selected location is dynamically presented to the user on this screen. When the “Data Reporting” button in this module is clicked, the data is reported according to the selected date range and the data is presented to the user graphically, as shown in Figure 15.

Information regarding the energy harvest and electricity savings of the designed system for the selected location is presented below.

Location : Izmir/Bornova  
 Irradiation : 5524 Wh/m<sup>2</sup> – day  
 Optimum Angle : 32°  
 Temperature : 25 °C  
 Shading : There is no shadowing in the area

Print

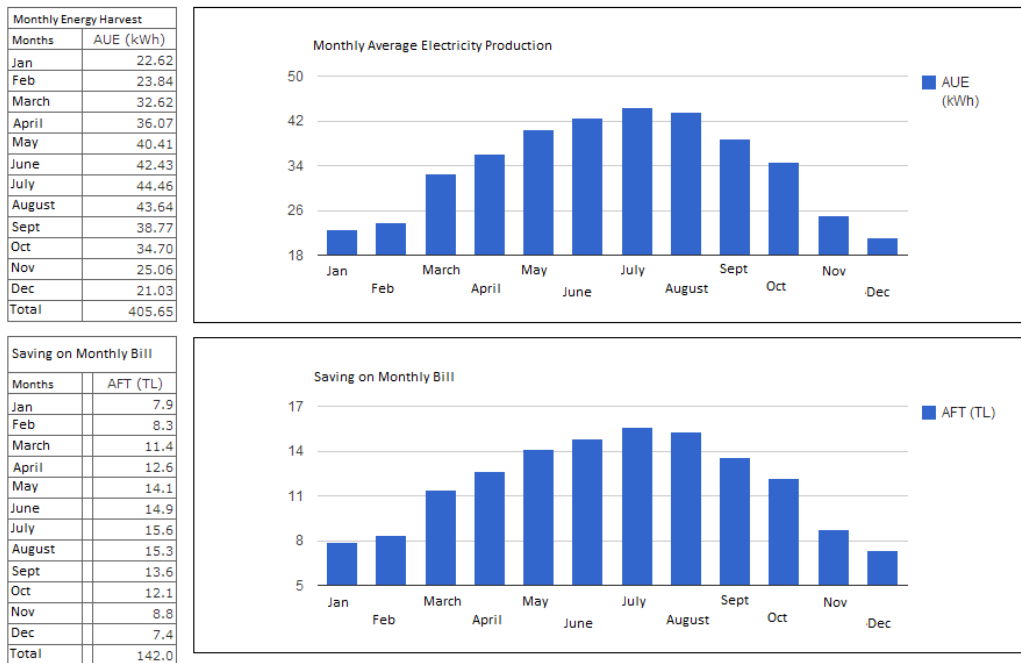


**Figure 15.** Dynamic data monitoring module data tracking and display screen

When the user clicks on “Reporting Module” via the Module Selection Screen, periodic reports on wind-sun and other meteorological data for the location previously selected by the user are presented to the user on this screen. When the location is selected by the user and the “Report” button is clicked on this module screen, the software asks the user for which date range, how often and what quality data they need.

The reporting of the following data, including annual, monthly, daily and hourly, can be done through this module.

- Average Radiation
- Average Wind Speed
- Average Wind Direction
- Average Temperature, Humidity, Pressure

In addition, for a wind-PV system designed and recorded with the “System Design Module” previously, the expected potential energy harvest in annual, monthly, daily and hourly periods can also be reported to the user via the “Reporting Module” as in Figure 16.

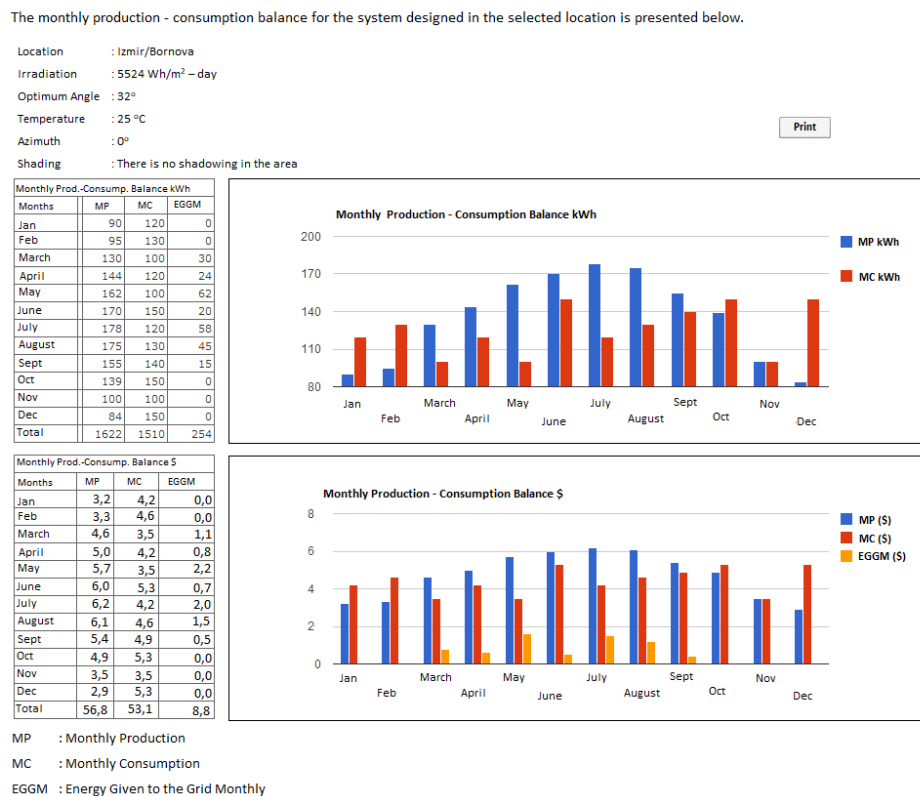


Figure 16. Reporting module report screen

#### 4. CONCLUSION

As an example of the output provided by the software, the static wind and solar maps produced by the General Directorate of Renewable Energy Resources in Turkey can be shown. Among these examples, only long-term data obtained from 60 wind measurement stations and meteorology stations throughout Turkey (for weather forecasting) were used for REPA. This small number of samples is insufficient to make reliable investments and precise predictions. Moreover, these existing maps are static in nature and do not rely on real-time data analysis and thus, do not have a dynamic continuity. The software developed with this study is important in that it can make calculations based on real measurement data in high resolution and that the obtained data can be observed dynamically.

The web-based software that emerged as a result of this study has a very high potential for being commercially utilized both as a finished product and an embedded tool. More than personal use, it is planned to seek a corporate membership/subscription required for access to the software. In this context, it is planned to generate user-based income from the software by converting the software into a commercial product in the future. As the target group; Large-scale system investors, Universities, System installation companies, Electricity Distribution Companies and related public institutions/organizations can be mentioned.

**CONFLICT OF INTEREST**

The authors declare no conflict of interest.

**NOMENCLATURE**

- $\delta$  : declination angle
- $\beta_{opt}$  : optimum tilt angle
- $\sigma$  : azimuth angle
- $S_{module}$  : the solar radiation value on the PV panel at the tilt angle
- $\eta_{sys}$  : system efficiency
- $\eta_{PV}$  : PV panel efficiency
- $\eta_{inv}$  : inverter efficiency
- $\eta_{bat}$  : battery efficiency
- $\eta_r$  : module efficiency expressed by the module manufacturer
- $\beta_T$  : string efficiency temperature coefficient
- $T_c$  : average monthly cell temperature
- $T_r$  : reference temperature given for cell efficiency
- $I_k$  : total solar radiation on 1 m<sup>2</sup> area at the k hour of the year, kWh/m<sup>2</sup>
- $G_{PV}$  : annual energy harvest of 1 m<sup>2</sup> photovoltaic panel
- $V_r$  : wind speed (m/s) to be obtained as a result of the calculation
- $V_{ref}$  : reference wind speed (m/s) used in the calculation
- $H$  : hub height (m)
- $H_{ref}$  : reference height (m)
- $\mu$  : friction coefficient
- $P_w(V_r)$  : power generation of wind turbine at  $V_r$  wind speed (W)
- $P_r$  : rated power of wind turbine, (W)
- $V_r$  : wind speed at hub height (m/s)
- $V_{ci}$  : cut-in wind speed, (m/s)
- $V_{rated}$  : wind speed at the rated power of the wind turbine, (m/s)
- $V_{co}$  : cut-out wind speed, (m/s)
- $V_i$  : wind speed to be calculated (m/s)
- $V_{ave}$  : average wind speed (m/s)
- $h_r$  : daily blowing time (h)
- $h_{r,i,j}$  : wind blowing time at i m/s wind speed at j hour of the year
- $C_p$  : wind turbine power coefficient

**REFERENCES**

- Amiri, B., Gómez-Orellana, A. M., Gutiérrez, P. A., Dizène, R., Hervás-Martínez, C., & Dahmani, K. (2021). A novel approach for global solar irradiation forecasting on tilted plane using Hybrid Evolutionary Neural Networks. *Journal of Cleaner Production*, 287, 125577. doi:[10.1016/j.jclepro.2020.125577](https://doi.org/10.1016/j.jclepro.2020.125577)
- BP (January 2011). Energy Outlook 2030. (Accessed:22/04/2022) [URL\(PDF\)](#)
- EİGM, General Directorate of Energy Affairs (2022a). Solar Energy Potential Atlas, *Güneş Enerjisi Potansiyel Atlası, GEPA*. (Accessed:22/04/2022) [URL](#)
- EİGM, General Directorate of Energy Affairs (2022b). Turkey Wind Energy Potential, *Türkiye Rüzgâr Enerjisi Potansiyeli, REPA*. (Accessed: 22/04/2022) [URL](#)
- Fotso, H. R. F., Kazé, C. V. A., & Kenmoé, G. D. (2021). Real-time rolling bearing power loss in wind turbine gearbox modeling and prediction based on calculations and artificial neural network. *Tribology International*, 163, 107171. doi: [10.1016/j.triboint.2021.107171](https://doi.org/10.1016/j.triboint.2021.107171)
- Honsberg, C. B., & Bowden, S. G. (2019). Solar Radiation on a Tilted Surface. (Accessed:27/10/2021) [URL](#)
- IEA, International Energy Agency (2020). Global Energy Review 2019. doi:[10.1787/90c8c125-en](https://doi.org/10.1787/90c8c125-en)
- IEA, International Energy Agency (2021). Electricity Market Report, July 2021. doi:[10.1787/f4044a30-en](https://doi.org/10.1787/f4044a30-en)
- NREL, National Renewable Energy Laboratory (2021). Geospatial Data Science. (Accessed:23/10/2021) [URL](#)
- Salmanoğlu, F., & Çetin, N. S. (2013). The software package for design optimization of the wind/photovoltaic autonomous hybrid power system: A case study for Ankara city. *Energy Sources, Part A: Recovery, Utilization, and Environmental Effects*, 35(20), 1946-1955. doi:[10.1080/15567036.2011.572114](https://doi.org/10.1080/15567036.2011.572114)
- Serban, A., Paraschiv, L.S., & Paraschiv, S. (2020). Assessment of wind energy potential based on Weibull and Rayleigh distribution models. *Energy Reports*, 6, 250-267. doi: [10.1016/j.egy.2020.08.048](https://doi.org/10.1016/j.egy.2020.08.048)
- Sharma, A., Kallioğlu, M. A., Awasthi, A., Chauhan, R., Fekete, G., & Singh, T. (2021). Correlation formulation for optimum tilt angle for maximizing the solar radiation on solar collector in the Western Himalayan region. *Case Studies in Thermal Engineering*, 26, 101185. doi:[10.1016/j.csite.2021.101185](https://doi.org/10.1016/j.csite.2021.101185)
- Stanciu, C., & Stanciu, D. (2014). Optimum tilt angle for flat plate collectors all over the World - A declination dependence formula and comparisons of three solar radiation models. *Energy Conversion and Management*, 81, 133-143. doi:[10.1016/j.enconman.2014.02.016](https://doi.org/10.1016/j.enconman.2014.02.016)
- Sultan, S. M., Tso, C. P., & Efan, M. N. E. (2020). A new approach for photovoltaic module cooling technique evaluation and comparison using the temperature dependent photovoltaic power ratio. *Sustainable Energy Technologies and Assessments*, 39, 100705. doi:[10.1016/j.seta.2020.100705](https://doi.org/10.1016/j.seta.2020.100705)
- Suvire, G. O. (2011). *Wind Farm: Technical Regulations, Potential Estimation and Siting Assessment*. In Tech Publishing.
- Takilalte, A., Harrouni, S., Yaiche, M. R., & Mora-López, L. (2020). New approach to estimate 5-min global solar irradiation data on tilted planes from horizontal measurement. *Renewable Energy*, 145, 2477-2488. doi:[10.1016/j.renene.2019.07.165](https://doi.org/10.1016/j.renene.2019.07.165)
- UNFCCC, United Nations Climate Change (2020). What is the Kyoto Protocol? (Accessed:20/10/2021) [URL](#)



Gazi University

**Journal of Science**

PART A: ENGINEERING AND INNOVATION

<http://dergipark.org.tr/gujisa>

# Radiochemical Procedure for Measurement Specific Activities of Uranium Isotopes in Asphaltite Bioleaching Liquor by Alpha-Particle Spectrometry

Meryem SEFERİNOĞLU<sup>1,2\*</sup> <sup>1</sup>Luleå University of Technology, Department of Chemical and Metallurgical Engineering, Division of Process Metallurgy, Sweden<sup>2</sup>Sinop University Faculty of Engineering and Architecture, Department of Nuclear Engineering, Türkiye

Keywords	Abstract
Radiochemical Separation Bioleaching Liquor Uranium Measurement Alpha-Particle Spectrometry	An analytical procedure for the alpha-source preparation is investigated in the study to determine uranium radioisotopes specific activities in the bioleaching liquor leach from asphaltite samples taken from the Silopi region in Türkiye. The purpose is to develop a new radiochemical method that can provide the alpha-particle spectrometry requirements. The proposed analytical procedure includes sample preparation, radiochemical purification of uranium from bioleaching liquor, alpha-source preparation on a substrate and alpha-particle spectrometric analysis of isolated uranium. The method is valid for availability using the z-test, relative bias, and relative uncertainty outlier tests. The results show that the proposed analytical procedure is successfully implemented for measuring the activity concentration of uranium with high accuracy and precision in the bioleaching liquor.
Cite	
	Seferinoğlu, M. (2022). Radiochemical Procedure for Measurement Activity Concentration of Uranium in Asphaltite Bioleaching Liquor by Alpha-Particle Spectrometry. <i>GU J Sci, Part A, 9(2)</i> , 79-86.
Author ID (ORCID Number)	Article Process
M. Seferinoglu, 0000-0002-3260-6598	<b>Submission Date</b> 16.05.2022 <b>Revision Date</b> 25.05.2022 <b>Accepted Date</b> 07.06.2022 <b>Published Date</b> 08.06.2022

## 1. INTRODUCTION

The rapid increase of nuclear power plants leads to the progressive depletion of high-grade reserves of uranium ores and also increases tailing generation produced by uranium mining activities (Abhilash & Pandey, 2013; Sarkar, 2019). The sustained depletion of high-grade uranium reserves and raised awareness about environmental degradation due to the conventionally extracted methods give rise to the development of a new extraction technique that is efficient, less polluting, and economic to recover uranium from low-grade deposits and secondary sources. Biological leaching is simple, efficient, less polluting, and relatively less expensive including low energy consumption. Therefore this technique is a suitable alternative procedure and rapidly expanding worldwide to leach uranium from low-grade sources (Pal et al., 2010; Abhilash et al., 2013). The micro-organisms used in the bioleaching process catalyze the oxidizing and reducing reaction of uranium along with related metals and hence the uranium solubility. Most uranium deposits consist of a mixture of uranium-bearing minerals in either U(IV) or U(VI) state. The solubility of uranium varies depending on the oxidation state. The oxidation state being U(VI) is the most soluble form of uranium. The bioleaching mechanism of uranium is mainly controlled by the common action of iron (III) and protons produced by the micro-organisms. They use either iron or sulfur as an energy source for their growth. U(IV) is oxidized to the soluble form of uranium by ferric ions, and the rate of oxidation increases when micro-organisms like *Acidithiobacillus ferrooxidans*. Kinetics of uranium leaching occurs much more rapidly when the redox potential (Fe(III)/Fe(II) ratio) of the leaching solution is high (Eisapour et al., 2013).

Asphaltite is a petroleum-derived substance that is classified as a solid aromatic asphaltic oil containing mineral matter primarily sulfates, carbonates, silicates, and sulfides. Variations in oil deposits during migration

\*Corresponding Author, e-mail: [mseferinoglu@sinop.edu.tr](mailto:mseferinoglu@sinop.edu.tr)



and solidification result in the formation of asphaltic substances (Ballice, 2002; Hiçyılmaz & Altun, 2006; Saydut et al., 2008). Apart from compositions originating from petroleum, these substances are associated with mineral matter consisting of valuable metals like molybdenum, nickel, vanadium, and radioactive elements such as uranium and thorium. Although the abundance of uranium and thorium is in the low range, a cost-effective method of extraction can make asphaltite a viable alternative source. Biological leaching can play a crucial role as a cost-effective method. Hence, the measurement of radionuclide activities in the bioleaching liquor is very important in determining uranium recovery.

The uranium activity of the leaching liquor is measured by alpha-particle spectrometry which is among the most accurate and precise methods for alpha-emitting radionuclides (Aggarwal, 2016). Nevertheless, the spectrometric measurement requires very pure, uniform, and thin alpha sources. Because of competing significant salt contributions, known as "matrix effects," determining the specific activity of uranium in bioleaching liquor is usually exceedingly difficult. These effects are especially troublesome since they strongly depend on the composition of bioleaching solution and mineralogical components in asphaltite.

The study is aimed to develop a radio-analytical technique for evaluating the activity concentration of uranium radioisotopes in the leaching liquor obtained by bioleaching of asphaltite with a mixed culture containing iron oxidizers, sulfur oxidizers, and a few archaeal species. The radiochemical separation of the radionuclide of interest from all other interfering elements, radioactive or non-radioactive in the leaching liquor, is essential before the measurement of alpha sources since the interfering elements create a lower spectral resolution and higher detection limit (Reis et al., 2011; Zhu et al., 2015; Reis & Monterio, 2020).

## 2. MATERIAL AND METHOD

The radio-analytical method is conducted by four main steps; i) source preparation, ii) radiochemical separation, iii) alpha-source preparation, and iv) counting of alpha-source. Every step may and can contribute to the error propagation in the measurement of the specific activity. To overcome the propagation, the study presents improvements in source preparation and radiochemical separation methods to avoid the interfering elements in the alpha spectrum of the bioleaching liquor.

### 2.1. Instrumentation and Calibration

Alpha-particle spectrometry was performed for the measurement of the specific activity of uranium radioisotopes. Uranium sources were counted by a Passivated Implanted Planar Silicon (PIPS) detector with 450 mm<sup>2</sup> of active surface area. An electroplated mixed standard alpha source consisting of 1.67 Bq (5.2%) for <sup>238</sup>U; 1.63Bq (4.9%) for <sup>234</sup>U, 1.91 Bq (5.5%) for <sup>239</sup>Pu, and 1.81 Bq (5.5%) for <sup>241</sup>Am provide by Eckert & Ziegler Isotopes Products was used for the energy calibration of spectrometry.

### 2.2. Reagents and Tracer

The analytical grade reagents taken from Merck were used in this study. The UTEVA chromatographic resin with 100-150 µm was supplied by Eichrom Technologies, Inc. (Darien, Illinois, USA). The yield of the radiochemical separation technique was determined by using <sup>232</sup>U standard reference solution as a tracer. The National Institute of Standards and Technology (NIST) traceable radionuclide, <sup>232</sup>U (SRM 4324B) with 38.22 Bq g<sup>-1</sup> was purchased in the form of UO<sub>2</sub>Cl<sub>2</sub> dissolved in 2M HCl solution. The specific activity of <sup>232</sup>U was reduced to 0.1090 Bq g<sup>-1</sup> ± 0.0085% (k=1) by diluting with 2M HCl.

### 2.3. Sample Description

A mixed culture of acidophilic mesophiles consisting of iron and sulfur oxidizers with a few archaeal species was used to leach uranium from asphaltite. 9K nutrient medium [(NH<sub>4</sub>)<sub>2</sub>SO<sub>4</sub>, 15.0 g; KCl, 0.5 g; K<sub>2</sub>HPO<sub>4</sub>, 2.5 g; MgSO<sub>4</sub> 7 H<sub>2</sub>O, 2.5g; Ca(NO<sub>3</sub>)<sub>2</sub> 4 H<sub>2</sub>O, 0.05 g for 5L solution] supplemented with 4.5 g/L of Fe<sup>3+</sup> and tetrathionate (K<sub>2</sub>S<sub>4</sub>O<sub>6</sub>) solution is used for the cultivation of micro-organisms and bioleaching of asphaltite samples. The bioleaching process was conducted in the leaching medium containing an iron-free 9K mineral salt medium with mixed microbial culture at 1.0 and 1.5 pH values.

Analyzing two spiked tap water samples provided by the IAEA-Cu-2010-04 ALMERA Proficiency Test Exercise was used to validate the proposed analytical approach. The pH values of water samples were determined by using Opaus ST300-G Model portable pH meter. If needed, the pH of water samples was adjusted to 2.00 by adding concentrated  $\text{HNO}_3$  to ensure that the trace elements and radionuclides were kept in the sample.

## 2.4. Analytical Procedures

### 2.4.1. Sample Preparation

The Eichrom ACW02 (Eichrom, 2014a) analytical process, which is used to separate and analyze uranium in water, was improved to include uranium isotope analysis in the bioleaching liquor. This method was chosen because of its efficiency and reliability for the measurement of actinides in the water. The sample preparation approach and radiochemical separation procedures were previously reported and used in various alpha-particle spectrometry tests (Seferinoğlu et al., 2014). A sub-sample of 50 mL of bioleaching liquor was taken with a volumetric flask. The quantification of radiochemical recoveries and correction of results to improve precision and accuracy was performed with  $^{232}\text{U}$  isotopes as a tracer. A weighed aliquot of  $^{232}\text{U}$  standard solution with an analytical balance calibrated with SI traceable weights was added to the sample at the beginning of the procedure; 0.1045 Bq was put in total. A calcium phosphate precipitation was performed to concentrate the actinides that exist in bioleaching liquor. 0.5 mL of 1.25M  $\text{Ca}(\text{NO}_3)_2$  was added to the liquor and heated with stirring at the medium setting for 60 min. After adding 2 drops of phenolphthalein indicator and 1 mL of 3.2M  $(\text{NH}_4)_2\text{HPO}_4$  solution, enough concentrated  $\text{NH}_4\text{OH}$  was added and heated for another 30 min to co-precipitate uranium with calcium phosphate ( $\text{Ca}_3(\text{PO}_4)_2$ ). The precipitate was cooled to room temperature and allowed to settle until the solvent would be separated by decantation or centrifugation. After discarding the supernatant, the precipitate was washed with an amount of deionized water approximately twice the volume of precipitate and centrifuged again for about 5 or 10 min at 2500 rpm. The residue was dissolved with 5 mL of concentrated  $\text{HNO}_3$  and evaporated to incipient dryness. The residue was re-dissolved with 10 mL of the solution of 3M  $\text{HNO}_3$ -1.0M  $\text{Al}(\text{NO}_3)_3$ . The effect of phosphate on the separation of uranium isotopes from other interfering radioisotopes like neptunium and thorium is very important. The phosphate anion readily complexes with tetravalent actinides such as Th (IV) and Np (IV) ions. The phosphate complexes are not extracted from the UTEVA resin used for isolating uranium isotopes. 1.0 M  $\text{Al}(\text{NO}_3)_3$  is added to the leaching solution for counteracting the phosphate effects. Aluminum effectively ties up the phosphate, so this step prevents phosphate interference with neptunium/thorium uptake by the resin. The radiochemical separation step of Th (IV) and Np (IV) ions from the UTEVA resin was improved by the addition of Al. Another important problem is the iron deposition on the substrate material of alpha-source. The iron present in the liquor is coming from the 9K nutrient medium supplemented with  $\text{Fe}^{3+}$  for the cultivation of micro-organisms and from the pyrite content of asphaltite. The iron deposition should be prevented in the analysis of uranium isotopes because the iron easily contributes to the deposition of uranium on the substrate materials during the electrodeposition process. This increases the thickness of the deposit and inhibits the uranium deposition on the substrate materials. For the counteracting of iron effects, 2 mL of freshly prepared 0.6M ferrous sulphate solution, 1M ammonium thiocyanate indicator, and ascorbic acid should be added to the liquor prior to the radiochemical purification steps of uranium. Hence, three-valent of Fe ions and also tetra-valent of Pu ions are reduced to iron (II) and to plutonium (III) to avoid the retaining of iron and plutonium isotopes on UTEVA resin. The uranium in the solution was then purified by the chromatographic resin.

### 2.4.2. Radiochemical Purification of Uranium

The radiochemical separation step must be performed to isolate the uranium isotopes from other radionuclides with unresolvable alpha energies such as  $^{241}\text{Am}$  and  $^{238}\text{Pu}$ ,  $^{237}\text{Np}$ , and  $^{234}\text{U}$  exist in the liquor with UTEVA resin prior to the measurement. UTEVA resin selectively absorbs the uranium isotopes from interfering elements. The UTEVA resin column placed on a vacuum box has been pre-conditioned by adding 5 mL of 3M  $\text{HNO}_3$  before transferring the sample to the column. The bioleaching liquor was poured into the resin reservoir, and the solution was allowed to drain before being washed with 5 mL of 3M  $\text{HNO}_3$  solution. A 5 mL solution of 8M  $\text{HNO}_3$  was also run through the column. Uranium isotopes with tetravalent ions like Np and Th isotopes were absorbed by the resin, while other interfering elements passed through the column. The resin should be converted from nitrate to the chloride system by adding 5 mL of 9M  $\text{HCl}$  solution for the elution of plutonium,

thorium, and neptunium from the resin. 20 mL of 5M HCl-0.05M oxalic acid solution was added into the column and allowed to drain. This rinse removed any plutonium, thorium, and neptunium retained in the resin. Uranium was finally stripped with 15 mL of 1.00 M HCl solution. The purified uranium fraction was evaporated to dryness.

### 2.4.3. Alpha-Source Preparation and Measurement

Alpha-particle spectrometry requires a uniform and thin source to ensure that the alpha particles are not absorbed by radioactive materials deposited on the substrate and counted with high-resolution spectra. Electrodeposition is one of the most common source preparation methods for radiometric measurement routinely (Crespo, 2012). The Eichrom SPA02 analytical procedure was performed to prepare thin and uniform alpha sources (Eichrom, 2014b). The electrodeposition method with a sulfate system on a stainless steel disc was used in this study. The polished stainless steel disc was used as a substrate for uranium deposits along with a cathode in the electrolytic cell. The evaporated uranium solution was dissolved in the mix solution including 2.5 mL of 5.0 wt% NaHSO<sub>4</sub>, 2.0 mL of deionized water, 5.0 mL of 15 wt% of Na<sub>2</sub>SO<sub>4</sub>, and then added 1.0 mL of ammonium oxalate to the electrolysis cell. After electrodeposition at 0.75 A for 90 min, the reaction was ended by adding 2.0 mL of 25 wt% KOH. The disc was rinsed with NH<sub>4</sub>OH, ethanol, and acetone sequentially. After drying the alpha source at 200°C for 5 min, the count rate of uranium radioisotopes was measured by a PIPS detector.

## 3. RESULTS AND DISCUSSION

The proposed analytical procedure in the study comprises one of the evaluation parameters for determining the uranium recovery from asphaltite by the bioleaching process. The contribution of the leaching liquor is not easily determined by alpha-particle spectrometry due to its matrix effects. The proposed analytical procedure is comprised of four steps: i) sample preparation to get rid of some elements and salt interfering properties during the radiochemical separation including electrodeposition, ii) radiochemical separation to isolate the uranium from other interfering radionuclides such as <sup>237</sup>Np, <sup>238</sup>Pu, and <sup>232</sup>Th on the alpha spectrum, iii) alpha-source preparation on the substrate disc, and finally iv) measurement of alpha-source. Sample preparation and radiochemical steps allow obtaining a pure uranium fraction via chemical and radiochemical ways. One of the main troubles is the formation of the phosphate ions and tetravalent actinides (especially Np and Th radionuclides) complexes. The complexes are easily up taken by UTEVA resin and are not extracted from the column. This can be counteracted via adding Al in the sample separation step because Al is selectively bounding with phosphate anion. Another difficulty is the iron deposition during the electrodeposition process. Iron ions contribute to uranium deposition on the substrate materials and cause the inhibition of uranium deposition. Therefore, the reduction of Fe<sup>3+</sup> ions must be reduced to Fe<sup>2+</sup> by ferrous sulphonate before the radiochemical separation. Consequently, the proposed procedure separates radionuclides that can interfere with the measurement of uranium by alpha-particle spectrometry.

### 3.1. Validation of Analytical Procedure

The proposed analytical procedure was inspected by testing two spiked tap water supplied by IAEA-Cu-2010-04 ALMERA Proficiency Test Exercises. The main aim was to elucidate the applicability of the proposed method to the measurement of activity concentration of uranium radioisotopes in the bioleaching liquor obtained from asphaltite. The evaluation of the results was made in terms of the relative bias, z-score, u-test, trueness, and precision. The results for uranium isotopes concentration compared to recommended values given by the proficiency test were shown in Table 1. The relative bias for spike tap water1 (the so-called STW1) and spike tap water2 (the so-called STW2) are found as 0.00%, -6.38% for <sup>234</sup>U, and 2.86%, -6.45% for <sup>238</sup>U, respectively. The value of the u-test parameter was assigned to 2.58 for the 99% confidence level. The u-score values for STW1 and STW2 samples are found as 0.00, -1.29 for <sup>234</sup>U, and 0.19, -1.25 for <sup>238</sup>U, respectively. Overall, the results of relative bias, z-score, and u-score showed that measured specific activities and their uncertainties were within the recommended reference interval. In this study, the measured results were also evaluated according to the acceptance criteria for trueness and precisions.

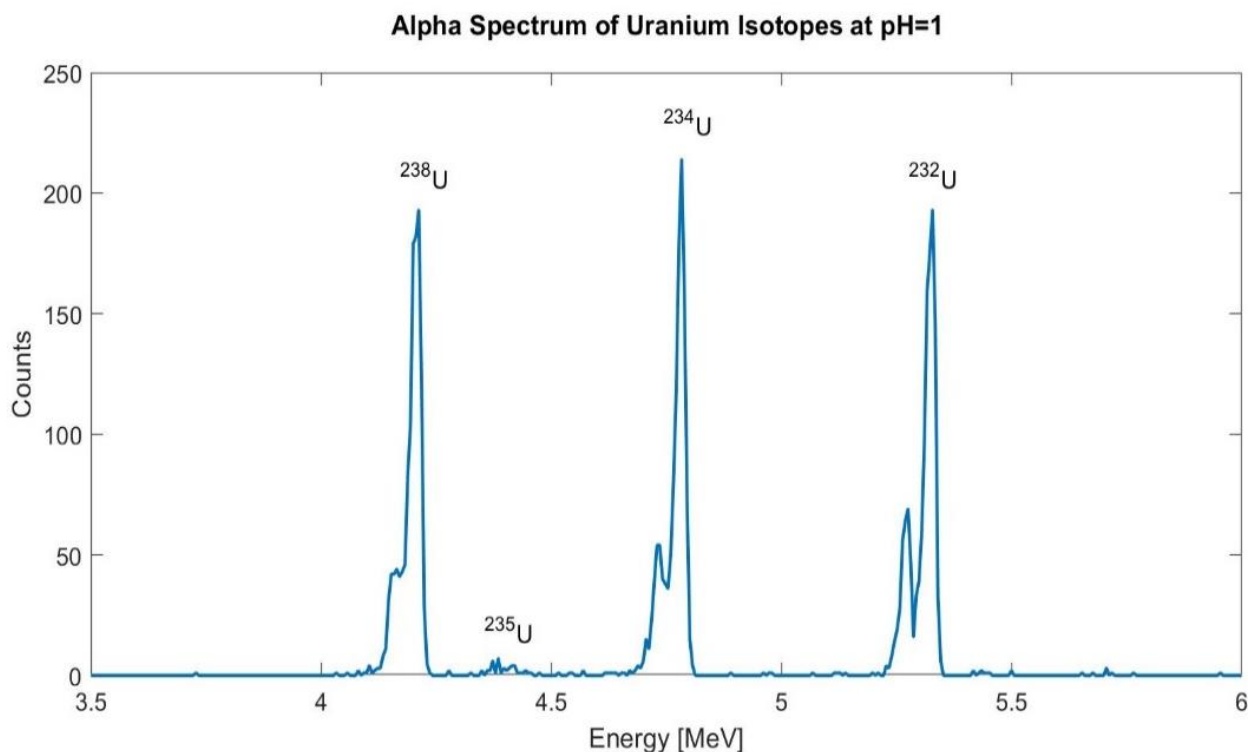
**Table 1.** The measured results of  $^{234}\text{U}$  and  $^{238}\text{U}$  radioisotopes compared to the recommended values of the activity concentration in the spike tap water samples taken from the proficiency test organized by the IAEA

Institution	Sample	Analyte	Measured Value (Unc. k=1) (Bq kg <sup>-1</sup> )	Relative Unc. k=1	Recommended Value (Unc. k=1) (Bq kg <sup>-1</sup> )	Relative Unc. k=1	Relative Bias (%)	Z Score	U Test	A1*	A2	P* (%)	FS*
IAEA-Cu 2010-04 Almera	STW1	$^{234}\text{U}$	1.30 (8)	6.15%	1.30 (3)	2.31%	0.00%	0.00	0.00	0.00	0.22	6.57	A
		$^{238}\text{U}$	0.72 (6)	8.33%	0.70 (2)	2.86%	2.86%	0.06	0.19	0.02	0.16	8.81	A
	STW2	$^{234}\text{U}$	0.44 (3)	7.14%	0.47 (1)	2.13%	-6.38%	-0.13	-1.29	0.03	0.08	7.14	A
		$^{238}\text{U}$	0.29 (2)	7.41%	0.31 (1)	3.23%	-6.45%	-0.13	-1.25	0.02	0.06	7.61	A

The final score is assigned “Acceptable” status if it passed both trueness and precision criteria. The criteria for trueness is passed if the A1 value is smaller than the A2 value. For precision criteria (P), the limited value was determined as 15% for uranium radionuclides. If the P value  $\leq 15\%$ , the precision criteria value passes. The trueness and precision criteria were met, as shown in Table 1. Consequently, the measured specific activities of  $^{234}\text{U}$  and  $^{238}\text{U}$  were found in agreement with recommended values assigned by IAEA.

### 3.2. Determination of Activity Concentration of Uranium in the Bioleaching Liquor

The validated analytical procedure was implemented to determine the specific activity of uranium isotopes in the bioleaching liquor collected from bioleaching of asphaltite at pH values of 1.00 and 1.50. The uranium isotopes spectrum of bioleaching liquor at pH=1.00 was presented in Figure 1. The regions of interest were adjusted between 3.95-4.46 MeV for  $^{238}\text{U}$ , 4.37-4.60 MeV for  $^{235}\text{U}$ , 4.69-4.86 for  $^{234}\text{U}$ , and 5.13-5.39 MeV for  $^{232}\text{U}$ . The spectrum shows that the peak resolution is sufficient (no overlapping peaks) to skip spectral deconvolution calculations. Therefore, the peak area for each radionuclide was straightforwardly determined.

**Figure 1.** The alpha spectrum of the bioleaching liquor collected from the leaching of asphaltite at pH=1

The experiments were done with three replicates. The specific activities and the uncertainties of  $^{234}\text{U}$ ,  $^{235}\text{U}$ , and  $^{238}\text{U}$  isotopes were presented in Table 2. The specific activities at pH=1.00 range between 21.80 (2.80) BqL<sup>-1</sup> and 23.21 (2.59) BqL<sup>-1</sup> for  $^{234}\text{U}$ , 0.71 (0.25) BqL<sup>-1</sup> and 0.86 (0.25) BqL<sup>-1</sup> for  $^{235}\text{U}$ , and 20.50 (2.82) BqL<sup>-1</sup> and 22.07 (2.27) BqL<sup>-1</sup> for  $^{238}\text{U}$ . The specific activities at pH=1.50 were found less than those at pH=1.00.

**Table 2.** The specific activities of uranium isotopes in the bioleaching liquors collected from the asphaltite bioleaching process at pH values are 1.00 and 1.50

Bioleaching liquor	pH Value	Specific Activity of $^{234}\text{U}$		Specific Activity of $^{235}\text{U}$		Specific Activity of $^{238}\text{U}$	
		A (BqL <sup>-1</sup> )	Unc. (BqL <sup>-1</sup> , k=2)	A (BqL <sup>-1</sup> )	Unc. (BqL <sup>-1</sup> , k=2)	A (BqL <sup>-1</sup> )	Unc. (BqL <sup>-1</sup> , k=2)
ABL1	1.00	21.80	2.80	0.71	0.22	20.50	2.82
ABL1	1.00	22.05	2.20	0.85	0.23	21.41	2.45
ABL1	1.00	23.21	2.59	0.86	0.25	22.07	2.27
<b>Mean</b>		<b>22.35</b>	<b>2.53</b>	<b>0.81</b>	<b>0.23</b>	<b>21.33</b>	<b>2.51</b>
ABL2	1.50	14.34	1.39	0.53	0.11	14.50	1.43
ABL2	1.50	14.50	1.45	0.55	0.09	15.10	1.48
ABL2	1.50	15.40	1.48	0.57	0.10	15.70	1.51
<b>Mean</b>		<b>14.75</b>	<b>1.44</b>	<b>0.55</b>	<b>0.10</b>	<b>15.10</b>	<b>1.47</b>

\*ABL1 and ABL2 mean that asphaltite bioleaching liquor at pH=1 and pH=1.50, respectively.

The specific activities were observed in good agreement with each other. No outlier values were found in any of the measurements. The results indicated that the proposed analytical method is applicable to measure a reliable and accurate specific activity of uranium isotopes in the bioleaching liquor by alpha-particle spectrometry.

Radiochemical recovery of the proposed method for  $^{238}\text{U}$  and  $^{234}\text{U}$  isotopes was calculated by the count rate of the tracer ( $^{232}\text{U}$ ). The detector efficiency ( $\epsilon$ ) was determined as 0.150 by the relative solid angle method. The radiochemical recoveries for two isotopes ( $^{234}\text{U}$  and  $^{238}\text{U}$ ) were found in approximately the same range from 60% to 68%.

#### 4. CONCLUSION

The results obtained for two IAEA-Cu-2010-04 ALMERA proficiency test samples indicated that the proposed analytical method is applicable to determine the specific activities of uranium isotopes in the bioleaching liquor matrix with high accuracy and precision. The evaluated results in terms of the relative bias, z-score, and u-score showed the measured activities and uncertainties were in good agreement with reference values assigned by IAEA.

The procedure was tested on bioleaching liquors obtained from the asphaltite bioleaching process at various pH levels. The results of uranium isotopes were in keeping with each other and resulted in no outlier. In the alpha-particle spectrometric measurements, the sample preparation and radiochemical separation stages removed all interfering components, whether radioactive or not. The mean specific activities and their uncertainties for  $^{234}\text{U}$ ,  $^{235}\text{U}$  and  $^{238}\text{U}$  radioisotopes at pH=1.00 were found as 22.35 (2.53) Bq L<sup>-1</sup>, 0.81 (0.23) Bq L<sup>-1</sup>, and 21.33 (2.51) Bq L<sup>-1</sup>, respectively. When the pH value was increased to 1.50, the specific activities were changed to 14.75 (1.44) Bq L<sup>-1</sup> for  $^{234}\text{U}$ , 0.55 (0.10) Bq L<sup>-1</sup> for  $^{235}\text{U}$ , and 15.10 (1.47) Bq L<sup>-1</sup> for  $^{238}\text{U}$ .

Consequently, for samples acquired by bioleaching processes, alpha spectrometry produces a distinctive spectrum. Thus the uranium recovery in the bioleaching processes for low-level uranium resources can be evaluated by the proposed analytical procedure.

## ACKNOWLEDGEMENT

The author is thankful to Professor Jan Paul and Professor Åke Sandström from the Luleå University of Technology, Department of Chemical and Metallurgical Engineering, Division of Process Metallurgy, Sweden for supplying bioleaching liquor. The author would like to thank Dr. Hüseyin Şahiner for reviewing the paper and providing valuable comments.

## CONFLICT OF INTEREST

The author declares no conflict of interest.

## REFERENCES

- Abhilash, & Pandey B. D. (2013). Microbially assisted leaching of uranium-A review. *Mineral Processing and Extractive Metallurgy Review*, 34(2), 81-113. doi:[10.1080/08827508.2011.635731](https://doi.org/10.1080/08827508.2011.635731)
- Abhilash, Pandey B. D., & Singh, A. K. (2013). Comparative performance of uranium bioleaching from low-grade Indian apatite rock in column and bioreactor. *Energy Procedia*, 39, 20-32. doi:[10.1016/j.egypro.2013.07.188](https://doi.org/10.1016/j.egypro.2013.07.188)
- Aggarwal, S. K. (2016). Alpha-particle spectrometry for the determination of alpha emitting isotopes in nuclear, environmental and biological samples: Past, Present and Future. *Analytical Methods*, 8(27), 5353-5371. doi:[10.1039/C6AY00920D](https://doi.org/10.1039/C6AY00920D)
- Ballice, L. (2002). Classification of volatile products evolved from temperature-programmed pyrolysis of Soma-Lignite and Şırnak-Asphaltite from Turkey. *Journal of Analytical and Applied Pyrolysis*, 63(2), 267-281. doi:[10.1016/S0165-2370\(01\)00159-0](https://doi.org/10.1016/S0165-2370(01)00159-0)
- Crespo, M. T. (2012). A review of electrodeposition methods for the preparation of alpha-radiation sources. *Applied Radiation and Isotopes*, 70(1), 210-215. doi:[10.1016/j.apradiso.2011.09.010](https://doi.org/10.1016/j.apradiso.2011.09.010)
- Eichrom (2014a). *Uranium in water* (Method No: ACW02). Analytical Procedure, Rev.1.4, 1-8, Eichrom Technologies, LLC. [URL\(PDF\)](#)
- Eichrom (2014b). *Electrodeposition of actinides* (Method No: SPA02). Analytical Procedure, Rev.1.0, 1-6, Eichrom Technologies, LLC. [URL\(PDF\)](#)
- Eisapour, M., Keshtkar, A., Moosavian, M. A., & Rashidi, A. (2013). Bioleaching of uranium in batch stirred tank reactor: process optimization using Box-Behnken design. *Annals of Nuclear Energy*, 54, 245-250. doi:[10.1016/j.anucene.2012.11.006](https://doi.org/10.1016/j.anucene.2012.11.006)
- Hiçyılmaz, E., & Altun, E. N. (2006). Improvements on combustion properties of asphaltite and correlation of activation energies with combustion results. *Fuel Processing Technology*, 87(6), 563-570. doi:[10.1016/j.fuproc.2005.07.010](https://doi.org/10.1016/j.fuproc.2005.07.010)
- Pal, S., Pradhan, D., Das, T., Sukla, L. B., & Chaudhury, G. R. (2010). Bioleaching of low-grade uranium ore using *Acidithiobacillus ferrooxidans*. *Indian Journal of Microbiology*, 50(1), 70-75. doi:[10.1007/s12088-010-0015-z](https://doi.org/10.1007/s12088-010-0015-z)
- Reis, A. S., Temba E. S. C., Kastner, G. F., & Monteiro R. P. G. (2011). Combined procedure using radiochemical separation of plutonium, americium and uranium radionuclides for alpha-spectrometry. *Journal of Radioanalytical and Nuclear Chemistry*, 287(2), 567-572. doi:[10.1007/s10967-010-0774-3](https://doi.org/10.1007/s10967-010-0774-3)
- Reis, A. S., & Monterio R. P. G. (2020). Study of thorium and uranium isotopes activity concentration after percolation or agitation leaching, in mining lixiviation liquor samples. *Brazilian Journal of Radiation Sciences*, 80(1), 1-12. doi:[10.15392/bjrs.v8i1.933](https://doi.org/10.15392/bjrs.v8i1.933)
- Sarkar, A. (2019). Nuclear power and uranium mining: current global perspectives and emerging public health risks. *Journal of Public Health Policy*, 40, 383-392. doi:[10.1057/s41271-019-00177-2](https://doi.org/10.1057/s41271-019-00177-2)
- Saydut, A., Duz, M. Z., Tonbul, Y., Baysal, A., & Hamamci, C. (2008). Separation of liquid fractions obtained from flash pyrolysis of asphaltite. *Journal of Analytical and Applied Pyrolysis*, 81(1), 95-99. doi:[10.1016/j.jaap.2007.09.003](https://doi.org/10.1016/j.jaap.2007.09.003)

- Seferinođlu, M., Dirican, A., Erden, P. E., & Erçin, D. (2014). Evaluation of uncertainty components associated with alpha-particle spectrometric measurements of uranium isotopes in water. *Applied Radiation and Isotopes*, 94, 355-362. doi:[10.1016/j.apradiso.2014.09.002](https://doi.org/10.1016/j.apradiso.2014.09.002)
- Zhu, Z., Pranolo, Y., & Cheng, C. Y. (2015). Separation of uranium and thorium from rare earth for rare earth production-A review. *Minerals Engineering*, 77, 185-196. doi:[10.1016/j.mineng.2015.03.012](https://doi.org/10.1016/j.mineng.2015.03.012)



Gazi University

**Journal of Science**

PART A: ENGINEERING AND INNOVATION

<http://dergipark.org.tr/gujsa>

## *Moringa oleifera* (Lam.) and *Momordica charantia* (Lam.−) as Potential Larvicides and Fumigants of *Culex Mosquitoes*

Olajide Joseph AFOLABI<sup>1\*</sup> , Akinbode Ayekooto OLONISAKIN<sup>1</sup> <sup>1</sup>Department of Biology, Federal University of Technology Akure, Nigeria

Keywords	Abstract
Larvicide	Mosquitoes cause life threatening diseases such as yellow fever, malaria, filariasis, encephalitis infection etc. The focus of this research is to evaluate the larvicidal and fumigant properties of <i>Moringa oleifera</i> and <i>Momordica charantia</i> extracts on the larvae and adult mosquitoes. The leaves of both plants were dried and pulverized into fine powder. Rotary evaporator was used to extract the plant oils. The results showed that <i>Momordica charantia</i> was more effective as larvicide than <i>Moringa oleifera</i> as its evoked 100% larval mortality at 20% concentration for 3 hours with LC50 and LC90 of 0.5% and 8.5% respectively. <i>Moringa oleifera</i> produced 100% larval mortality and LC50 (0.75%) and LC90 (10%) at 25% concentration for 4 hours. Similarly, the leaf extract of <i>Momordica charantia</i> is a better fumigant than <i>Moringa oleifera</i> , the former produced LC50 of 0.5% and LC90 of 3.75%, while the latter produced LC50 and LC90 of 1.05% and 4.25% respectively. The significantly higher larvicidal and fumigant activities observed in <i>Momordica charantia</i> is due to the presence of cardiac glycosides only in the plant in addition to saponins, tannins, flavonoids and alkaloids which are common to both plants. Therefore botanicals are advocated to be included in vector control programs. This is because botanicals are relatively safe, cheap and easy to obtain in many parts of the world.
Fumigant	
Moringa	
Momordica	
Culex	

### Cite

Afolabi, O. J., & Olonisakin, A. A. (2022). *Moringa oleifera* (Lam.) and *Momordica charantia* (Lam.−) as Potential Larvicides and Fumigants of *Culex Mosquitoes*. *GU J Sci, Part A, 9(2)*, 87-95.

Author ID (ORCID Number)	Article Process	
O. J. Afolabi, 0000-0002-8134-8222	<b>Submission Date</b>	25.02.2022
A. A. Olonisakin, 0000-0003-4237-2809	<b>Revision Date</b>	26.05.2022
	<b>Accepted Date</b>	08.06.2022
	<b>Published Date</b>	09.06.2022

## 1. INTRODUCTION

Mosquitoes are vectors of important parasites such as protozoans and nematodes which are responsible for fatal infections such as malaria, yellow fever and filariasis (Dahmana & Mediannikov, 2020; Bamou et al., 2021). The vectorial capacity of mosquitoes is as a result of their hematophagous attitude, during blood meal, mosquitoes acquire the pathogen from one vertebrate host and transmit to another (Powell, 2019). Highly efficient vectors must live in close association with the hosts and have a relatively long lifespan (Powell, 2019).

Plants are globally useful in protecting people from hematophagous insects and several researches have reported the repellent efficacy of plant oils. These plant oils are easily decomposed, ecologically friendly, popular and generally have low mammalian toxicity. Moreover, the plants are easily obtainable at cheaper cost in most endemic areas. In addition, plant oils contain several important properties. First, they easily penetrate insect cuticles, which increases their bioavailability. These properties could be of useful in reducing insect longevity on treated surface. Secondly, active ingredients in the plant oils may have specific mode of action, which make them good alternative to pyrethroids. Among plants that are useful as protectants are *Moringa* and bitter melon. *Moringa*, which is the only genus in the family Moringaceae and common called drumstick tree (Milla et al., 2021). *Moringa* is a fast growing plant which is resistant to drought and originated from the southern foothill of Himalayas in northern India, and widely cultivated in

\*Corresponding Author, e-mail: [ojafolabi@futa.edu.ng](mailto:ojafolabi@futa.edu.ng)



tropical and subtropical area. It is used in water purification, and herbal medicine. *M. oleifera* leaf powder is also effective as soap for hand washing (Fidrianny et al., 2022). *M. oleifera* could be used as functional food and other industrial food applications (Oyeyinka & Oyeyinka, 2018). Therefore, *M. oleifera* provides nutrients that benefit health, making it a key food for food security in areas with fewer economic resources (Sagona et al., 2020). According to Kumar et al. (2010), the introduction of *Moringa oleifera* seed flour improves the organoleptic properties of different breads and biscuits; In addition, almost all parts of the plant: root, bark, gum, leaf, fruit (pods), flowers, seeds and seed oil, have been used to treat various disease such as skin infections, swelling, anemia, asthma, bronchitis, diarrhea, headache, joint pain, rheumatism, gout, diarrhea, heart problems, fevers, digestive disorders, wounds, diabetes, conjunctivitis, haemorrhoids, goitre, earache, measles and smallpox in the indigenous system of medicine (Thakur & Sharma, 2016). *Momordica charantia* or bitter gourd, is widely grown in Africa, Asia, and the Caribbean as edible fruit, which is extremely bitter. It originated in India subcontinent and introduced into China in the 14<sup>th</sup> century. Bitter gourd is important in Chinese cooking because of its bitter flavour (Abu-Odeh & Talib, 2021). Especially in soup and herbal teas. *M. charantia* on the other hand is useful as cancer prevention, diabetes treatment, fever, and in reducing blood glucose level (Afolabi et al., 2018). This study explored the larvicidal and fumigant properties of the *Moringa oleifera* and *Momordica charantia* leaf extracts on *Culex* mosquitoes.

## 2. MATERIALS AND METHOD

### 2.1. Preparation of the Plant Extracts

The leaves of *Moringa oleifera* and *Momordica charantia* used for this research were obtained from Apatapiti environment of Federal University of Technology Akure. The leaves were mildly washed in a bowl of clean water and subsequently air dried at room temperature ( $28 \pm 2^\circ\text{C}$ ) for 25 days, at the undergraduate research laboratory of the biology department. The dried leaves were pulverized into powder and blended with the electric blender. The powders were kept separately in labeled containers until when use.

### 2.2. Insect Culture

Larvae of mosquitoes used for this research were obtained from Sabo environment in Akure, the larvae were harvested and brought to the laboratory. The larvae were transferred to another plastic container containing water, where they were fed with yeast. Ten larvae were used for the larvicidal experiment and the rest were allowed to develop or emerge as adult in the experimental cage. The pupae transformed to adult in 4 days at temperature of  $27 \pm 2^\circ\text{C}$ , relative humidity of  $70 \pm 10\%$  and a cycle 14h of light and 10h darkness (Chiroma et al., 2018).

### 2.3. Preparation of Plant Extracts

The leaf powders of the plants were soaked in absolute ethanol for 72hrs to obtain the extracts. The soaked powders were mixed for 30 minutes every 24hrs to enhance more concentration of the extract. The mixture was filtered using muslin cloth. The filtrates were transferred into rotary evaporator to evaporate solvent at its boiling temperature  $70^\circ\text{C}$ . After this stage, the standard extract obtained was stored in a bottle till usage (Fidrianny et al., 2022).

### 2.4. Phytochemicals Screening

*Moringa oleifera* and *Momordica charantia* extracts were screened for the presence of tannin, phlobatannin, cardiac glycosides, saponins, steroids, terpenoids and flavonoids. For tannin, 5 g of each portion of the plant extracts was stirred with 10 ml of distilled water and filtered as described by Gul et al. (2017). Blue black, green, or blue-green precipitates formed following the addition of few drops of 5% ferric chloride were taken as evidence for the presence of tannins. Deposition of a red precipitate when aqueous solutions of leaf extract was boiled with 1% (v/v) HCl was taken as evidence for the presence of phlobatannin (Gul et al., 2017). Salkowski's test, as described by Akinneye and Afolabi (2014), was used to test for cardiac glycosides. Leaf extract (0.5 g) was dissolved in 2 ml of chloroform prior to the careful addition of 1% (v/v)  $\text{H}_2\text{SO}_4$  to form a lower layer. A reddish-brown colour at the interface was taken as evidence for the cardiac glycoside. Concentration of saponin, steroids and terpenoids were measured adopting the methods of Akinneye and

Afolabi (2014). Plant materials (0.5 g) were mixed with acetic anhydride (2 ml) in the presence of concentrated H<sub>2</sub>SO<sub>4</sub> (2 ml) to measure the concentration of steroids. For terpenoids, plant materials (0.5 g) re-suspended in distilled water were mixed with chloroform (2 ml) in the presence of concentrated H<sub>2</sub>SO<sub>4</sub> (3 ml). Colour change in the presence of re-suspended plant materials and diluted ammonium solution (5 ml) was used to estimate the concentration of flavonoids.

## 2.5. Larvicidal Experiment

The stock solutions for the larvicidal experiment was prepared following the standard procedure of Pam et al. (2021). Crude extract of each plants was added to ethanol to achieve the desired concentrations (5%, 10%, 15%, 20%, and 25%). The extracts were mixed with water in a plastic container at the desired concentration in the presence of small amount of sucrose to serve as food source for the larvae. Then 10 mosquito larvae were transferred into the plastic containers including the control. There were 5 replicates including one control for every concentration. Insect death was recorded every 1hour for 4hrs, after which the larvae were introduced into distilled water to notice recovery. A recovery time of 5 minutes was allowed (Pam et al., 2021). The larval death in treatments was corrected for the controls (Kalimuthu et al., 2020). Larvae considered to be dead when insensitive to probe (Adedire et al., 2011).

## 2.6. Fumigant Test

The fumigant test was evaluated by placing ten mosquito adults in a test-tube covered with cotton wool suspended with a muslin cloth. 1ml of 5%, 10%, 15%, 20%, and 25% concentrations of the plant extracts was then injected in the cotton wool on the test-tube. Death rate was determined every 5minutes for 20 minutes.

## 2.7. Data Analysis

Research data were subjected to one-way analysis of variance and means were separated using Tukey's test at  $p \leq 0.05$ . All data generated were processed using SPSS version 22.

## 3. RESULTS

The results presented in Table 1 showed the phytochemical analysis results of *Moringa oleifera* and *Momordica charantia* leaf extracts. The results revealed the presence of terpenoid, saponins, steroid, tannins, flavonoids, alkaloids in both plant extracts. Meanwhile, phlebotannins and cardiac glycosides were absent in the leaf extract of *Moringa oleifera* while only phlebotannins were absent in *Momordica charantia*. In addition, only the leaf extract of *Momordica charantia* was noted to contain cardiac glycosides.

**Table 1.** Phytochemical analysis of the *Moringa oleifera* and *Momordica charantia*

Phytochemicals	<i>Moringa oleifera</i> Leaves	<i>Momordica charantia</i> Leaves
Terpenoids	+	+
Saponins	+	+
Phlebotannins	-	-
Steroids	+	+
Tannins	+	+
Cardiac glycosides	-	+
Flavonoids	+	+
Alkaloids	+	+

The larvicidal effect of the two plant extracts was presented in Table 2 and 3. The results showed that *Moringa oleifera* achieved 73.33% larval mortality at 25% concentration for 1 hour of exposure, the mortality increased to 96.67% at the same concentration for 2 hours of exposure. Meanwhile, the plant recorded 100% larval mortality at 25% concentration for 3 hours of exposure (Table 2). The highest larval mortality evoked by the *Moringa oleifera* was 100% at 3 hours of exposure while the lowest mortality (30%) was recorded at 1 hour of exposure. The larvicidal result of the leaf extract of *Momordica charantia* as presented in Table 3 showed that the plant extract evoked 100% larval mortality at 20% concentration for 3 hours of exposure while the lowest larval mortality (53.33%) was recorded at 5% concentration for 1 hour.

Generally it was observed that the larvicidal effects of both plant extracts were concentration and time dependent. This shows that the larval mortality increased as the concentration and time of exposure increased.

**Table 2.** Larvicidal effect of *Moringa oleifera* leaf extract on *Culex* mosquitoes

Concentration (%)	Mortality (%)			
	1 hour	2 hours	3 hours	4 hours
Control	0.00 <sup>a</sup> ± 0.00	0.00 <sup>a</sup> ± 0.00	0.00 <sup>a</sup> ± 0.00	0.00 <sup>a</sup> ± 0.00
5	30.00 <sup>a</sup> ± 10.00	60.00 <sup>b</sup> ± 11.67	73.00 <sup>b</sup> ± 3.33	83.33 <sup>b</sup> ± 0.00
10	50.00 <sup>a</sup> ± 10.00	80.00 <sup>b</sup> ± 5.80	86.67 <sup>b</sup> ± 3.33	90.00 <sup>b</sup> ± 5.80
15	45.77 <sup>a</sup> ± 3.33	76.67 <sup>b</sup> ± 8.88	83.33 <sup>b</sup> ± 0.33	86.67 <sup>b</sup> ± 5.80
20	70.00 <sup>a</sup> ± 10.00	86.67 <sup>a</sup> ± 6.67	90.00 <sup>a</sup> ± 0.58	90.00 <sup>a</sup> ± 5.80
25	73.33 <sup>a</sup> ± 3.33	96.67 <sup>b</sup> ± 3.33	100.00 <sup>b</sup> ± 0.00	100.00 <sup>b</sup> ± 0.00

**Table 3.** Larvicidal effect of *Momordica charantia* leaf extract on *Culex* mosquitoes

Concentration (%)	Mortality (%)			
	1 hour	2 hours	3 hours	4 hours
Control	0.00 <sup>a</sup> ± 0.00	0.00 <sup>a</sup> ± 0.00	0.00 <sup>a</sup> ± 0.00	0.00 <sup>a</sup> ± 0.00
5	53.00 <sup>a</sup> ± 3.33	83.33 <sup>b</sup> ± 3.33	83.33 <sup>b</sup> ± 3.33	83.33 <sup>b</sup> ± 5.80
10	73.33 <sup>a</sup> ± 6.67	93.33 <sup>b</sup> ± 3.33	93.33 <sup>b</sup> ± 3.33	96.67 <sup>b</sup> ± 5.80
15	86.67 <sup>a</sup> ± 3.33	93.33 <sup>b</sup> ± 3.33	93.33 <sup>b</sup> ± 3.33	93.33 <sup>b</sup> ± 3.33
20	90.00 <sup>a</sup> ± 5.80	96.67 <sup>a</sup> ± 3.33	100.00 <sup>a</sup> ± 0.00	100.00 <sup>a</sup> ± 0.00
25	73.33 <sup>a</sup> ± 3.33	86.67 <sup>a</sup> ± 6.67	100.00 <sup>a</sup> ± 0.00	100.00 <sup>a</sup> ± 0.00

The results as presented in Table 4 and 5 showed that *Moringa oleifera* produced mortalities of 46.67%, 93.33%, 100% and 100% adult mortalities at 25% concentration for 5, 10, 15 and 20 minutes respectively. However, the least adult mortality (10%) of the plant extract was observed at 5% concentration for 5 minutes while the highest mortality (100%) was recorded at 25% concentration for 15 minutes. The fumigant effect of *Momordica charantia* showed that the leaf extract evoked 63.33%, 96.67%, 100% and 100% at 25% concentration for 5, 10, 15 and 20 minutes respectively.

**Table 4.** Fumigant effect of *Moringa oleifera* leaf extract on *Culex* mosquitoes

Concentration (%)	Mortality (%)			
	1 hour	2 hours	3 hours	4 hours
Control	0.00 <sup>a</sup> ± 0.00	0.00 <sup>a</sup> ± 0.00	0.00 <sup>a</sup> ± 0.00	0.00 <sup>a</sup> ± 0.00
5	10.00 <sup>a</sup> ± 0.00	23.33 <sup>a</sup> ± 5.80	90.00 <sup>b</sup> ± 5.80	100.00 <sup>b</sup> ± 0.00
10	13.33 <sup>a</sup> ± 3.33	53.33 <sup>b</sup> ± 5.80	93.33 <sup>c</sup> ± 6.67	100.00 <sup>c</sup> ± 0.00
15	33.33 <sup>a</sup> ± 3.33	66.67 <sup>b</sup> ± 5.80	96.67 <sup>c</sup> ± 3.33	100.00 <sup>c</sup> ± 0.00
20	40.00 <sup>a</sup> ± 10.00	86.67 <sup>b</sup> ± 5.80	96.67 <sup>b</sup> ± 3.33	100.00 <sup>b</sup> ± 0.00
25	46.67 <sup>a</sup> ± 5.80	93.33 <sup>b</sup> ± 6.67	100.00 <sup>b</sup> ± 0.00	100.00 <sup>b</sup> ± 0.00

**Table 5.** Fumigant effect of *Momordica charantia* leaf extract on *Culex* mosquitoes

Concentration (%)	Mortality (%)			
	1 hour	2 hours	3 hours	4 hours
Control	0.00 <sup>a</sup> ± 0.00	0.00 <sup>a</sup> ± 0.00	0.00 <sup>a</sup> ± 0.00	0.00 <sup>a</sup> ± 0.00
5	13.33 <sup>a</sup> ± 3.33	46.67 <sup>b</sup> ± 8.80	86.67 <sup>c</sup> ± 3.33	96.67 <sup>c</sup> ± 3.33
10	16.67 <sup>a</sup> ± 3.33	53.33 <sup>b</sup> ± 5.80	96.67 <sup>c</sup> ± 3.33	100.00 <sup>c</sup> ± 0.00
15	50.00 <sup>a</sup> ± 3.33	73.33 <sup>b</sup> ± 3.33	100.00 <sup>c</sup> ± 0.00	100.00 <sup>c</sup> ± 0.00
20	50.00 <sup>a</sup> ± 5.67	80.00 <sup>b</sup> ± 5.67	100.00 <sup>c</sup> ± 0.00	100.00 <sup>b</sup> ± 0.00
25	63.33 <sup>a</sup> ± 3.33	96.67 <sup>b</sup> ± 3.33	100.00 <sup>b</sup> ± 0.00	100.00 <sup>b</sup> ± 0.00

The toxicities of the two plant extracts were compared using LC50 and LC90 as shown in Table 6. The results showed that leaf extract of *Momordica charantia* was more toxic as larvicide than that of *Moringa oleifera*. This is because 50% and 90% population of the test animals (*Culex* mosquitoes) died when 0.5% and 8.5% concentrations of *Momordica charantia* were applied to the mosquitoes respectively. Meanwhile 50% and 90% population of *Culex* mosquitoes died when 0.75% and 10% concentrations were applied to the *Culex* mosquitoes. Similarly, leaf extract of *Momordica charantia* was more toxic to the mosquitoes than the leaf extract of *Moringa oleifera*. This implies that at 0.5% and 3.75% concentrations, 50% and 90% *Culex*

mosquito populations were killed by *Moringa oleifera* while the same mortalities were achieved by *Momordica charantia* at 1.05% and 4.25% concentrations respectively (Table 6).

**Table 6.** Lethal toxicity of the plant extracts on *Culex* mosquitoes

Plant extracts	Concentration (%)	LC50	LC90
Larvicides			
<i>Moringa oleifera</i>	5		
	10		
	15		
	20	0.75	10.0
	25		
<i>Momordica charantia</i>	5		
	10		
	15	0.5	8.5
	20		
	25		
Fumigant			
<i>Moringa oleifera</i>	5		
	10	1.05	4.25
	15		
	20		
	25		
<i>Momordica charantia</i>	5		
	10	0.5	3.75
	15		
	20		
	25		

#### 4. DISCUSSION

The result revealed that *Moringa oleifera* and *Mormodica charantia* extracts tested as larvicide and fumigant had significant effects on larvae and adult *Culex* mosquitoes and were all effective at different concentrations and time intervals. All these plants are relatively safe, cheap and easy to obtain in many parts of the world and their activities is traceable to their active ingredients. This finding agrees with the report of Pam et al. (2021) who elucidated that the toxicity of phytochemicals on target species depends on the plant's parts used. Other factors are the species response and the life stages exxposed to the specific extract, extraction solvent, plant origin, phyto-sensitivity of phytochemicals, species growth and reproduction (Kalimuthu et al., 2020). The plant oils are effective as larvicides, because the oils could block the spiracles, resulting in asphyxiation and death of the larvae. This antioxidant activity of oil has been reported by other authors (Bukar et al., 2010; Adedire et al., 2011). The results also showed *Momordica charantia* leaf to be the most potent of the two plants as there was 100% larval mortality at 20% concentration for 3hours with LC50 and LC90 of 0.5%

and 8.5% respectively, this is followed by *Moringa oleifera* leaf extract with a total mortality of 25% for 3hour and LC50 and LC90 of 0.75% and 10% respectively. This maybe due to the presence of flavonoid present in both plant extracts (Anwari et al., 2007). The research work of Aina et al. (2009) supports the findings. The authors affirmed that *Moringa oleifera* leaf is highly potent antidiabetic plant, due to the presence of flavonoids which inhibit a-amylase activity to regulate the blood glucose which results in mosquito death. The significant higher larvicidal property observed in *Momordica charantia* might be as a result of the presence of cardiac glycosides which are only present in *Momordica charantia* and absent in *Moringa oleifera* leaf extract. It was observed in the experiment that zero mortality was recorded in all the control experiments. This suggests that mosquito death was caused by the plant extracts. *M. oleifera* toxicity has been confirmed, as many studies have found variou phytochemicals to be toxic against insects and lower mammals (Asare et al., 2012). The leaf has a high concentration of saponins, which can be potentially harmful for vegetarians, as their consumption reduces the bioavailability of divalent and trivalent metals such as Zn and Mg (Canett-Romero et al., 2014). Moringin alkaloids, spirochin and the phytochemical benzothiocyanate have been found in the root and bark, toxic substances that predominate in the root and bark; The spirochin has been found to block the insect spiracles and asphyxiate the insects (Chiroma et al., 2018).

In the fumigant experiment, significant death was reported for all experimental concentrations but at different time interval. Adult death (100%) was recorded at 5%, 10%, 15%, 20% and 25% concentrations for 20minutes for *Moringa oleifera* extract. However, the lethal concentration (LC50: 0.5% and LC90: 3.75%) showed that *Momordica charantia* was more effective as fumigant on the adult *Culex* mosquitoes than the *Moringa oleifera* with LC50 of 1.05% and LC90 of 4.25%. The high toxicity of *Momordica charantia* against mosquito adults could be due to its strong pungent smell which blocked insect trachea and killed the insect by asphyxiation. Plants with high pungent smell have been reported to have fumigant effect against insect pests (Aina et al., 2009). It was generally observed for all the experiments that mortality increases as the concentration and time interval increase.

## 5. CONCLUSION

The two botanicals (*Moringa oleifera* and *Momordica charantia*) used in this research had showed strong larvicidal and adulticidal efficacies and hence can be used in controlling the mosquito larvae and adults in order to reduce the prevalence of malaria in endemic areas. The phytochemical screening of the plants has also shown that the plants are relatively safe, inexpensive and readily available in many parts of the world.

## ACKNOWLEDGEMENT

The authors acknowledged the contribution of Mrs E.T. Ojo in the preparation and extraction of the plant extracts and oils respectively.

## CONFLICT OF INTEREST

The authors declare no conflict of interest.

## REFERENCES

- Abu-Odeh, A. M., & Talib, W. H. (2021). Middle East Medicinal Plants in the Treatment of Diabetes: A Review. *Molecules*, 26(3), 742. doi:[10.3390/molecules26030742](https://doi.org/10.3390/molecules26030742)
- Adedire, C. O., Obembe, O. M., Akinkurolere, R. O., & Oduleye, S. O. (2011). Response of *Callosobruchus maculatus* (Coleoptera: Chrysomelidae: Bruchinae) to extracts of cashew kernels. *Journal of Plant Diseases Protection*, 118(2), 75-79.
- Afolabi, O. J., Simon-Oke, I. A., Elufisan, O. O., & Oniya, M. O. (2018). Adulticidal and repellent activities of some botanical oils against malaria mosquito: *Anopheles gambiae* (Diptera: Culicidae). *Beni-Suef University Journal of Basic and Applied Sciences*, 7(1), 135-138. doi:[10.1016/j.bjbas.2017.09.004](https://doi.org/10.1016/j.bjbas.2017.09.004)
- Aina, S. A., Banjo, A. D., Lawal, O. A., & Jonathan, K. (2009). Efficacy of Some Plant Extracts on *Anopheles gambiae* Mosquito Larvae. *Academic Journal of Entomology*, 2(1), 31-35.

- Akinneye, J. O., & Afolabi, O. J. (2014). Toxicity and fumigant effect of powder and oil extracts of *Cleisthopholis pathens* (Benth) against larvae and adults *Anopheles* mosquito. *Journal of Mosquito Research*, 4(11), 1-6. doi:[10.5376/jmr.2014.04.0011](https://doi.org/10.5376/jmr.2014.04.0011)
- Anwari, F., Latif, S., Ashraf, M., & Gilani, A. H. (2007). *Moringa oleifera*: a food plant with multiple medicinal uses. *Phytotherapy Research*, 21, 17-25. doi:[10.1002/ptr.2023](https://doi.org/10.1002/ptr.2023)
- Asare, G. A., Gyan, B., Bugyei, K., Adjei, S., Mahama, R., Addo, P., Otu-Nyarko, L., Wiredu, E. K., & Nyarko, A. (2012). Toxicity potentials of the nutraceutical *Moringa oleifera* at supra-supplementation levels. *Journal of Ethnopharmacology*, 139(1), 265-272. doi:[10.1016/j.jep.2011.11.009](https://doi.org/10.1016/j.jep.2011.11.009)
- Bamou, R., Mayi, A. P. M., Djiappi-Tchamen, B., Nana-Ndjangwo, S. M., Nchoutpouen, E., Cornel, A. J., Awono-Ambene, P., Parola, P., Tchuinkam, T., & Antonio-Nkondjio, C. (2021). An update on the mosquito Fauna and mosquito-borne diseases distribution in Cameroon. *Parasites & Vectors*, 14, 527. doi:[10.1186/s13071-021-04950-9](https://doi.org/10.1186/s13071-021-04950-9)
- Bukar, A., Uba, A., & Oyeyi, T. I. (2010) Antimicrobial profile of *moringa oleifera* lam. Extracts against some food - borne microorganisms. *Bayero Journal of Pure & Applied Sciences*, 3(1), 43-48. doi:[10.4314/bajopas.v3i1.58706](https://doi.org/10.4314/bajopas.v3i1.58706)
- Canett-Romero, R., Arvayo-Mata, K. L., & Ruvalcaba-Garfias, N. V. (2014). Aspectos tóxicos más relevantes de *Moringa oleifera* y sus posibles daños. *Biotechnia*, 16(2), 36-43.
- Chiroma, A., Adamu, T., Bandiya, H. M., Rabah, A. B., & Mabu, J. M. (2018). Phytochemical Screening of *Terminalia avicennioides* (Guill and Perr). A Potential Pharmaceutical Ingredient. *Dutse Journal of Pure and Applied Sciences*, 4(2), 301-309.
- Dahmana, H., & Mediannikov, O. (2020). Mosquito-borne diseases emergence/resurgence and how to effectively control it biologically. *Pathogens*, 9(4), 310. doi:[10.3390/pathogens9040310](https://doi.org/10.3390/pathogens9040310)
- Fidrianny, I., Kanapa, I., & Singgih, M. (2022). Phytochemistry and pharmacology of Moringa tree: an overview. *Biointerface Research in Applied Chemistry*, 11(3), 10776-10789. doi:[10.33263/BRIAC113.1077610789](https://doi.org/10.33263/BRIAC113.1077610789)
- Gul, R., Jan, S. U., Faridullah, S., Sherani, S., & Jahan, N. (2017). Preliminary phytochemical screening quantitative analysis of alkaloids, and antioxidant activity of crude plant extracts from *Ephedra intermedia* indigenous to Balochistan. *The Scientific World Journal*, 2017, 1-7. doi:[10.1155/2017/5873648](https://doi.org/10.1155/2017/5873648)
- Kalimuthu, K., Tseng, L.-C., Murugan, K., Panneerselvam, C., Aziz, A. T., Benelli, G., & Hwang, J.-S. (2020). Ultrasonic Technology Applied against Mosquito Larvae. *Applied Sciences*, 10(10), 3546. doi:[10.3390/app10103546](https://doi.org/10.3390/app10103546)
- Kumar, P., Singh, K., & Kumar, A. (2010). Hepatoprotective studies on aerial parts of *Moringa oleifera* Lam. On carbon tetrachloride induced liver cell damage in albino rats. *Annals of Biological Research*, 1(1), 27-35.
- Milla, P. G., Penalver, R., & Nieto, G. (2021). Health benefits of uses and applications of *Moringa oleifera* in bakery products. *Plants*, 10(2), 318. doi:[10.3390/plants10020318](https://doi.org/10.3390/plants10020318)
- Oyeyinka, A. T., & Oyeyinka, S. A. (2018). *Moringa oleifera* as food fortificant: recent trends and prospects. *Journal of the Saudi Society of Agricultural Sciences*, 17(2), 127-136. doi:[10.1016/j.jssas.2016.02.002](https://doi.org/10.1016/j.jssas.2016.02.002)
- Pam, V. A., Odey, S. A., Ombugadu, A., Uzoigwe, N. R., Yohanna, J. A., Maikenti, J. I., Adejoh, V. A., Ahmed, H. O., Aimankhu, P. O., Aliyu, A. A., Ayuba, S. O., Anyebe, G. E., & Ashigar, M. A. (2021). Larvicidal activity of the leaf extracts and powder of *Millettia aboensis* against larvae of *Anopheles gambiae* s.l collected from Lafia, Nasarawa State, Nigeria. *Biomedical Journal of Scientific and Technical Research*, 39(2), 31103-31109. doi:[10.26717/BJSTR.2021.39.006263](https://doi.org/10.26717/BJSTR.2021.39.006263)
- Powell, J. R. (2019). An evolutionary perceptive on vector-borne diseases. *Frontiers in Genetics*, 10, 1266. doi:[10.3389/fgene.2019.01266](https://doi.org/10.3389/fgene.2019.01266)

Sagona, W. C. J., Chirwa, P. W., & Sajidu, S. M. (2020) The miracle mix of Moringa: status of moringa research and development in Malawi. *South African Journal of Botany*, 129, 138-145. doi:[10.1016/j.sajb.2019.03.021](https://doi.org/10.1016/j.sajb.2019.03.021)

Thakur, M., & Sharma, R. K. (2016). Bitter gourd: health properties and value addition at farm scale. *Marumegh*, 1(2), 17-21.





Gazi University

**Journal of Science**

PART A: ENGINEERING AND INNOVATION

<http://dergipark.org.tr/gujisa>

## Investigation of Arsenic Content in Field Pesticides Using Inductively Coupled Plasma Optical Emission Spectroscopy (ICP-OES)

Şükrü KALAYCI<sup>1\*</sup> <sup>1</sup>Department of chemistry, Vocational School of Technical Sciences, Gazi University, 06500, Ankara, Turkey

Keywords	Abstract
Fields Pesticides Arsenic Microwave Digestion ICP-OES DPP	In this study, Arsenic, which is found in the structure of field medicines, was determined by ICP-OES. For arsenic analysis, Turkey was elected four different commonly used pesticides. These pesticides were commercially named A, B, C, and D samples. These samples were solubilized using the appropriate procedure by microwave digestion method. For arsenic determination, 188.980 nm wavelength measurements were made. The determination of the known acid first with ICP-OES was measured at high sensitivity. Arsenic amounts were measured as approximately 0.46 to 0.81 µg/g as the 95% confidence level in the samples and the average of 5 measurements. The validation process of this method was done according to the reference article. The results of the experiment were made with the electrochemical method, differential pulse polarography (DPP), and the results were found to be in agreement.

Cite
Kalayci, S. (2022) Investigation of Arsenic Content in Field Pesticides Using Inductively Coupled Plasma Optical Emission Spectroscopy (ICP-OES). <i>GU J Sci, Part A</i> , 9(2), 96-103.

Author ID (ORCID Number)	Article Process
Ş. Kalaycı, 0000-0002-8643-6731	<b>Submission Date</b> 09.04.2022 <b>Revision Date</b> 18.04.2022 <b>Accepted Date</b> 09.06.2022 <b>Published Date</b> 10.06.2022

### 1. INTRODUCTION

Field pesticides are used to kill harmful insects in the field. Field pesticides affect our health through direct nutrition of drug residues in fruits, vegetables and cereals. It is also known to pollute soil, water and air. Arsenic contained in field pesticides has a toxic effect. Arsenic also has a carcinogenic effect in terms of human health (IARC, 2004).

Pesticides, such as Insecticide, herbicide, fungicide, rodenticide, molluscicide etc. pesticides are widely used in agriculture as well as for non-agricultural purposes, as they provide benefits such as improved product and yield quality (Baksh et al., 2020; Caetano et al., 2020; Dong et al., 2020). They are easily released into environmental areas such as soil, water, edible foods, groundwater, and drinking water, making it nearly impossible to avoid exposure to pesticides in the environment (Baksh et al., 2020; Raju, 2022). With the increase in their amount, it has caused health problems both for the environment and for living things.

Chromatographic, spectroscopic (Caetano et al., 2020) and electroanalytical methods (Demir & Silah, 2020; Demir et al., 2021) are used in the analysis of peptides.

Rapid growing industrialization has caused contamination of heavy metals, agricultural chemicals, pesticides and hydrocarbons. These have significantly damaged the environment and human health. (Maduka, 2006).

Arsenic is an element with high toxicity. The amount of arsenic in natural waters was measured with AAS (Andrae, 1977). Arsenic in agriculture (Christian & Feldman, 1970), in biological samples (Chu et al., 1972), the effect on the environment was studied (Clement & Faust, 1973; Fishman & Spencer, 1977). It has been

\*Corresponding Author, e-mail: [skalayci@gazi.edu.tr](mailto:skalayci@gazi.edu.tr)

determined that the most effective substance in the pollution of water with population growth is arsenic. (USEPA, 1999; Chauhan & Flora, 2010).

It has been determined that arsenic and pesticides have a possible role in the increase of diabetes. (Bahadar et al., 2014). A similar study was conducted in Pakistan and the use of different types of pesticides has led to an extraordinary increase in the amount of diabetes in recent years. It has been revealed that there are different types of cancer in humans due to the amount of arsenic it contains. In one study, the amount of arsenic in the well reached 620 µg / L in a certain period of time due to the arsenic-containing pesticides placed on the land next to the wells of families (Li et al., 2016).

In one study, heavy metal levels were measured in river creatures. It was determined that the Turia River basin was contaminated with pesticides such as DDT (Bordajandi et al., 2003). In another study, various pesticides contain harmful elements. Some of these drugs have been found to contain arsenic, mercury, chromium and lead (Campos, 2003).

The toxic effect of arsenic is known quality Arsenic has a detrimental effect on plants growing in the field, people and animals eating these foods, irrigation water and groundwater and the environment. It is important to determine the arsenic content in field pesticides. Therefore, arsenic amounts in four different field pesticides were determined by ICP-OES. The verification certificate of the method was measured by analyzing the reference substance. The results of the experiment were made with the electrochemical method, differential pulse polarography (DPP), and the results were found to be in agreement.

## 2. MATERIAL AND METHOD

### 2.1. Reagents and Instruments

Field pesticides, Turkey as well as in the world is available in agricultural areas too. In this study, four different brand pesticides were selected as examples. These commercial examples were given the names A, B, C, D. All determinations were performed using an ICP-OES model of Perkin Elmer Optima 5300 Dv. When performing the analysis, the device was made using the conditions in the previous study (Kalayci, 2020). The operational conditionals are presented in Table 1.

*Table 1. The operational conditionals of ICP-OES*

Parameter	Across
Auxiliary gas flow rate (L min <sup>-1</sup> )	0.2
Plasma gas flow of rate (L min <sup>-1</sup> )	15
Injector diameter	2.0
View	Axial
Interface	Shear gas
Applied power (kW)	1.3
Nebulization gaz flow of rate (L min <sup>-1</sup> )	0.6

## 2.2. Solubilization of Field Insecticides Samples

Milestone microwave decoding system was used to dissolve the water-insoluble pesticides. Samples were thawed in a microwave thawing system at specific pressures and temperatures using acid mixtures using the appropriate procedure (Tarla et al., 2020).

The samples were brought to a fixed scale in the oven. Samples were washed and dried at 100°C for 48 hours. The cleaned samples were ground in the grinding machine. Before the amount of metal was determined, a microwave digestion procedure was performed by a Milestone microwave digestion system in order to achieve a total digestion in a short time, thus avoiding loss of metal by volatilization and minimizing the amount of added acid. The digestion procedure was as follows: 0.5 g of sample was placed in a polytetrafluoroethylene (PTFE) digestion vessel, 1.5 mL of nitric acid and 2 mL of hydrogen peroxide were added. The samples were then kept at room temperature for 6 hours for homogenization and slow digestion. Afterwards, the containers were closed and the digestion process was carried out by applying a temperature program of 170°C for 18 minutes to the samples inside (Kalayci & Muhammet, 2022).

After the digestion procedure, all digestion vessels were left closed overnight for cooling. The next day, container contents were transferred to vials and the final volume adjusted to 10 mL with ultrapure water.

## 3. RESULTS AND DISCUSSION

### 3.1. Determination of the Optimum Conditions of ICP-OES for Arsenic

Prior to arsenic quantification, optimum conditions for analysis were determined. Calibration procedures were done and samples were prepared. The limits of determination were measured. Wavelength, correlation coefficient ( $R^2$ ), detection limit (LOD) and quality limit (LOQ) of arsenic in ICP-OES are shown in Table 2. Calibration standard contained 0.01-5 mg/L As (Kalayci, 2020).

*Table 2. Analytical criteria of this method*

Element	$\lambda$ (nm)	$R^2$	LOD (mg/L)	LOQ (mg/L)
Arsenic (As)	188.980	0.9997	0.007	0.022

### 3.2. Method Validation and Determination of Arsenic in Field Pesticides Using ICP

Validation of the proposed method was carried out by using a NIST-SRM 1547-Peach Leaves certified reference material. The amount of arsenic with certified reference substance is shown in Table 3. It has been observed that the results obtained are very close to the values given in the certified reference material.

*Table 3. Comparison of the measured value with the reference value ( $\mu\text{g/g}$ ),  
95% confidence interval and  $N=5$*

Element	Certified value	Microwave digestion	RSD (%)
Arsenic (As)	$0.068 \pm 0.011$	$0.071 \pm 0.014$	4.56

Field pesticide samples with different brands brought from four different parts of Turkey were solubilized by microwave incineration method. The amount of arsenic in the samples was analyzed with high precision and the results are shown in Table 4.

**Table 4.** Arsenic contents ( $\mu\text{g/g}$ ) in four different field pesticides (A, B, C and D) after microwave digestion, 95% confidence interval and  $N=5$

Element	A	B	C	D
Arsenic (As)	$0.52 \pm 0.06$	$0.73 \pm 0.11$	$0.81 \pm 0.13$	$0.46 \pm 0.04$

Field pesticide samples with different brands brought from four different parts of Turkey were solubilized by microwave incineration method. The amount of arsenic in the samples was analyzed with high precision and the results are shown in Table 4. While arsenic was at a normal level in samples A and D, it was high in samples B and C.

The comparison of the results of our study with the arsenic values obtained in other studies is given in Table 5. It is seen that the sensitivity and selectivity of the applied method are high.

**Table 5.** Comparison of arsenic values measured with ICP-OES

Samples	LOD (mg/L)	Reference
Spray	2.08	<a href="#">Proch &amp; Niedzielski, 2020</a>
Ketchup	0.5	<a href="#">Massadeh &amp; Al-Massaedh, 2018</a>
Food samples	0.8	<a href="#">Ahmad et al., 2021</a>
Fuel samples	0.05	<a href="#">García et al., 2017</a>
Spinach	0.85	<a href="#">González et al., 2008</a>
Water	0.38	<a href="#">Idris et al., 2017</a>
Pepticides	0.007	This work

### 3.3. Determination of Arsenic Using DPP

The most sensitive result of arsenic determination in polarography was made by using the catalytic hydrogen peak. 10 ml of 0.25 M HAc buffer (pH = 3.5) electrolyte was placed in our cell and its polarogram was taken. Approximately 1000 times Mo (VI) was added on it and its polarogram was taken. Then, when 0.2 mL of our pesticide samples were added, it was seen that the peak at -1.1 V grew. The peak in Figure 1 is the catalytic arsenic peak.

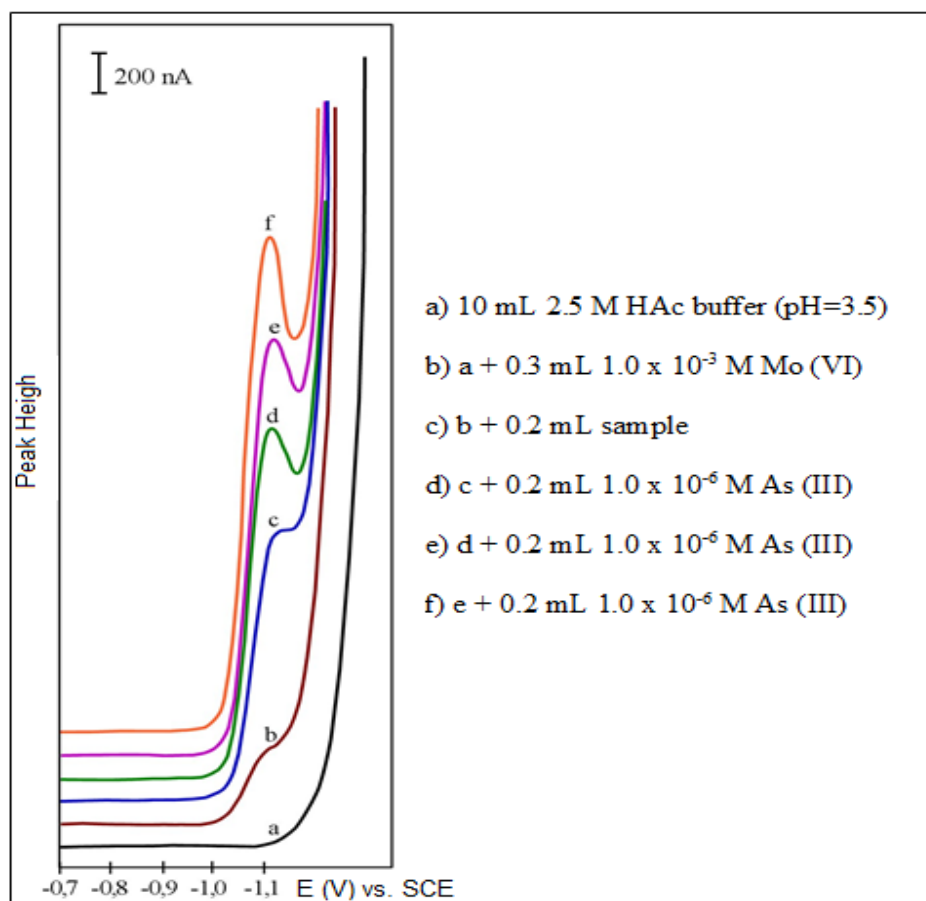


**Figure 1.** Determination of arsenic using DPP

When arsenic standard solution was added on it, arsenic concentrations were calculated by using the peak heights (Somers & Almas, 2006; Somers & Kalayci, 2014). The amounts of arsenic found by this method are given in table 6. The t test was applied to the results obtained from both methods and it was seen that they were compatible with each other.

**Table 6.** Comparison of arsenic amounts with ICP-OES and DPP, 95% confidence interval and N=5

Methods	A	B	C	D
ICP-OES	$0.52 \pm 0.06$	$0.73 \pm 0.11$	$0.81 \pm 0.13$	$0.46 \pm 0.04$
DPP	$0.52 \pm 0.07$	$0.74 \pm 0.14$	$0.80 \pm 0.25$	$0.47 \pm 0.11$
t-test ( $t_{\text{Critical}}=3.18$ )	2.15	2.68	2.72	1.96

#### 4. CONCLUSION

Field pesticides are used to kill harmful insects in the field. Field pesticides affect our health through direct nutrition of drug residues in fruits, vegetables and cereals. It is also known to pollute soil, water and air. Arsenic contained in field pesticides has a toxic effect. Therefore, in this study, we used to define the amount of arsenic in Turkey in the field of pesticides. We identified four different field pesticides (A, B, C and D) as samples. We solved these samples with microwave digestion system. Arsenic analyzes were done with ICP-OES. The validation process for the method used in the measurements was carried out with the reference material. Then, arsenic amounts in samples were determined. The results of the experiment were made with the electrochemical method, differential pulse polarography (DPP), and the results were found to be in agreement. While the amount of arsenic in samples A and D was between normal values, the amount of arsenic in samples B and C was excessive.

#### ACKNOWLEDGEMENT

Every stage of this study was conducted in Gazi University Chemistry Research Laboratory. No financial support was received for this study.

#### CONFLICT OF INTEREST

The authors declare that they have no competing interests.

#### REFERENCES

- Ahmad, H., Zhao, L., Liu, C., Cai, C., & Ma, F. (2021). Ultrasound assisted dispersive solid phase microextraction of inorganic arsenic from food and water samples using CdS nanoflowers combined with ICP-OES determination. *Food Chemistry*, 338, 128028. doi:[10.1016/j.foodchem.2020.128028](https://doi.org/10.1016/j.foodchem.2020.128028)
- Andreae, M. O. (1977). Determination of arsenic species in natural waters. *Analytical Chemistry*, 49(6), 820-825. doi:[10.1021/ac50014a037](https://doi.org/10.1021/ac50014a037)
- Bahadar, H., Mostafalou, S., & Abdollahi, M. (2014). Growing burden of diabetes in Pakistan and the possible role of arsenic and pesticides. *Journal of Diabetes & Metabolic Disorders*, 13, 117. doi:[10.1186/s40200-014-0117-y](https://doi.org/10.1186/s40200-014-0117-y)
- Bordajandi, L. R., Gómez, G., Fernández, M. A., Abad, E., Rivera, J., & González, M. J. (2003). Study on PCBs, PCDD/Fs, organochlorine pesticides, heavy metals and arsenic content in freshwater fish species from the River Turia (Spain). *Chemosphere*, 53(2), 163-171. doi:[10.1016/S0045-6535\(03\)00417-X](https://doi.org/10.1016/S0045-6535(03)00417-X)
- Baksh, H., Buledi, J. A., Khand, N. H., Solangi, A. R., Mallah, A., Sherazi, S. T., & Abro, M. I. (2020). Ultra-selective determination of carbofuran by electrochemical sensor based on nickel oxide nanoparticles stabilized by ionic liquid. *Monatshefte für Chemie - Chemical Monthly*, 151(11), 1689-1696. doi:[10.1007/s00706-020-02704-4](https://doi.org/10.1007/s00706-020-02704-4)
- Caetano, K. dos S., da Rosa, D. S., Pizzolato, T. M., dos Santos, P. A. M., Hinrichs, R., Benvenutti, E. V., Dias, S. L. P., Arenas, L. T., & Costa, T. M. H. (2020). MWCNT/zirconia porous composite applied as electrochemical sensor for determination of methyl parathion. *Microporous and Mesoporous Materials*, 309, 110583. doi:[10.1016/j.micromeso.2020.110583](https://doi.org/10.1016/j.micromeso.2020.110583)
- Campos, V. (2003). Trace Elements in Pesticides. *Communications in Soil Science and Plant Analysis*, 34(9-10), 1261-1268. doi:[10.1081/CSS-120020442](https://doi.org/10.1081/CSS-120020442)
- Chauhan, S., & Flora, S. J. (2010). Arsenic and fluoride: two major ground water pollutants. *Indian J. Exp. Biol.*, 48(7), 666-688.
- Christian, G. D., & Feldman, F. J. (1970). *Atomic absorption spectroscopy; Applications in agriculture, biology, and medicine*. New York, John Wiley.
- Chu, R. C., Barron, G. P., & Baumgartner, P. A. W. (1972). Arsenic determination at sub-microgram levels by arsine evolution and flameless atomic absorption spectrophotometric technique. *Analytical Chemistry*, 44(8), 1476-1479. doi:[10.1021/ac60316a042](https://doi.org/10.1021/ac60316a042)

- Clement, W. H., & Faust, S. D. (1973). A new convenient method for determining arsenic (+3) in natural waters. *Environmental Letters*, 5(3), 155-164. doi:[10.1080/00139307309435522](https://doi.org/10.1080/00139307309435522)
- Demir, E., & Silah, H. (2020). Development of a New Analytical Method for Determination of Veterinary Drug Oxyclozanide by Electrochemical Sensor and Its Application to Pharmaceutical Formulation. *Chemosensors*, 8(2), 25. doi:[10.3390/chemosensors8020025](https://doi.org/10.3390/chemosensors8020025)
- Demir, E., Silah, H., & Aydogdu, N. (2021). Electrochemical Analysis of Pesticide in Food Samples. In: H. Kaya & H. Kafadar (Eds.), *Medicine and Health*, (pp. 213-234), Efe Academy Publishing.
- Dong, W., Zhang, Y., & Quan, X. (2020). Health risk assessment of heavy metals and pesticides: A case study in the main drinking water source in Dalian, China. *Chemosphere*, 242, 125113. doi:[10.1016/j.chemosphere.2019.125113](https://doi.org/10.1016/j.chemosphere.2019.125113)
- Fishman, M., & Spencer, R. (1977). Automated atomic absorption spectrometric determination of total arsenic in water and streambed materials. *Analytical Chemistry*, 49(11), 1599-1602. doi:[10.1021/ac50019a035](https://doi.org/10.1021/ac50019a035)
- García, M., Aguirre, M. A., & Canals, A. (2017). Determination of As, Se, and Hg in fuel samples by in-chamber chemical vapor generation ICP OES using a flow Blurring multinebulizer. *Analytical and Bioanalytical Chemistry*, 409, 5481-5490. doi:[10.1007/s00216-017-0484-6](https://doi.org/10.1007/s00216-017-0484-6)
- González, A., Armenta, S., & De La Guardia, M. (2008). Trace elements composition of curry inductivity coupled plasma optical emission spectrometry (ICP-OES). *Food Additives & Contaminants: Part B*, 1(2), 114-121. doi:[10.1080/02652030802520845](https://doi.org/10.1080/02652030802520845)
- IARC (International Agency for Research on Cancer). (2004). *Some Drinking-water Disinfectants and Contaminants, including Arsenic*. IARC Monographs on the Evaluation of Carcinogenic Risks to Humans, No. 84, Lyon, France.
- Idris, A. O., Mafa, J. P., Mabuba, N., & Arotiba, O. A. (2017). Nanogold modified glassy carbon electrode for the electrochemical detection of arsenic in water. *Russian Journal of Electrochemistry*, 53, 170-177. doi:[10.1134/S1023193517020082](https://doi.org/10.1134/S1023193517020082)
- Kalayci, S. (2020). Hirfanlı baraj gölünde eser elementlerin ICP-OES ile tayini. *GU J Sci, Part C*, 8(2), 451-457. doi:[10.29109/gujsc.718105](https://doi.org/10.29109/gujsc.718105)
- Kalayci, S., & Muhammet, S. M. (2022). Determination of some trace elements in dried red plum using Inductively coupled plasma optical emission spectroscopy (ICP-OES). *Iranian Journal of Chemistry and Chemical Engineering* (in Press). doi:[10.30492/ijcce.2022.529125.4700](https://doi.org/10.30492/ijcce.2022.529125.4700)
- Li, Y., Ye, F., Wang, A., Wang, D., Yang, B., Zheng, Q., Sun, G., & Gao, X. (2016). Chronic Arsenic Poisoning Probably Caused by Arsenic-Based Pesticides: Findings from an Investigation Study of a Household. *International Journal of Environmental Research and Public Health*, 13(1), 133. doi:[10.3390/ijerph13010133](https://doi.org/10.3390/ijerph13010133)
- Maduka, H. C. C. (2006). Water pollution and man's health. *The Internet Journal of Gastroenterology*, 4(1), 1-8. [URL](https://doi.org/10.21960/ijgastro.4.1.1)
- Massadeh, A. M., & Al-Massaedh, A. T. (2018). Determination of heavy metals in canned fruits and vegetables sold in Jordan market. *Environmental Science and Pollution Research*, 25, 1914-1920. doi:[10.1007/s11356-017-0611-0](https://doi.org/10.1007/s11356-017-0611-0)
- Proch, J., & Niedzielski, P. (2020). In-spray chamber hydride generation by multi-mode sample introduction system (MSIS) as an interface in the hyphenated system of high performance liquid chromatography and inductivity coupled plasma optical emission spectrometry (HPLC/HG-ICP-OES) in arsenic species determination. *Talanta*, 208, 120395. doi:[10.1016/j.talanta.2019.120395](https://doi.org/10.1016/j.talanta.2019.120395)
- Raju, N. J. (2022). Arsenic in the geo-environment: A review of sources, geochemical processes, toxicity and removal technologies. *Environmental Research*, 203, 111782. doi:[10.1016/j.envres.2021.111782](https://doi.org/10.1016/j.envres.2021.111782)
- Somer, G., & Almas, Z. (2006). Differential pulse polarographic determination of trace quantities of arsenic using catalytic hydrogen wave and its application. *Journal of Electroanalytical Chemistry*, 593(1-2), 179-184. doi:[10.1016/j.jelechem.2006.03.047](https://doi.org/10.1016/j.jelechem.2006.03.047)

- Somer, G., & Kalayci, S. (2014). A new and sensitivity method for determination of trace arsenic using differential pulse polarography. *Canadian Journal of Chemistry*, 92(3), 221-227. doi:[10.1139/cjc-2013-0350](https://doi.org/10.1139/cjc-2013-0350)
- Tarla, D. N., Erickson, L. E., Hettiarachchi, G. M., Amadi, S. I., Galkaduwa, M., Davis, L. C., Nurzhanova, A., & Pidlisnyuk, V. (2020). Phytoremediation and bioremediation of pesticide-contaminated soil. *Applied Sciences*, 10(4), 1217. doi:[10.3390/app10041217](https://doi.org/10.3390/app10041217)
- USEPA (US Environmental Protection Agency). (1999). *Arsenic in Drinking Water: Analytical Methods*. Washington, DC.





Gazi University

**Journal of Science**

PART A: ENGINEERING AND INNOVATION

<http://dergipark.org.tr/gujsa>

## Computer Aided Simulation with Finite Element Analysis of the Effect of Face Mask Use Against COVID-19 and Other Infections

Canan İNAL<sup>1</sup>, Kadir GÖK<sup>2\*</sup>, H. Deniz ADA<sup>3</sup>, Sermet İNAL<sup>4</sup>, Arif GÖK<sup>5</sup><sup>1</sup>Kutahya Health Sciences University, Department of Anesthesiology and Intensive Care, Kutahya/Turkey<sup>2</sup>Izmir Bakircay University, Engineering and Architecture Faculty, Department of Biomedical Engineering, Izmir, Turkey<sup>3</sup>Dumlupinar University, Kutahya Vocational School of Technical Sciences, Chemical Technologies, Germiyan Campus, Kutahya/Turkey<sup>4</sup>Izmir Bakircay University, Department of Orthopaedics and Traumatology, Izmir/Turkey<sup>5</sup>Kutahya Dumlupinar University, Architecture Faculty, Department of Industrial Design, Kutahya/Turkey

Keywords	Abstract
Covid-19	Viruses are the leading infectious diseases. Viruses spread very fast and has a mortal risk to people with chronic diseases. Different methods are being sought to protect against the virus. In this study, the effect of face mask used against Covid-19 and other infections were investigated using finite element analysis. The effects of droplets formed because of cough or sneezing on the masked and without masked human model were analyzed. The human model without mask has a negative effective on the human face. The risk of infection is higher on the unmasked human model than on the masked human model.
Face Mask	
Pandemic	
Finite Element Analysis	

### Cite

İnal, C., Gök, K., Ada, H. D., İnal, S., & Gök, A. (2022). Computer Aided Simulation with Finite Element Analysis of the Effect of Face Mask Use Against COVID-19 and Other Infections. *GU J Sci, Part A, 9(2)*, 104-111.

Author ID (ORCID Number)	Article Process
C. İnal, 0000-0002-8119-6978	<b>Submission Date</b> 07.03.2022
K. Gök, 0000-0001-5736-1884	<b>Revision Date</b> 18.04.2022
H. D. Ada, 0000-0001-9991-8396	<b>Accepted Date</b> 06.06.2022
S. İnal, 0000-0003-0868-5633	<b>Published Date</b> 21.06.2022
A. Gök, 0000-0003-2840-9601	

## 1.INTRODUCTION

Viruses such as coronavirus disease (COVID-19), Measles, Flu, Rubella, Mumps, Chickenpox and Parvovirus B19 threaten respiratory system of health workers, patients, and all people in the human community. COVID-19 is known as an infectious disease affected by SARS-CoV-2, which is caused severe acute respiratory syndrome. The first case was encountered in December 2019 in Wuhan, China's Hubei province. It has continued to spread ever since and caused an ongoing pandemic. As of March 26, 2021, COVID-19 cases are 480,666,827, deaths are 6,145,158 and recovered are 414,844,261 in the worldwide.

Protective equipment is very effective in protecting against viruses. The use of face masks is crucial. The masks help to protect the social distance with infected people, if you are infected, they prevent you from passing this virus by respiratory system. However, some controversy has arisen about whether to use face masks during the pandemic process. Especially, there are simulation studies using finite element analysis (FEA) or Computational Fluid Dynamics (CFD) in this topic.

Finite element-based computer aided solution methods give very effective results in solving engineering problems. An accurate and reliable finite element model reduces the costs in solving the problem by eliminating experimental studies. While finite element analysis (FEA) is used for solid body mechanics, computational fluid dynamics (CFD) stands out in cases where the dynamic motion of liquids is examined. The defining the correct load and boundary conditions are very important in terms of good results from the methods. Else, we may get unwanted results Gok (2015). Today, FEA is used in engineering problems and simulations of COVID-19 and other infections (Gok et al., 2015; Gok, 2015; 2021; Gok & Inal, 2015; Erdem

et al., 2017; Gok et al., 2017; 2019; 2021a; Inal et al., 2018; Pirhan et al., 2020; Türkes et al., 2020; Ada et al., 2021).

There are some studies in the literature about the effects of protective masks. Jia et al. (2020) reported the developments in three-dimensional (3D) mask spoofing and anti-spoofing works in last decade. Swennen et al. (2020) have shown the concept and prototype of a custom-made face mask, which can be used anywhere in the world in case of any need, with computer aided design (CAD) data and 3D additive manufacturing method. Alenezi et al. (2021) were designed a novel face mask which is a reusable respirator, and it has small and highly efficient disposable fabric filter. Another paper was highlighted how the combination of current technologies such as 3D scanning, Finite Element simulation, machine learning, and additive manufacturing offers a seamless workflow to generate a sterilizable, reusable and validated custom-fit mask by Degueldre et al. (2020). The custom-made mask design has been used to avoid virus infection by Gok et al. (2021b). Another study is available about human face mask by Gok (2021). Although there are some studies in the literature that argue that face masks are effective against the virus, some groups have also mentioned the negative effects of mask use. The effect of face mask use against Covid- 19 and other infections were investigated using FEA.

## 2. COMPUTER AIDED SIMULATION

FEA is crucial for the development of optimum designs of mechanics and devices. It is preferable as a important method for verifying experimental and analytical results. In this study, the effect of face mask use against Covid- 19 and other infections were investigated using FEA. Computer-aided simulations were carried out in AnsysWorkbench Explicit Dynamics.

### 2.1. 3D Process of Human Face Mask

3D model of a human face was obtained using the Reverse Engineering (RE) method. RE is a widely used method in many areas of engineering to obtain 2D or 3D CAD data of existing objects. It accelerates the design process and enables the prototype of the product to be produced in a shorter time. 3D scanners with one or more cameras are used for this process. The 3D solid model of the classic face mask used for protection from viruses or in hospitals and clinics is modeled in the SolidWorks CAD program, as shown in Figure 1.

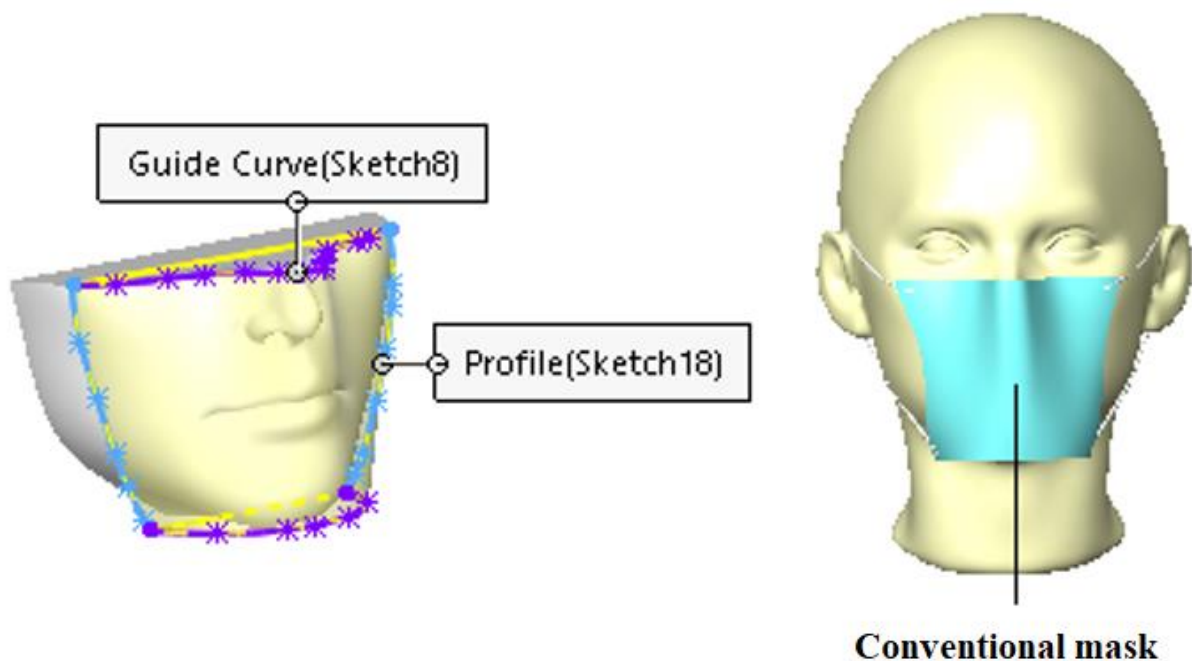


*Figure 1. 3D process of human face mask*

## 2.2. FEA Process

FEA process was given in Figure 2, hex dominant element type, 21698 nodes and 96051 elements. The element size of the human model was chosen as 5 mm and the element size of the other components was spontaneously chosen by the program. The fixed parts were seen in Figure 3. A speed of 160 to 800 km/h of the water droplets (Chhavi et al., 2011). A speed of 69.44 m/s was applied to the water droplet. Table 1 was seen material properties.

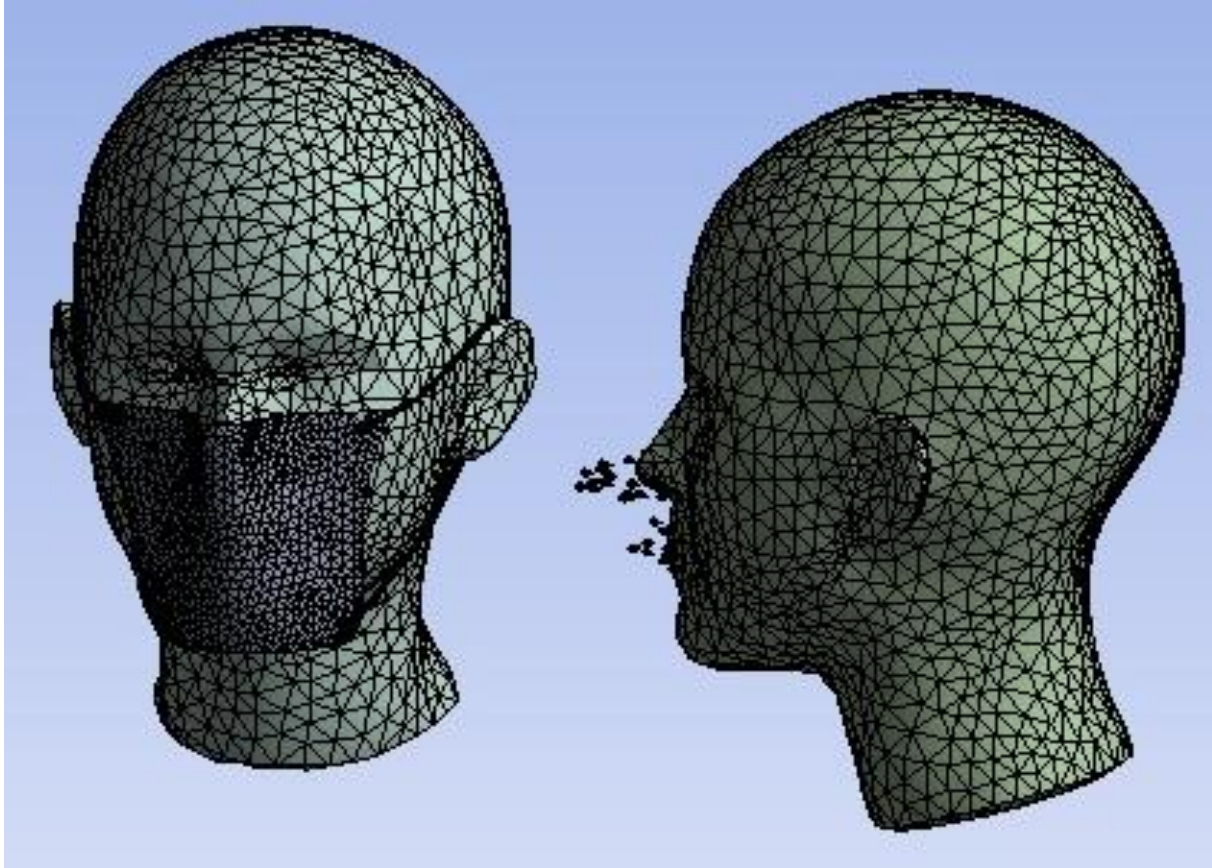


*Figure 2. Mesh process*

*Table 1. Materials properties (Duck, 1990; Endow & Russell, 2015; AnsysWorkbench, 2020)*

Parametreler	Human Skin	Rubber Band	Resin epoxy	Droplet
Density (kg/m <sup>3</sup> )	1000	110	1160	998
Shear Modulus (MPa)	4,79	0.58	1400	1e-06
Young's Modulus (MPa)	14.30	1.75	3780	3e-06
Poisson's Ratio	0.49	0.5	0.35	0.5

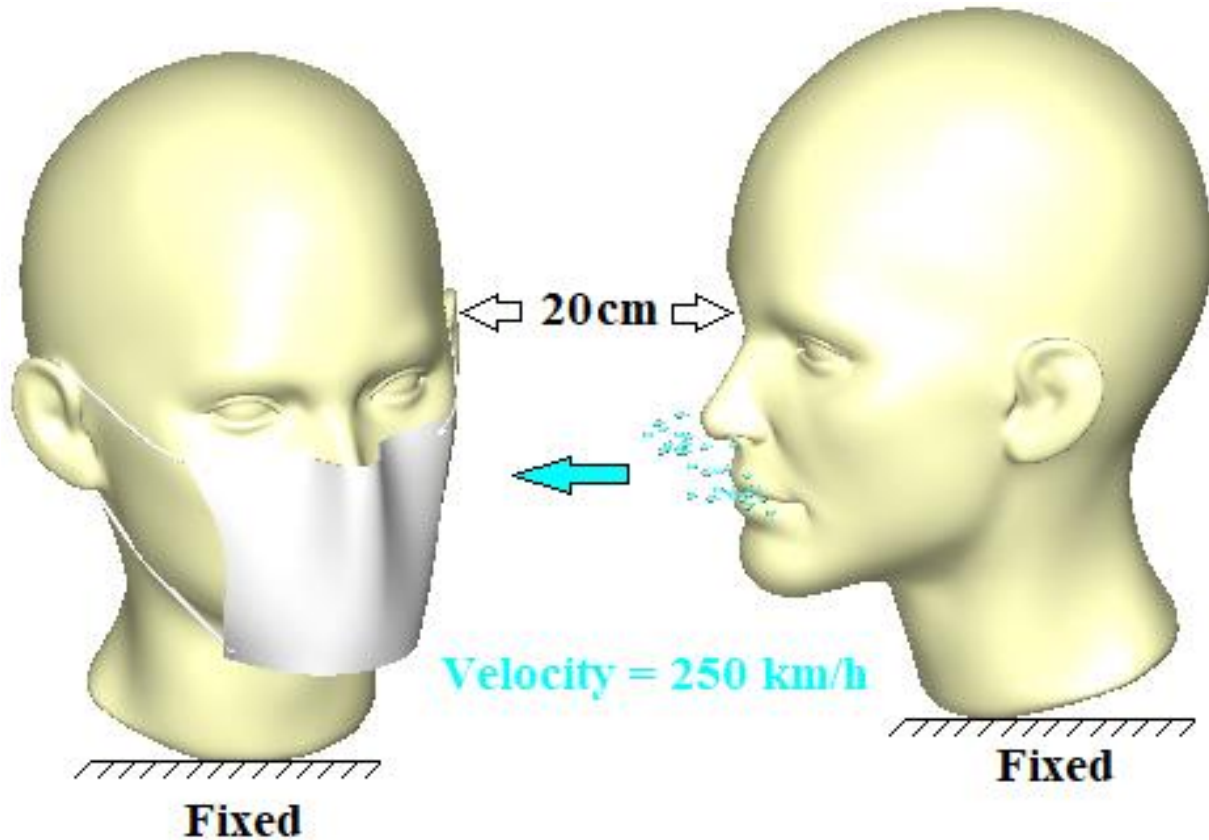


*Figure 3. Loading and boundary conditions*

### 3. RESULTS AND DISCUSSION

As seen in Figure 4, the droplets ejected by a person coughing from approximately 20 cm (droplet velocity = 69.44 m/s) hit the mask of the person in front of him. Considering that coronavirus-style viruses pass from person to person through droplets, it is noticed how effective the use of masks is. In Figure 5, if someone who does not wear a mask is coughed on the face zone, the droplets contact around the mouth and nose, causing the virus to spread more easily. However, if the person wore a mask as in Figure 4, the probability of being protected from viruses is higher.

Protective equipment is very effective in protecting against viruses. Disposable, standard and hygienic production reveals the importance of protective equipment in protecting against viruses. Experts say that masks prevent the spread of the disease and that everyone should use them in collective environments. Especially those coming from abroad will have a high risk of disease, so these people should use a mask. In addition, it is stated that not every mask is effective against the virus. Experts recommend the use of masks that comply with the specified standards. As seen in Figure 6, the classic face masks cause problems for human skin such as itching, redness and irritation. Itching, redness and irritation when used for a long time, but these masks have serious protection potential against the viruses [Gok \(2021\)](#).

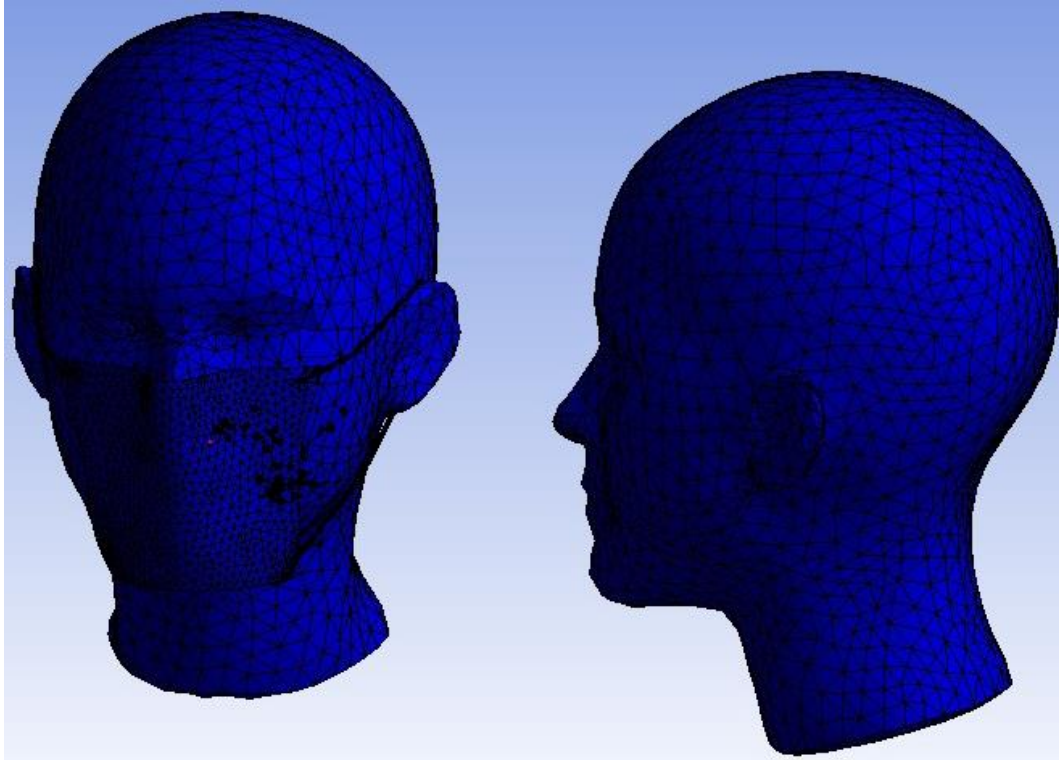


*Figure 4. Droplet effect on the face of a with mask person*

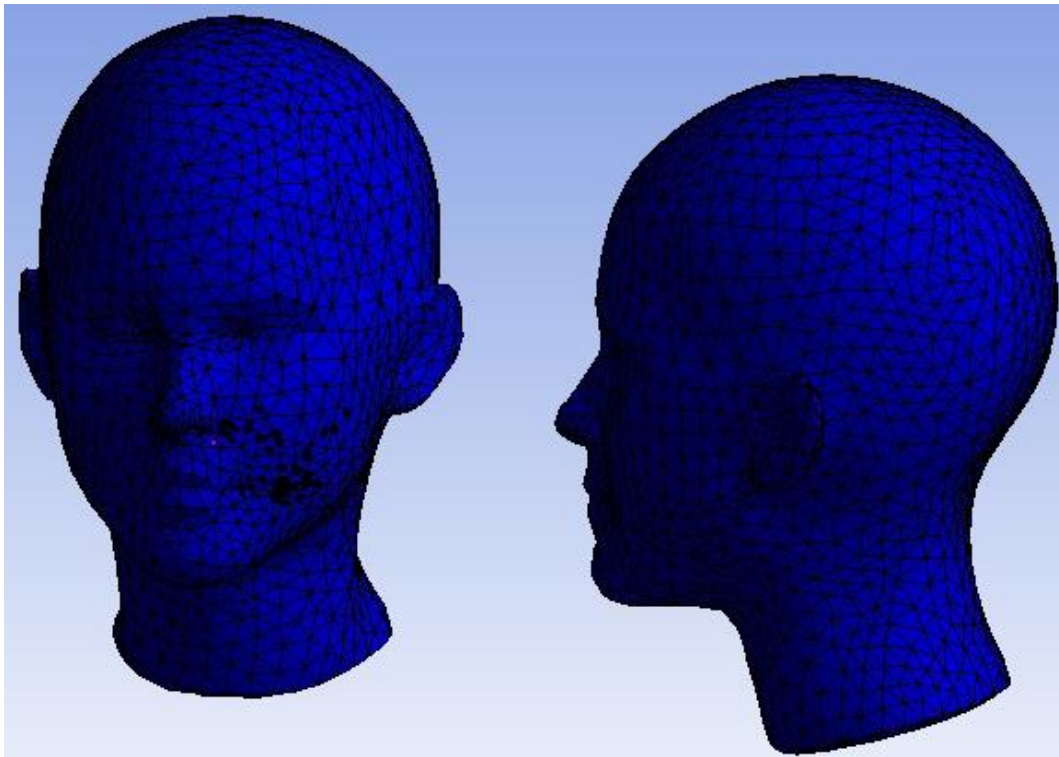


*Figure 5. Droplet effect on the face of a without mask person*

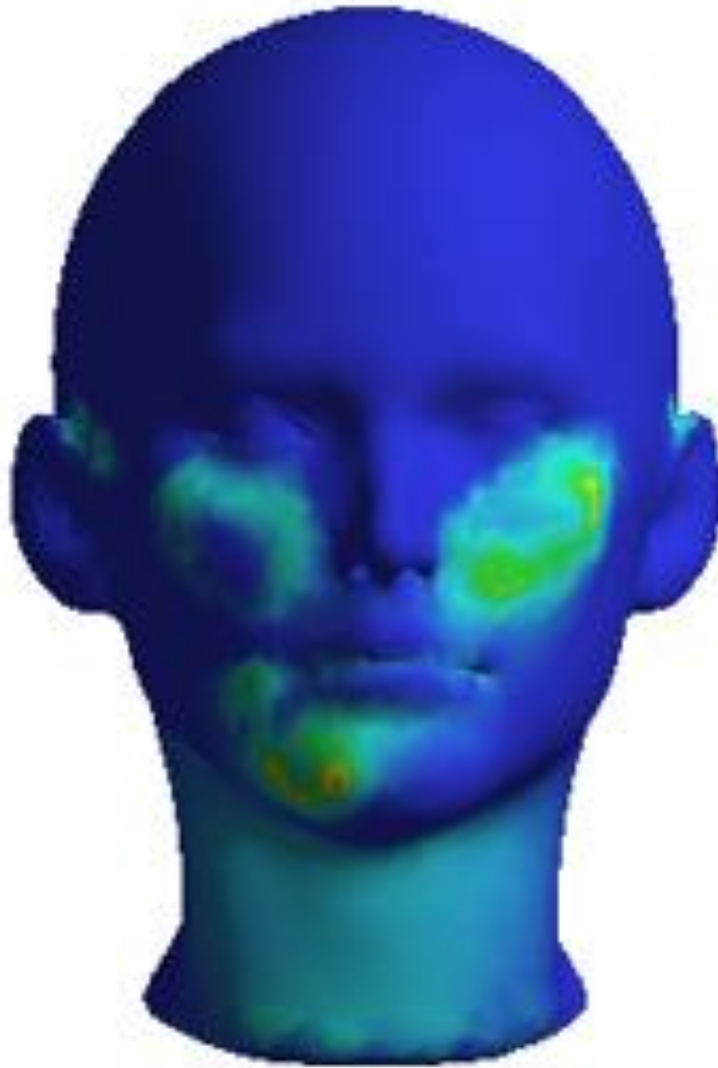


*Figure 6. Stresses occurring from face mask (Gok, 2021)*

#### **4. CONCLUSION**

The effect of face mask use against Covid- 19 and other infections were investigated using FEA. The computer simulations were carried out using AnsysWorkbench. Although, the conventional face masks have a harmful effective in terms of itching, redness and irritation on the human face skin, these masks have serious protection potential against the viruses. In the future, authors are planning to research the effects of cough magnitude (droplet velocity) and distance between the persons.

FEA is very important for solve the of engineering problems. It is used as a reliable technique for verifying experimental and analytical results. This method, which has been used effectively in the solution of engineering problems in the field of health in recent years, is especially effective in reducing experimental costs.

#### **CONFLICT OF INTEREST**

There is no conflict of interest

**REFERENCES**

- Ada, H. D., Erdem, M., & Gok, K. (2021). Computational Fluid Dynamics Simulation of Erosion-Corrosion in Abrasive Water Jet Machining. *Surface Review and Letters*, 28(05), 2150031. doi:[10.1142/S0218625X21500311](https://doi.org/10.1142/S0218625X21500311)
- Alenezi, H., Cam, M. E., & Edirisinghe, M. (2021). A novel reusable anti-COVID-19 transparent face respirator with optimized airflow. *Bio-Design and Manufacturing*, 4, 1-9. doi:[10.1007/s42242-020-00097-1](https://doi.org/10.1007/s42242-020-00097-1)
- AnsysWorkbench, 2020. AnsysWorkbench Material Library.
- Chhavi, S., Sushma, D., Ravinder, V., Anju, D., & Asha, S. (2011). Recent update on proficient bone fracture revivifying herbs. *International Research Journal of Pharmacy*, 2(11), 3-5.
- Degueldre, L., Borduas, J., Dion, F., Laurin, P., Castonguay, A., Viens, S-P., Le Navéaux, F., Hachem, B., Benoit, D., & Clin, J. (2020). Improving the Fit of Respiratory Face Masks through 3D Scanning, Finite Elements Analysis and Additive Manufacturing. In: Proceedings of the 11th Int. Conference and Exhibition on 3D Body Scanning and Processing Technologies (3DBODY.TECH 2020), 33.
- Duck, F. A. (1990). Mechanical Properties of Tissue. In: *Physical Properties of Tissues: A Comprehensive Reference Book* (pp. 137-165). Academic Press, London.
- Endow, S. A., & Russell, A. P. (2015). Biophysics - A Step-by-Step Introduction to Concepts for Students, Lesson Plan : Elasticity.
- Erdem, M., Gok, K., Gokce, B., & Gok, A. (2017). Numerical Analysis of Temperature, Screwing Moment and Thrust Force Using Finite Element Method in Bone Screwing Process. *Journal of Mechanics in Medicine and Biology*, 17(01), 1750016. doi:[10.1142/S0219519417500166](https://doi.org/10.1142/S0219519417500166)
- Gok, K. (2015). Development of three-dimensional finite element model to calculate the turning processing parameters in turning operations. *Measurement*, 75, 57-68. doi:[10.1016/j.measurement.2015.07.034](https://doi.org/10.1016/j.measurement.2015.07.034)
- Gok, K. (2021). Investigation of the use of silicone pads to reduce the effects on the human face of classical face masks used to prevent from COVID-19 and other infections. *Proceedings of the Institution of Mechanical Engineers, Part E: Journal of Process Mechanical Engineering*, 235(5), 1742-1747. doi:[10.1177/09544089211019581](https://doi.org/10.1177/09544089211019581)
- Gok, K., & Inal, S. (2015). Biomechanical comparison using finite element analysis of different screw configurations in the fixation of femoral neck fractures. *Mech. Sci.*, 6(2), 173-179. doi:[10.5194/ms-6-173-2015](https://doi.org/10.5194/ms-6-173-2015)
- Gok, A., Gok, K., & Bilgin, M. B. (2015). Three-dimensional finite element model of the drilling process used for fixation of Salter–Harris type-3 fractures by using a K-wire. *Mech. Sci.*, 6(2), 147-154. doi:[10.5194/ms-6-147-2015](https://doi.org/10.5194/ms-6-147-2015)
- Gok, K., Inal, S., Gok, A., & Pinar, A. M. (2017). Biomechanical effects of three different configurations in Salter Harris type 3 distal femoral epiphyseal fractures. *Journal of the Brazilian Society of Mechanical Sciences and Engineering*, 39(4), 1069-1077. doi:[10.1007/s40430-016-0666-8](https://doi.org/10.1007/s40430-016-0666-8)
- Gok, K., Inal, S., Urtekin, L., & Gok, A. (2019). Biomechanical performance using finite element analysis of different screw materials in the parallel screw fixation of Salter–Harris Type 4 fractures. *Journal of the Brazilian Society of Mechanical Sciences and Engineering*, 41(3), 143. doi:[10.1007/s40430-019-1640-z](https://doi.org/10.1007/s40430-019-1640-z)
- Gok, K., Erdem, M., Kisioglu, Y., Gok, A., & Tumsek, M. (2021a). Development of bone chip-vacuum system in orthopedic drilling process. *Journal of the Brazilian Society of Mechanical Sciences and Engineering*, 43(4), 224. doi:[10.1007/s40430-021-02959-w](https://doi.org/10.1007/s40430-021-02959-w)
- Gok, K., Selçuk, A. B., & Gok, A. (2021b). Computer-Aided Simulation Using Finite Element Analysis of Protect Against to Coronavirus (COVID-19) of Custom-Made New Mask Design. *Transactions of the Indian Institute of Metals*, 74(5), 1029-1033. doi:[10.1007/s12666-021-02227-4](https://doi.org/10.1007/s12666-021-02227-4)
- Inal, S., Gok, K., Gok, A., Uzumcugil, A. O., & Kuyubasi, S. N. (2018). Should we really compress the fracture line in the treatment of Salter–Harris type 4 distal femoral fractures? A biomechanical study. *Journal of the Brazilian Society of Mechanical Sciences and Engineering*, 40(11), 528. doi:[10.1007/s40430-018-1448-2](https://doi.org/10.1007/s40430-018-1448-2)

- Jia, S., Guo, G., & Xu, Z. (2020). A survey on 3D mask presentation attack detection and countermeasures. *Pattern Recognition*, 98, 107032. doi:[10.1016/j.patcog.2019.107032](https://doi.org/10.1016/j.patcog.2019.107032)
- Pirhan, Y., Gök, K., & Gök, A. (2020). Comparison of two different bowel anastomosis types using finite volume method. *Computer Methods in Biomechanics and Biomedical Engineering*, 23(8), 323-331. doi:[10.1080/10255842.2020.1722809](https://doi.org/10.1080/10255842.2020.1722809)
- Swennen, G. R. J., Pottel, L., & Haers, P. E. (2020). Custom-made 3D-printed face masks in case of pandemic crisis situations with a lack of commercially available FFP2/3 masks. *Int. J. Oral Maxillofac. Surg.*, 49(5), 673-677. doi:[10.1016/j.ijom.2020.03.015](https://doi.org/10.1016/j.ijom.2020.03.015)
- Türkes, E., Erdem, M., Gok, K., & Gok, A. (2020). Development of a new model for determine of cutting parameters in metal drilling processes. *Journal of the Brazilian Society of Mechanical Sciences and Engineering*, 42(4), 169. doi:[10.1007/s40430-020-2257-y](https://doi.org/10.1007/s40430-020-2257-y)





Gazi University

**Journal of Science**

PART A: ENGINEERING AND INNOVATION

<http://dergipark.org.tr/gujisa>

## Amalgamated Rings with $n$ - $UJ$ -Properties

Esra MEMİŞOĞULLARINDAN<sup>1\*</sup>, Tufan ÖZDİN<sup>2</sup><sup>1</sup>Gazi University, Graduate School of Natural and Applied Sciences, 06500, Ankara, Turkey<sup>2</sup>Erzincan Binali Yıldırım University, Science and Art Faculty, 24100, Erzincan, Turkey

Keywords	Abstract
Amalgamated Rings $UU$ -rings $UJ$ -rings Unit Elements Jacobson Radikal	This paper examines the transfer of $n$ - $UJ$ -rings between $A$ and $B$ in an amalgamated duplication of a ring $A$ along some ideal $K$ of a ring $B$ with a ring homomorphism $f: A \rightarrow B$ (denoted by $A \bowtie^f K$ ).

### Cite

Memişoğullarından, E., & Özdin, T. (2022). Amalgamated Rings with  $n$ - $UJ$ -Properties. *GU J Sci, Part A, 9(2)*, 112-119.

Author ID (ORCID Number)	Article Process
E. Memişoğullarından, 0000-0002-7827-8972	<b>Submission Date</b> 20.04.2022
T. Özdin, 0000-0001-8081-1871	<b>Revision Date</b> 23.05.2022
	<b>Accepted Date</b> 24.06.2022
	<b>Published Date</b> 25.06.2022

## 1. INTRODUCTION

In this article all rings are associative with nonzero identity elements. For a ring  $R$ , the Jacobson radical, the set of nilpotent elements and the set of unit elements of  $R$  are denoted by  $J(R)$ ,  $Nil(R)$  and  $U(R)$  with respectively.

Let  $A, B$  be rings,  $K$  be an ideal of  $B$  and  $f: A \rightarrow B$  a ring homomorphism. We consider the following subring of  $A \times B$ :

$$A \bowtie^f K = \{(a, f(a) + k) \mid a \in A, k \in K\}$$

which is called the amalgamation of  $A$  with  $B$  along  $K$  with respect to  $f$  (D'Anna et al., 2009).

In Farshad et al. (2021), the authors studied  $UU$ -rings (if  $U(R) = 1 + Nil(R)$ ) i.e., rings whose units are unipotent (Calugareanu, 2015) and clean like features of the amalgamation ring  $A \bowtie^f K$  as the followings:

- (1) If  $A$  and  $f(A) + K$  are  $UU$ -rings, then  $A \bowtie^f K$  is  $UU$ -ring. (Farshad et al., 2021; Theorem 3.2 (1));
- (2) If  $A \bowtie^f K$  is a  $UU$ -ring, then  $A$  is a  $UU$ -ring (Farshad et al., 2021; Theorem 3.2 (2)).
- (3) If  $A \bowtie^f K$  is a nil-clean ring, then  $A$  and  $f(A) + K$  are nil-clean rings (Farshad et al., 2021; Proposition 2.7 (1)) where a ring  $R$  is clean if each element of  $R$  is a sum of a unit and an idempotent in  $R$  (Nicholson, 1977), and  $R$  is nil-clean if each element of  $R$  is a sum of a nilpotent and an idempotent in  $R$  (Diesl, 2013);

- (4) If  $A$  is nil-clean ring and  $K \subset Nil(B)$ , then  $A \bowtie^f K$  is a nil-clean ring (Farshad et al., 2021; Theorem 2.10 (1)).
- (5) If  $A \bowtie^f K$  is a  $J$ -clean ring, then  $A$  and  $f(A) + K$  are  $J$ -clean rings (Farshad et al., 2021; Proposition 2.16 (1)) where a ring  $R$  is  $J$ -clean if each element of  $R$  is a sum of an idempotent and an element from  $J(R)$  (Chen, 2010).
- (6) If  $A$  is  $J$ -clean ring and  $K \subset Nil(B)$ , then  $A \bowtie^f K$  is  $J$ -clean (Farshad et al., 2021; Theorem 2.18 (1)).

The main propose of the president paper is to examine  $UJ$ ,  $n-UJ$  and  $J$ -clean properties of the amalgamation ring  $A \bowtie^f K$ . Here,

- $R$  is said to be a  $UJ$ -ring if  $U(R) = 1 + J(R)$  (Koşan et al., 2018);
- $R$  is is said to be an  $n-UJ$ -ring if  $u - u^n \in J(R)$  for each  $u \in U(R)$  where  $n > 1$  is a fixed integer and  $R$  is said to be an  $\infty-UJ$ -ring if for each  $u \in U(R)$  there exist  $n > 1$  such that  $u - u^n \in J(R)$  (Koşan et al., 2020)

Notice that every  $UJ$ -ring with nil Jacobson radical is  $UU$ -rings and  $R$  is a  $UJ$ -ring if and only if all clean elements of  $R$  are  $J$ -clean (Koşan et al., 2018; Proposition 4.1); every  $UJ$ -rings are  $n-UJ$ -rings and hence  $\infty-UJ$ -rings.

We denote by  $\mathbb{Z}$  and  $\mathbb{Z}_n$ , respectively, the ring of integers and the ring of integers modulo  $n$  for a positive integer  $n$ .

## 2. RESULTS

Firstly, we start to with the following useful lemma which is about the general properties of the set of units and Jacobson radical in an amalgamated ring.

**Lemma 2.1.** We have the following statements for the amalgamated ring  $A \bowtie^f K$  of the rings  $A$  and  $B$ .

- (1)  $U(A \bowtie^f K) = \{u, f(u) + k \mid u \in U(A), f(u) + k \in U(f(A) + K)\}$ .
- (2)  $J(A \bowtie^f K) = \{a, f(a) + k \mid a \in U(A), f(a) + k \in J(f(A) + K)\}$ .
- (3)  $\frac{A \bowtie^f K}{0 \times K} \simeq A$  and  $\frac{A \bowtie^f K}{f^{-1}(K) \times 0} \simeq f(A) + K$ .
- (4)  $Nil(A \bowtie^f K) = \{a, f(a) + k \mid a \in Nil(A), f(a) + k \in J(f(A) + K)\}$ .

**Proof:** (1), (2) and (4) are Farshad et al. (2021) (Lemma 2.5 and Lemma 2.15).

(3) We have the natural projections  $\pi_A: A \bowtie^f K \rightarrow A$  defined by  $\pi_A(a, f(a) + k) = a$  and  $\pi_B: A \bowtie^f K \rightarrow B$  defined by  $\pi_B(a, f(a) + k) = f(a) + k$  by D’Anna et al. (2009) (Proposition 5.1). Hence desired canonical isomorphisms hold. ■

For  $n \in \mathbb{Z}$ , we consider the following notions adapted by Koşan et al. (2020).

$$\mathcal{U}_n(R) = \{u^{n-1} : u \in U(R)\} \subseteq U(R)$$

$$\mathcal{V}_n(R) = \{u \in U(R) : u^{n-1} \in 1 + J(R)\}$$

By using above notation, we have

$$\mathcal{U}_n(A \bowtie^f K) = \{(u^{n-1}, (f(u) + k)^{n-1}) : u \in U(A), f(u) + k \in U(f(A) + K)\}$$

and

$$\mathcal{V}_n(A \bowtie^f K) = \{(u, f(u) + k) \in U(A \bowtie^f K) : (u^{n-1}, (f(u) + k)^{n-1}) \in (1,1) + J(A \bowtie^f K)\}.$$

**Lemma 2.2.** We have the following statements for the amalgamated ring  $A \bowtie^f K$  of the rings  $A$  and  $B$ .

- (1)  $\mathcal{U}_n(A \bowtie^f K) \subseteq U(A \bowtie^f K)$
- (2) If  $A$  and  $B$  are commutative rings, then  $\mathcal{U}_n(A \bowtie^f K)$  and  $\mathcal{V}_n(A \bowtie^f K)$  are subgroups of  $U(A \bowtie^f K)$ .
- (3) If  $A \bowtie^f K$  is an  $n$ - $UJ$ -ring, then  $\mathcal{V}_n(A \bowtie^f K) = U(A \bowtie^f K)$  and hence  $\mathcal{U}_n(A \bowtie^f K) \subseteq (1,1) + J(A \bowtie^f K)$ .
- (4) An amalgamated ring  $A \bowtie^f K$  is  $\infty$ - $UJ$ -ring if and only if  $\bigcup_{n \in \mathbb{N}} \mathcal{V}_n(A \bowtie^f K) = U(A \bowtie^f K)$ .
- (5) If the amalgamated ring  $A \bowtie^f K$  is  $n$ - $UJ$ -ring such that  $(n - 1, n - 1) \in U(A \bowtie^f K)$  then  $Nil(A \bowtie^f K) \subseteq J(A \bowtie^f K)$ .

**Proof:** They are obvious. ■

**Proposition 2.3.** We have the following statements for the amalgamated ring  $A \bowtie^f K$  of the rings  $A$  and  $B$ , and  $n, m \in \mathbb{N}, n, m > 1$ .

- (1) If the amalgamated ring  $A \bowtie^f K$  is  $n$ - $UJ$ -ring, then  $(2,2) \in J(A \bowtie^f K)$  if  $n$  is an even number.
- (2) If the amalgamated ring  $A \bowtie^f K$  is  $n$ - $UJ$ -ring and  $n - 1$  divides  $m - 1$ , then  $A \bowtie^f K$  is an  $m$ - $UJ$ -ring.

**Proof:** (1) We assume that  $n$  is an even number and  $A \bowtie^f K$  is an  $n$ - $UJ$ -ring. Then

$$(-1, -1) = ((-1)^{(n-1)}, (-1)^{(n-1)}) \in (1,1) + J(A \bowtie^f K)$$

which implies that  $(2,2) \in J(A \bowtie^f K)$ .

- (2) Since  $n - 1$  divides  $m - 1$ , we get  $\mathcal{V}_n \subseteq \mathcal{V}_m$  which implies that  $A \bowtie^f K$  is an  $m$ - $UJ$ -ring by Lemma 2.2 (3). ■

**Theorem 2.4.** We have the following statements for the amalgamated ring  $A \bowtie^f K$  of the rings  $A$  and  $B$ .

- (1) If  $A$  and  $f(A) + K$  are  $n$ - $UJ$ -rings (respectively,  $\infty$ - $UJ$ -rings), then  $A \bowtie^f K$  is an  $n$ - $UJ$ -ring (respectively,  $\infty$ - $UJ$ -ring).
- (2) Let  $f: A \rightarrow B$  be a ring monomorphism and  $f^{-1}(K) \subseteq J(A)$  an ideal. If  $A \bowtie^f K$  is an  $n$ - $UJ$ -ring, then  $A$  and  $f(A) + K$  are  $n$ - $UJ$ -rings.

**Proof:** (1) Let  $(u, f(u) + k) \in U(A \bowtie^f K)$ . By Lemma 2.1 (1), we have  $u \in U(A)$  and  $f(u) + k \in U(f(A) + K)$ . Since  $A$  and  $f(A) + K$  are  $n$ - $UJ$ -rings (respectively,  $\infty$ - $UJ$ -rings), we obtain that  $1 - u^{n-1} \in J(A)$  which implies  $u - u^n \in J(A)$  and  $f(u^{n-1}) + k - 1 \in J(f(A) + K)$ . Hence  $(u^{n-1}, f(u^{n-1}) + k) - (1,1) \in J(A \bowtie^f K)$ . Therefore  $A \bowtie^f K$  is an  $n$ - $UJ$ -ring.

(2) Let  $A \bowtie^f K$  be an  $n$ - $UJ$ -ring. By Koşan et al. (2020) (Proposition 2.9 (1)),  $A$  and  $f(A) + K$  are  $n$ - $UJ$ -rings because  $\frac{A \bowtie^f K}{0 \times K} \cong A$  and  $\frac{A \bowtie^f K}{f^{-1}(K) \times 0} \cong f(A) + K$  by Lemma 2.1 (3). ■

Let  $I \subseteq J(R)$  be an ideal of  $R$ . By Koşan et al. (2020) (Proposition 2.9 (1)),  $R$  is an  $n$ - $UJ$ -ring if and only if  $R/I$  is an  $n$ - $UJ$ -ring.

**Corollary 2.5.** We have the following statements for the amalgamated ring  $A \bowtie^f K$  of the rings  $A$  and  $B$ .

- (1) If  $B = K$  or  $f: A \rightarrow B$  is an epimorphism, then  $A \bowtie^f K$  is an  $n$ - $UJ$ -ring if and only if  $A$  and  $B$  are  $n$ - $UJ$ -rings, since in this case  $A \bowtie^f K = A \times B$ .
- (2) If  $f^{-1}(K) = 0$ , then  $A \bowtie^f K$  is an  $n$ - $UJ$ -ring if and only if  $f(A) + K$  is an  $n$ - $UJ$ -ring (by Lemma 2.1 (3) and Koşan et al., 2020; Proposition 2.9 (1)).
- (3) If  $K = 0$ , then  $A \bowtie^f K$  is an  $n$ - $UJ$ -ring if and only if  $A$  is an  $n$ - $UJ$ -ring (by Lemma 2.1 (3) and Koşan et al., 2020; Proposition 2.9 (1)).

**Theorem 2.6.** Let  $R$  be a ring and let  $M$  be an  $(R, R)$  bimodule.  $R$  is an  $n$ - $UJ$ -ring if and only if the trivial extension  $T(R, M)$  is an  $n$ - $UJ$ -ring.

**Proof:** This is proven in Koşan et al. (2020) (Theorem 3.1). ■

Since  $UJ$ -rings are  $n$ - $UJ$ -rings, we have following theorem.

**Theorem 2.7.** We have the following statements for the amalgamated ring  $A \bowtie^f K$  of the rings  $A$  and  $B$ .

- (1) If  $A$  and  $f(A) + K$  are  $UJ$ -rings, then  $A \bowtie^f K$  is a  $UJ$ -ring.
- (2) Let  $f: A \rightarrow B$  be a ring monomorphism and  $f^{-1}(K) \subseteq J(A)$  an ideal. If  $A \bowtie^f K$  is a  $UJ$ -ring, then  $A$  and  $f(A) + K$  are  $UJ$ -rings.

In Theorem 2.7, the assumption “ $f^{-1}(K) \subseteq J(A)$ ” is not superflous because if we can take  $A = B = \mathbb{Z}_4 \times \mathbb{Z}_4$ ,  $K = 0 \times 2\mathbb{Z}_4 \subseteq J(B) = 2\mathbb{Z}_4 \times 2\mathbb{Z}_4$  and a ring homomorphism  $f: A \rightarrow B$  defined by  $f((a, b)) = (0, a)$ . Then  $f^{-1}(K) = 2\mathbb{Z}_4 \times \mathbb{Z}_4 \not\subseteq J(A) = 2\mathbb{Z}_4 \times 2\mathbb{Z}_4$ .

**Corollary 2.7.** We have the following statements for the amalgamated ring  $A \bowtie^f K$  of the rings  $A$  and  $B$ .

- (1) If  $B = K$  or  $f: A \rightarrow B$  is an epimorphism, then  $A \bowtie^f K$  is a  $UJ$ -ring if and only if  $A$  and  $B$  are  $UJ$ -rings, since in this case  $A \bowtie^f K = A \times B$ .
- (2) If  $f^{-1}(K) = 0$ , then  $A \bowtie^f K$  is a  $UJ$ -ring if and only if  $f(A) + K$  is a  $UJ$ -ring (by Lemma 2.1 (3) and Koşan et al., 2018; Proposition 2.3 (5)).

If  $K = 0$ , then  $A \bowtie^f K$  is a  $UJ$ -ring if and only if  $A$  is a  $UJ$ -ring (by Lemma 2.1 (3) and Koşan et al., 2018; Proposition 2.3 (5)).

### 3. EXAMPLES

**Example 3.1.** Let  $A = \mathbb{Z}_6$ ,  $B = \mathbb{Z}_3 \times \mathbb{Z}_3$ ,  $K = 0 \times \mathbb{Z}_3$  and  $f: A \rightarrow B$  defined by

$$f(0) = f(3) = (0,0), f(1) = f(4) = (1,1), \text{ and } f(2) = f(5) = (2,2).$$

Clearly,

$$\begin{aligned} f(A) + K &= \{(0,0), (0,1), (0,2), (1,1), (1,2), (1,0), (2,2), (2,0), (2,1)\}, \\ A \bowtie^f K &= \{(0, (0,0)), (0, (0,1)), (0, (0,2)), (1, (1,1)), (1, (1,2)), (1, (1,0)), \\ &\quad (2, (2,2)), (2, (2,0)), (2, (2,1)), (3, (0,0)), (3, (0,1)), (3, (0,2)), \\ &\quad (4, (1,1)), (4, (1,2)), (4, (1,0)), (5, (2,2)), (5, (2,0)), (5, (2,1))\} \end{aligned}$$

and

$$\begin{aligned} U(A \bowtie^f K) &= \{(1, (1,1)), (1, (1,2)), (5, (2,2)), (5, (2,1))\}, \\ J(A \bowtie^f K) &= \{(0, (0,0)), (0, (0,1)), (4, (1,1)), (4, (1,0))\}. \end{aligned}$$

If we compute  $u - u^n$  for  $n = 2, 3, 4$ ;

$$\begin{aligned} u - u^2 &= (1, (1,1)) - (1, (1,1)) = (0, (0,0)) \in J(A \bowtie^f K) \\ u - u^2 &= (1, (1,2)) - (1, (1,1)) = (0, (0,1)) \in J(A \bowtie^f K) \\ u - u^2 &= (5, (2,2)) - (1, (1,1)) = (4, (1,1)) \in J(A \bowtie^f K) \\ u - u^2 &= (5, (2,1)) - (1, (1,1)) = (4, (1,0)) \in J(A \bowtie^f K) \\ u - u^3 &= (1, (1,1)) - (1, (1,1)) = (0, (0,0)) \in J(A \bowtie^f K) \\ u - u^3 &= (1, (1,2)) - (1, (1,2)) = (0, (0,0)) \in J(A \bowtie^f K) \\ u - u^3 &= (5, (2,2)) - (5, (2,2)) = (0, (0,0)) \in J(A \bowtie^f K) \\ u - u^3 &= (5, (2,1)) - (5, (2,1)) = (0, (0,0)) \in J(A \bowtie^f K) \\ u - u^4 &= (1, (1,1)) - (1, (1,1)) = (0, (0,0)) \in J(A \bowtie^f K) \\ u - u^4 &= (1, (1,2)) - (1, (1,1)) = (0, (0,1)) \in J(A \bowtie^f K) \\ u - u^4 &= (5, (2,2)) - (1, (1,1)) = (4, (1,1)) \in J(A \bowtie^f K) \\ u - u^4 &= (5, (2,1)) - (1, (1,1)) = (4, (1,0)) \in J(A \bowtie^f K) \end{aligned}$$

If we continue in a similar way, we get  $(u - u^n) \in J(A \bowtie^f K)$ .

**Example 3.2.** Let  $A = \mathbb{Z}_6$ ,  $B = \mathbb{Z}_3 \times \mathbb{Z}_3$ ,  $K = 0 \times \mathbb{Z}_3$  and  $f: A \rightarrow B$  defined as follow,

$$f(0) = f(3) = (0,0), f(1) = f(4) = (1,1), \text{ and } f(2) = f(5) = (2,2).$$

Clearly,  $U(A) = \{1,5\}$ ,  $Id(A) = \{0,1,3,4\}$ . Let  $K = \{(0,0), (0,1), (0,2)\}$ . Then,

$$R = A \rtimes^f K = \{(0, (0,0)), (0, (0,1)), (0, (0,2)), (1, (1,1)), (1, (1,2)), (1, (1,0)), (2, (2,2)), (2, (2,0)), (2, (2,1)), (3, (0,0)), (3, (0,1)), (3, (0,2)), (4, (1,1)), (4, (1,2)), (4, (1,0)), (5, (2,2)), (5, (2,0)), (5, (2,1))\}.$$

So,

$$\begin{aligned} U(f(A)) + K &= \{(1,1), (1,2), (2,2), (2,1)\} \\ U(A \rtimes^f K) &= \{(1, (1,1)), (1, (1,2)), (5, (2,2)), (5, (2,1))\} \\ Id(A \rtimes^f K) &= \{(0, (0,0)), (0, (0,1)), (1, (1,1)), (1, (1,0)), (3, (0,0)), (3, (0,1)), (4, (1,1)), (4, (1,0))\} \\ f(A) + K &= \{(0,0), (0,1), (0,2), (1,1), (1,2), (1,0), (2,2), (2,0), (2,1)\} \\ f(U(A)) + K &= \{(1,1), (1,2), (1,0), (2,2), (2,0), (2,1)\} \end{aligned}$$

and  $x(f(A) + K) = y(f(A) + K)$  then  $(2,0)(f(A) + K) = (1,0)(f(A) + K)$ . However,

$$(2,0) \neq (1,0) \cdot (1,2)$$

(i.e  $x \neq yu$ ). By Koşan et al. (2018) (Corollary 2.5),  $A = \mathbb{Z}_6$  is a  $UJ$ -ring but we can easily see that  $f(A) + K$  is not a  $UJ$ -ring, and so  $R = A \rtimes^f K$  is not a  $UJ$ -ring.

#### 4. J-CLEANNESS

Let  $M = (M_i)_{i=1}^n$  be a family of  $R$ -modules and  $\varphi = \{\varphi_{i,j}\}_{\substack{i+j \leq n \\ 1 \leq i,j \leq n-1}}$  be a family of bilinear maps such that each  $\varphi_{i,j}$  is written multiplicatively:

$$\begin{aligned} \varphi_{i,j}: M_i \times M_j &\longrightarrow M_{i+j} \\ (m_i, m_j) &\longmapsto \varphi_{i,j}(m_i, m_j) := m_i m_j \end{aligned}$$

In particular, if all  $M_i$  are submodules of the same  $R$ -algebra  $L$ , then the bilinear maps, if they are not specified, are just the multiplication of  $L$  (see examples in Anderson et al. (2017) (Section 2)). The  $n$ - $\varphi$ -trivial extension of  $R$  by  $M$  is the set denoted by  $R \rtimes_{\varphi} M_1 \rtimes \dots \rtimes M_n$  or simply  $R \rtimes_{\varphi} M$  whose underlying additive group is  $R \oplus M_1 \oplus \dots \oplus M_n$  with multiplication given by

$$(m_0, \dots, m_n)(m'_0, \dots, m'_n) = \left( \sum_{j+k=i} m_j m'_k \right)$$

for all  $(m_i), (m'_i) \in R \rtimes_{\varphi} M$ .

We could also define the product  $\varphi_{i,j}: M_i \times M_j \longrightarrow M_{i+j}$  as an  $R$ -bimodule homomorphism  $\tilde{\varphi}_{i,j}: M_i \otimes M_j \rightarrow M_{i+j}$ ; see Anderson et al. (2017) (Section 2) for details.

For the sake of simplicity, it is convenient to set  $M_0 = R$ . In what follows, if no ambiguity arises, the  $n$ - $\varphi$ -trivial extension of  $R$  by  $M$  will be simply called an  $n$ - $\varphi$ -trivial extension of  $R$  by  $M$  and denoted by  $R \rtimes_{\varphi} M_1 \rtimes \dots \rtimes M_n$  or simply  $R \rtimes_n M$ . Moreover,  $R \rtimes_{\varphi} M$  is naturally isomorphic to the subring of the generalized triangular matrix ring

$$\begin{pmatrix} R & M_1 & M_2 & \dots & M_n \\ 0 & R & M_1 & \dots & M_{n-1} \\ \vdots & \ddots & \ddots & \ddots & \vdots \\ 0 & 0 & 0 & \dots & M_1 \\ 0 & 0 & 0 & \dots & R \end{pmatrix}$$

consisting of matrices

$$\begin{pmatrix} r & m_1 & m_2 & \dots & m_n \\ 0 & r & m_1 & \dots & m_{n-1} \\ \vdots & \ddots & \ddots & \ddots & \vdots \\ 0 & 0 & 0 & \dots & m_1 \\ 0 & 0 & 0 & \dots & r \end{pmatrix}$$

where  $r \in R$  and  $m_i \in M_i$  for every  $i \in \{1, \dots, n\}$ . Any  $n$ - $\varphi$ -trivial extension  $R \rtimes_{\varphi} M_1 \rtimes \dots \rtimes M_n$  can be seen as the amalgamation of  $R$  with  $R \rtimes_{\varphi} M_1 \rtimes \dots \rtimes M_n$  along  $0 \rtimes_{\varphi} M_1 \rtimes \dots \rtimes M_n$  with respect to the canonical injection (Anderson et al., 2017).

**Proposition 4.1.** If all clean element of  $A$  and  $f(A) + K$  are  $J$ -clean, then  $A \rtimes^f K$  is a  $UJ$ -ring.

**Proof:**  $x = (u, f(u) + k)$  which implies  $u \in U(A)$  and  $f(u) + k \in U(f(A) + K)$ .  $x = (u, f(u) + k)$  is a clean element of  $A \rtimes^f K$ . Again  $u$  is a clean element of  $A$  and  $f(u) + k$  is a clean element of  $f(A) + K$  by Farshad et al. (2021) (Lemma 2.5 (2)). By hypothesis  $u$  and  $f(u) + k$  are  $J$ -clean of  $A$  and  $f(A) + K$  respectively. Hence  $u = e_1 + j_1$  where  $e_1 \in Id(A)$  and  $j_1 \in J(A)$ .  $f(u) + k = e_2 + j_2$  where  $e_2 \in Id(f(A) + K)$  and  $j_2 \in J(f(A) + K)$ . Since  $1 = e_1 u^{-1} + j_1 u^{-1}$  we obtain that  $e_1 u^{-1} = 1 - j_1 u^{-1}$  is a unit of  $A$ . Hence  $e_1 = 1$  which implies that  $u = e_1 + j_1 = 1 + j_1$ . Similarly, we get that  $(f(u) + k)^{-1}$  is a unit of  $f(A) + K$  and hence  $e_2 = 1$ .  $x = (u, f(u) + k) = (e_1 + j_1, e_2 + j_2) = (1 + j_1, 1 + j_2)$ . ■

**Corollary 4.2.** If  $A$  and  $f(A) + K$  are  $J$ -clean rings, then  $A \rtimes^f K$  is a clean  $UJ$ -ring.

**ACKNOWLEDGEMENT**

We would like to thank the referees for their valuable comments and suggestions to improve the article.

**CONFLICT OF INTEREST**

The authors declare no conflict of interest.

**REFERENCES**

Anderson, D. D., Bennis, D., Fahid, B., & Shaiea, A. (2017). On  $n$ -trivial extension of rings. *Rocky Mountain J. Math.*, 47(8), 2439-2511. doi:[10.1216/RMJ-2017-47-8-2439](https://doi.org/10.1216/RMJ-2017-47-8-2439)

Calugareanu, G. (2015). UU rings. *Carpathian J. Math.*, 31(2), 157-163. doi:[10.37193/CJM.2015.02.02](https://doi.org/10.37193/CJM.2015.02.02)

Chen, H. (2010). On strongly  $J$ -clean rings. *Communications in Algebra*, 38(10), 3790-3804. doi:[10.1080/00927870903286835](https://doi.org/10.1080/00927870903286835)

D’Anna, M., Finocchiaro, C. A., & Fontana, M. (2009). Amalgamated algebras along an ideal. In: M. Fontana, S-E. Kabbaj, B. Olberding & I. Swanson (Eds.), *Commutative Algebra and Its Applications, Proceedings of the Fifth International Fez Conference on Commutative Algebra and Applications*, Morocco, June 23-28, 2008, (pp. 155-172), De Gruyter, Berlin. doi:[10.1515/9783110213188.155](https://doi.org/10.1515/9783110213188.155)

- Diesl, A. J. (2013). Nil clean rings. *Journal of Algebra*, 383, 197-211. doi:[10.1016/j.jalgebra.2013.02.020](https://doi.org/10.1016/j.jalgebra.2013.02.020)
- Farshad, N., SafariSabet, S. A., & Moussavi, A. (2021). Amalgamated rings with clean-type properties. *Hacettepe J. Mathematics and Statistics*, 50(5), 1358-1370. doi:[10.15672/hujms.676342](https://doi.org/10.15672/hujms.676342)
- Koşan, M. T., Leroy, A., & Matczuk, J. (2018). On UJ-rings. *Communications in Algebra*, 46(5), 2297-2303. doi:[10.1080/00927872.2017.1388814](https://doi.org/10.1080/00927872.2017.1388814)
- Koşan, M. T., Quynh, T. C., & Yildirim, T. (2020). Rings such that, for each unit  $u$ ,  $u - u^n$  belongs to the Jacobson radical. *Hacettepe J. Mathematics and Statistics*, 49(4), 1397-1404. doi:[10.15672/hujms.542574](https://doi.org/10.15672/hujms.542574)
- Nicholson, W. K. (1977). Lifting idempotents and exchange rings. *Trans. Amer. Math. Soc.*, 229, 269-278. doi:[10.1090/S0002-9947-1977-0439876-2](https://doi.org/10.1090/S0002-9947-1977-0439876-2)





Gazi University

**Journal of Science**

PART A: ENGINEERING AND INNOVATION

<http://dergipark.org.tr/guj.1107158>

## Production and Characterization of Bilayer Tissue Scaffolds Prepared with Different Alginate-Salts and Fibroin

Özge ÇELİK<sup>1</sup> , Salma A. Taher MOHAMED<sup>2</sup> , Nuray EMİN<sup>2,3\*</sup> <sup>1</sup>Kastamonu University, Engineering and Architecture Faculty, Genetic and Bioengineering Department, Kastamonu, 37150, Turkey<sup>2</sup>Kastamonu University, Institute of Science and Technology, Material Science and Engineering Department, Kastamonu, 37150, Turkey<sup>3</sup>Kastamonu University, Engineering and Architecture Faculty, Biomedical Engineering Department, Kastamonu, 37150, Turkey

Keywords	Abstract
Silk Fibroin	The presented study aimed to design and characterize bilayer Alginate/Fibroin scaffolds to provide faster and higher quality treatment of skin tissue losses with tissue engineering approach. In this context, it was tried to form the dermis and epidermis layers with alginate salts (sodium and calcium) and fibroin with a biomimetic approach, and it was aimed to determine the most suitable alginate salt-fibroin composite scaffold by trying different production methods. The optimum design was determined by macroscopic measurement and dimensional analysis of the scaffolds produced by four different methods and their chemical structures were controlled with FTIR. Among the produced scaffolds, calcium alginate/fibroin (CaAlg/Fb) scaffolds were determined to have the most suitable morphological and chemical structure. With further characterization, the pore distribution and size were examined by SEM analysis and it was determined that surface pore diameters vary from 30 µm to 300 µm which are suitable for cell settlement. The thermal stability of the structure was determined by thermal gravimetry, and the degradation rate was calculated from the thermograms. According to the TG analysis, decomposition of the CaAlg/Fb scaffolds occurs much faster with temperature than homo-biopolymeric (CaAlg and Fb) structures. As a result, it was found that bilayer CaAlg/Fb scaffolds were capable of forming full-thickness dermal and/or also osteochondral wound dressings both morphologically and structurally. It is recommended to perform the tissue forming ability of this scaffold structure by performing advanced biological analyzes.
Alginate	
Tissue Scaffold	
Biomimetic Patch	
Lymphilization	

### Cite

Çelik, Ö., Mohamed, S. A. T., & Emin, N. (2022). Production and Characterization of Bilayer Tissue Scaffolds Prepared with Different Alginate-Salts and Fibroin. *GU J Sci, Part A, 9(2)*, 120-135.

Author ID (ORCID Number)	Article Process	
O. Çelik, 0000-0001-5186-0519	<b>Submission Date</b>	21.04.2022
S. A. T. Mohamed, 0000-0002-6210-9920	<b>Revision Date</b>	13.06.2022
N. Emin, 0000-0002-0859-2536	<b>Accepted Date</b>	25.06.2022
	<b>Published Date</b>	26.06.2022

## 1. INTRODUCTION

The skin consists of epidermis originated from ectoderm which is an epithelial lamina, dermis originated from mesoderm, which is a connective tissue lamina, and hypodermis. In addition, there are some supplements such as hair follicles, sweat and sebaceous glands, immune system cells and neural cells in the structure of the skin (Kanitakis, 2002; Woo, 2019). Damage to the skin occurs as a result of trauma, illness, burns and surgical procedures, and this can cause serious problems (Çakir & Yeğen, 2004). Burn trauma is one of the most common causes of major skin loss. As a result of thermal, chemical or electrical injuries, burns that are difficult to repair can occur on the skin (Summer et al., 2007; Toon et al., 2011). This causes contracture of the wound, scar tissue formation in the skin and loss of functional properties of the skin. All these negativities experienced in the ongoing routine treatment methods necessitated the search for a new treatment method. For this purpose, tissue engineering applications for regenerative treatment have gained importance (Priya et al., 2008; Chen & Liu, 2016). In this direction, various wound closure grafts have been designed, especially with the use of polymeric biomaterials, and the products that have been shown to be effective in experiments are patented under the name of therapeutic wound dressing (Reinholz et al., 2004; Yu et al., 2019). Skin conjugates

\*Corresponding Author, e-mail: [nurayemin@gmail.com](mailto:nurayemin@gmail.com)

produced with the skin tissue engineering approach degrade while providing new tissue formation in the damaged area. Tissue-engineered wound dressings can consist of only three- or two-dimensional scaffolds, as well as contain isolated autologous cells and bio-signal molecules. Polymeric structures used in tissue engineering are produced from biocompatible natural or synthetic materials that can perform their functions by repairing tissues that cannot fulfil their functions or are used to support these tissues (Freed et al., 1994; Sittinger et al., 1996; Reinholz et al., 2004).

Silkworm silk has two different proteins. The first major protein is fibroin that gives silk its specific properties. The amino acid sequence of fibroin, which is hydrophobic, consists of 43% glycine, 30% alanine and 12% serine amino acids. Fibroin has been studied especially as a biomaterial for dermal patches, creating different designs, as it supports the adhesion and proliferation of the cells such as keratinocytes and fibroblasts (Ju et al., 2014). Sericin, which is the second major component of silkworm silk and holds fibroin together in the cocoons and constitutes 25-30% of the silk cocoon (Porter & Vollrath, 2009). Silk has widespread use in biomaterials applications thanks to its superior properties such as mechanical strength, good substance and gas permeability, biocompatibility, biodegradability and minimal inflammation (Hardy & Scheibel, 2010; Qi et al., 2017). It can be produced in the desired morphology (film, fiber, hydrogel and porous sponge) after being brought into solution (Vepari & Kaplan, 2007).

Alginic acid is a natural biopolymer isolated from red-brown seaweeds. It has a copolymer structure and consists of L-guluronic acid blocs and D-mannuronic acid blocs (Knill et al., 2004). Alginate has been proven to be non-toxic and biologically metabolized when taken orally. For this reason, it is used especially in pharmacological applications such as drug active ingredient, controlled released systems and tissue engineering. Alginate can be crosslinked with divalent metal cations to form hydrogel structure. For this purpose, calcium ions are often preferred (Peretz, 2004). Calcium alginate hydrogel is used in cell immobilization and encapsulation processes. Calcium alginate is used as a wound dressing in burn treatments because of its high biocompatibility and less pain (Kalia & Avérous, 2011).

The study aims to create a multi-layered wound dressing by using biopolymers with different properties by simulating the epidermis and dermis layers of the skin with a biomimetic approach. The epidermis is main lamina that is responsible for protection of the body against the both external influences and loss of substance from within the body. For this purpose, fibroin was preferred for the epidermis-mimicking surface, considering its good mechanical strength, more hydrophobic structure, antibacterial and wound healing properties (Clark et al., 2007; Hunt et al., 2009). The dermis is the main component of type I collagen. However, it is suggested that the use of collagen in the scaffold structure may be harmful in wound healing when the cells will be start producing their own collagen. However, animal-derived materials can promote the risk of immune rejection and disease infection (Clark et al., 2007). Therefore, there is a need for raw materials produced from non-animal sources for 2-layer dermal dressings. Because of that, alginate was chosen for the dermis-mimicking surface due to its water absorption ability, biocompatibility, faster biodegradation, and forming higher porose structure (Park et al., 2007; Hunt et al., 2009). While the alginate scaffold was produced in full thickness as a design, fibroin was applied in a thinner layer on the alginate scaffold, taking into account the layer thickness of the epidermis (MacNeil, 2007). The chemical structure of the produced 3D-tissue scaffolds was analyzed by FTIR, thermal properties were analyzed by Thermogravimetry (TG), the morphological structure was analyzed by Scanning Electron Microcopy (SEM) and the dimension analysis was analyzed by photographing. In order to give an idea about its biocompatibility, water holding capacity and biodegradability analyzes were performed for the scaffold structure, which was determined to be suitable.

## 2. MATERIAL AND METHOD

### 2.1. Preparation of Polymer Solutions

Two different natural polymers, silk fibroin and sodium alginate, were used in the preparation of composite tissue scaffolds. An aqueous solution of silk fibroin 3.64% and sodium alginate 3% (w/v) was used. The processing steps, which were carried out are described below.

### 2.1.1. Isolation and Purification of Fibroin

Silkworm cocoons were obtained from Bursa Koza Birlik (Türkiye). Fibroin was produced from silkworm cocoons using the standard alkaline method. Firstly, sericin in the Bombyx mori silkworm cocoons was removed by treatment in 500 ml of 0.02 M Na<sub>2</sub>CO<sub>3</sub> (Sigma, USA) aqueous solution at boiling temperature for 30 minutes. Raw fibroin fibers were obtained and washed 2 times. Then, they were dissolved in 20,4 M LiBr (Sigma, USA) solution by incubation at 60°C for 3 hours. Then, it was taken into the dialysis membrane to purify it from salt and impurities, and it was dialyzed in distilled water for 3 days. Following the end of the dialysis process to remove the solid impurities, fibroin mixture was centrifuged at 4500 rpm for 20 minutes. The average solution concentration was calculated as 3.6% (w/v) by the gravimetric method.

### 2.1.2. Preparation of Sodium Alginate Solution

The alginate solution at the concentration of 3% (w/v) was prepared in 0.89% NaCl (Sigma, USA) solution. CaCl<sub>2</sub> solution was used as the crosslinker of sodium alginate. For this purpose, 0.4 M CaCl<sub>2</sub> (Sigma, USA) solution was prepared in 0.89% NaCl solution. All prepared solutions were stored at +4°C.

## 2.2. Scaffolds Fabrication

In the formation of tissue scaffolds as wound dressing, 4 different types of composite structures were created using the methods given in Table 1.

*Table 1. Composite structures planned to be formed and biopolymer mixing ratios*

No.	Scaffolding Composition	Fibroin Concentration (w/v %)	Alginate Concentration (w/v %)	Blend Ratio (v/v)
1	Na-Alginate/Fibroin	3,6	3	1:1
2	Na-Alginate/Fibroin-M (methanol applied)	3,6	3	1:1
3	Ca-Alginate/Fibroin	3,6	3	1:1
4	Ca-Alginate/Fibroin-M (methanol applied)	3,6	3	1:1

### 2.2.1. Preparation of the Sodium Alginate Scaffolds

Different methods were tried in the formation of composite scaffolds numbered 1 and 2 (NaAlg/Fb and NaAlg/Fb-M) which are given in Table 1, and optimum results were obtained by following the procedures given below.

- The polymer blend was prepared by mixing fibroin and sodium alginate at a 1:1 ratio by volume given in Table 1.
- After the polymer blend (NaAlg/Fb) was transferred to a 12-well petri dish, it was mixed gently.
- For the NaAlg/Fb-M scaffold, blend was prepared in the same way first. Then, 500 µl of methanol was added onto it.
- Polymer blends transferred to the mold were frozen at -24°C for 12 hours and at -86°C for 24 hours, respectively.
- After the first freezing process, the methanol-treated composite structures were washed with distilled water to remove excess methanol. Then, step 4 was repeated.
- The frozen polymer blends were placed in the lyophilizer and left to dry at -55°C for 24 hours.

### 2.2.2. Preparation of Calcium Alginate Scaffolds

Different methods were tried in the formation of composite scaffolds numbered 1 and 2 (CaAlg/Fb and CaAlg/Fb-M) which are given in Table 1, and optimum results were obtained by following the procedures given below.

- While forming the CaAlg/Fb and CaAlg/Fb-M composite scaffolds, firstly, CaAlg hydrogel was formed and then Fb coating was applied to it.
- For this, a 6-well petri dish was used as a mold and sodium alginate was added to each well.
- 0.4 M CaCl<sub>2</sub> was added to sodium alginate to form hydrogel by physical cross-linking.
- Fibroin solution was added so that the hydrogel was completely covered.
- CaAlg/Fb-M composite was prepared in the same way and 500 µl of methanol was added to it.
- Hydrogel-polymer composites were frozen at -24°C for 12 hours and at -86°C for 24 hours, respectively.
- After the first freezing process, the methanol-treated composite structures were washed with distilled water to remove excess methanol. Then, step 6 was repeated.
- The frozen polymer composites were placed in the lyophilization device and left to dry at -55°C for 24 hours.

### 2.3. Characterization of Composite Tissue Scaffolds

Macroscopic measurement and dimensional analysis of scaffolding structures were carried out metrically by photographing and the data were evaluated comparatively with each other. Bruker Alpha (USA) ATR-FTIR spectroscopy was used for the structural analysis of composite dressing materials. Measurements were carried out at a scanning speed of 4 cm<sup>-1</sup> in the range of 400-4000 cm<sup>-1</sup>. Further characterization was continued with the CaAlg/Fb sample, which was determined to have surface properties that could be used as a wound dressing according to the results of macroscopic size and morphology analysis and FTIR analysis. The FEI Quanta FEG 250 (USA) The surface morphology of the composite wound dressing materials was analyzed using Scanning Electron Microscopy (SEM). Thermal degradation changes were tested with Hitachi STA7300 (Japan) Thermal analyzer in a nitrogen atmosphere between 25°C-800°C.

According to the characterization analysis results, the water uptake capacity of the CaAlg/Fb scaffold, which was determined to have sufficient properties was calculated gravimetrically by keeping it in distilled water at 37°C for 24 hours. In addition, the pH change was monitored for 24 h by taking hourly measurements for first 6 hours.

## 3. RESULTS AND DISCUSSION

### 3.1. Macroscopic Measurements

Macroscopic measurement and dimensional analysis were performed by photographing against a metric scale. First of all, it was tried to determine the most suitable method in macroscopic morphology for the scaffolds produced with 2 different methods according to Table-1 in the study program. It was determined that the structural integrity of the NaAlg/Fb scaffolds was more preserved than the NaAlg/Fb-M structure. It was measured that NaAlg/Fb scaffolds had a diameter of approximately 2.0 cm and a diameter of approximately 2.3 cm for NaAlg/Fb-M scaffolds (Figure 1A-B). Although the samples treated with methanol had a larger diameter, it was observed that the surface morphology and scaffold thickness did not conform to expectations. Similar results were obtained for CaAlg/Fb and NaAlg/Fb scaffolds. It was determined that among all scaffold samples, CaAlg/Fb scaffolds had the most suitable structure in terms of structural integrity and surface homogeneity and thickness. Dimensionally, CaAlg/Fb scaffolds have a diameter of 2.5 cm, and CaAlg/Fb-M scaffolds have a diameter of around 2 cm (Figure 1C-D). In addition, in CaAlg/Fb-M samples, it was determined that the fibroin layer was not sufficiently integrated into the alginate surface and separated from the surface after methanol treatment.

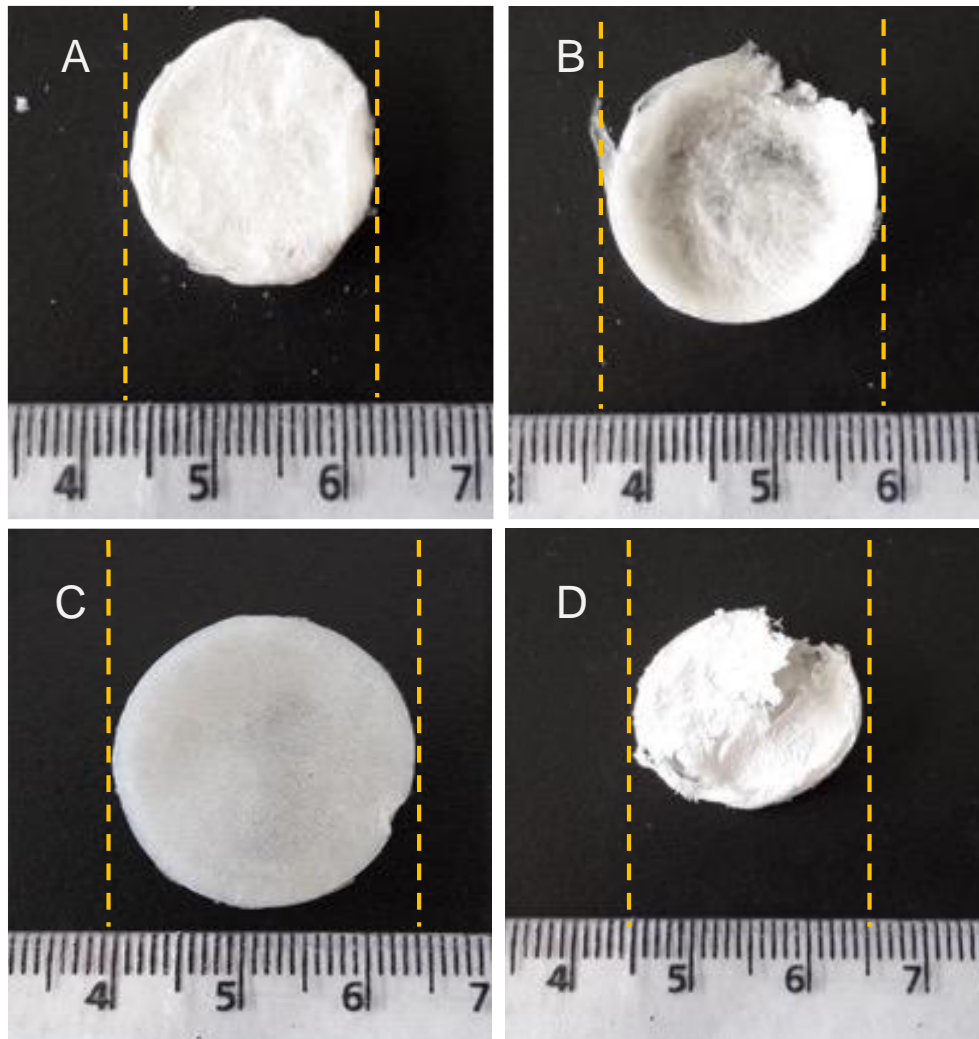


**Figure 1.** Macroscopic dimension evaluation of composite scaffolds;

**A)** Na-Alg/Fb, **B)** Na-Alg/Fb-M treated with methanol, **C)** CaAlg/Fb, **D)** NaAlg/Fb-M treated with methanol

The use of methanol reduces its degradation in aqueous media by supporting the  $\beta$ -layer structure and increasing the interaction between the layers (Qi et al., 2017; Zhao et al., 2021). Studies have shown that organic solvents disrupt the  $\beta$ -layer structure of fibroin, causing irregular pore structure in a mono-alcohol-treated fibroin scaffolds (Zhang et al., 2021). In this respect, the literature findings are consistent with our results and support that the shape distortions in all methanol-treated scaffold samples are due to the effect of methanol on amide bonds.

### 3.2. Chemical Structure Properties of Composite Tissue Scaffolds

FT-IR spectra for the structural analysis of the obtained scaffolds are given in Figure 2. The stretching vibrations of the O–H bonds of the alginate were observed in the range of 3000–3600. Aliphatic C–H stretching vibrations were observed at 2920–2850  $\text{cm}^{-1}$ . The bands observed at 1597 and 1411  $\text{cm}^{-1}$  in NaAlg, 1604  $\text{cm}^{-1}$  and 1420  $\text{cm}^{-1}$  in CaAlg show the asymmetric and symmetric stretching vibrations of the carboxylate salt ion, respectively. These alginate-specific peaks were observed at a higher wavenumber in the calcium salt structure compared to the sodium salt. Subsequent bands are very important and can be used to characterize the alginate from the blends and derivatives. The bands at 1107 and 935  $\text{cm}^{-1}$  were evaluated as C–O stretching with contributions from the C–O stretching vibration of the pyranose rings and the C–O–H and C–C–H deformation. Symmetric and asymmetric tensile bands belonging to the C–O–C group were found at 1087  $\text{cm}^{-1}$  and 1028  $\text{cm}^{-1}$  respectively. In CaAlg, it was observed that the peaks in this range expanded and new peaks of weak intensity were formed. This is due to the chelate structures formed by Ca and gluconic acid in the pyran ring structure.

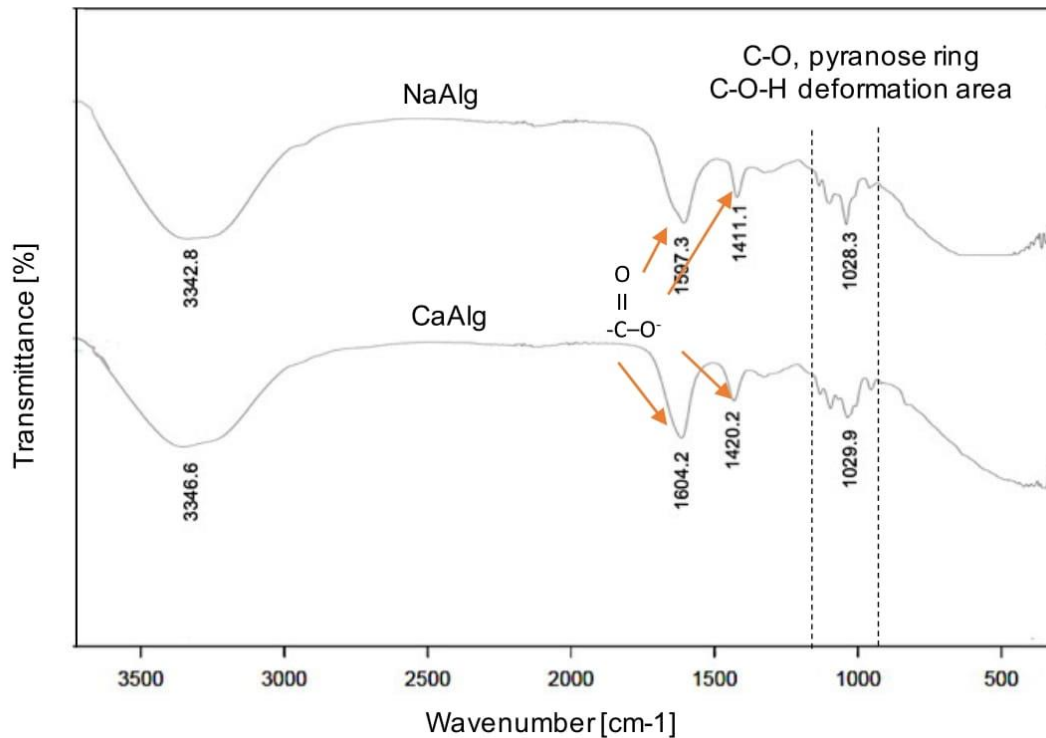


**Figure 2.** FTIR spectrum of Na-Alginate and Ca-Alginate

When the FTIR spectra of Na-Alg/Fb and NaAlg/Fb-M scaffolds were compared; Before treatment with methanol, the characteristic bands of amide I and amide II in silk-I structure, were observed at  $1621\text{ cm}^{-1}$  (amide I),  $1519\text{ cm}^{-1}$  (amide II), respectively. It has been observed that the -NH stresses are in the region of  $3279\text{ cm}^{-1}$ . After the treatment with methanol, it is seen that these bands shifted to  $1620\text{ cm}^{-1}$  and  $1518\text{ cm}^{-1}$ , respectively, and the peak intensity increased (Figure 3). This proves that the transition to the  $\beta$ -layer structure has been achieved (Amiraliyan et al., 2010). Furthermore, as it can be seen in (Figure3), there is a small split doublet between band values  $1620\text{ cm}^{-1}$  and  $1518\text{ cm}^{-1}$ , indicating conformation from random coil to  $\beta$ -sheet. The results showed that the use of methanol has resulted in the conformation to  $\beta$ -sheet structure (Zhang & Mo, 2011; Shen et al., 2022; Xie et al., 2022).

In the FTIR spectra of silk fibroin and composites stabilized by methanol treatment, amide bands are examined in the range of  $1700\text{ cm}^{-1}$ - $1500\text{ cm}^{-1}$ . Amid I covers the range of  $1700\text{ cm}^{-1}$ - $1600\text{ cm}^{-1}$ , and amide II covers the range of  $1600\text{ cm}^{-1}$ - $1500\text{ cm}^{-1}$  (Jaramillo-Quiceno et al., 2017). The  $1610$ - $1630$ ,  $1695$ - $1700$  and  $1510$ - $1520\text{ cm}^{-1}$  peaks are the characteristic absorption peaks for the secondary structure silk-II conformation (Bhattacharjee et al., 2013). Absorption peaks of  $1648$ - $1654\text{ cm}^{-1}$  and  $1535$ - $1542\text{ cm}^{-1}$  are characteristic pics of the amorphous silk-I conformation (Hu et al., 2006; Lu et al., 2011).

In the FTIR graph of the fibroin scaffold, the stretching vibrations of the -OH bonds were seen at  $3279\text{ cm}^{-1}$  and between  $3600$ - $3200\text{ cm}^{-1}$  area. Stretching vibrations of aliphatic -C-H were observed between  $3065\text{ cm}^{-1}$  and  $2935\text{ cm}^{-1}$  peaks. Amid I bond shows C=O stretching at  $1621\text{ cm}^{-1}$ ; Amid II bond shows N-H bending at  $1519\text{ cm}^{-1}$ ; Amid III bond shows C-N stretching at  $1233\text{ cm}^{-1}$  were observed (Bhattacharjee et al., 2013). The beta-layer structure of fibroin, which is composed of antiparallel polypeptide chains, is rich in glycine and generally contains chains formed by repeating the Gly-Ser-Gly-Ala\_Gly\_Al sequence. In addition, small amounts of amino acids with large side chains such as Tyr, Val, Arg and Asp are also present in the structure. These cause the structure to deviate from the crystalline order (Nelson & Cox, 2008/2013; Pamuk, 2011). In our study, peaks of fibroin-specific gly-gly and gly-ala petit motifs were observed in the  $1000$  and  $970\text{ cm}^{-1}$  area. These bonds and functional groups are specific to the protein structure of fibroin. It is seen that the chemical structure of fibroin is preserved in the experimental stages.

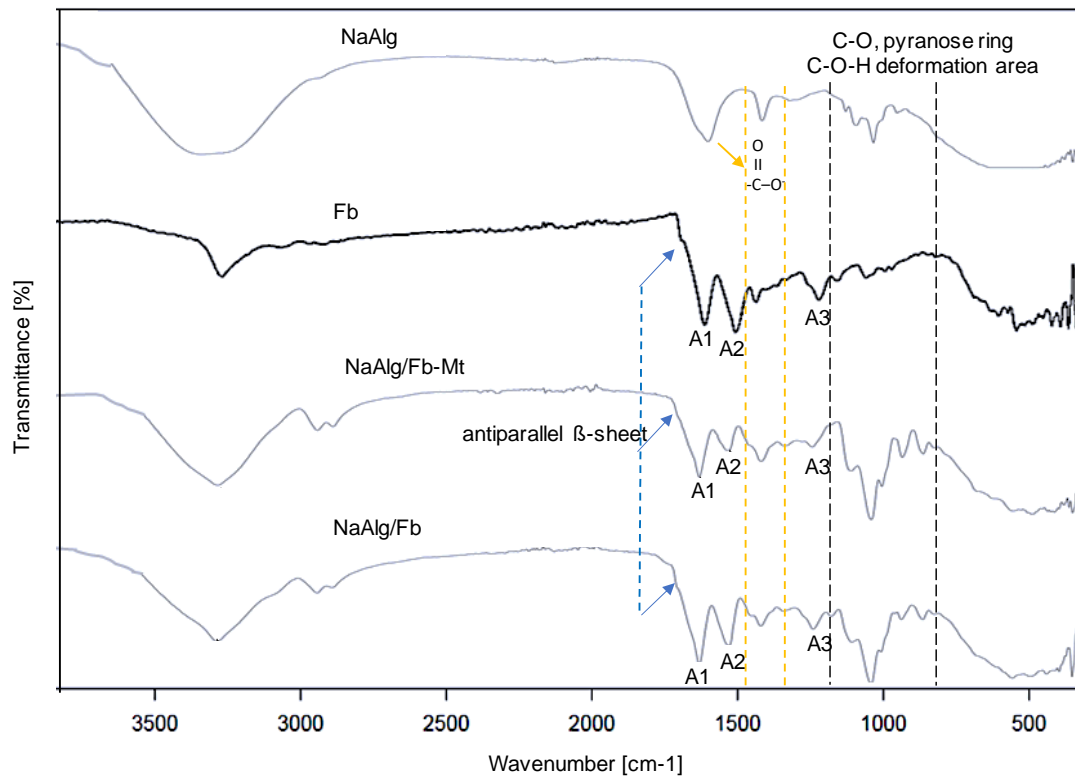


**Figure 3.** FTIR spectra of NaAlg, NaAlg/Fb, Silk Fibroin (Fb), and NaAlg/Fb-M  
A1: Amide I, A2: Amide II, A3: Amide III

Bhattacharjee et al. (2013) detected tensile bands at 1622, 1506 and 1227  $\text{cm}^{-1}$  for Amide I, II and III, respectively, for the 3D silk fibroin sample. It has been reported that shifting of these bands is expected in the treated samples. In this study, the measured values for amide bonds of fibroin were obtained at 1621, 1519 and 1233  $\text{cm}^{-1}$  in accordance of the literature (Bhattacharjee et al., 2013; Hofmann et al., 2014; Shen et al., 2022; Xie et al., 2022). In addition, it was determined that these values showed a shift according to the applied scaffolding production methods and composite composition (Xie et al., 2022).

The characteristic peaks representing the protein structure of fibroin in the CaAlg/Fb and CaAlg/Fb-M scaffolds are caused by the stretching of the amide I and amide II bonds and are 1635  $\text{cm}^{-1}$ , 1515  $\text{cm}^{-1}$  for CaAlg/Fb, and 1621  $\text{cm}^{-1}$ , 1516  $\text{cm}^{-1}$  for CaAlg/Fb-M, respectively. These are the peaks at wavenumbers of 1621  $\text{cm}^{-1}$  and 1516  $\text{cm}^{-1}$ . By comparing the spectra of both structures, the presence of fibroin in CaAlg/Fb was determined qualitatively (Figure 4).

Silkworm silk fibroin can be found in its secondary structure in two basic conformations, silk I and silk II. Although the structure of the Silk I conformation is not fully understood, it is known to be a mixture of  $\alpha$ -helix and random helical structures. This metastable nature of silk fibroin is not a desirable conformation for many applications due to its water solubility. Instead, silk II structured materials containing anti-parallel  $\beta$ -layers are preferred. Alcohols like that ethanol and methanol can be used for crystallization of the silk fibroin molecules (Bhattacharjee et al., 2013; Hofmann et al., 2014; Shen et al., 2022). It is thought that the crystallization mechanism is primarily in the form of the interaction of the polar alcohol, which can form hydrogen bonds, with the water in the environment, and as a result, hydrophobic amino acids such as alanine and glycine cluster to form the planar  $\beta$ -layer structure. Amide bond concentration increase was also observed in methanol treatment samples with increasing physically cross-linking between chains (Um et al., 2001).

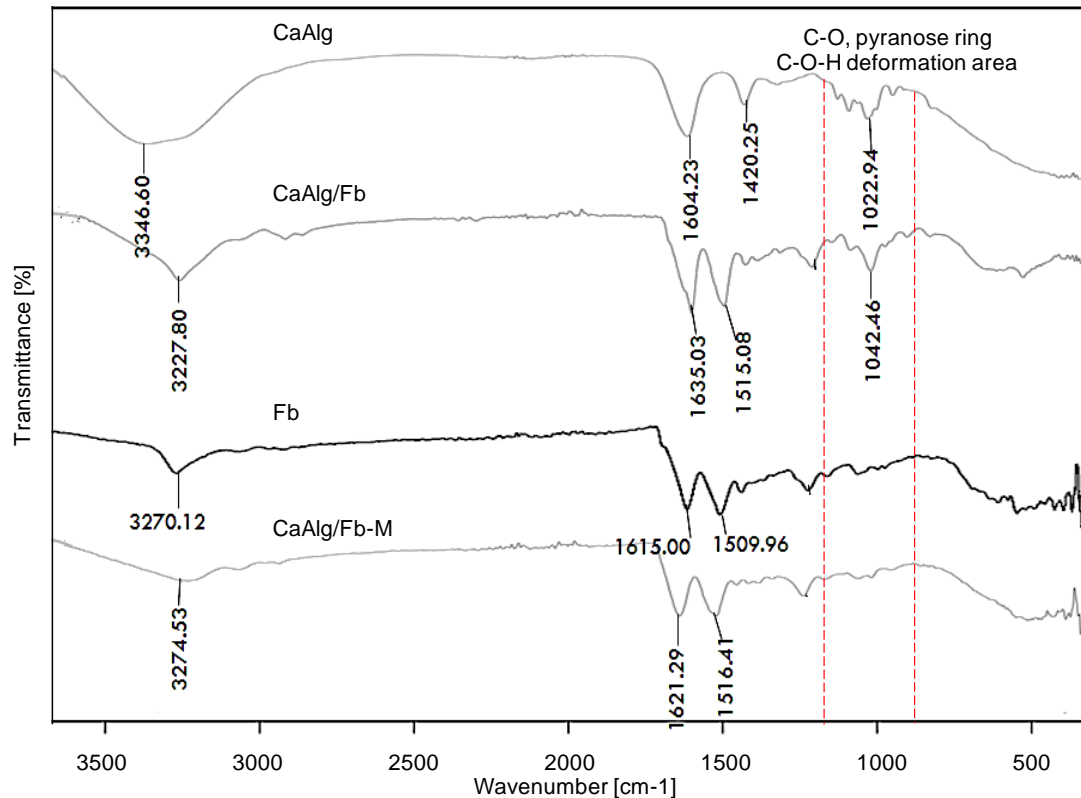


**Figure 4.** FTIR spectra of CaAlg, CaAlg/Fb, Silk Fibroin (Fb), and CaAlg/Fb-M

### 3.3. Evaluation of Surface Morphology

SEM images were taken to examine the structure of the composite tissue scaffolds and to determine the pore diameters (Figure 5). In the SEM image of the scaffold produced by lyophilization using only fibroin (Figure 5C), layered structures are remarkable. On the other hand, it is seen that the scaffold produced under the same conditions using calcium alginate has a more porous structure. The layered parts seen in the SEM micrographs of the CaAlg/Fb composite scaffold in Figure 5A-B are fibroin. When the overall SEM image of the composite scaffold at 100x magnification is examined, it is seen that the scaffold has a porous structure. In addition, there is no sign of damage or impairment, meaning that the integrity of the whole scaffold remained intact. Consequently, porous scaffolds, which are three-dimensional polymeric scaffolds with increased porosities and a homogenous interconnected pore network, are very advantageous in tissue engineering practices (Loh & Choong, 2013). The porous structure can be seen more clearly in SEM micrographs at 250x magnification at Figure 5B. It is seen that the pores in the structure are interconnected and have an open pore structure. Moreover, it is seen that the pore distribution showed homogeneous patterning, and the surface pore diameters vary from 30-70  $\mu\text{m}$  to 300  $\mu\text{m}$ . It has been determined that the pore diameters of the composite scaffold are suitable for the placement of the cells. However, it is seen that the pores with diameters in the range of 35-140  $\mu\text{m}$  are more in the structure. In tissue engineering applications for wound dressings, porosity in the range of 20-125  $\mu\text{m}$  is reported to be ideal for growth and regeneration of skin tissue (Xie et al., 2022). In this respect, it can be said that the pore structure of CaAlg/Fb scaffolds is suitable for skin tissue engineering.

Although direct mixing was not applied to the polymers it was determined that fibroin interacted with Ca-Alginate and thus its layered structure was disrupted and its porosity increased (Xie et al., 2022). Shen et al. (2022), in their study in which they examined the effects of sodium alginate nanoparticle uses on silk fibroin-sodium alginate scaffolds, SEM images of fibroin-alginate scaffolds prepared by lyophilization are similar to our samples in terms of porosity (Shen et al., 2022). The literature supports that the layered areas in the CaAlg/Fb composite structure originate from fibroin. This morphological feature is of great significance as implant location and 3D tissue development are influenced by the scaffold's porous nature and porosity. Pores are necessary for tissue creation because they allow for cell migration and proliferation, as well as vascularization and nutrition transport (Griffon et al., 2006; Xie et al., 2022).



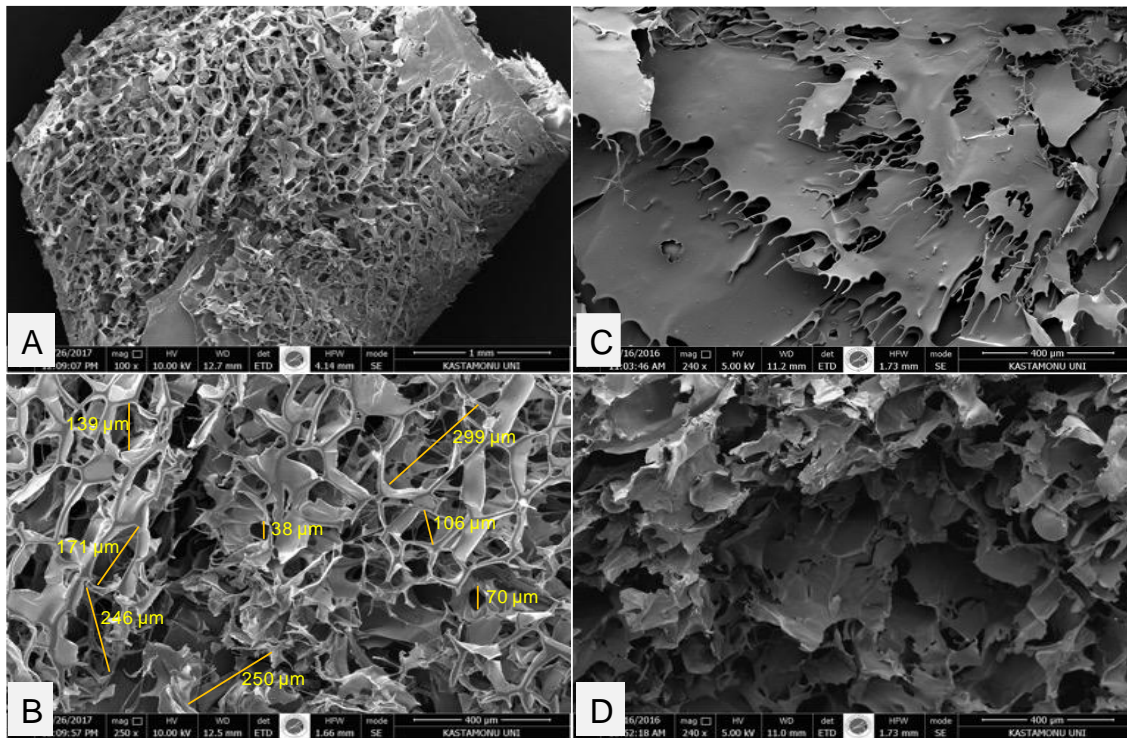


**Figure 5.** SEM images of scaffolds;

A) 100x and B) 250x magnified view of CaAlg/Fb composite scaffold, C) fibroin and D) alginate scaffold

### 3.4. TGA Analysis

It is conventional knowledge that finding materials with better properties for a specific application requires a comprehensive understanding of polymer degradation characteristics when heated (Coats & Redfern, 1963). Thermal Analysis is a method in which the physical and chemical properties of materials are examined depending on temperature. Temperature change causes several chemical and physical effects such as evaporation of the structural water, desorption, degradation reactions etc. on the material. TGA analysis was preferred to determine the relationship between the change in mass of fibroin scaffolds and temperature. Thermograms of composite scaffolds and homopolymeric structures (CaAlg and Fb) are given in Figure 6. In these thermograms, it was determined that the chemical structure of calcium alginate underwent thermal degradation at five points (105.2°C, 151.4°C, 265.8°C, 421.9°C, 505.1°C) in the range of 25-800°C. It was observed that the chemical structure of pure fibroin underwent thermal degradation at three points (37.2°C, 255.6°C, 609.3°C) in the same temperature range. In the CaAlg/Fb scaffold sample, on the other hand, it was determined that the chemical structure occurred as thermal decomposition at only four points (230.9°C, 419.5°C, 505.8°C, 631.3°C). In CaAlg/Fb composite scaffolds, the increase in thermal stability of the structure and the occurring degradation at different temperatures than the pure biopolymeric structures showed that first hydrogelation of sodium alginate with  $\text{Ca}^{2+}$  ions and then treatment with fibroin solution provided better integration amongst biopolymers. This would mean that the thermal stability of the composite scaffolds has been improved in a clear manner, as a consequence of the decelerated disintegration rate, a higher heating rate gave greater thermal stability (Coats & Redfern, 1963).

The mass changes of CaAlg/Fb and homopolymeric structures on the decomposition temperatures in the thermograms were calculated as a percentage of degradation for all samples and are given in Table 2. Although the thermal degradation stability of CaAlg/Fb scaffolds increased, the rate of degradation by mass decreased only in the range of 151-266°C compared to biopolymeric structures.

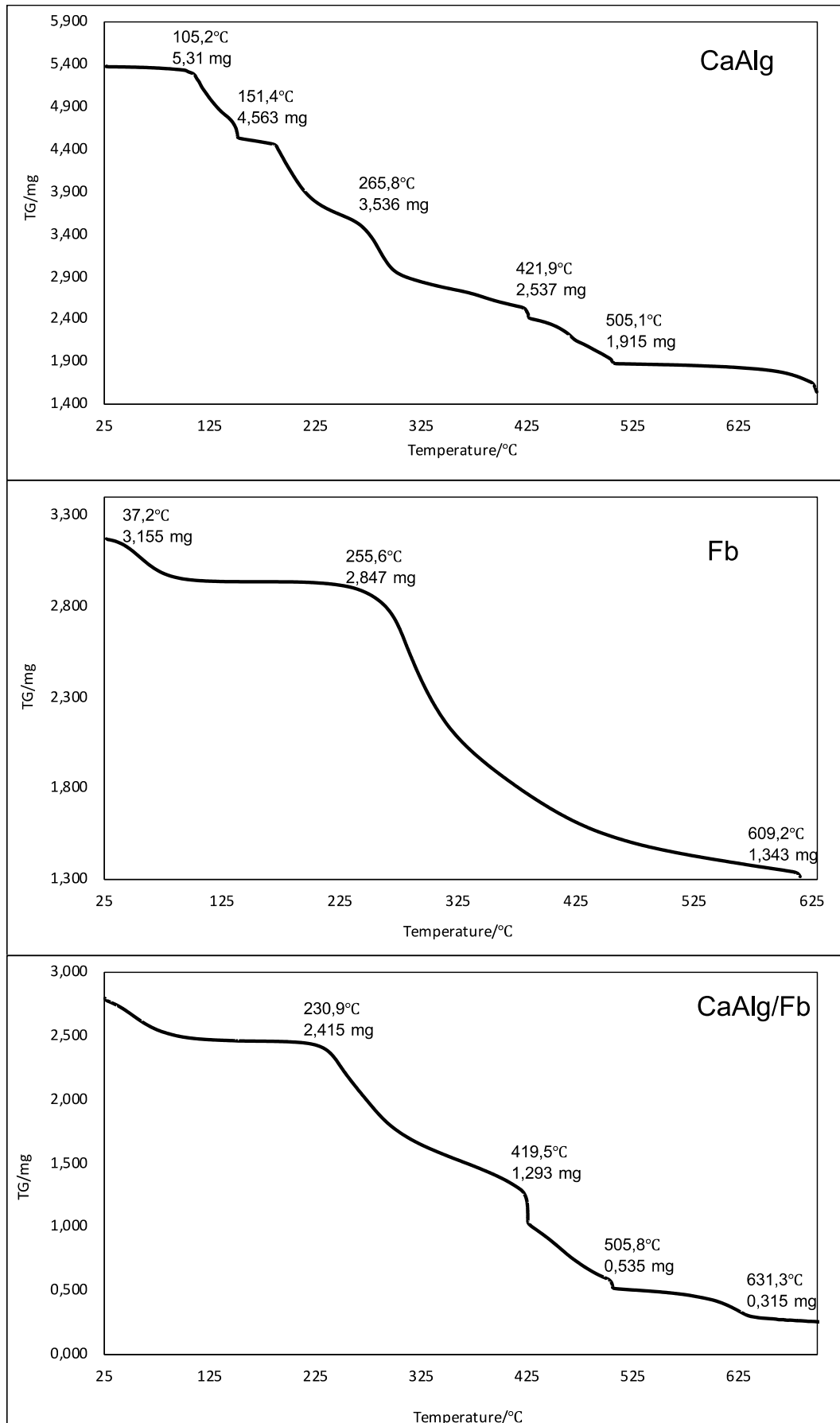


Figure 6. TG thermograms of the CaAlg, Fb and CaAlg/Fb

**Table 2.** Thermal degradation rates of CaAlg, Fb and CaAlg/Fb samples

TEMPERATURE (°C)	DEGRADATION RATIO (%)		
	CaAlg	Fb	CaAlg/Fb
37,16	0,13	0,65	2,09
105,18	1,24	7,27	11,25
151,40	15,29	7,48	12,12
230,85	30,51	8,29	13,88
255,57	33,17	10,36	22,11
265,80	34,47	12,28	25,97
419,49	52,69	48,56	53,89
421,90	52,90	48,81	54,70
505,10	64,45	54,18	80,05
505,82	64,70	54,21	80,91
609,83	65,73	57,73	85,62
631,30	66,03	58,67	88,75

The some physical, chemical and mechanical properties of fibroin can be changed in the presence of various crosslinkers or by the use of thermal processes (Rujiravanit et al., 2003; Mirahmadi et al., 2013; Ghezzi et al., 2014; Yodmuang et al., 2015). For example, water solubility, durability and porous structure formation can be changed by changing thermal processes or by using chemical reagents such as methyl alcohol and glutaraldehyde (Wang et al., 2015). Evaluation of the TG findings, it has been determined that the decomposition of the structure occurs much faster with temperature than in homo-biopolymeric structures. In the fibroin molecule, there are many hydrogen bonds within and between the chains. This might be attributed to the reason that neighboring chains are kept together in an anti-parallel configuration by strong hydrogen bonds to form ( $\beta$ -sheets) and as a result, the fibroin's strength is substantially reinforced (Cheng et al., 2014). For this reason, fibroin is resistant to thermal degradation and to acids and bases due to its amphoteric properties. On the other hand, significant shifts were determined in the thermal degradation of fibroin in the composite structure. This shows that CaAlg reduces intramolecular secondary interactions in the structure of fibroin and thus, increases its thermal degradation.

### 3.5. Water Uptake Capacity and pH Changes

The ability of a biomaterial to retain water is an indicator for its biocompatibility. Materials that can easily absorb water also facilitate the adhesion of cells to the surface (Hu et al., 2021). The water holding capacity of CaAlg/Fb scaffolds, which were determined to have sufficient properties as a result of physical and chemical characterization analyzes, was tested. The treatments were carried out in distilled water under physiological temperature conditions in 3 repetitions. The results obtained are given in Table 3, and it was determined that the composite scaffold could absorb water up to 211.07% of its dry weight.

**Table 3.** Water uptake capacity of the CaAlg/Fb

Sample	Average Water Uptake (%)	Standard Derivation
CaAlg/Fb	211,07	22,72

When a scaffold is taken into cell culture, daily or every other day media change is performed considering its biodegradability and tissue development. Therefore, how the CaAlg/fb scaffold changed the physiological pH conditions of HANK's balanced medium was followed for 24 hours using a pH-meter. The first 6 hours of the experiment were measured hourly. The results are given in Figure 7. The pH change in the first 6 hours was close to linear, and then it remained horizontal. At the end of 24 hours, the pH was measured as 7.83. The pH change remained within the range where the skin cells could maintain their vital functions.

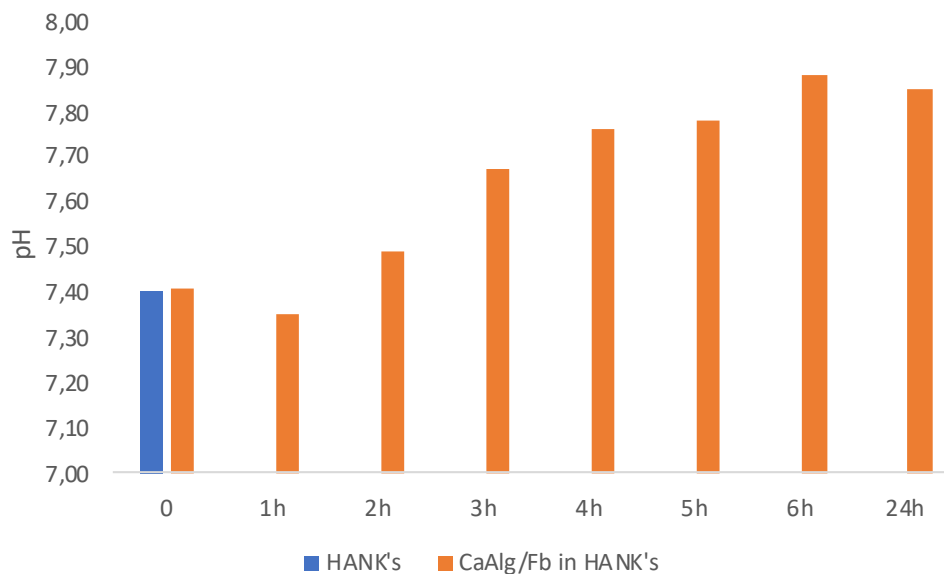


*Figure 7. pH changes of the culture media with CaAlg/Fb scaffold*

#### 4. CONCLUSION

Within the scope of the study, which was carried out using the sodium salt of alginic acid, four different scaffold structures were obtained that can be used in dermal wounds. The design of the scaffolds was made by considering the dermis and epidermis for dressing use. Within the scope of the study, which was carried out using the salts of alginic acid, four different scaffold structures were obtained that can be used in dermal wounds. The design of the scaffolds was made by considering the dermis and epidermis for dressing use. For the dermis structure, alginic acid was preferred in accordance with the literature, taking into account its mechanical and chemical properties (Park et al., 2007; Hunt et al., 2009). Considering the more stable structure and natural wound healing properties of fibroin and its routine use, it was preferred for the epidermis layer. Our evaluations were also conducted considering its usability as a two-layer full-thickness dressing. While sodium alginate-fibroin scaffolds were formed by mixing fibroin and sodium alginate solutions, calcium alginate-fibroin scaffolds were obtained by coating calcium alginate hydrogel with fibroin solution. It showed that alginate derivatives and fibroin were integrated to each other at certain rates in all scaffold structures.

FTIR results showed that fibroin chains were rearranged by the interaction of fibroin with methanol. In this way, it is understood that there is a transformation of the crystalline  $\beta$ -layer structure. However, these rearrangements of fibroin chains themselves reduced the affinity of fibroin to alginate. As a result, although an obvious interface was formed at the border between the polymer surfaces, it was determined that fibroin was separated from the alginate surface and its macroscopic morphology lost its homogeneity. According to the dimensional and chemical analysis of the produced scaffolds, the best results were obtained in CaAlg/Fb samples obtained by hydrogelation of calcium alginate and then coating with fibroin solution (Figure 8). For this reason, further characterization was carried out on this scaffold sample.

With CaAlg/Fb scaffolds, bi-layer and full-thickness scaffolds with morphology which can be used as dermal wound dressing were obtained. Although these scaffolds were not mixed together in solution, it was clearly seen in the SEM and TG analysis that the penetration of the fibroin solution into the calcium alginate hydrogel took place. It has been determined that the chemical structure deterioration of calcium alginate, which starts at lower temperatures, decreases in the composite structure and occurs at higher temperatures. On the other hand, it has been determined that the rate of thermal degradation occurs at a near linear rate in scaffold structures and in a more controlled manner than homo-polymeric structures. As a result, a bi-layer wound dressing like scaffold, compatible with the anatomical and histological structure of the dermis and epidermis, was obtained using by alginate and fibroin respectively. In these processes, it has been shown that the use of alginic acid, a block copolymer with polyanion structure, in hydrogel form increases the stability of the structure and can be physically cross-linked with amphoteric fibroin using hydrogen bonds and dipole interactions.

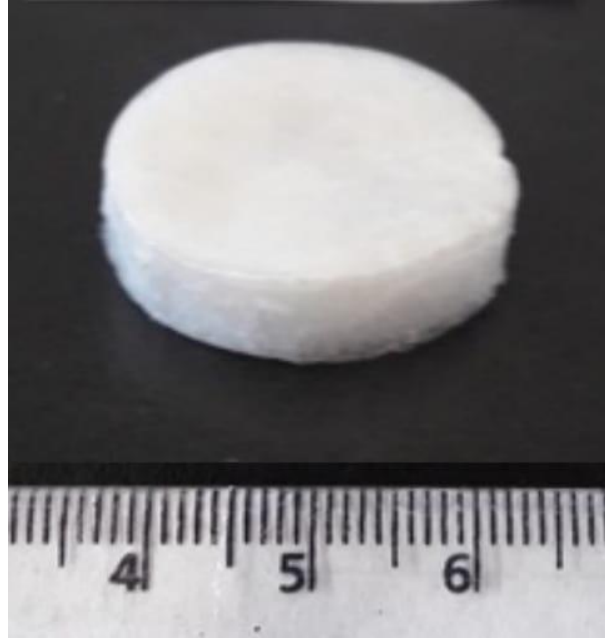


*Figure 8. CaAlg/Fb scaffold*

#### **ACKNOWLEDGEMENT**

This study was partially supported by Kastamonu University BAP Office with the KÜBAP 2015-27 research project number. The authors would like to thank Kastamonu University Central Research Laboratory Research and Application Center for the infrastructure support they provided in the realization of the study.

#### **CONFLICT OF INTEREST**

This study was conducted as a postgraduate study under the supervision of Nuray Emin. The authors declare no conflict of interest.

#### **REFERENCES**

- Amiraliyan, N., Nouri, M., & Haghghat Kish, M. (2010). Structural characterization and mechanical properties of electrospun silk fibroin nanofiber mats. *Polymer Science Series A*, 52(4), 407-412. doi:[10.1134/S0965545X10040097](https://doi.org/10.1134/S0965545X10040097)
- Bhattacharjee, M., Schultz-Thater, E., Trella, E., Miot, S., Das, S., Loparic, M., Ray, A. R., Martin, I., Spagnoli, G. C., & Ghosh, S. (2013). The role of 3D structure and protein conformation on the innate and adaptive immune responses to silk-based biomaterials. *Biomaterials*, 34(33), 8161-8171. doi:[10.1016/j.biomaterials.2013.07.018](https://doi.org/10.1016/j.biomaterials.2013.07.018)
- Chen, F.-M., & Liu, X. (2016). Advancing biomaterials of human origin for tissue engineering. *Progress in Polymer Science*, 53, 86-168. doi:[10.1016/j.progpolymsci.2015.02.004](https://doi.org/10.1016/j.progpolymsci.2015.02.004)
- Cheng, Y., Koh, L.-D., Li, D., Ji, B., Han, M.-Y., & Zhang, Y.-W. (2014). On the strength of  $\beta$ -sheet crystallites of Bombyx mori silk fibroin. *Journal of the Royal Society Interface*, 11(96), 20140305. doi:[10.1098/rsif.2014.0305](https://doi.org/10.1098/rsif.2014.0305)
- Clark, R. A. F., Ghosh, K., & Tonnesen, M. G. (2007). Tissue engineering for cutaneous wounds. *Journal of Investigative Dermatology*, 127(5), 1018-1029. doi:[10.1038/sj.jid.5700715](https://doi.org/10.1038/sj.jid.5700715)
- Coats, A. W., & Redfern, J. P. (1963). Thermogravimetric analysis. A review. *Analyst*, 88(1053), 906-924. doi:[10.1039/AN9638800906](https://doi.org/10.1039/AN9638800906)
- Çakir, B., & Yeğen, B. Ç. (2004). Systemic responses to burn injury. *Turkish Journal of Medical Sciences*, 34(4), 215-226.

- Freed, L. E., Marquis, J. C., Langer, R., Vunjak-Novakovic, G., & Emmanuel, J. (1994). Composition of cell-polymer cartilage implants. *Biotechnology and Bioengineering*, 43(7), 605-614. doi:[10.1002/bit.260430710](https://doi.org/10.1002/bit.260430710)
- Ghezzi, C. E., Marelli, B., Donelli, I., Alessandrino, A., Freddi, G., & Nazhat, S. N. (2014). The role of physiological mechanical cues on mesenchymal stem cell differentiation in an airway tract-like dense collagen–silk fibroin construct. *Biomaterials*, 35(24), 6236-6247. doi:[10.1016/j.biomaterials.2014.04.040](https://doi.org/10.1016/j.biomaterials.2014.04.040)
- Griffon, D. J., Sedighi, M. R., Schaeffer, D. V., Eurell, J. A., & Johnson, A. L. (2006). Chitosan scaffolds: interconnective pore size and cartilage engineering. *Acta Biomaterialia*, 2(3), 313-320. doi:[10.1016/j.actbio.2005.12.007](https://doi.org/10.1016/j.actbio.2005.12.007)
- Hardy, J. G., & Scheibel, T. R. (2010). Composite materials based on silk proteins. *Progress in Polymer Science*, 35(9), 1093-1115. doi:[10.1016/j.progpolymsci.2010.04.005](https://doi.org/10.1016/j.progpolymsci.2010.04.005)
- Hofmann, S., Stok, K. S., Kohler, T., Meinel, A. J., & Müller, R. (2014). Effect of sterilization on structural and material properties of 3-D silk fibroin scaffolds. *Acta Biomaterialia*, 10(1), 308-317. doi:[10.1016/j.actbio.2013.08.035](https://doi.org/10.1016/j.actbio.2013.08.035)
- Hu, K., Hu, M., Xiao, Y., Cui, Y., Yan, J., Yang, G., Zhang, F., Lin, G., Yi, H., Han, L., Li, L., Wei, Y., & Cui, F. (2021). Preparation recombination human-like collagen/fibroin scaffold and promoting the cell compatibility with osteoblasts. *Journal of Biomedical Materials Research Part A*, 109(3), 346-353. doi:[10.1002/jbm.a.37027](https://doi.org/10.1002/jbm.a.37027)
- Hu, X., Kaplan, D., & Cebe, P. (2006). Determining beta-sheet crystallinity in fibrous proteins by thermal analysis and infrared spectroscopy. *Macromolecules*, 39(18), 6161-6170. doi:[10.1021/ma0610109](https://doi.org/10.1021/ma0610109)
- Hunt, N. C., Shelton, R. M., & Grover, L. (2009). An alginate hydrogel matrix for the localised delivery of a fibroblast/keratinocyte co-culture. *Biotechnology Journal*, 4(5), 730-737. doi:[10.1002/biot.200800292](https://doi.org/10.1002/biot.200800292)
- Jaramillo-Quiceno, N., Álvarez-López, C., & Restrepo-Osorio, A. (2017). Structural and thermal properties of silk fibroin films obtained from cocoon and waste silk fibers as raw materials. *Procedia Engineering*, 200, 384-388. doi:[10.1016/j.proeng.2017.07.054](https://doi.org/10.1016/j.proeng.2017.07.054)
- Ju, H. W., Lee, O. J., Moon, B. M., Sheikh, F. A., Lee, J. M., Kim, J.-H., Park, H. J., Kim, D. W., Lee, M. C., Kim, S. H., Park, C. H., & Lee, H. R. (2014). Silk fibroin based hydrogel for regeneration of burn induced wounds. *Tissue Engineering and Regenerative Medicine*, 11(3), 203-210. doi:[10.1007/s13770-014-0010-2](https://doi.org/10.1007/s13770-014-0010-2)
- Kalia, S., & Avérous, L. (2011). *Biopolymers: biomedical and environmental applications* (Vol. 70). John Wiley & Sons.
- Kanitakis, J. (2002). Anatomy, histology and immunohistochemistry of normal human skin. *European Journal of Dermatology*, 12(4), 390-401.
- Knill, C. J., Kennedy, J. F., Mistry, J., Miraftab, M., Smart, G., Grocock, M. R., & Williams, H. J. (2004). Alginate fibres modified with unhydrolysed and hydrolysed chitosans for wound dressings. *Carbohydrate Polymers*, 55(1), 65-76. doi:[10.1016/j.carbpol.2003.08.004](https://doi.org/10.1016/j.carbpol.2003.08.004)
- Loh, Q. L., & Choong, C. (2013). Three-dimensional scaffolds for tissue engineering applications: role of porosity and pore size. *Tissue Engineering Part B: Reviews*, 19(6), 485-502. doi:[10.1089/ten.teb.2012.0437](https://doi.org/10.1089/ten.teb.2012.0437)
- Lu, Q., Zhang, B., Li, M., Zuo, B., Kaplan, D. L., Huang, Y., & Zhu, H. (2011). Degradation mechanism and control of silk fibroin. *Biomacromolecules*, 12(4), 1080-1086. doi:[10.1021/bm101422j](https://doi.org/10.1021/bm101422j)
- MacNeil, S. (2007). Progress and opportunities for tissue-engineered skin. *Nature*, 445(7130), 874-880. doi:[10.1038/nature05664](https://doi.org/10.1038/nature05664)
- Mirahmadi, F., Tafazzoli-Shadpour, M., Shokrgozar, M. A., & Bonakdar, S. (2013). Enhanced mechanical properties of thermosensitive chitosan hydrogel by silk fibers for cartilage tissue engineering. *Materials Science and Engineering: C*, 33(8), 4786-4794. doi:[10.1016/j.msec.2013.07.043](https://doi.org/10.1016/j.msec.2013.07.043)
- Nelson, D. L., & Cox, M. M. (2013). *Lehninger Principles of Biochemistry* (Y. M. Elçin, Ed. & Trans. from 5th Ed.). Palme. (Original work published 2008).
- Pamuk, F. (2011). *Biyokimya*. Gazi Kitabevi.

- Park, D. H., Choi, W. S., Yoon, S. H., Shim, J. S., & Song, C. H. (2007). A developmental study of artificial skin using the alginate dermal substrate. *Key Engineering Materials*, 342-343, 125-128. doi:[10.4028/www.scientific.net/KEM.342-343.125](https://doi.org/10.4028/www.scientific.net/KEM.342-343.125)
- Peretz, S. (2004). Interaction of alginate with metal ions, cationic surfactants and cationic dyes. *Rom. Journal. Phys.*, 49(9-10), 857-865.
- Porter, D., & Vollrath, F. (2009). Silk as a biomimetic ideal for structural polymers. *Advanced Materials*, 21(4), 487-492. doi:[10.1002/adma.200801332](https://doi.org/10.1002/adma.200801332)
- Priya, S. G., Jungvid, H., & Kumar, A. (2008). Skin tissue engineering for tissue repair and regeneration. *Tissue Engineering Part B: Reviews*, 14(1), 105-118. doi:[10.1089/teb.2007.0318](https://doi.org/10.1089/teb.2007.0318)
- Qi, Y., Wang, H., Wei, K., Yang, Y., Zheng, R.-Y., Kim, I. S., & Zhang, K.-Q. (2017). A review of structure construction of silk fibroin biomaterials from single structures to multi-level structures. *International Journal of Molecular Sciences*, 18(3), 237. doi:[10.3390/ijms18030237](https://doi.org/10.3390/ijms18030237)
- Reinholz, G. G., Lu, L., Saris, D. B. F., Yaszemski, M. J., & O'Driscoll, S. W. (2004). Animal models for cartilage reconstruction. *Biomaterials*, 25(9), 1511-1521. doi:[10.1016/S0142-9612\(03\)00498-8](https://doi.org/10.1016/S0142-9612(03)00498-8)
- Rujiravanit, R., Kruaykitanon, S., Jamieson, A. M., & Tokura, S. (2003). Preparation of crosslinked chitosan/silk fibroin blend films for drug delivery system. *Macromolecular Bioscience*, 3(10), 604-611. doi:[10.1002/mabi.200300027](https://doi.org/10.1002/mabi.200300027)
- Shen, Y., Wang, X., Li, B., Guo, Y., & Dong, K. (2022). Development of silk fibroin-sodium alginate scaffold loaded silk fibroin nanoparticles for hemostasis and cell adhesion. *International Journal of Biological Macromolecules*, 211, 514-523. doi:[10.1016/j.ijbiomac.2022.05.064](https://doi.org/10.1016/j.ijbiomac.2022.05.064)
- Sittinger, M., Bujia, J., Rotter, N., Reitzel, D., Minuth, W. W., & Burmester, G. R. (1996). Tissue engineering and autologous transplant formation: practical approaches with resorbable biomaterials and new cell culture techniques. *Biomaterials*, 17(3), 237-242. doi:[10.1016/0142-9612\(96\)85561-X](https://doi.org/10.1016/0142-9612(96)85561-X)
- Summer, G. J., Puntillo, K. A., Miaskowski, C., Green, P. G., & Levine, J. D. (2007). Burn injury pain: the continuing challenge. *The Journal of Pain*, 8(7), 533-548. doi:[10.1016/j.jpain.2007.02.426](https://doi.org/10.1016/j.jpain.2007.02.426)
- Toon, M. H., Maybauer, D. M., Arceneaux, L. L., Fraser, J. F., Meyer, W., Runge, A., & Maybauer, M. O. (2011). Children with burn injuries-assessment of trauma, neglect, violence and abuse. *Journal of Injury & Violence Research*, 3(2), 98-110. doi:[10.5249/ijvr.v3i2.91](https://doi.org/10.5249/ijvr.v3i2.91)
- Um, I. C., Kweon, H., Park, Y. H., & Hudson, S. (2001). Structural characteristics and properties of the regenerated silk fibroin prepared from formic acid. *International Journal of Biological Macromolecules*, 29(2), 91-97. doi:[10.1016/S0141-8130\(01\)00159-3](https://doi.org/10.1016/S0141-8130(01)00159-3)
- Vepari, C., & Kaplan, D. L. (2007). Silk as a biomaterial. *Progress in Polymer Science*, 32(8-9), 991-1007. doi:[10.1016/j.progpolymsci.2007.05.013](https://doi.org/10.1016/j.progpolymsci.2007.05.013)
- Wang, X., Partlow, B., Liu, J., Zheng, Z., Su, B., Wang, Y., & Kaplan, D. L. (2015). Injectable silk-polyethylene glycol hydrogels. *Acta Biomaterialia*, 12, 51-61. doi:[10.1016/j.actbio.2014.10.027](https://doi.org/10.1016/j.actbio.2014.10.027)
- Woo, W.-M. (2019). Skin Structure and Biology. In: C. Xu, X. Wang, & M. Pramanik (Eds.) *Imaging Technologies and Transdermal Delivery in Skin Disorders* (pp. 1-14). Wiley. doi:[10.1002/9783527814633.ch1](https://doi.org/10.1002/9783527814633.ch1)
- Xie, H., Bai, Q., Kong, F., Li, Y., Zha, X., Zhang, L., Zhao, Y., Gao, S., Li, P., & Jiang, Q. (2022). Allantoin-functionalized silk fibroin/sodium alginate transparent scaffold for cutaneous wound healing. *International Journal of Biological Macromolecules*, 207, 859-872. doi:[10.1016/j.ijbiomac.2022.03.147](https://doi.org/10.1016/j.ijbiomac.2022.03.147)
- Yodmuang, S., McNamara, S. L., Nover, A. B., Mandal, B. B., Agarwal, M., Kelly, T.-A. N., Chao, P.-h. G., Hung, C., Kaplan, D. L., & Vunjak-Novakovic, G. (2015). Silk microfiber-reinforced silk hydrogel composites for functional cartilage tissue repair. *Acta Biomaterialia*, 11, 27-36. doi:[10.1016/j.actbio.2014.09.032](https://doi.org/10.1016/j.actbio.2014.09.032)
- Yu, J. R., Navarro, J., Coburn, J. C., Mahadik, B., Molnar, J., Holmes IV, J. H., Nam, A. J., & Fisher, J. P. (2019). Current and future perspectives on skin tissue engineering: key features of biomedical research, translational assessment, and clinical application. *Advanced Healthcare Materials*, 8(5), 1801471. doi:[10.1002/adhm.201801471](https://doi.org/10.1002/adhm.201801471)

Zhang, K. H., & Mo, X. M. (2011). Influence of Post-treatment with Methanol Vapor on the Properties of SF/P (LLA-CL) Nanofibrous Scaffolds. *Advanced Materials Research*, 236-238, 2221-2224. doi:[10.4028/www.scientific.net/AMR.236-238.2221](https://doi.org/10.4028/www.scientific.net/AMR.236-238.2221)

Zhang, T., Xiong, Q., Shan, Y., Zhang, F., & Lu, S. (2021). Porous Silk Scaffold Derived from Formic Acid: Characterization and Biocompatibility. *Advances in Materials Science and Engineering*, 2021, 3245587. doi:[10.1155/2021/3245587](https://doi.org/10.1155/2021/3245587)

Zhao, M., Qi, Z., Tao, X., Newkirk, C., Hu, X., & Lu, S. (2021). Chemical, thermal, time, and enzymatic stability of silk materials with silk i structure. *International Journal of Molecular Sciences*, 22(8), 4136. doi:[10.3390/ijms22084136](https://doi.org/10.3390/ijms22084136)





Gazi University

**Journal of Science**

PART A: ENGINEERING AND INNOVATION

<http://dergipark.org.tr/guj.1104126>

# Experimental and Modelling Comparison of the Effects of UV Energy on Liquefaction Efficiency in Coal Liquefaction Mechanism

Yelda ALTINSOY<sup>1\*</sup> , Emir H. ŞİMŞEK<sup>1</sup> <sup>1</sup>Ankara University, Department of Chemical Engineering

Keywords	Abstract
Liquefaction	Coal liquefaction process gives very efficient results, especially for value-added chemicals production from low-quality coal. However, when the literature is examined, notably there is not enough scientific study for liquefaction mechanisms. Here, in this study, There are five different liquefaction mechanisms of Beypazari coals. It includes four different UV light power and a catalyst environment using 180 watts of UV power. Created first-order linear discrete models were proposed and compared with the experimental results. Additionally, the reaction rate constants for each proposed kinetic model were calculated using the Kalman filter method. However, to evaluate the compatibility of the experimental results and the modeling results, the sum of the squared differences of the values calculated from the experimental data and the models was examined. Because of these studies, it has been observed that the rate constants of direct oil formation from coal at 120 and 180 watts of UV power are at least three times greater than the rate constants for the formation of asphaltene and pre-asphaltene from coal. Simultaneously, The results demonstrate that models with reversible and parallel steps are more compatible with experimental data. Experimental data and modeling results are much more compatible with the studies conducted on Beypazari coals in a 180-watt UV-catalyzed environment compared to a 180-watt catalyst-free environment. In the presence of ZnO catalyst, the rate constants occurring in the conversion reaction from coal to oil were again three times faster than the conversion rate constants from coal to asphaltene and from coal to preasphaltene. In the modeling and experimental results conducted in the catalyst environment, the efficiency was higher than the catalyst-free environment. The best fit was obtained using model that has both reversible (between asphaltene: coal, asphaltene: oil, and asphaltene: preasphaltene) and irreversible (coal: oil, coal: preasphaltene and preasphaltene: oil) reaction steps. The model also evidenced that reversible reactions are critical on the liquefaction of Beypazari coal.
Kinetic Model	
Coal	
MatLab	

Cite
Altınsoy, Y., & Şimşek, E. H. (2022). Experimental and Modelling Comparison of the Effects of UV Energy on Liquefaction Efficiency in Coal Liquefaction Mechanism. <i>GU J Sci, Part A, 9(2)</i> , 136-155.

Author ID (ORCID Number)	Article Process
Y. Altınsoy, 0000-0002-5277-6981	<b>Submission Date</b> 15.04.2022
E. H. Şimşek, 0000-0001-7945-8222	<b>Revision Date</b> 16.05.2022
	<b>Accepted Date</b> 22.06.2022
	<b>Published Date</b> 27.06.2022

## 1. INTRODUCTION

Coal liquefaction is an advantageous process in which coal can be converted into more valuable and cleaner liquid hydrocarbons that can be used in liquid fuels and petro-chemistry (Cunliffe, 2001; Wang et al., 2009; Li et al., 2017; Gao et al., 2018; Hao et al., 2017; Liu et al., 2018). The main purpose in coal liquefaction processes is to obtain products from coal, primarily petroleum, liquid, asphaltene and pre-asphalten. The main approaches used to convert coal into liquid hydrocarbons revolve around breaking down large, complex "structures" by hydrogenation reactions and increasing the solubility of the organic fraction (Speight, 2008; Li et al., 2017; Gao et al., 2018; Hao et al., 2018). For this purpose, there are two basic liquefaction processes in liquefaction processes. One of them is indirect liquefaction and the other is direct liquefaction. The conversion of the syngas (CO+H<sub>2</sub>) obtained because of the gasification process of coal into liquid products using special catalysts is known as the indirect liquefaction process of coal (Karacan, 2004). The basis of the direct coal

\*Corresponding Author, e-mail: [yeldaaltinsoy@enerji.gov.tr](mailto:yeldaaltinsoy@enerji.gov.tr)

liquefaction process is due to the thermal decomposition of coal in an H-donating solvent using a heat source and hydrogenation of its decomposition products. The solvent used in the process to directly obtain hydrogen gives hydrogen directly in the stabilization of free radicals and provides hydrogen transfer from the hydrogen-rich parts of the coal to other reactive regions that need hydrogen. The resulting reactions provide coal, gas, liquid and solid products (Allen & Gavalas, 1984; Hsiang-Hui & Stock, 1984).

The coal liquefaction process, which occurs in a hydrogen donor environment, depends on many independent chemical reactions. These reactions support the formation of many active and inactive substances as they progress. Stabilization of active species and free radicals is of great importance in terms of ensuring reaction efficiency (Cronauer et al., 1979; Mohan & Silla, 1981; Huang et al., 1998; Li et al., 2008; Şimşek et al., 2017). For this reason, to understand these reactions and mechanisms, the direction of studies recently has been directed to this area (Farcasiu et al., 1977; Cronauer et al., 1978; Han et al., 1978; Shah et al., 1978; Shalabi et al., 1979; Angelova et al., 1989; Ceylan & Olcay, 1998; Şimşek et al., 2017). Liebenberg & Potgieter (1973) proposed liquefaction mechanism includes following steps asphaltene from coal and heavy oil formation from asphaltene, as well as two parallel reactions; coal  $\rightarrow$  asphaltenes and coal  $\rightarrow$  heavy oil reactions. Cronauer et al. (1978) conducted a study on the lower bituminous coal conducting in a continuous stirred reactor (CSTR) with the help of anthracene oil and phenanthrene solvents, and a first-order irreversible kinetic analysis of coal  $\rightarrow$  oil, oil  $\rightarrow$  asphaltene, coal  $\rightarrow$  preasphaltene, preasphaltene  $\rightarrow$  asphaltene, coal  $\rightarrow$  asphaltene and coal  $\rightarrow$  gas. model has been proposed. The kinetic mechanisms of dissolution in the presence of tetralin in a bituminous coal with high volatility were investigated and three model mechanisms were proposed by Ayappa et al. (1991). Two models were predicted for the liquefaction kinetics of the coals dissolving in the presence of tetralin. A model is the same as the one proposed by Shalabi et al. (1979).

Significant liquefaction reactions occur when coals are exposed to direct heat with the use of a thermal source in pressurized furnaces due to long heating and cooling periods. However, it does not show realistic liquefaction reaction mechanisms under these reaction conditions with the use of a pressure furnace and thermal source. Therefore, in the direct liquefaction process of coal, the use of microwave or UV light sources, which increases efficiency due to short startup and internal heating periods, becomes more effective as a heat source (Ayappa et al., 1991).

In both two studies, the liquefaction mechanisms of coal in the presence of tetralin and the formation rate constants of preasphalten, asphaltene and oil were investigated using microwave source (Şimşek et al., 2001; Shui et al., 2010).

The rate of formation of preasphaltene, asphaltene and oil was investigated during the liquefaction of six different reactive coals in tetralin as a hydrogen donor solvent using microwave heating in the literature (Şimşek et al., 2001; Shui et al., 2010). Within the scope of the studies, five different liquefaction models were determined and it was assumed that the reactions occurring here were irreversible and pseudo-first order. It has been observed that the reactions proceed in parallel in the conversion mechanism from coal to asphaltene, pre-asphaltene and oils. It is noteworthy that coal has much higher carbon content in parallel reactions. Five different liquefaction models, defined as irreversible and pseudo-first order, were proposed and studied. Models consisting of parallel liquefaction from coal to preasphaltenes, asphaltenes and oils show that coal with higher carbon is most appropriate, while models involving serial and parallel liquefaction reactions show that lower carbon coals are more suitable.

Two of the studies conducted with the use of UV rays in the liquefaction of coal is the studies by Yürüm and Yiğinsu (1982) and Söğüt and Olcay (1998). In these studies, photochemical reactions of coal were investigated without the need for high pressure and temperature. It has been determined that oil formation in liquid products formed because of photochemical reactions has much higher formation rates than asphaltene and preasphalten formations. Therefore, the use of UV rays in coal liquefaction processes has made it more effective (Yürüm & Yiğinsu, 1982; Söğüt & Olcay, 1998). In a study by Doetschman et al. (1992) the liquefaction of coal in a tetrahydrofuran solvent with the effect of UV rays was investigated in the coal liquefaction process. In this study, different coal samples were irradiated at different powers and showed that the effect of UV irradiation power was directly proportional to the liquefaction efficiency. The study proved that liquefaction is five times more efficient in coal exposed to continuous irradiation compared to the

liquefaction process performed in the dark without the use of UV irradiation power. Studies have shown that the stimulation of molecules in the solvent/coal extract using UV causes the fragmentation of coal particles. When the extract structures were examined, it was seen that the fragmentation caused by the UV rays in the coal macromolecular structure chain provided the return to the aromatic structure (Doetschman et al., 1992).

## 2. EXPERIMENTAL STUDIES

This study constitutes the kinetic modeling of the coal liquefaction processes. In order to determine the kinetic mechanism, the MatLab programme was performed with experimental results. For a highly efficient determination of kinetic model study, it is necessary to find out the kinetic approach that is compatible with the experimental results.

### 2.1. Experimental Data

The experimental data used in the discrete-time models of coal liquefaction models in this study were obtained from the study by Karacan (2004). Coal samples were supplied from Beypazarı-Çayırhan and were crushed and then ground in size using a mill-ball. The grinded samples were sieved with a particle size of sub-300 microns using standard lab scale sieves. The coal samples were then dried under atmospheric conditions until they reached a constant weight and then stored in plastic bottles with lids to be used in the experiments. Experiments were conducted with different UV light powers of 0, 60, 120, and 180 Watt using a tetralin/charcoal mixture of 5/1 by weight for 1, 2, 3, 5, and 10 days.

To investigate the effect of UV power in liquefaction experiments, a UV chamber whose energy power changes approximately 30 to 210W was used. In this chamber, a round bottomed flask with a volume of 500 ml and a magnetic stirrer with adjustable stirring speed was used. For the non-catalytic study, 15 g coal and 75 g of tetralin were weighed into the quartz flask, and for catalytic tests, 0.75 g catalyst was added to the quartz flask at a ratio of 5% catalyst/lignite by weight. However, in the catalyst addition stage, TiO<sub>2</sub> and ZnO were added to the medium by physical mixing, while ZnO was added by being absorbed into the coal particles. The addition of tetralin was added after the homogenization of the charcoal catalyst mixture had taken place before the experiment under catalytic conditions.

Before UV experiments to be conducted in both catalytic and non-catalytic conditions, the mixtures were mixed for 2-3 minutes in order to increase the interaction of the particles with each other during the reaction. After the experimental conditions were established, the desired UV rays were exposed to the tetralin/catalyst/coal and tetralin/coal mixtures in the round bottomed flask and the reactions were conducted. However, experiments with a power of 0 watts were conducted in a dark environment. All experiments were conducted at atmospheric pressure and room temperature, at the end of the determined test times, the system was turned off and the reaction temperatures were physically measured. After it was defined that the measured reaction temperatures did not exceed 33 °C, the round bottomed flask in the UV chamber was removed and the mixture was filtered and the solid/liquid phases were separated from each other. The remaining fractions in the flask were obtained by washing with tetrahydrofuran and the solid phase was first washed with this mixture and then washed again with tetrahydrofuran. The filtrate obtained from the washed solid phase was mixed with the liquid phase. Before mixing, rotary evaporator removed THF under atmospheric pressure. As a result, the liquid phase contains tetralin and charcoal dissolved in tetralin.

To keep the tetralin in a certain amount, it was ensured that the tetralin was removed from the mixture under vacuum and the concentration was increased in the rotary evaporator. To allow the liquid product to be separated into fractions as oil, asphaltene and preasphalten, the concentrated mixture was kept overnight by adding 200 ml hexane. An overnight waiting period facilitated the separation of the oils from the asphaltene and pre-asphaltene, as it caused the oils to dissolve in hexane. The removal of hexane from the filtrate was achieved using a rotary evaporator and oils were obtained. Due to the dissolution of asphaltenes in toluene, 200 ml toluene was used to separate the remaining mixture from the preasphalten, and toluene was also removed in the rotary evaporator. Products insoluble in toluene were taken from the mixture as preasphalten. In this way, oil, asphaltene and preasphaltene formations obtained from coal liquefaction process were determined. Experimental studies are given in Table 1 by calculating the percentage of products (oil, asphaltene and preasphalten) obtained at each UV exposure for different time periods and the weight percentage of

liquefied products (preasphaltenes, asphaltenes and oils) per weight of lignite (daf) used. Additionally, the physical properties of coal are given in Table 2.

**Table 1.** Beypazarı coal experimental study (Karacan, 2004)

UV Power	Time (day)	Oil %	Asphaltene %	Preasphaltene %	Liquid product %
0 W (in dark)	1	4.81	0.46	1.03	6.30
	2	4.34	0.75	0.97	6.06
	3	4.10	0.88	0.87	5.85
	5	4.48	0.91	0.54	5.93
	10	5.04	1.20	0.57	6.81
60 W	1	13.53	1.88	0.38	15.79
	2	15.98	2.77	1.10	19.85
	3	15.36	2.91	0.61	18.88
	5	15.47	2.80	0.48	18.75
	10	13.60	6.26	1.26	21.12
120 W	1	13.58	2.33	0.40	16.31
	2	15.75	3.82	0.80	20.37
	3	14.41	3.25	1.16	18.82
	5	17.03	2.05	1.87	20.95
	10	20.91	3.82	2.01	26.74
180 W	1	13.49	3.10	0.80	17.39
	2	18.36	1.81	0.40	20.57
	3	17.72	2.38	1.14	21.24
	5	19.23	2.09	0.42	21.74
	10	27.53	2.70	2.76	32.99
180 W TiO <sub>2</sub>	1	17.36	2.38	0.64	20.38
	2	15.16	2.66	0.68	18.50
	3	19.92	2.20	1.01	23.13
	5	15.78	1.11	0.52	17.41
	10	24.17	3.15	2.67	29.99
180 W ZnCl <sub>2</sub>	1	13.37	1.76	0.86	15.99
	2	15.92	3.52	1.08	20.52
	3	14.65	2.31	1.31	18.27
	5	28.99	2.84	1.42	33.25
	10	16.67	2.71	0.96	20.34
180 W ZnO	1	12.15	1.46	0.26	13.87
	2	14.52	2.83	0.37	17.72
	3	16.71	2.91	2.01	21.63
	5	23.78	1.27	0.26	25.31
	10	26.12	1.50	0.36	27.98

**Table 2.** Analysis of Beypazari coal samples (Karacan, 2004)

Ultimate Analysis (w/w %)	
Moisture	13.00
Ash	25.55
Volatile Matter	29.19
Fix Carbon	32.26

Sulfur Distribution Hit (w/w %)	
S <sub>total</sub>	4.59
S <sub>oxy</sub>	3.52

Elemental Analysis (w/w %)	
C	69.56
H	4.50
N	1.25
S <sub>oxy</sub>	4.72
O	19.97

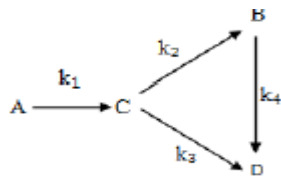
Maseral Composition (vol %)	
Huminite	94.3
Liptinit	2.60
Inertinite	3.10

Lower Calorific Value (kcal/kg)	3978
---------------------------------	------

## 2.2. Recommended Coal Liquefaction Models

In the model suggested for five different coal liquefaction depending on three parameters; (A) represents the reactive coal, (B) the asphaltene liquefied from the reactive coal, (C) the preasphaltenes and (D) the oils. In the literature, many reaction models have been investigated for the liquefaction mechanism in coals of different structures. In this study, five different models proposed for Beypazari coals are given in Figure 1. The models consist of parallel and series as well as reversible and irreversible steps. The gaseous products were not obtained due to the low reaction (at 25°C) temperatures, and in this case, possible reaction steps were removed from the proposed models. The reaction rate equations of the proposed models are given in Equations 1-20. In this study, the comparison of experimental data with modeling data is also evaluated. The mechanisms given in Model 1 and Model 2 were explained as suggested by Shalabi et al. (1978). In Model 1, there is a transformation from coal to preasphalten, from preasphalten to both asphaltene and oils due to serial reactions, while oil is formed from asphaltene at the same time. All reactions are assumed to occur first-order and irreversibly. In Model 2, while direct oil conversion occurs from coal, there are also direct asphaltene and pre-asphaltene formations from coal, and asphaltene and oil formations from pre-asphaltene formed from coal. In this model, the reactions are considered parallel, first-order and irreversible. In a study proposed by Şimşek et al. (2021) Model 3 includes reversible, irreversible parallel and serial first-order reactions. This model, which includes reversible and irreversible mechanisms, which is one of the remarkable details in the explanation of the coal liquefaction mechanism, is discussed again in this study. Model 3, in addition to Model 2, consists of reversible reaction steps between coal ↔ asphaltenes, asphaltenes ↔ preasphaltenes and asphaltenes ↔ oils. Model 4 and Model 5 are the models recommended within the scope of this study, and Şimşek (1997) and Söğüt (1997) in both models are the models recommended after a decrease in oil yield after a maximum when their studies are examined. Therefore, Models 4 and 5 are assumed to have steps in which oil gives reversible reactions. Model 4 assumes the reversible formation of oils and preasphaltenes, preasphaltenes, oils from coal, as well as the formation of asphaltenes, asphaltenes, preasphaltenes and oils from coal. In Model 5, reversible formation of asphaltenes and oils from coal and reversible formations of oils from preasphaltenes and asphaltenes are predicted.

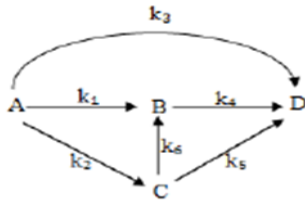


$$\frac{dA}{dt} = -k_1 A \tag{1}$$

$$\frac{dB}{dt} = k_2 C - k_4 B \tag{2}$$

$$\frac{dC}{dt} = k_1 A - (k_2 + k_3) C \tag{3}$$

$$\frac{dD}{dt} = k_3 C + k_4 B \tag{4}$$

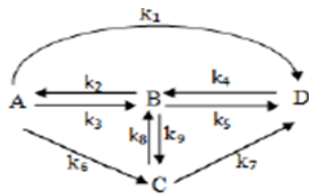


$$\frac{dA}{dt} = -\theta A \tag{5}$$

$$\frac{dB}{dt} = k_1 A + k_6 C - k_4 B \tag{6}$$

$$\frac{dC}{dt} = k_2 A - (k_5 + k_6) C \tag{7}$$

$$\frac{dD}{dt} = k_3 A + k_4 B + k_5 C \tag{8}$$

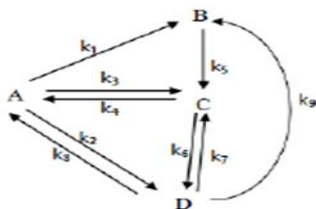


$$\frac{dA}{dt} = k_2 B - (k_1 + k_3 + k_6) A \tag{9}$$

$$\frac{dB}{dt} = k_4 D + k_8 C + k_3 A - (k_2 + k_5 + k_9) B \tag{10}$$

$$\frac{dC}{dt} = k_6 A + k_9 B - (k_7 + k_8) C \tag{11}$$

$$\frac{dD}{dt} = k_1 A + k_5 B + k_7 C - k_4 D \tag{12}$$

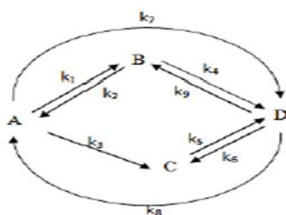


$$\frac{dA}{dt} = k_4 C + k_8 D - (k_1 + k_2 + k_3) A \tag{13}$$

$$\frac{dB}{dt} = k_1 A + k_9 D - k_5 B \tag{14}$$

$$\frac{dC}{dt} = k_3 A + k_5 B + k_7 D - (k_4 + k_6) C \tag{15}$$

$$\frac{dD}{dt} = k_2 A + k_6 C - (k_7 + k_8 + k_9) D \tag{16}$$



$$\frac{dA}{dt} = k_2 B + k_8 D - k_7 A \tag{17}$$

$$\frac{dB}{dt} = k_1 A + k_9 D - (k_2 + k_4) B \tag{18}$$

$$\frac{dC}{dt} = k_3 A + k_6 D - k_5 C \tag{19}$$

$$\frac{dD}{dt} = k_7 A + k_4 B + k_5 C - (k_6 + k_8 + k_9) D \tag{20}$$

Figure 1. Suggested coal liquefaction models; A) Reactive coal, B) Asphaltene, C) Preasphaltene, D) Oil

### 2.3. Comparison of Models with Experimental Data

The compatibility of the proposed liquefaction reactions with the experimental results regarding the liquefaction mechanisms of coal belonging to the Beypazarı region has been revealed by creating first-order discrete-time models. The Kalman Filtering method was used for each reaction rate constant in the models and was determined using the MatLab program (version 7.11). If given as an example; The discrete-time model used for Model 2

Additionally, the reaction rate constants for each reaction in the models are determined using a MatLab program (written in ver 7.11, The MathWorks Inc. Natick, MA, USA) using the Kalman filter. For example, discrete-time model equations used for Model-1 in this study are given in Equations 21-24.

$$C_A (i+1) = C_A i (1 - (k_1 + k_2 + k_3) \Delta t) \quad (21)$$

$$C_B (i+1) = C_B i (1 - k_4 \Delta t) + (k_1 C_A + k_6 C_C i) \Delta t \quad (22)$$

$$C_C (i+1) = C_C i (1 - (k_5 + k_6) \Delta t) + k_2 C_A i \Delta t \quad (23)$$

$$C_D (i+1) = C_D i + k_3 C_A i \Delta t + k_4 C_B i \Delta t + k_5 C_C i \Delta t \quad (24)$$

Where,  $C_A$  is unreacted coal (daf) and  $C_B$ ,  $C_C$ ,  $C_D$  are percentages of asphaltene, preasphaltene and oil yield, respectively.

In the literature, the Kalman filter method is an algorithm in which a set of measurements observed over time can be used, including statistical noise and other errors. It can predict unknown variables more precisely than those based on a single measure (Wei et al., 2013). To control a dynamic system, it is necessary to know what is happening in the system. However, it is impossible to identify every variable in an impossible process, especially for measuring liquefaction such as coal processes. Therefore, the Kalman filter can predict state variables from available known data with minimal change to unknown current data. The rate constants of the proposed liquefaction mechanisms can be estimated using the Kalman filter, and there are many studies in the literature with the use of MatLab (Grewal & Andrews, 2001; Welch & Bishop, 2006; Şimşek et al., 2017; 2019).

### 3. CONCLUSIONS AND DISCUSSIONS

The use of first-order linear discrete-time models for the compatibility of experimental data and data obtained from models is a study in the literature. Simultaneously, a program was created in the MatLab application to calculate the rate constants of the reactions occurring, and predictions were made with the Kalman Filtering Method (Kalman, 1960). Within the scope of this study, the experimental data and the most compatible model of the proposed model are given in Model 3 and Equation 25. The compatibility of this model with the experimental data was decided by looking at the square of the difference between the data calculated from the model and the experimental data (Kavuştu, 2012).

$$\sum_i (y_{m_i} - y_{e_i})^2 = (AS_m - AS_e)^2 + (PAS_m - PAS_e)^2 + (YA_m - YA_e)^2 \quad (25)$$

Here;

$y_{m_i}$  and  $y_{e_i}$  = Values calculated from the model and experimental data

$AS_m$  and  $AS_e$  = Asphaltene yields calculated from the model and experimental data

$PAS_m$  and  $PAS_e$  = Preasphaltene yields calculated from the model and experimental data

$YA_m$  and  $YA_e$  = Oil yields calculated from the model and experimental data

When examining the compositional properties of coal to examine their behavior in direct liquefaction, it is impossible to say that a single property sufficiently predicts the transformations for all coal. Therefore, to understand the liquefaction behavior of coal, correlations with sulfur, reactive maceral and volatile matter contents, vitrinite reflection and H/C ratios were established for coals from certain geological regions. Based on this study, bituminous coals provide higher conversions than low-grade coals at short residence times, but under typical hydro-liquefaction processing conditions, distillate yields are generally higher than low-grade coals. The lack of information about aromatic, aliphatic and heteroatomic groups and the concentrations of low molecular weight components in coals preclude more precise structural correlations with liquefaction behavior. Analytical results from studies on how organic coal structure affects liquefaction are still being

evaluated. (Snape, 1987). It is assumed that coals provide the formation of coal liquefaction patterns due to their amorphous, cross-linked polymeric structure. Aromatic structures with high molecular weight in coal containing heteroatomic structure form the macromolecular structure of these coals and this structure supports the formation of many free radicals due to its easy exposure to photochemical decomposition. Free radicals can easily react with hydrogen or polymerize with other molecules. Here, the hydrogen donor source is tetralin, the hydrogen donor solvent. Low molecular weight and hydrogen-rich products, namely, oils, which are formed because of the stabilization of free radicals with hydrogen, can be produced very easily. In contrast, the formation of high molecular weight H/Cs can be observed due to the polymerization of free radicals without reversible and irreversible reactions. In Table 3, the squares of the difference between Model 1 and experimental data and the rate constants formed at different UV light powers are given.

**Table 3.** The squares of the difference between Model 1 and the experimental data and the rate constants ( $h^{-1}$ ) and the percent liquid yields at different UV powers

UV Power (W)	$\sum_i (y_{m_i} - y_{e_i})^2$	Rate constant ( $h^{-1}$ ) x $10^3$				oil conversion % experimental
		k <sub>1</sub>	k <sub>2</sub>	k <sub>3</sub>	k <sub>4</sub>	
0	83.8723	5.5	12.3	13.2	10.2	Day 10 5.04
60	655.9149	14.1	14.1	15.9	10.4	Day 2 15.98
120	740.3083	16.2	13.9	16.9	10.7	Day 10 20.91
180	965.5916	18.0	14.1	18.1	10.8	Day 10 27.53
180/TiO <sub>2</sub>	963.1773	16.8	13.9	17.4	10.7	Day 10 24.17
180/ZnCl <sub>2</sub>	1033	16.8	14.1	17.5	10.7	Day 5 28.99
180/ZnO	926.6212	16.8	13.9	18.0	10.8	Day 10 26.12

In Figure 2, the comparison of the data obtained from Model 1 with the experimental studies conducted at four different powers, 0, 60, 120, and 180 Watt UV power, is given graphically.

In Model 1, it is assumed that there are first-order irreversible reactions from reactive coal to preasphalten, from preasphalten to asphaltene and oils in parallel and from asphaltene to oils. At Figure 2, although the experiments conducted in the dark are more compatible with Model 1, Model 1 is completely incompatible with the experimental data. The assumed approach in this model is that the bonds will break during the coal liquefaction process (Şimşek et al., 2017). In the experiments conducted for the decomposition of coal using UV energy, it is seen that as the UV light power increases, the oil formations and generally increased around the 10th day, but these increases in the model are not at the same rate as the experimental data. In the evaluations for the decomposition of coal under UV light, firstly, polar groups are formed due to decomposition by UV effect, and then pre-cracking products due to liquefaction reaction, which can be considered as preasphalten. Preasphaltenes are H/Cs insoluble in toluene. In fact, Arrhenius cracking and coal chemistry do not support such possibilities. Generally, in liquefaction processes, it can be deduced that the weakest bonds on the structure are the bonds that dissociate in liquefaction processes. The weakest bonds can form two products, both of which have the property of dissolving in toluene, and only preasphaltene formations can be seen from the breaking of the less weak bonds. Another assumption considered while creating the model is that H/Cs insoluble in toluene can turn into soluble products in toluene or hexane. Additionally, coal liquefaction processes in the hydrogen donor solvent environment support the formation of free radicals. Hydrogens from solvent (Şimşek et al., 2017) can stabilize free radicals because solvent donates hydrogen under the influence of UV light to the free radicals (Şimşek et al., 2017). Due to this stabilization, products with smaller molecular weights are directly produced (Şimşek et al., 2017).



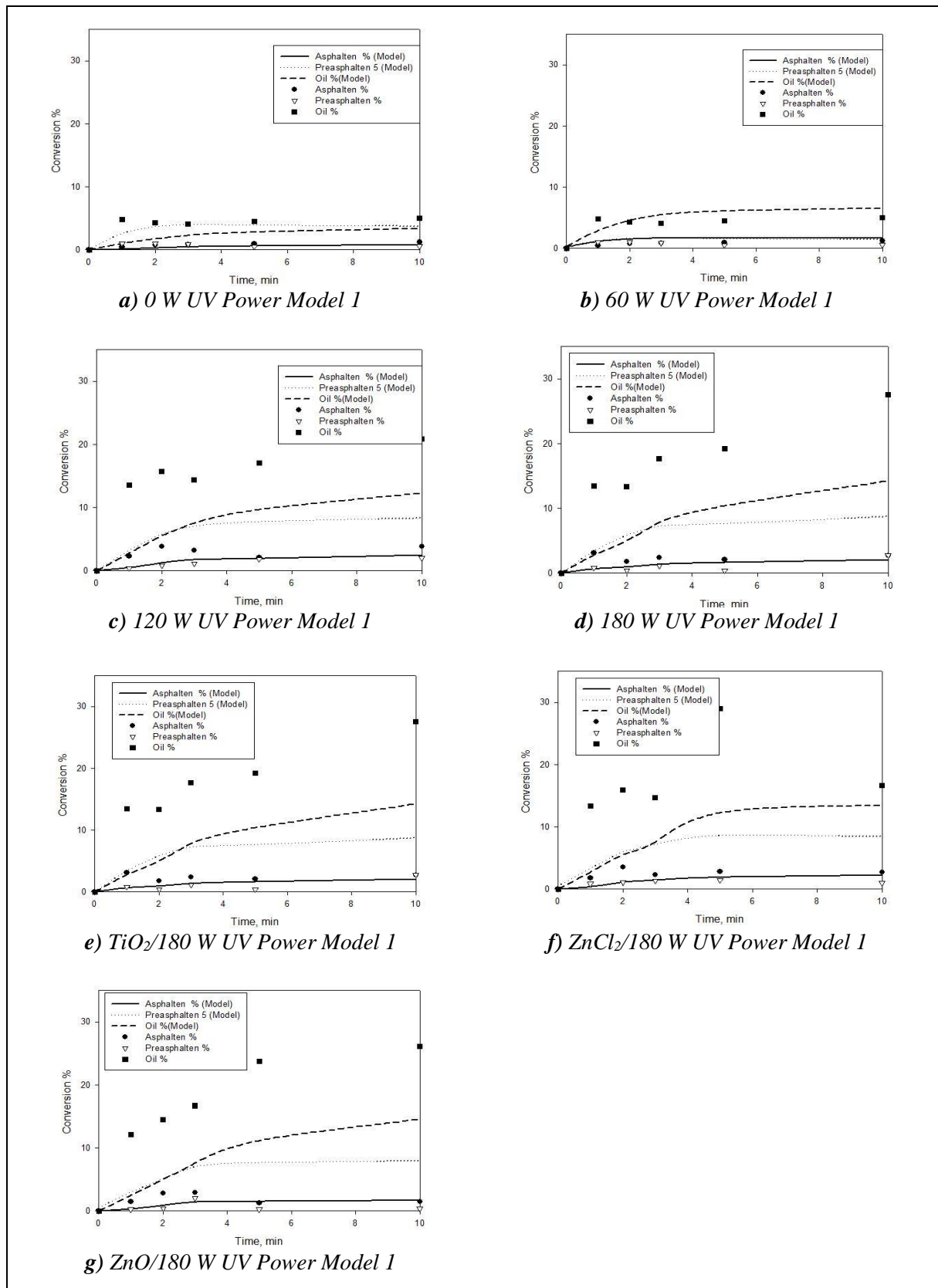


**Figure 2.** Comparison of the liquefaction mechanism obtained using Model 1 with experimental data at different UV powers  
 a) 0 W, b) 60 W, c) 120 W, d) 180 W e) TiO<sub>2</sub>/180 W f) ZnCl<sub>2</sub>/180 W g) ZnO/180 W

The reason for the inconsistency with the experimental data in Model 1 is the properties of coal, other than pre-asphalten, which is formed as insoluble in toluene. Because pre-asphaltene formations are very few both experimentally and modelally under the effect of each UV power. The data obtained from Model 2 and the squares of the experimental data differences and the rate constants formed at different UV light powers are given in Table 4.

In Model 2, asphaltenes (B), preasphaltenes (C) and oils (D) and additionally preasphaltenes (C) oils (D) are formed from coal (A) by parallel reactions, as well as preasphaltenes (C) asphaltenes (B) and oils from asphaltenes (D) formation is assumed. In this model, there are no reversible reactions and all reactions are deemed first order. The square of the differences between the experimental data and the data obtained from the model was the lowest, as in Model 1, in the studies conducted in the dark environment. However, when Model 2 is compared with Model 1, the square of the differences is more consistent than Model 1, but when the graphs given in Figure 3 are examined, the consistency with the experimental data is not better. Notably, asphaltene formations are quite parallel in the data obtained from the model with the experiments conducted in the dark in Model 2, but it is not very consistent for the hexane-soluble oil yields. However, asphaltene and pre-asphaltene formations generally follow a flat course after the 2nd day. In the presence of 180 Watt UV light, oil formations are in full agreement with the experimental data. As a result, it shows that the Model-2 model cannot provide a good definition of the liquefaction of Beypazarı coal for four different UV powers. The inconsistency between Model-2 and experimental data indicates that hexane-soluble H/Cs are more common in the formation of oils, as observed in Model-1.

**Table 4.** The data obtained from Model 2 and the squares of the experimental data and the rate constants and the oil formation percentages at different UV light powers

UV Power (W)	$\sum_i (y_{m_i} - y_{e_i})^2$	Rate constant ( $h^{-1}$ ) x $10^3$						oil conversion % experimental
		k <sub>1</sub>	k <sub>2</sub>	k <sub>3</sub>	k <sub>4</sub>	k <sub>5</sub>	k <sub>6</sub>	
0	50.7958	1.5	1.2	5.5	10.1	-	-	Day 10 5.04
60	252.4420	6.1	3.0	17.5	9.9	10.2	10.0	Day 2 15.98
120	188.4263	5.7	4.1	20.6	10.3	10.2	10.0	Day 10 20.91
180	192.3157	5.4	4.5	24.6	10.7	10.4	10.0	Day 10 27.53
180/ TiO <sub>2</sub>	316.0903	5.0	4.1	22.9	10.4	10.2	10.0	Day 10 24.17
180/ZnCl <sub>2</sub>	369.4902	5.4	3.8	22.9	10.4	10.3	10.0	Day 5 28.99
180/ZnO	139.3742	4.6	3.4	24.8	10.7	10.4	10.0	Day 10 26.12

For this reason, it is important to make assumptions on models with reversible reactions to achieve a more realistic model fit. Model 3 assumes reversible and irreversible reactions. The sum of the squares of the difference of the experimental data obtained from model 3, the rate constants and experimental oil conversion rates are given in Table 5.

In Model 3, in addition to the reversible formation of both oil (D) and preasphaltene (C) from coal (A), asphaltene (B) from coal (A), oils (D) from coal (A), pre-asphaltenes (C) and oils (D) from pre-asphaltenes (D) is assumed to be irreversible and first-order formation.

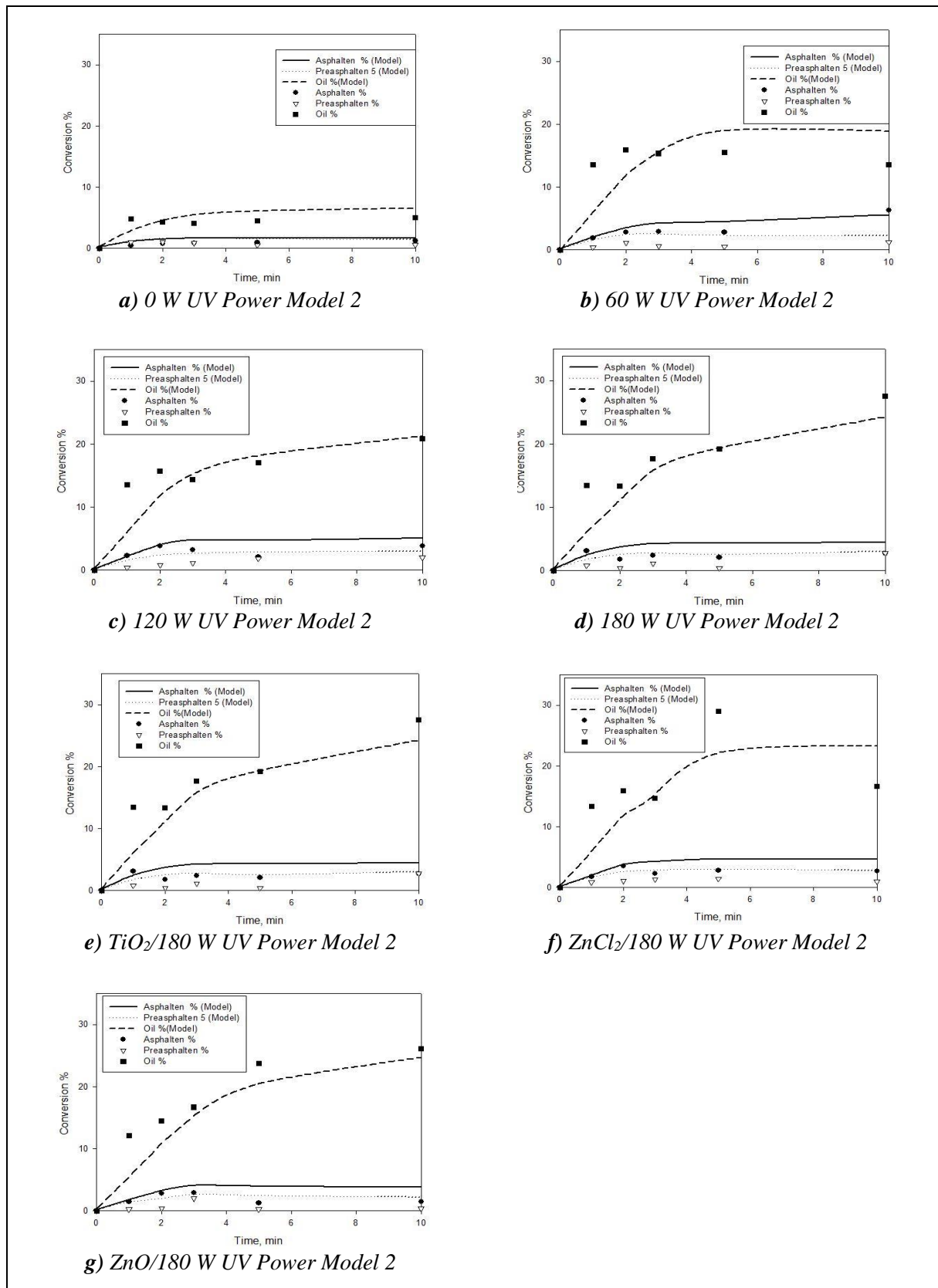


**Figure 3.** Comparison of the liquefaction mechanism obtained using Model 2 with experimental data at different UV powers  
 a) 0 W, b) 60 W, c) 120 W, d) 180 W e) TiO<sub>2</sub>/180 W f) ZnCl<sub>2</sub>/180 W g) ZnO/180 W

**Table 5.** The data obtained from Model 3 and the squares of the experimental data and the rate constants and the oil formation percentages at different UV light powers

UV Power (W)	$\sum_i (y_{m_i} - y_{e_i})^2$	Rate constant (h <sup>-1</sup> ) x 10 <sup>3</sup>									oil conversion % experimental
		k <sub>1</sub>	k <sub>2</sub>	k <sub>3</sub>	k <sub>4</sub>	k <sub>5</sub>	k <sub>6</sub>	k <sub>7</sub>	k <sub>8</sub>	k <sub>9</sub>	
0	8.6956	3.9	10.7	0.9	9.9	10.1	6.0	-	-	-	Day 10 5.04
60	67.8816	10.7	10.8	4.8	10.5	10.0	2.5	10.1	10.0	9.9	Day 2 15,98
120	62.2039	15.3	10.9	4.7	9.2	10.3	4.2	10.2	10.0	10.0	Day 10 20.91
180	73.4293	19.9	10.7	5.2	8.1	10.4	5.4	10.2	10.0	10.0	Day 10 27.53
180/TiO <sub>2</sub>	113.2106	17.0	10.9	4.5	9.1	10.2	4.6	10.2	10.0	10.0	Day 10 24.17
180/ZnCl <sub>2</sub>	140.0404	15.1	10.9	3.7	9.8	10.2	3.1	10.2	10.0	10.0	Day 5 28.99
180/ZnO	49.6152	19.3	10.8	4.0	8.0	10.5	3.7	10.3	10.0	10.0	Day 10 26.12

In Model-3, the liquefaction of coal is therefore improved by three reversible reactions; In addition to Model-2, assuming that there are three reversible reactions between coal ↔ asphaltenes, asphaltenes ↔ oils and asphaltenes ↔ preasphaltenes, the experimental results given in Figure 4 and the modeling results are compatible. Compared to other models, Model-3 fits best with experimental data for UV power of 90, 120, 150, and 180W. Furthermore, the sum of the squared differences shown in Table 5 also proves that Model-3 has a better explanation for liquefaction of coal compared to the other two models. It also shows that the models fit better with experimental results at higher UV powers of 180 W compared to 90 W with lower UV powers. Thanks to these three reversible reactions, which are the only difference from Model-2, Model-3 fits much better with the experimental data. Thus, the main free radicals are formed from reactive coal, as mentioned above, and many competitive and simultaneous chemical reactions can occur during the liquefaction of reactive coals (Şimşek et al., 2017).

The reaction rate constants of Model-3 at four different UV powers, 90, 120, 150, and 180 W, were determined using multiple regression analysis and the results are presented in Table 5. The calculated rate constants for Model 4 at four different UV powers are given in Table 6 and the comparison of the liquefaction mechanism data obtained by modeling with the experimental data is given in Figure 5.

Comparison of the liquefaction mechanism obtained using model 5 with experimental data at different UV power is given in Figure 6 and the data obtained from Model 5 and the squares of the experimental data and the rate constants and oil formation percentages at different UV light powers are given in Table 7 respectively.

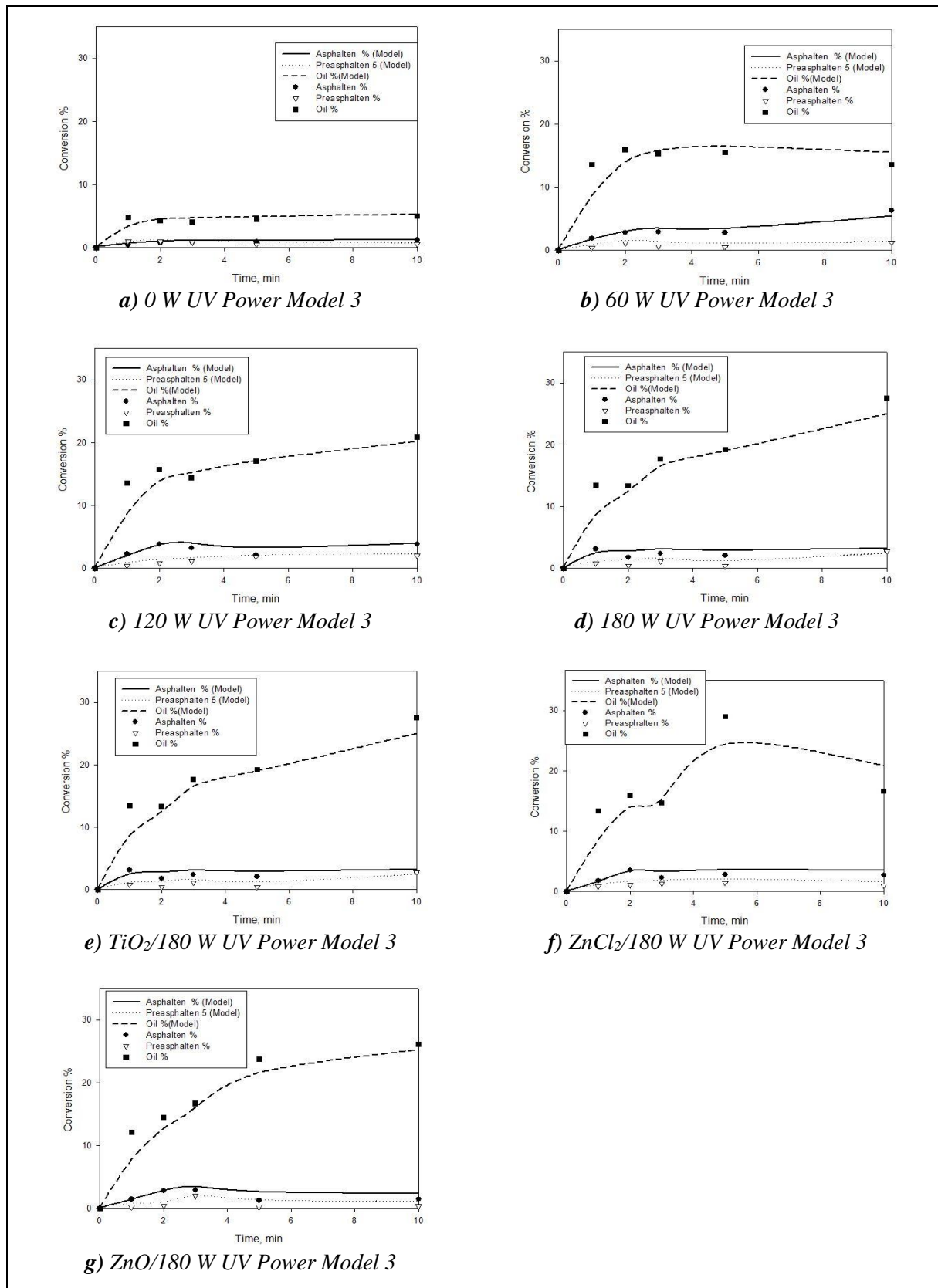


**Figure 4.** Comparison of the liquefaction mechanism obtained using Model 3 with experimental data at different UV powers  
 a) 0 W, b) 60 W, c) 120 W, d) 180 W e) TiO<sub>2</sub>/180 W f) ZnCl<sub>2</sub>/180 W g) ZnO/180 W

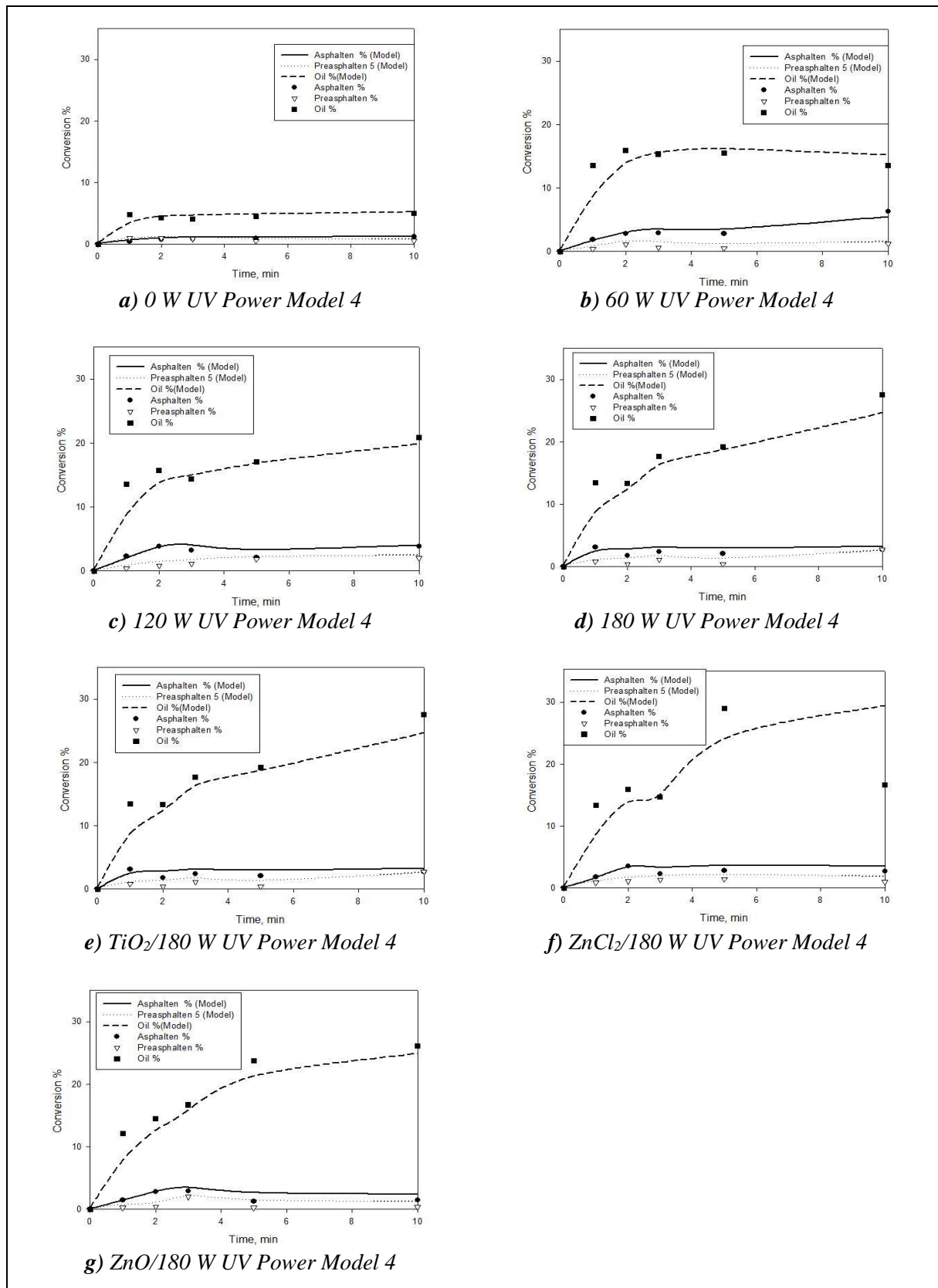


**Figure 5.** Comparison of the liquefaction mechanism obtained using Model 4 with experimental data at different UV powers  
 a) 0 W, b) 60 W, c) 120 W, d) 180 W e) TiO<sub>2</sub>/180 W f) ZnCl<sub>2</sub>/180 W g) ZnO/180 W

**Table 6.** The data obtained from Model 4 and the squares of the experimental data and the rate constants and the oil formation percentages at different UV light powers

UV Power (W)	$\sum_i (y_{m_i} - y_{e_i})^2$	Rate constant (h <sup>-1</sup> ) x 10 <sup>3</sup>									oil conversion % experimental
		k <sub>1</sub>	k <sub>2</sub>	k <sub>3</sub>	k <sub>4</sub>	k <sub>5</sub>	k <sub>6</sub>	k <sub>7</sub>	k <sub>8</sub>	k <sub>9</sub>	
0	8.3350	8.0	4.8	0.3	10.6	10.0	10.1	9.8	11.1	9.8	Day 10 5.04
60	65.0700	4.7	12.6	19.0	10.6	9.9	10.1	9.7	12.0	10.1	Day 2 15.98
120	61.9166	4.5	17.2	3.6	10.6	10.0	10.2	9.0	10.8	8.9	Day 10 20.91
180	75.5692	5.1	21.7	4.9	10.6	10.0	10.3	8.0	9.4	7.8	Day 10 27.53
180/TiO <sub>2</sub>	112.5464	4.4	19.1	4.1	10.6	10.0	10.2	8.9	11.0	8.7	Day 10 24.17
180/ZnCl <sub>2</sub>	137.4485	3.6	17.3	2.5	10.7	10.0	10.2	9.3	12.6	9.3	Day 5 28.99
180/ZnO	51.9861	3.9	21.1	3.2	10.6	10.0	10.3	7.7	9.5	7.6	Day 10 26.12

**Table 7.** The data obtained from Model 5 and the squares of the experimental data and the rate constants and the oil formation percentages at different UV light powers

UV Power (W)	$\sum_i (y_{m_i} - y_{e_i})^2$	Rate constant (h <sup>-1</sup> ) x 10 <sup>3</sup>									oil conversion % experimental
		k <sub>1</sub>	k <sub>2</sub>	k <sub>3</sub>	k <sub>4</sub>	k <sub>5</sub>	k <sub>6</sub>	k <sub>7</sub>	k <sub>8</sub>	k <sub>9</sub>	
0	8.3925	10.0	10.7	2.5	10.1	10.1	9.8	4.6	11.1	9.8	Day 10 5.04
60	65.2008	5.0	10.8	2.1	10.0	10.1	9.7	12.4	12.0	10.1	Day 2 15.98
120	61.8398	4.8	10.9	3.7	10.3	10.2	9.0	17.0	10.8	8.9	Day 10 20.91
180	75.5094	5.4	10.7	4.9	10.5	10.4	8.0	21.5	9.4	7.8	Day 10 27.53
180/TiO <sub>2</sub>	112.6105	4.7	10.9	4.1	10.3	10.2	8.9	18.9	11.0	8.7	Day 10 24.17
180/ZnCl <sub>2</sub>	137.4365	3.9	10.9	2.6	10.3	10.2	9.3	17.1	12.6	9.4	Day 5 28.99
180/ZnO	51.9647	4.2	10.7	3.3	10.5	10.3	7.7	20.9	9.5	7.6	Day 10 26.12

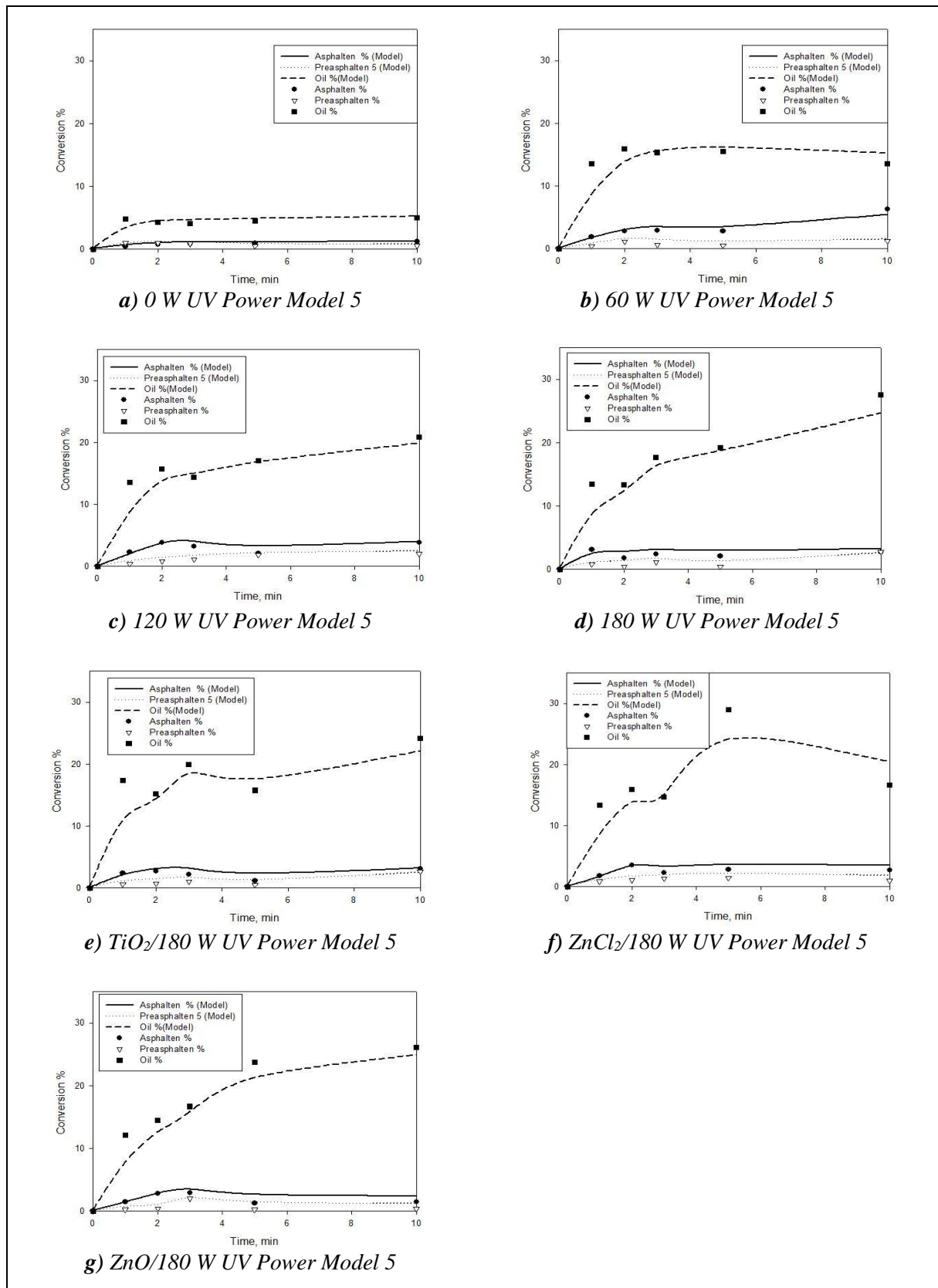


**Figure 6.** Comparison of the liquefaction mechanism obtained using Model 5 with experimental data at different UV powers  
 a) 0 W, b) 60 W, c) 120 W, d) 180 W e) TiO<sub>2</sub>/180 W f) ZnCl<sub>2</sub>/180 W g) ZnO/180 W



The reaction rate from reactive charcoal to oils is four times more compared to other reaction rate constants shown in 3rd Model. The reaction rate constant for the liquefaction reaction from reactive coal to oils is about  $10.0 \times 10^{-3} \text{ h}^{-1}$ , while the reaction rate constants for the other reactions in the model are about  $2.5.0 \times 10^{-3} \text{ h}^{-1}$ . Additionally, UV forces affect the reaction rate constants of Beypazarı coal liquefaction reaction are insignificantly. Model 4 and Model 5 liquefaction mechanism rate constants are very close to each other. Simultaneously, the square of the difference between the experimental data and the data obtained from the model, in other words, the compatibility of the experimental data with the experimental data is very close to each other and the data obtained from Model 3. When these results are evaluated together, it has been shown that models with reversible reactions are quite successful in explaining the liquefaction mechanism of Beypazarı coals. Therefore, Model 3, Model 4 and Model 5 include model mechanisms suitable for Beypazarı liquefaction process.

The general liquefaction steps of a reactive coal consist of four steps;

- (i) bond cleavage between structural species and then
- (ii) stabilization of free radicals by breaking bonds by hydrogen transfer, and then either
- (iii) formation of liquefied molecules of smaller molecular weight or
- (iv) repolymerization of free radicals due to hydrogen deficiency. The formation of high molecular weight of poly-aromatic species similar to Char can cause depolymerization.

The increase in oil yield during the liquefaction process can be attributed to the stabilization of free radicals by hydrogen transfer from hydrogen-rich hydrocarbons instead of hydrogen donor solvent (Şimşek et al., 2017). The presence of reversible reactions in the liquefaction model prove that the hydrogen donor solvent can not be able to transfer sufficient hydrogen to free radicals (Şimşek et al., 2020) This study shows that reversible reaction steps are the decisive steps in the liquefaction of Beypazarı lignite under UV power. Additionally, reversible models show the best agreement with experimental data regardless of reaction steps, coal types, and power sources such as UV (Şimşek et al., 2017; 2019). However, with the use of catalyst in the experimental data, an increase in the yield of the liquid product stands out. In particular, the use of  $\text{ZnCl}_2$  led to a more effective yield in a shorter time. However, the data obtained from the experimental data and the model show the compatibility of the most compatible model with the use of catalyst and the studies conducted without UV power. In other words, in the experimental and modeling studies conducted with 0 Watt UV power in a catalyst-free environment, the harmony gives the best results between Model 3-4 and Model 5.

Experimental data show that oil yields increase with increasing UV use. The modeling work performed in Model 4, which includes reversible reactions in parallel with the experimental studies, draw attention as the model most compatible with the experimental data. It was also found that the liquefaction step from coal to oils had the highest reaction rate constant compared to the reactions given in other models proposed in Model-4. Also, the reaction rate constants are independent of the liquefaction power in the liquefaction process using UV as the liquefaction power source. Apart from this study, another study on the liquefaction of Beypazarı coals under UV power is the study of Şimşek et al. (2019). They showed that reversible steps play a major role in the liquefaction mechanism in his study. Additionally, the aforementioned study also showed that the Kalman filter is one of the useful methods to estimate the model parameter for liquefaction of coals using minimal experimental results (Şimşek, 1997). Şimşek et al. (2020) did not suggest any mechanism in the catalyst environment for Beypazarı coal based on experimental data with modeling of the mechanism. In this publication, in addition to the work of Şimşek (1997), it is focused on the liquefaction mechanism modeling of the experimental studies conducted in the catalyst environment. The efficiency of  $\text{TiO}_2$ ,  $\text{ZnCl}_2$ , and  $\text{ZnO}$  catalysts under 180 Watt UV power, where the experimental data gave the best results, was examined both experimentally and model. While the experimental data revealed that the oil yields were much higher in the environments with  $\text{ZnO}$  catalysts, it was concluded that Model 4 gave the appropriate values in the presence of  $\text{ZnO}$  catalyst in the modeling studies.

Additionally, when the elemental analysis of the coal used in the experiments is considered, especially in terms of O content, it is striking that the sample is a very young lignite. Also, Both ash and maceral content of the coal used in the experiments show a diluting effect during the liquefaction process. Maceral density increases in the order of liptinite <vitrinite <inertinite. Due to the different vegetative tissues that make up the macerals, the molecular structures of the macerals are also different. The different properties and behavior of the macerals are the result of their different molecular structures. In the amount of combustible volatile matter and easily volatile fixed carbon, approximately 40% of the mass, carbon has the feature of formation change due to bond breaking easily according to the structural features. Due to the mentioned structural feature, the potential of obtaining liquid products is high thanks to the hydrogenation provided by tetralin in liquefaction for the sample of Beypazarı lignite.

#### 4. CONCLUSION

Model 2, Model 3, Model 4 and Model 5, where parallel reactions form products, is more compatible with the experimental results of liquefaction using 5/1 tetralin/coal ratio from reactive charcoal than Model 1, which includes serial reactions. Although the experimental oil yields are low in the experimental studies based on the use of UV, when the modeling studies are compared with the experimental data, the most compatible data is seen to be quite compatible in the experiments conducted in the dark, especially in Model 4, without using the UV power. Notably, the conversion rate constants from asphaltene to oil, from asphaltene to preasphalten, and from preasphalten to oil in Model 4 in the dark environment are higher than the other formations. Model 3, Model 4 and Model 5 consist of reversible reaction steps in addition to parallel liquefaction steps. Here, it makes the liquefaction kinetics of Beypazarı coal much better understood. In the experiments conducted with the catalyst, 180 Watt UV power, which is the UV power with the highest efficiency, was used. However, there is not much difference in terms of oil yield between the use of catalyst and the studies conducted in a catalyst-free environment, and the closeness of the experimental data with the data obtained from the model was found to be more compatible with Model 4.

Although the applicability of UV power for coal liquefaction in mass production is very difficult due to the long reaction time, it is thought that this study can be a guide for the design of UV Lamp Photochemical Reactor in the presence of catalysts of pilot scale liquefaction processes. Additionally, this work can lead to the formation of higher quality (low molecular weight) liquid products in thermal coal liquefaction process supported by UV irradiation energy. Additionally, in future studies, it will be more meaningful to explain the reaction rate steps more clearly and to establish mechanisms that can interfere with the reaction in terms of the efficiency of the coal liquefaction process.

#### CONFLICTS OF INTEREST

The authors declare no conflict of interest.

#### REFERENCES

- Allen, D. T., & Gavalas, G. R. (1984). Reactions of methylen and ether bridges. *Fuel*, 63(5), 586-592. doi:[10.1016/0016-2361\(84\)90150-9](https://doi.org/10.1016/0016-2361(84)90150-9)
- Angelova, G., Kamenski, D., & Dimova, N. (1989). Kinetics of donor-solvent liquefaction of Bulgarian brown coal. *Fuel*, 68(11), 1434-1438. doi:[10.1016/0016-2361\(89\)90042-2](https://doi.org/10.1016/0016-2361(89)90042-2)
- Ayappa, K. G., Davis, H. T., Davis, E. A., & Gordon, J. (1991). Analysis of microwave heating of materials with temperature-dependent properties. *AIChE J*, 37(3), 313-322. doi:[10.1002/aic.690370302](https://doi.org/10.1002/aic.690370302)
- Ceylan, K., & Olcay, A. (1998). Kinetic rate models for dissolution of Turkish lignites in tetralin under nitrogen or hydrogen atmospheres. *Fuel Processing Technology*, 53(3), 183-195. doi:[10.1016/S0378-3820\(97\)00054-4](https://doi.org/10.1016/S0378-3820(97)00054-4)
- Cronauer, D. C., Shah, Y. T., & Ruberto, R. G. (1978). Kinetics of thermal liquefaction of Belle Ayr subbituminous coal. *Industrial & Engineering Chemistry Process Design and Development*, 17(3), 281-288. doi:[10.1021/i260067a013](https://doi.org/10.1021/i260067a013)

- Cronauer, D. C., Jewell, D. M., Shah, Y. T., & Modi, R. J. (1979). Mechanism and kinetics of selected hydrogen transfer reactions typical of coal liquefaction. *Industrial & Engineering Chemistry Fundamentals*, 18(2), 153-162. doi:[10.1021/i160070a011](https://doi.org/10.1021/i160070a011)
- Cunliffe, B. (Ed.). (2001). *The Oxford illustrated history of prehistoric Europe*. Oxford Illustrated History.
- Doetschman, D. C., Ito, E., Ito, O., & Kameyama, H. (1992). Photochemical extraction from tetrahydrofuran slurries of representative coals. *Energy & Fuels*, 6(5), 635-42. doi:[10.1021/ef00035a015](https://doi.org/10.1021/ef00035a015)
- Farcasiu, M., Mitchell, T. O., & Whitehurst, D. D. (1977). Asphaltols - Keys to Coal Liquefaction. *Chemtech*, 7, 680-686.
- Gao, D., Ye, C., Ren, X., & Zhang, Y. (2018). Life cycle analysis of direct and indirect coal liquefaction for vehicle power in China. *Fuel Processing Technology*, 169, 42-49. doi:[10.1016/j.fuproc.2017.09.007](https://doi.org/10.1016/j.fuproc.2017.09.007)
- Grewal, M. S., & Andrews, A. P. (2001). *Kalman Filtering: Theory and Practice Using MATLAB* (2nd ed.). John Wiley & Sons.
- Han, K. W., Dixit, V. B., & Wen, C. Y. (1978). Analysis and scale-up consideration of bituminous coal liquefaction rate processes. *Industrial & Engineering Chemistry Process Design and Development*, 17(1), 16-21. doi:[10.1021/i260065a004](https://doi.org/10.1021/i260065a004)
- Hao, P., Bai, Z.-Q., Zhao, Z.-T., Yan, J.-C., Li, X. Guo, Z.-X., Xu, J.-L., Bai, J., & Li, W. (2017). Study on the preheating stage of low rank coals liquefaction: product distribution, chemical structural change of coal and hydrogen transfer. *Fuel Processing Technology*, 159, 153-159. doi:[10.1016/j.fuproc.2017.01.028](https://doi.org/10.1016/j.fuproc.2017.01.028)
- Hao, P., Bai, Z.-Q., Zhao, Z.-T., Ge, Z.-F., Hou, R.-R., Bai, J., Guo, Z.-X., Kong, L.-X., & Li, W. (2018). Role of hydrogen donor and non-donor binary solvents in product distribution and hydrogen consumption during direct coal liquefaction. *Fuel Processing Technology*, 173, 75-80. doi:[10.1016/j.fuproc.2018.01.012](https://doi.org/10.1016/j.fuproc.2018.01.012)
- Hsiang-Hui, K., & Stock, L. M. (1984). Aspects of the chemistry of donor solvent coal dissolution: Promotion of the bond cleavage reactions of diphenylalkanes and the related ethers and amines. *Fuel*, 63(6), 810-815. doi:[10.1016/0016-2361\(84\)90072-3](https://doi.org/10.1016/0016-2361(84)90072-3)
- Huang, H., Wang, K., Wang, S., Klein, M. T., & Calkins, W. H. (1998). Studies of coal liquefaction at very short reaction times. 2. *Energy & Fuels*, 12(1), 95-101. doi:[10.1021/ef970073c](https://doi.org/10.1021/ef970073c)
- Kalman, R. E. (1960). A new approach to linear filtering and prediction problems. *J. Basic Eng.*, 82(1), 35-45. doi:[10.1115/1.3662552](https://doi.org/10.1115/1.3662552)
- Karacan, F. (2004). *Ultraviyole Işınlarnın Katalizörlü Ortamda Kömür Sıvılaştırmasına Etkisi*. PhD Thesis, Ankara University.
- Kavuştu, H. (2012). *Kömürlerin Tetralinde UV Işınları ve Mikrodalga Enerji ile Sıvılaştırma Mekanizmalarının Kesikli Zaman Modelleri Kullanılarak Belirlenmesi*. MSc Thesis, Ankara University.
- Li, X., Hu, H., Zhu, S., Hu, S., Wu, B., & Meng, M. (2008). Kinetics of coal liquefaction during heating up and isothermal stages. *Fuel*, 87(4-5), 508-513. doi:[10.1016/j.fuel.2007.03.041](https://doi.org/10.1016/j.fuel.2007.03.041)
- Li, W., Bai, Z.-Q., Bai, J., & Li, X. (2017). Transformation and roles of inherent mineral matter in direct coal liquefaction: a mini-review. *Fuel*, 197, 209-216. doi:[10.1016/j.fuel.2017.02.024](https://doi.org/10.1016/j.fuel.2017.02.024)
- Liebenberg, B. J., & Potgieter, H. G. J. (1973). The uncatalysed hydrogenation of coal. *Fuel*, 52(2), 130-133. doi:[10.1016/0016-2361\(73\)90036-7](https://doi.org/10.1016/0016-2361(73)90036-7)
- Liu, R., Li, Y., Wang, C., Xiao, N., He, L., Guo, H., Wan, P., Zhou, Y., & Qiu, J. (2018). Enhanced electrochemical performances of coal liquefaction residue derived hard carbon coated by graphene as anode materials for sodium-ion batteries. *Fuel Processing Technology*, 178, 35-40. doi:[10.1016/j.fuproc.2018.04.033](https://doi.org/10.1016/j.fuproc.2018.04.033)
- Mohan, G., & Silla, H. (1981). Kinetics of donor-solvent liquefaction of bituminous coals in nonisothermal experiments. *Industrial & Engineering Chemistry Process Design and Development*, 20(2), 349-358. doi:[10.1021/i200013a026](https://doi.org/10.1021/i200013a026)

- Shah, Y. T., Cronauer, D. C., McIlvried, H. G., & Paraskos, J. A. (1978). Kinetics of catalytic liquefaction of Big Horn coal in a segmented bed reactor. *Industrial & Engineering Chemistry Process Design and Development*, 17(3), 288-301. doi:[10.1021/i260067a014](https://doi.org/10.1021/i260067a014)
- Shalabi, M. A., Baldwin, R. M., Bain, R. L., Gary, J. H., & Golden, J. O. (1978). Kinetics of coal liquefaction. *Coal Processing Technology*, 4, 82-86.
- Shalabi, M. A., Baldwin, R. M., Bain, R. L., Gary, J. H., & Golden, J. O. (1979). Noncatalytic coal liquefaction in a donor solvent. Rate of formation of oil, asphaltenes, and preasphaltenes. *Industrial & Engineering Chemistry Process Design and Development*, 18(3), 474-479. doi:[10.1021/i260071a021](https://doi.org/10.1021/i260071a021)
- Shui, H., Chen, Z., Wang, Z., & Zhang, D. (2010). Kinetics of Shenhua coal liquefaction catalyzed by  $\text{SO}_4^{2-}/\text{ZrO}_2$  solid acid. *Fuel*, 89(1), 67-72. doi:[10.1016/j.fuel.2009.02.019](https://doi.org/10.1016/j.fuel.2009.02.019)
- Snape, C. E. (1987). Characterisation of organic coal structure for liquefaction. *Fuel Processing Technology*, 15, 257-279. doi:[10.1016/0378-3820\(87\)90050-6](https://doi.org/10.1016/0378-3820(87)90050-6)
- Söğüt, F. (1997). *UV ışınları ile linyitlerin desülfürizasyonu*. PhD Thesis, Ankara University.
- Söğüt, F., & Olcay, A. (1998). Dissolution of lignites in tetralin at ambient temperature: effects of ultraviolet irradiation. *Fuel Processing Technology*, 55(2), 107-115. doi:[10.1016/S0378-3820\(98\)00045-9](https://doi.org/10.1016/S0378-3820(98)00045-9)
- Speight, J. G. (2008). *Synthetic fuels handbook: properties, process and performance*. The McGraw-Hill Companies, Inc.
- Şimşek, E. H. (1997). *Türk kömürlerinin mikrodalga enerji etkisiyle tetralindeki hidrojenasyonu*. PhD Thesis, Ankara University.
- Şimşek, E. H., Karaduman, A., & Olcay, A. (2001). Investigation of dissolution mechanism of six Turkish coals in tetralin with microwave energy. *Fuel*, 80(15), 2181-2188. doi:[10.1016/S0016-2361\(01\)00102-8](https://doi.org/10.1016/S0016-2361(01)00102-8)
- Şimşek, E. H., Güleç, F., & Kavuştu, H. (2017). Application of Kalman filter to determination of coal liquefaction mechanisms using discrete time models. *Fuel*, 207, 814-820. doi:[10.1016/j.fuel.2017.06.004](https://doi.org/10.1016/j.fuel.2017.06.004)
- Şimşek, E. H., Güleç, F., Kavuştu, H., & Karaduman, A. (2019). Determination of liquefaction mechanisms of Zonguldak, Soma and Beypazarı coals using discrete time models. *Journal of the Faculty of Engineering and Architecture of Gazi University*, 34(1), 79-88. doi:[10.17341/gazimmfd.416464](https://doi.org/10.17341/gazimmfd.416464)
- Şimşek, E. H., Güleç, F., & Akçadağ, F. S. (2020). Understanding the liquefaction mechanism of Beypazarı lignite in tetralin with ultraviolet irradiation using discrete time models. *Fuel Processing Technology*, 198, 106227. doi:[10.1016/j.fuproc.2019.106227](https://doi.org/10.1016/j.fuproc.2019.106227)
- Wang, Z., Shui, H., Zhu, Y., & Gao, J. (2009). Catalysis of  $\text{SO}_4^{2-}/\text{ZrO}_2$  solid acid for the liquefaction of coal. *Fuel* 88, 885-889. doi:[10.1016/j.fuel.2008.10.040](https://doi.org/10.1016/j.fuel.2008.10.040)
- Wei, L., Jian, Z., Chunzhi, W., & Hui, X. (2013). Kalman filter Localization algorithm based on SDS-TWR ranging. *TELKOMNIKA Indonesian Journal of Electrical Engineering*, 11(3), 1436-48. doi:[10.11591/telkonnika.v11i3.2225](https://doi.org/10.11591/telkonnika.v11i3.2225)
- Welch, G., & Bishop, G. (2006). *An introduction to the Kalman filter* (Technical Report: TR 95-041). University of North Carolina at Chapel Hill.
- Yürüm, Y., & Yiğinsu, I. (1982). Depolymerization of Turkish lignites: 3. Effect of ultraviolet radiation. *Fuel*, 61(11), 1138-1140. doi:[10.1016/0016-2361\(82\)90200-9](https://doi.org/10.1016/0016-2361(82)90200-9)



Gazi University

**Journal of Science**

PART A: ENGINEERING AND INNOVATION

<http://dergipark.org.tr/gujsa>

## Evaluation of Surface Dose for Intensity Modulated Radiotherapy of Head and Neck Cancer Using Thermoluminescent Dosimeters

Osman Vefa GUL<sup>1\*</sup> , Nihal BUYUKCIZMECI<sup>2</sup> , Hamit BASARAN<sup>1</sup> <sup>1</sup>Selcuk University, Faculty of Medicine, Department of Radiation Oncology, Konya, Turkey<sup>2</sup>Selcuk University, Faculty of Science, Department of Physics, Konya, Turkey

Keywords	Abstract
Thermoluminescent Dosimeter	Accurate estimation of the surface dose in radiotherapy of patients with head and neck cancer is very important in terms of treatment. The aim of this study is to evaluate the surface dose for intensity-modulated radiotherapy (IMRT) of head and neck cancer using thermoluminescent dosimeters (TLDs). In addition, it is aimed to examine the surface dose estimates of the treatment planning system (TPS) for different grid sizes. Before the computed tomography (CT) images were taken for 15 head and neck cancer patients, 5 different points determined in the neck region were marked in a way that would not cause artifacts. IMRT plans are created for 1.5 and 2.5 mm grid sizes. Surface doses were obtained for TPS calculations and TLD measurements at 5 different points in the neck region. Surface doses obtained from TLD measurements and TPS calculations with different grid sizes were compared. All patients received 3-stage adaptive radiotherapy (ART) and the surface dose comparison was repeated for each plan. According to plan 0, the height of TLD measurements for the 1.5 and 2.5 mm grid size were 4.06% and 7.87%, respectively. In Plan 1, the difference between TPS and TLD doses was 4.00% and 8.15% for grid size 1.5mm and 2.5mm, respectively (p=0.00 and p=0.00). For dose measurements from Plan 2, the difference between TPS and TLD doses was 4.07% and 9.96% for grid size 1.5mm and 2.5mm, respectively (p=0.00 and p=0.00). Surface doses obtained in TLD measurements for all treatment plans were higher than in TPS dose calculations. Accurate estimation of the surface dose in head and neck cancer radiotherapy is very important for treatment. Surface doses calculated with TPS are usually lower than the prescribed dose. Therefore, during the evaluation of radiotherapy plans, it should be considered that TPS underestimates the surface dose. This ratio can be determined by dosimetric measurements. Thermoluminescent dosimeters are suitable equipment for this process.
Head and Neck Cancer	
Surface Dose	
Dosimetry	
Radiotherapy	

### Cite

Gul, O. V., Buyukcizmeci, N., & Basaran, H. (2022). Evaluation of Surface Dose for Intensity Modulated Radiotherapy of Head and Neck Cancer Using Thermoluminescent Dosimeters. *GU J Sci, Part A, 9(2)*, 156-163.

### Author ID (ORCID Number)

O. V. Gul, 0000-0002-6773-3132  
N. Buyukcizmeci, 0000-0002-6030-9574  
H. Basaran, 0000-0002-2122-8720

### Article Process

<b>Submission Date</b>	26.04.2022
<b>Revision Date</b>	08.05.2022
<b>Accepted Date</b>	26.06.2022
<b>Published Date</b>	27.06.2022

## 1. INTRODUCTION

The existence of developments in technology from the past to the present has led to great advances in the field of medicine. These technological developments have been an important reform in the treatment of cancer with radiation. With the technological developments, the treatment techniques used in radiotherapy have also developed. As a result of these developments, the intensity-modulated radiotherapy (IMRT) technique is widely used today. The desired dose distribution with the IMRT technique is defined in the treatment planning system (TPS) (McLaughlin et al., 2017; Wang et al., 2022). Radiotherapy planning in head and neck cancers is a very complex procedure due to the complex anatomical structure and the presence of many sensitive tissues adjacent to the target volume (Lo Nigro et al., 2017). Accurately knowing the surface dose in IMRT is important for estimating side effects during the evaluation of the treatment plan. Acute skin reactions can be prevented by accurately knowing the surface dose (Lee et al., 2012). During radiotherapy, skin reactions occur depending on the dose rate, technique used, surface dose and total dose (Wei et al., 2019). Radiation is absorbed

\*Corresponding Author, e-mail: [vefagul@selcuk.edu.tr](mailto:vefagul@selcuk.edu.tr)

in all tissues it comes into contact with. Therefore, accurate calculation of these tissue doses by TPS is very important. Grid size affects especially surface dose calculations of complex treatments such as IMRT. However, the calculation grid size is usually left at a default value to minimize the time it takes for the TPS to perform dose calculations. Although TPSs calculate very similar dose distributions to actual doses in critical organs and tumor volume, they fail at surface doses. However, skin dose toxicity has a major impact on a patient's ability to tolerate treatment well (Sarkar et al., 2020). Since the radiation dose given by the IMRT technique is not homogeneous, it is difficult to calculate the surface dose accurately by TPS (Tai et al., 2019). Therefore, actual surface doses should be verified by more reliable methods. For this purpose, in vivo measurement for accurate surface doses may be a solution. In vivo measurement methods are used in the evaluation of radiation in the body. Knowing the correct surface dose will help in estimating the skin reactions that may occur during the treatment process. Thermoluminescent dosimeters (TLD) are widely used today to accurately measure surface doses. The effective atomic number of TLDs is very close to that of human tissue. Therefore, it is widely used in surface entrance dose measurements in radiotherapy (Moghaddam et al., 2013).

The aim of this study is to evaluate the surface dose for intensity modulated radiotherapy of head and neck cancer using thermoluminescent dosimeters. In addition, it is aimed to examine the surface dose estimates of the treatment planning system for different grid sizes.

## 2. MATERIAL AND METHOD

### Patient selection and Contouring

15 patients with head and neck cancer were included in this study and permission was obtained from the ethics committee of Selcuk University Faculty of Medicine with the decision numbered 2022/182. Since skin toxicity is generally seen around the neck of the patient in head and neck cancer patients, patients whose both necks were irradiated were selected. Other information about the patients is given in Table 1.

*Table 1. Patient characteristics*

Characteristics	Patients, n (%)
Sex	
Male	13 (86.7)
Female	2 (13.3)
Age, years	
Range	33-78
Median	57
KPS score	
100	2 (13.3)
90	7 (46.7)
80	6 (40.0)
BMI	
Range	21.1-38.8
Median	27
AJCC stage grouping	
I	1 (6.7)
II	5 (33.3)
III	8 (53.3)
IVA	1 (6.7)

*KPS; Karnofsky Performance Score, BMI; Body Mass Index*

Before the Computed tomography (CT) image of each patient was taken, 5 different points determined in the neck region were marked so as not to cause artifacts. CT scan of all patients was obtained with a slice thickness of 3 mm. All CT images were acquired with the Toshiba Aquilion S4 device. Plan0 was generated from initial CT images. Adaptive radiotherapy (ART) technique is the method that minimizes the dosimetric differences that may occur between the planned and applied treatment, taking into account the changes in the field where

the radiotherapy is applied. During the treatment, CT was taken for control purposes. The target volume and critical organs were recontoured on the control CT. The patient's plan was made over the new CT. Plan1 was generated from the control CT obtained in the 14th fraction and Plan2 was generated from the control CT obtained in fraction 24. When the volume and doses were compared and a significant difference was found, the patient continued his treatment with the new adaptive plan. ART was applied to all 15 patients included in the study. Target volume and critical organs for all patients are contoured by a single radiation oncologist.

### **Treatment planning and analysis**

Treatment plans were calculated with the AAA algorithm in the Eclipse 15.1 planning system. All plans were made in IMRT technique using 6 MV energy. For all treatment plans, 98% of target volumes were considered to cover 100% of the defined dose. Each IMRT plan was coplanar and had gantry angles of 0°, 52°, 104°, 156°, 204°, 256°, and 308°. A dose rate of 300 MU/min was used for all IMRT plans. 70 Gy in 33 fractions was planned for the primary target volume. Due to weight loss and decreased tumor volume in the patients included in the study, two adaptive radiotherapy was applied for each patient, except for the initial plan. IMRT plans with grid sizes of 1.5 and 2.5 mm were created using the AAA algorithm for each patient included in the study. TPS dose calculation results were obtained from 5 different points determined during CT for each IMRT plan. All patients received 3-phase adaptive radiotherapy due to weight loss and reduction of tumor volume. All patients received 3-stage ART. Accordingly, Plan0, plan1 and plan2 were applied between 0-14, 15-24 and 25-33 fractions, respectively.

### **In vivo surface dose measurements**

TLDs are among the most preferred in vivo dosimeters for measuring dose exposure in radiotherapy due to their small size and high sensitivity. TLDs used in this study were lithium fluoride (LiF:Mg,Ti ( TLD - 100 )) doped with magnesium (Mg) and titanium (Ti). The effective atomic number of these dosimeters is 8.2 and are considered tissue equivalent dosimeters ([Olaciregui-Ruiz et al., 2020](#)). Surface dose measurements were made on the Varian DHX device in the Radiation Oncology Clinic of Selcuk University Medical Faculty Hospital. Necessary dosimetric measurements were made before the treatment. The difference between the measurements obtained and the acceptance tests of the linear accelerator was found to be within 1%. Each TLD was irradiated to receive 1Gy in a 10 cm x 10 cm field at SSD=100 cm and 1.5 cm from the surface. TLD-100 chips were calibrated and TLDs with dose reproducibility within  $\pm 1\%$  were used for dose measurements. Annealing conditions of TLDs used in dose measurement; It was 1 hour at 100 °C and 2 hours at 100 °C. The Harshaw 3500 TLD reader, TLD furnace and aluminum tray separated by special partitions are shown in Figure 1, Figure 2 and Figure 3, respectively. TLDs were placed at 5 different marked points in the neck region in the 1st fraction for in vivo dose measurement. 5 different TLD locations on the patient's neck for TPS calculation and in vivo dose measurement are shown in the Figure 4. Three TLDs were placed in each region to minimize the deviation in the measured dose value. The dose value was calculated by averaging the dose value obtained from the three TLDs. TLDs were placed on the patient's skin before the treatment and removed at the end of the treatment. Afterwards, the TLDs were read and the surface dose was calculated. These dose measurements were repeated for each patient as adaptive radiotherapy was administered.

### **Statistical analysis**

For statistical analysis and calculations in the study, Paired Sample t-test was used in the Statistical Package for Social Sciences (SPSS 25.1) program. In statistical decisions,  $p < 0.01$  was accepted as an indicator of significant difference.



Figure 1. Harshaw 3500 TLD reader



Figure 2. TLD furnace

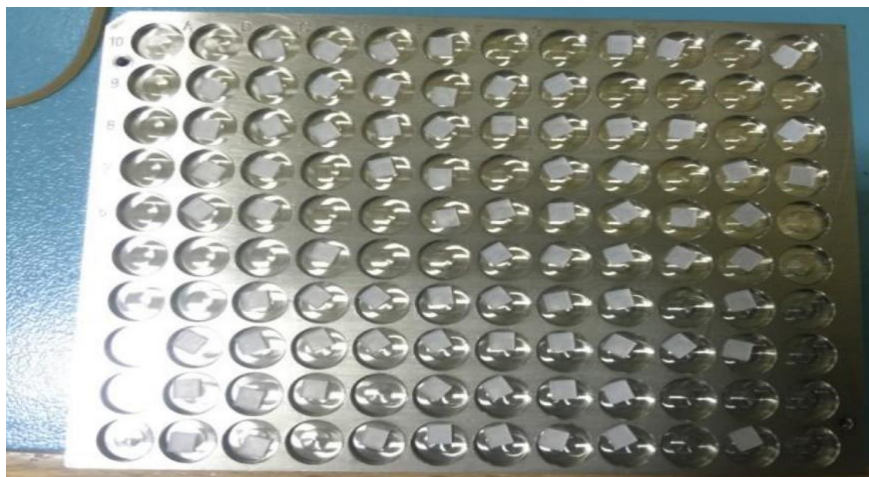
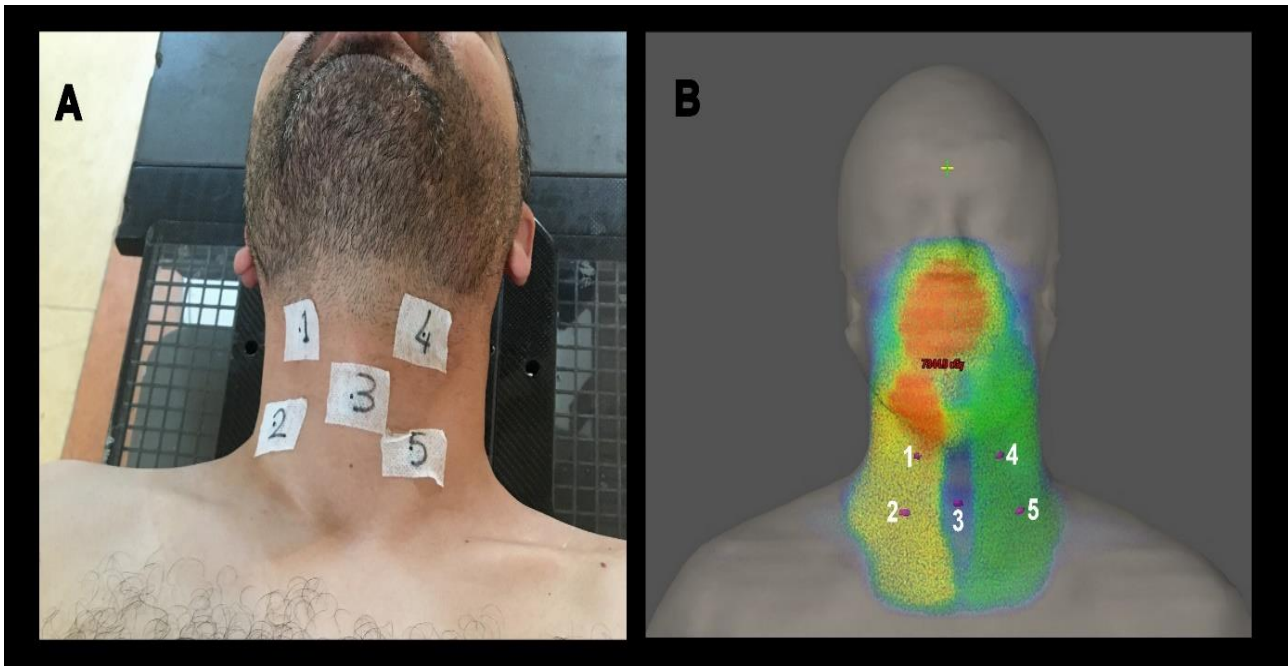


Figure 3. Aluminum tray





**Figure 4.** 5 different TLD locations on the patient's neck for TPS calculation and in vivo dose measurement,  
 A) Placement of TLDs at 5 different points on the neck before treatment,  
 B) Dose distribution for 5 different points determined in TPS calculation

### 3. RESULTS AND DISCUSSION

5 different TLD placement plans on the neck of each patient are shown in Figure 1. The results of Eclipse TPS calculations for surface dose at different grid sizes in the IMRT technique and TLD measurements are shown in Table 2. Surface doses obtained in TLD measurements for all treatment plans were higher than in TPS dose calculations. The mean surface dose calculated for grid size 1.5 mm and 2.5 mm for Plan 0 was 160.94 cGy and 155.25 cGy, respectively. However, the mean surface dose with TLD was measured as 167.48 cGy. Accordingly, the height of TLD measurements was 4.06% and 7.87% for grid size 1.5 mm and 2.5 mm, respectively. The average surface dose calculated for the grid size 1.5 mm and 2.5 mm for Plan 1 was 162.91 and 156.97, respectively. The mean surface dose of the same plan with TLD was measured as 169.77 cGy. Accordingly, the difference for grid size 1.5mm and 2.5mm was 4.00% and 8.15%, respectively ( $p=0.00$  and  $p=0.00$ ). For the mean of Plan 2 administered to patients in the 25 and 33 fraction range, the mean surface dose with TLD was measured as 170.47 cGy. For the grid size of this IMRT plan 1.5 mm and 2.5 mm, the difference was 4.07% and 7.96%, respectively ( $p=0.00$  and  $p=0.00$ ). The highest difference between TLD measurements and TPS calculations for 5 different points marked in the neck region was the 3rd point. The difference between TLD measurements and TPS calculations in this region was 8.28% and 13.61% for grid size 1.5 mm and 2.5 mm, respectively. The comparison of TPS calculations for surface dose and statistical significance for TLD measurements in the IMRT technique is shown in Table 3.

Radiation therapy for head and neck cancer is generally at a daily dose of 200-250 cGy and a total of 6000-7000 cGy with 30-33 treatment sessions over 6 weeks. Due to various factors, patients with head and neck cancer may undergo significant anatomical changes during radiation therapy. The reasons for these changes may be due to many factors. These factors are; reduction in tumor and nodal volumes, weight loss, changes in muscle mass and fat distribution. It is of great importance to apply the determined dose correctly in order to increase regional control and reduce complications in the patient during irradiation treatment of head and neck cancers. Surface dose measurement in the head and neck region is difficult. Accurate knowledge of the surface dose in the neck region helps clinical decisions. Accurate estimation of neck surface dose is important to minimize acute skin reactions and toxicities. In the study, the mean daily dose calculated by TPS at 135 different points for a 1.5 mm grid size was 162.55 cGy, and the mean dose measured by TLD was 169.24. In addition, the mean difference between TPS calculations and TLD measurements was 4.11%. For all points on the skin surface, the doses measured by TLDs were higher than the doses calculated by TPS.

**Table 2.** Results of TPS calculations and TLD measurements for surface doses

Plans	Location	TLD Mean±SD (cGy)	TPS Mean ± SD (cGy)			
			Grid size (1.5mm)	Deviation (%)	Grid size (2.5mm)	Deviation (%)
0	1	175.15±15.88	168.02±17.16	-4.07	161.33±18.38	-7.89
0	2	175.54±13.54	169.02±11.02	-3.71	164.74±11.67	-6.15
0	3	163.27±26.91	149.78±29.66	-8.26	141.97±29.53	-13.04
0	4	162.45±17.63	160.29±13.07	-1,32	153.59±12.89	-5.45
0	5	160.99±14.65	157.59±14.83	-2.11	154.65±16.06	-3.93
1	1	175.60±14.81	170.05±12.73	-3.16	165.42±12.38	-5.79
1	2	175.96±14.54	170.79±12.60	-2.93	165.43±10.33	-5.98
1	3	165.93±24.91	152.19±27.42	-8.28	143.34±29.06	-13.61
1	4	167.80±12.58	161.86±12.47	-3.53	155.46±14.58	-7.35
1	5	163.55±15.24	159.65±13.90	-2.38	155.22±14.81	-5.09
2	1	176.93±15.85	171.91±14.64	-2.83	166.64±15.21	-5.81
2	2	178.15±15.49	171.53±15.50	-3.71	166.05±13.52	-6.79
2	3	163.71±24.09	151.43±24.27	-7.50	141.44±26.77	-13,6
2	4	168.04±14.84	162.69 ±15.09	-3.18	158.97±15.35	-5.39
2	5	165.55±15.45	161.38±14.75	-2.51	156.40±15.09	-5.52

**Table 3.** Comparison of statistical significance of surface doses for TPS calculations and TLD measurements

Location	TLD vs TPS(Grid size;1,5mm)			TLD vs TPS(Grid size;2,5mm)		
	Plan 0	Plan 1	Plan 2	Plan 0	Plan 1	Plan 2
1	<b>0.002*</b>	<b>0.000*</b>	<b>0.000*</b>	<b>0.000*</b>	<b>0.000*</b>	<b>0.000*</b>
2	<b>0.000*</b>	<b>0.001*</b>	<b>0.000*</b>	<b>0.000*</b>	<b>0.000*</b>	<b>0.000*</b>
3	<b>0.000*</b>	<b>0.000*</b>	<b>0.000*</b>	<b>0.000*</b>	<b>0.000*</b>	<b>0.000*</b>
4	0.510	<b>0.000*</b>	<b>0.000*</b>	<b>0.000*</b>	<b>0.000*</b>	<b>0.000*</b>
5	<b>0.004*</b>	<b>0.001*</b>	<b>0.000*</b>	<b>0.000*</b>	<b>0.000*</b>	<b>0.000*</b>

$p < 0.01$

Price et al. (2014) investigated the TPS skin dose for different grid sizes in the IMRT treatment of head and neck cancer. According to this study, they found 21% and 9.5% difference between TPS and TLD measurements for 5 and 3 mm grid sizes, respectively. The research of Price et al. (2014) was found in parallel with our current study. Accordingly, 8.00% and 4.11% differences were found between TPS calculations and TLD measurements for 2.5 and 1.5 mm grid sizes, respectively.

Akbas et al. (2018) investigated the surface dose accuracy of TPS on a random phantom using radiochromic film for the treatment of laryngeal cancer with IMRT technique. They found that the surface doses calculated by TPS were lower than the radiochromic film measurements. In our study, the mean difference for TPS calculations and TLD measurements for IMRT plans was 8.00%.

Akino et al. (2013) compared the surface doses measured using EBT2 film in IMRT and field-in-field (FiF) treatment techniques for different grid sizes. He reported that the AAA algorithm failed to calculate the surface dose according to in-vivo measurements. They also suggested using the smaller computational grid size to accurately visualize the TPS dose. Our current research yielded similar results to the study of Akino et al. (2013). Accordingly, with the reduction of the grid size from 2.5mm to 1.5mm, the difference between TPS calculation and TLD measurements decreased from 8.00% to 4.11%, respectively.

Gopalakrishnan et al. (2021) measured in vivo surface doses uptake by the left breast and contralateral breast (CB). They compared the measured surface doses using OSLD with TPS calculations for five different treatment techniques. They found a 6.91% difference in surface dose between the TPS calculation and OSLD measurements for the IMRT technique. In our study, it was found that the surface dose calculated by TPS was lower than TLD measurements. This difference was 4.11% and 8% for grid size 1.5 and 2.5 mm, respectively.

#### 4. CONCLUSION

Patients with head and neck cancer may undergo significant anatomical changes during radiation therapy for various reasons, and side effects for the skin are expected during the long treatment period. Therefore, accurate estimation of the dose on the skin surface of the patient is very important in terms of treatment. In our study, the surface doses calculated by Eclipse TPS are generally lower than the prescribed dose. Therefore, during the evaluation of radiotherapy plans, it should be considered that TPS underestimates the surface dose. This ratio can be determined by dosimetric measurements. It is very important to take in vivo dose measurements to minimize side effects in the treatment process. Thermoluminescent dosimeters are suitable equipments for this process. We recommend further use of in vivo dose measurements with TLD.

#### ACKNOWLEDGEMENT

This study was produced from the first author's doctoral thesis.

#### CONFLICT OF INTEREST

The authors declare no conflict of interest.

#### REFERENCES

- Akbas, U., Kesen, N. D., Koksall, C., Ozkaya, K., Altun, M., & Bilge, H. (2018). Investigation of surface dose using film dosimetry and commercial treatment planning system for larynx cancer treatment with intensity-modulated radiotherapy and volumetric modulated arc therapy. *Turkish Journal of Oncology*, 33(1), 12-17. doi:[10.5505/tjo.2018.1736](https://doi.org/10.5505/tjo.2018.1736)
- Akino, Y., Das, I. J., Bartlett, G. K., Zhang, H., Thompson, E., & Zook, J. E. (2013). Evaluation of superficial dosimetry between treatment planning system and measurement for several breast cancer treatment techniques. *Medical Physics*, 40(1), 011714. doi:[10.1118/1.4770285](https://doi.org/10.1118/1.4770285)
- Gopalakrishnan, Z., Nair, R. K., Raghukumar, P., Bhasi, S., & Menon, S. V. (2021). Comparison of skin doses of treated and contralateral breasts during whole breast radiotherapy for different treatment techniques using optically stimulated luminescent dosimeters. *Journal of Radiotherapy in Practice*, 20(2), 176-182. doi:[10.1017/S1460396920000229](https://doi.org/10.1017/S1460396920000229)
- Lee, J., Poon, I., Balogh, J., Tsao, M., & Barnes, E. (2012). A Review of Radiotherapy for Merkel Cell Carcinoma of the Head and Neck. *Journal of Skin Cancer*, 2012, 563829. doi:[10.1155/2012/563829](https://doi.org/10.1155/2012/563829)
- Lo Nigro, C., Denaro, N., Merlotti, A., & Merlano, M. (2017). Head and neck cancer: improving outcomes with a multidisciplinary approach. *Cancer Management and Research*, 9, 363-371. doi:[10.2147/CMAR.S115761](https://doi.org/10.2147/CMAR.S115761)
- McLaughlin, P. W., Liss, A. L., Nguyen, P. L., Assimos, D. G., D'Amico, A. V., Gottschalk, A. R., Gustafson, G. S., Keole, S. R., Liauw, S. L., Lloyd, S., Movsas, B., Prestidge, B. R., Showalter, T. N., Taira, A. V., Vapiwala, N., & Davis, B. J. (2017). ACR Appropriateness Criteria® Locally Advanced, High-Risk Prostate Cancer. *American Journal of Clinical Oncology*, 40(1), 1-10. doi:[10.1097/coc.0000000000000354](https://doi.org/10.1097/coc.0000000000000354)

- Moghaddam, B. G., Vahabi-Moghaddam, M., & Sadremomtaz, A. (2013). Evaluation of target dose based on water-equivalent thickness in external beam radiotherapy. *Journal of Medical Physics*, 38(1), 44-51. doi:[10.4103/0971-6203.106605](https://doi.org/10.4103/0971-6203.106605)
- Olaciregui-Ruiz, I., Beddar, S., Greer, P., Jornet, N., McCurdy, B., Paiva-Fonseca, G., Mijnheer, B., & Verhaegen, F. (2020). In vivo dosimetry in external beam photon radiotherapy: Requirements and future directions for research, development, and clinical practice. *Physics and Imaging in Radiation Oncology*, 15, 108-116. doi:[10.1016/j.phro.2020.08.003](https://doi.org/10.1016/j.phro.2020.08.003)
- Price, R. A., Jr, Koren, S., Veltchev, I., Hossain, M., Lin, M.-H., Galloway, T., Flanagan, P., Haber, J., & Ma, C.-M. (2014). Planning target volume-to-skin proximity for head-and-neck intensity modulated radiation therapy treatment planning. *Practical Radiation Oncology*, 4(1), e21-e29. doi:[10.1016/j.prro.2013.04.002](https://doi.org/10.1016/j.prro.2013.04.002)
- Sarkar, V., Paxton, A., Rassiah, P., Kokeny, K. E., Hitchcock, Y. J., & Salter, B. J. (2020). Evaluation of dose distribution differences from five algorithms implemented in three commercial treatment planning systems for lung SBRT. *Journal of Radiosurgery and SBRT*, 7(1), 57-66.
- Tai, D. T., Oanh, L. T., Son, N. D., Loan, T. T. H., & Chow, J. C. L. (2019). Dosimetric and Monte Carlo verification of jaws-only IMRT plans calculated by the Collapsed Cone Convolution algorithm for head and neck cancers. *Reports of Practical Oncology & Radiotherapy*, 24(1), 105-114. doi:[10.1016/j.rpor.2018.11.004](https://doi.org/10.1016/j.rpor.2018.11.004)
- Wang, R., Shen, J., Yan, H., Gao, X., Dong, T., Li, S., Wang, P., & Zhou, J. (2022). Dosimetric comparison between intensity-modulated radiotherapy and volumetric-modulated arc therapy in patients of left-sided breast cancer treated with modified radical mastectomy: CONSORT. *Medicine*, 101(2), e28427. doi:[10.1097/md.00000000000028427](https://doi.org/10.1097/md.00000000000028427)
- Wei, J., Meng, L., Hou, X., Qu, C., Wang, B., Xin, Y., & Jiang, X. (2019). Radiation-induced skin reactions: mechanism and treatment. *Cancer Management and Research*, 11, 167-177. doi:[10.2147/CMAR.S188655](https://doi.org/10.2147/CMAR.S188655)



Gazi University

**Journal of Science**

PART A: ENGINEERING AND INNOVATION

<http://dergipark.org.tr/gujisa>

# Theoretical Evaluation of Angle-Dependent Optical Properties of a Thin Film Solar Cell including One-Dimension Photonic Crystals

Çağlar ÇETİNKAYA<sup>1\*</sup> <sup>1</sup>Istanbul University, Faculty of Science, Physics Department, 34134, Istanbul/Türkiye

Keywords	Abstract
Photonic Crystal CdTe Solar Cell Light Management Engineering Transfer Matrix Method Angular Dependent Optical Properties	The effective use of photonic-based integrated systems, whose optical properties can be tuned through light management engineering in optoelectronic devices, constitutes the backbone of today's technology. Especially in systems such as CdTe-based solar cells with well-known and high efficiency, one-dimensional photonic crystal designs emerge as an effective way to provide an electronic or optical improvement. With this intention, in this study, the optical spectra of the MgF <sub>2</sub> /MoO <sub>3</sub> one-dimensional photonic crystal integrated into the CdTe solar cell to improve photon harvesting were investigated theoretically under both bottom and top illumination according to the incidence angle of the electromagnetic wave. The transfer matrix method was used to calculate the angle dependent optical spectra. Since the electromagnetic wave interacts directly with the photonic crystal, it has been observed that the optical properties are more dependent on the angle under the top illumination compared to the bottom one. For top illumination, up to 30°, there is no significant change in reflection in the photonic band gap, but reflection drops significantly at incidence angles greater than 30°. Also, increasing the angle indicates that the low wavelength tail of the photonic band gap shifts to shorter wavelengths and enters the visible region. In the photonic band gap, for angles greater than 45°, the probability of absorption increases significantly as more electromagnetic waves enter the structure. For the bottom illumination, there is no serious dependence on the angle of incidence. For 75°, there is an increase in reflection for all wavelengths and, therefore, a decrease in absorption.

## Cite

Cetinkaya, C. (2022). Theoretical Evaluation of Angle-Dependent Optical Properties of a Thin Film Solar Cell including One-Dimension Photonic Crystals. *GU J Sci, Part A, 9(2)*, 164-172.

## Author ID (ORCID Number)

C. Cetinkaya, 0000-0001-9372-7847

## Article Process

<b>Submission Date</b>	12.06.2022
<b>Revision Date</b>	18.06.2022
<b>Accepted Date</b>	27.06.2022
<b>Published Date</b>	28.06.2022

## 1. INTRODUCTION

Photonic crystals (PC) are structures in which structures with different dielectric constants are spatially arranged in any direction (Liu et al., 2019). These structures are a hot topic of research in the field of photonics for optical fibers, light emitting diode (LED), sensors, photovoltaic devices, lasers, discrete and integrated optical components, illumination, and quantum computing (Lova et al., 2018). The propagation of the electromagnetic wave is modified by the periodic regulation of the dielectric constant and hence the index of refraction in a PC. During the propagation of the electromagnetic wave in a particular direction, Bragg scattering occurs, and thus the propagation of the electromagnetic wave in a particular frequency or wavelength range can be prohibited by the PC (Liu et al., 2019). This gap where the electromagnetic wave is not allowed to pass is called the photonic band gap (PBG) (Yablonovitch et al., 1991; Liu et al., 2019).

PCs are classified into 1-dimensional (1D), 2-dimensional (2D), and 3-dimensional (3D) depending on the number of spatial orientations in which the periodic dielectric constant changes. 1D-PCs are structures in which the dielectric constant changes periodically in only one direction, and they consist of structures with two or more dielectric constants that are superimposed or deposited in a single direction (Liu et al., 2019). Therefore, 1D-PCs have a PBG for the propagation of photons in only one direction. By integrating PBG created with

\*Corresponding Author, e-mail: [caglarcetinkaya@istanbul.edu.tr](mailto:caglarcetinkaya@istanbul.edu.tr)

PCs into solar cell (SC), the optical properties of SC can be changed significantly. These changes can be made to increase photovoltaic performance, improve semi-transparent (ST) properties, provide selective transmittance or color modification. Especially with the integration of 1D-PCs into ST organic SC (ST-OSC), structures showing improvement in cell performance have been designed (Hu et al., 2018). Although initial studies were aimed at improving cell performance, more recently 1D-PCs have also focused on modifying the optical properties of ST-OSCs (Hu et al., 2018; Zhang et al., 2019).

The integration of PCs into structures such as CdTe-based SCs with high efficiency of 22.1% (Green et al., 2020) and whose electrical properties are well known is very important in terms of improving optical properties. CdTe-based SCs are notable for their high absorption and direct optical band gap very close to 1.45eV. The absorber layer CdTe forms a heterojunction with a thin n-type CdS. The production of CdS/CdTe-based SCs for technological applications is highly advantageous in terms of their mechanical functionality, long-term thermal and mechanical stability, high efficiency and light weight. While the CdTe absorption coefficient is quite high for the visible region, it is quite low for wavelengths of 800 nm and longer. Therefore, SC structures in which CdTe is used as the absorber layer do not absorb photons efficiently in the near-infrared region (NIR). Therefore, in order to increase the photovoltaic performance in CdTe-based SCs, it is very important to carry out light management applications that will improve re-harvesting in the NIR region and to design functionally designed photonic crystals for this purpose. It is important to examine the optical characteristics and photon absorption properties depending on the angle of incidence of the light in SC structures with photonic crystal integration, especially for practical applications other than the ideal situation where the sun rays are perpendicular to the SC structure.

In this study, the optical spectra and photocurrent densities ( $J_{ph}$ ) of the CdTe-based SC, in which a 4-period magnesium fluoride/molybdenum trioxide ( $MgF_2/MoO_3$ ) photonic crystal with a PBG in the NIR region are integrated, are theoretically investigated.  $MgF_2$  is transparent over a wide range of wavelengths and is therefore used in windows, lenses and prisms.  $MoO_3$  is transparent in the visible region and is used as an electron transport layer in many optoelectronic devices. Optical spectra such as transmittance, reflection and absorption were calculated using the Transfer Matrix Method (TMM). Calculations were made depending on the angle of incidence of the electromagnetic wave according to the state of CdTe base SCs under upper and lower illumination, and bi-surface operating conditions were discussed optically.

## 2. MATERIAL AND METHOD

The structure of the CdTe-based SC in which the 4 period  $MgF_2/MoO_3$  photonic crystal examined in the study is integrated is given in Table 1. Fluorine Tin Oxide (FTO), which is very transparent in the visible region and offers excellent conductivity, is used as the bottom contact in SC structures (Çetinkaya et al., 2021a; 2021b).  $SnO_2$  is located on the bottom contact as the electron transport layer (ETL), which provides selective electron transmission in the structure.  $SnO_2$  also has a wide band gap value, so that most of the photons from the bottom side can be transferred to the active site (Xiong et al., 2018). In the SC structure, CdS is included as the window layer. Here, CdS is n-type and has a relatively thick p-type CdTe with an absorber layer on it. The free carriers formed as a result of photoproduction are collected by the internal electric field formed at the CdS/CdTe heterojunction. Finally, the  $MoO_3$  BSF layer was added to limit the movement of minority carriers around the pn junction, to collect more efficiently under the effect of the internal electric field and to reduce recombination. Thanks to the convenient work function of  $MoO_3$ , the electrons released as a result of photo-generation in the SC are prevented from reaching the top contact, and selective transport for the cavities can be achieved (Lin et al., 2010; He et al., 2020). Therefore,  $MoO_3$  acts as a hole transport layer (HTL) in the SC structure. Au metal may be present on the BSF for direct ohmic contact. However, in the SC structure presented in the study, only a SC structure that allows the modification of optical characteristics with photonic crystal has been investigated. For experimental studies, thin and strip metal contact can be made right next to the photonic crystal with appropriate masking in the CdTe-based SC to be produced. By designing the PBG in the NIR region in CdTe-based SC,  $MgF_2$  and  $MoO_3$  with different refractive indices were used to improve the absorption by re-harvesting.

**Table 1.** Structure of a CdTe-based SC with a 4 period MgF<sub>2</sub>/MoO<sub>3</sub> photonic crystal

One-dimension Photonic Crystal	(MgF <sub>2</sub> /MoO <sub>3</sub> ) <sup>4</sup>	155/100 nm
<b>BSF-Hole transport layer</b>	MoO <sub>3</sub>	30 nm
<b>Absorber layer</b>	CdTe	600 nm
<b>Window layer</b>	CdS	50 nm
<b>Electron transport layer</b>	SnO <sub>2</sub>	100 nm
<b>Transparent bottom contact</b>	FTO	--

Optical spectra such as absorption, reflection and transmittance of the CdTe-based SC in which the 4 period MgF<sub>2</sub>/MoO<sub>3</sub> photonic crystals examined in the study were integrated were calculated using the Transfer Matrix Method. TMM is a very effective method that examines the propagation of electromagnetic waves in multilayer material systems and is used to calculate the optical properties of the structure (Nguyen et al., 2012; Li et al., 2014; Wang et al., 2014; Çetinkaya et al., 2022). The application of TMM to the SC structure is achieved by connecting the electric and magnetic field components of the electromagnetic wave to each other with a transfer matrix in each layer. In addition, optical calculations of the structures formed as a result of the integration of conductive contacts in the SC structure with different dielectric materials can be made. The calculation method used in the study and the equation sets included in TMM is given in our previous study (Çetinkaya et al., 2021b).

### 3. RESULTS AND DISCUSSION

Currently, studies focused on material modification are not preferred for more efficient cell designs in systems with high efficiency such as CdTe/CdS SCs. In particular, approaches such as effective photonic crystal designs that will increase photon harvest by making more use of electromagnetic radiation, and the use of bifacial configuration by modifying the orientation of the light have been preferred. In this direction, with a suitable optical engineering method, increasing the absorption in this region may be an effective approach since the absorption of CdTe, which acts as the absorber layer in CdTe/CdS SC as the first target, is very weak in the long wavelength region of AM1.5G. The variation of the absorption coefficient of CdTe depending on the wavelength is given in Figure 1.

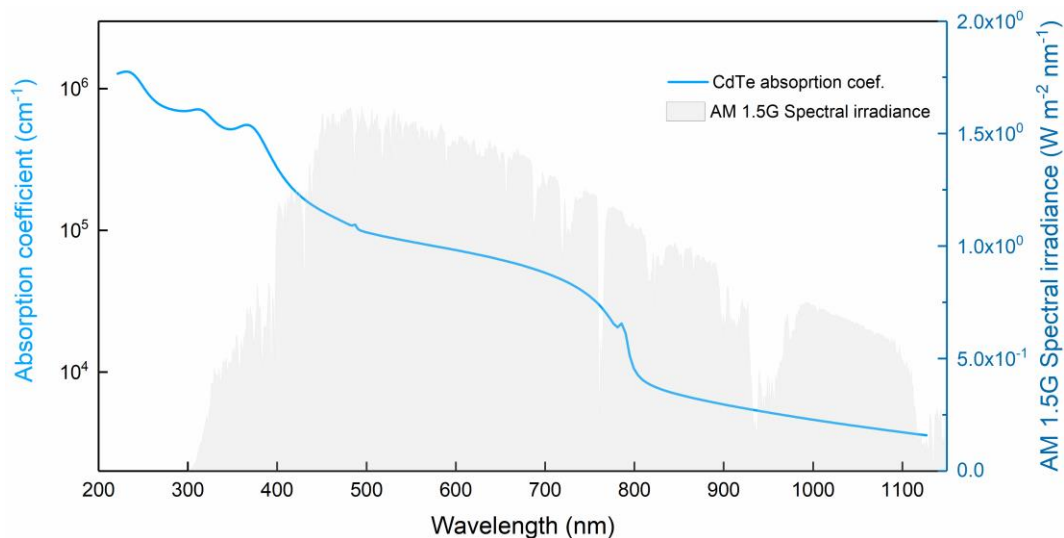


**Figure 1.** Variation of CdTe absorption coefficient with wavelength

When Figure 1 is examined, it is seen that the absorption characteristic of the absorber layer CdTe has decreased considerably in the NIR region. It is quite possible that photons in this region will pass through the CdTe-based SC without being absorbed. Therefore, in order to increase the absorption probability in this region, the photons can be reflected back into the structure and converted into efficient harvesting, which can positively affect the photovoltaic performance of the cell. Therefore, within the scope of the study, we started to analyze the angle dependence by first integrating it into the CdTe/CdS SC system of a 4 period MgF<sub>2</sub>/MoO<sub>3</sub> 1D-PC with a PBG center at  $\lambda_B=850$  nm. Theoretical analysis was made over optical spectra calculated according to the incidence angle of the electromagnetic wave on CdTe/CdS SC with MgF<sub>2</sub>/MoO<sub>3</sub> 1D-PC under top and bottom illumination. Firstly, optical spectra of SC under top illumination were studied. Because with the top illumination, the electromagnetic wave will first interact with the MgF<sub>2</sub>/MoO<sub>3</sub> 1D-PC system and the PBG characteristic can be observed directly in the optical spectra. The reflection, transmittance and absorption spectra calculated by TMM of CdTe/CdS SC with MgF<sub>2</sub>/MoO<sub>3</sub> 1D-PC under top illumination are given in Figure 2a, b and c, respectively.

In the reflection spectrum of the CdTe-based SC, the direct effect of PBG at  $\lambda_B=850$  nm formed with MgF<sub>2</sub>/MoO<sub>3</sub> 1D-PC is seen. In the case of perpendicularity of the electromagnetic wave ( $\theta=0^\circ$ ), the reflection characteristic of PBG, which has a center at 850 nm and a width of about 300 nm, shows itself. For  $\theta=0^\circ$  top illumination, wavelengths longer than 700 nm are directly reflected from the surface and electromagnetic waves cannot enter the SC. Therefore, a decrease in reflection and absorption spectra is observed in this region. This causes a serious decrease in photovoltaic performance by preventing sufficient foton harvesting in the SC's top illumination condition. Therefore, the integration of MgF<sub>2</sub>/MoO<sub>3</sub> 1D-PC with PBG at  $\lambda_B=850$  nm to the CdTe/CdS SC system may not be an effective approach for top illumination.

For top illumination, when the optical spectra are examined according to the incidence angle of the electromagnetic wave, there is no serious change in the reflection intensity in the region where the PBG is formed, up to  $\theta=30^\circ$ , but the reflection intensity drops significantly at incidence angles greater than  $\theta=30^\circ$ . Also, the increase in  $\theta$  indicates that the low wavelength tail of the PBG shifts to shorter wavelengths and enters the visible region. This situation can be explained by the shift of the central wavelength at which  $\lambda_B$  is adjusted in the PBG design, to short wavelengths, as seen in Equation 1, together with the angle of incidence. Therefore, it is seen that the wavelength range for which the PBG is designed and the intensity of reflection are directly dependent on the incidence angle of the electromagnetic wave.

$$\frac{\lambda_B}{4 \cos \theta} = n_i d_i \quad (1)$$

where,  $\lambda_B$  is the Bragg wavelength which is the central wavelength corresponding to the resonance wavelength of the PBG formed by the PC,  $n_i$  is the real part of the refractive index, and  $d_i$  is the layer thickness of each layer.

As a remarkable feature, the increase in the angle of incidence of the electromagnetic wave decreases the reflection intensity but increases the transmittance and especially the absorption intensity of the SC in the designed PBG. Especially in PBG, with incidence angles greater than  $\theta=45^\circ$ , the probability of absorption increases significantly as more electromagnetic waves enter the SC. At the same time, the shift of the PBG center to shorter wavelengths with increasing incidence angle reduces the absorption characteristic in the visible region.

As a general comment for top illumination, it is undesirable that the electromagnetic wave cannot penetrate the SC, especially for wavelengths longer than 700 nm. However, this disadvantage can be encountered as an effective way to increase photon harvest in the case of under-illumination. The reflection, transmittance and absorption spectra calculated by TMM of CdTe/CdS SC with MgF<sub>2</sub>/MoO<sub>3</sub> 1D-PC under bottom illumination are given in Figure 3a, b and c, respectively.



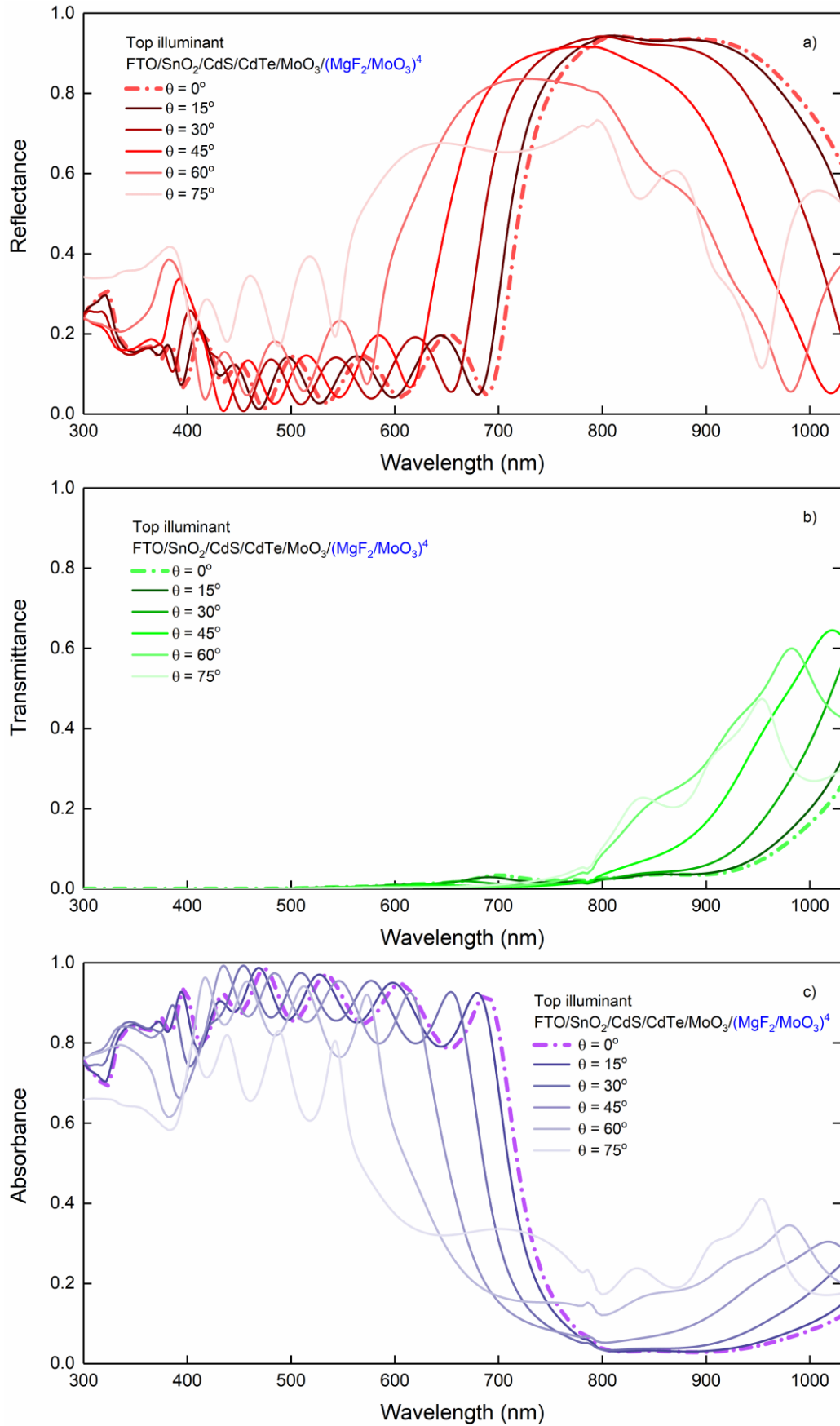


**Figure 2.** a) The reflection, b) transmittance and c) absorption spectra of a CdTe/CdS SC with MgF<sub>2</sub>/MoO<sub>3</sub> photonic crystal under top illumination are calculated depending on the angle of incidence of the electromagnetic wave

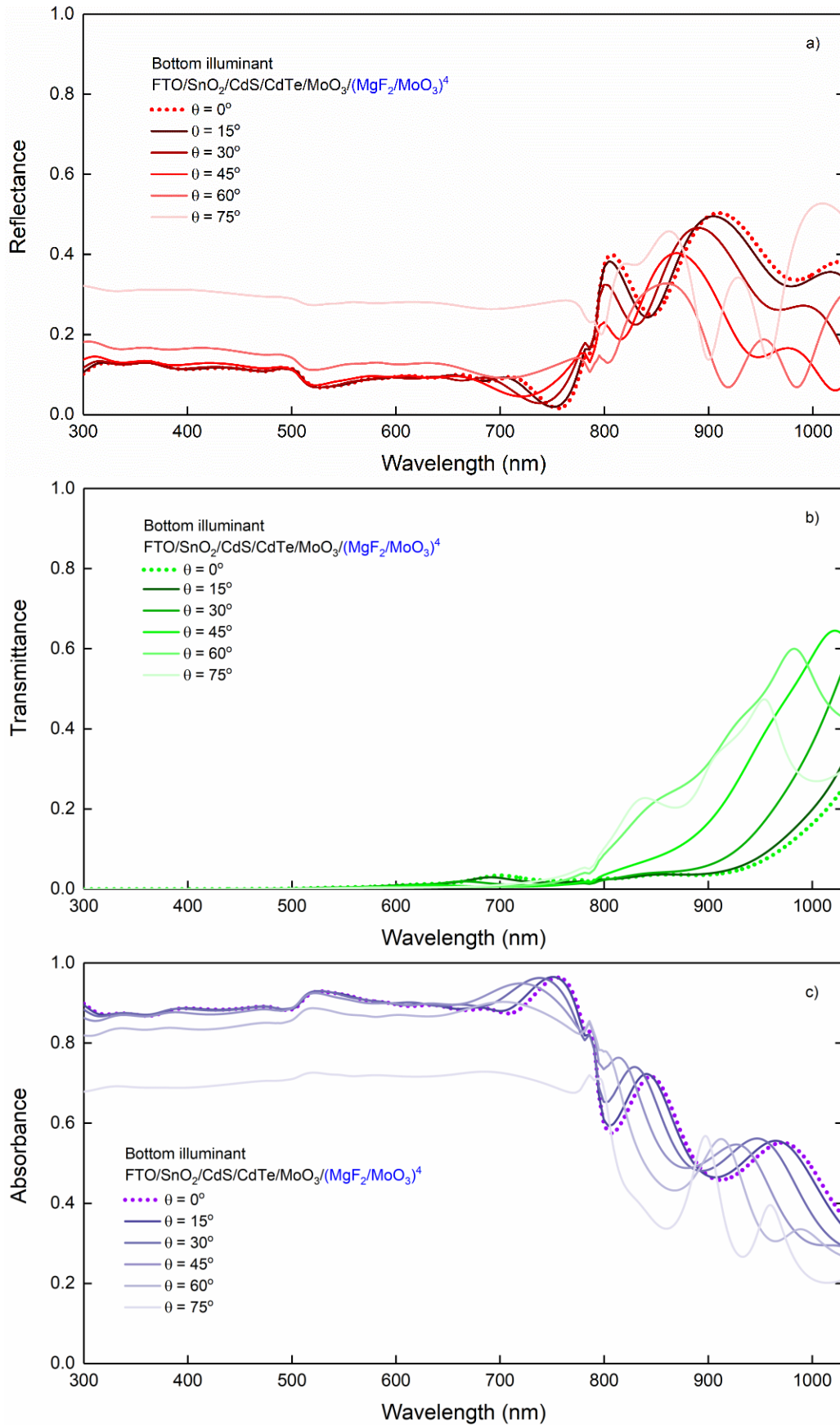


**Figure 3.** a) The reflection, b) transmittance, and c) absorption spectra of a CdTe/CdS SC with MgF<sub>2</sub>/MoO<sub>3</sub> photonic crystal under bottom illumination, calculated depending on the angle of incidence of the electromagnetic wave

When the reflection spectrum is examined under bottom-illumination in Figure 3a, it shows the effect of PBG designed at  $\lambda_B=850$  nm. However, this effect is not as effective and dominant as in top illumination. Also, there is no serious dependence on the angle of incidence of the electromagnetic wave. This is due to the fact that the  $\text{MgF}_2/\text{MoO}_3$  PC is the last system to interact with the electromagnetic wave under the bottom illumination, as opposed to the top illumination. In the bottom illumination, when the electromagnetic wave enters the SC, especially the interaction with the absorber CdTe layer first ensures that the effect of  $\text{MgF}_2/\text{MoO}_3$  PC on the angle-dependent optical spectra is not much. However, for  $\theta=75^\circ$ , there is an increase in reflection for all wavelengths and, therefore a decrease in absorption. This shows that a critical angle is formed, especially for angles greater than  $60^\circ$ . As the most important feature, the PBG effect is designed at  $\lambda_B=850$  nm is effective in the absorption spectrum for all angles and the weak absorption property of the CdTe absorber layer can be improved with  $\text{MgF}_2/\text{MoO}_3$ . Because most of the electromagnetic waves in the PBG could be reflected back into the SC.

For the evaluation of effective photovoltaic properties according to the angle of incidence of the electromagnetic wave in a CdTe-based SC, we calculated the absorption characteristic of SC and  $J_{ph}$  over  $S_{AM1.5G}$  using Equation 2. Because for this examination, the AM1.5G spectral irradiance distribution must also be taken into account.

$$J_{ph} = \int \frac{e\lambda}{hc} S_{AM1.5G}(\lambda) A(\lambda) d\lambda \quad (2)$$

where  $e$  is the electron charge,  $h$  is the Planck constant,  $c$  is the speed of light,  $S_{AM1.5G}$  is the photon flux, and  $A(\lambda)$  is the absorption coefficient. When calculating  $J_{ph}$ , it is assumed that each photon creates an electron and a hole in the structure (Çetinkaya et al., 2021b). This situation provides a relative evaluation and allows us to understand how the flow mechanisms in the structure change relatively. The variation of  $J_{ph}$  values in CdTe/CdS SC with  $\text{MgF}_2/\text{MoO}_3$  1D-PC according to the angle of incidence of the electromagnetic wave under the top and bottom illumination are given in Figure 4.

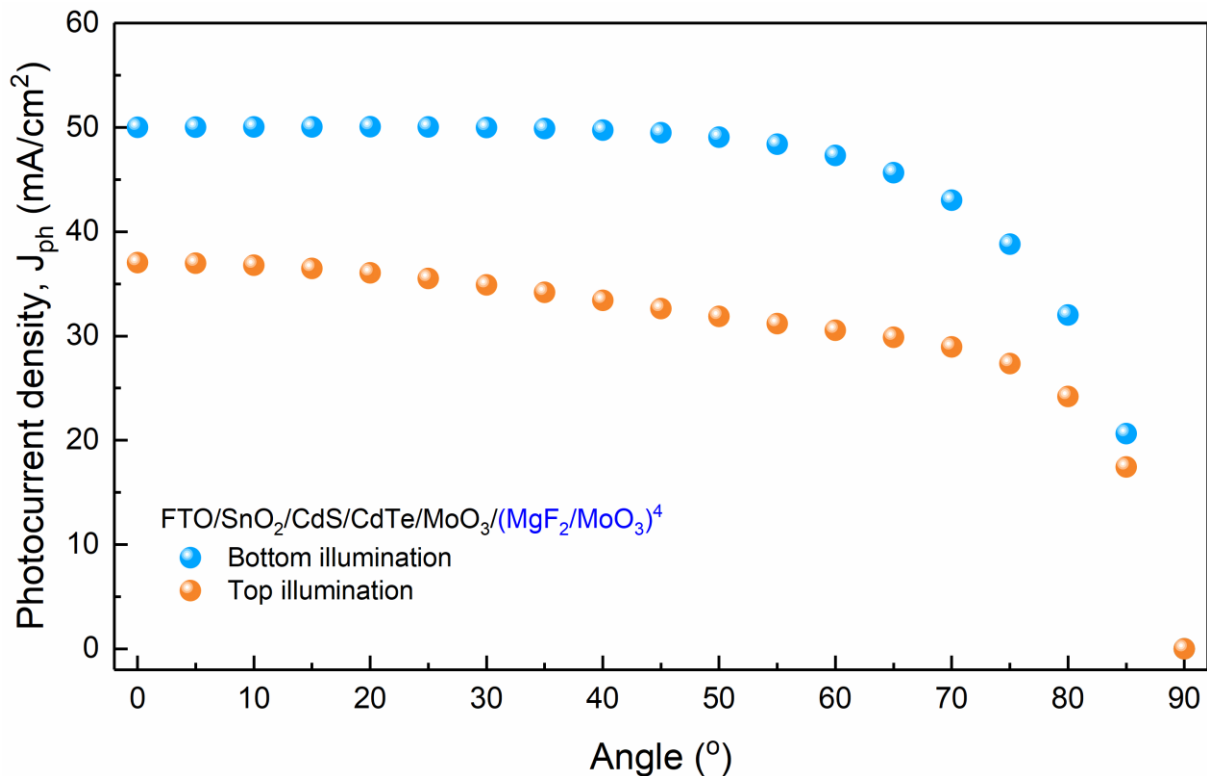


**Figure 4.** The variation of  $J_{ph}$  values in a CdTe/CdS SC with  $\text{MgF}_2/\text{MoO}_3$  photonic crystal according to the angle of incidence of the electromagnetic wave under the top and bottom illumination

In cases where the electromagnetic wave comes to the SC from the top and from the bottom, since the first interaction of the electromagnetic wave in the top interaction is PC, the electromagnetic wave in the PBG is directly reflected from the surface, so sufficient photon harvesting cannot be achieved in the SC and  $J_{ph}$  decreases significantly compared to the bottom illumination situation. For top illumination, as previously discussed, the absorption characteristic increased in the NIR region, especially at angles greater than  $\theta=30^\circ$ , as the reflection decreased. However, since the increase in incidence angle shifts the center of PBG to shorter wavelengths, a reflection characteristic occurs in the visible region, and the absorption weakens in the region of the CdTe absorber layer with high absorption. This results in a deterioration in  $J_{ph}$  for angles greater than  $\theta=30^\circ$ . For bottom illumination, no significant change in  $J_{ph}$  is observed directly due to a specific angle. Because in the bottom illumination, since the electromagnetic wave MgF<sub>2</sub>/MoO<sub>3</sub> interacts with the PC system last, the dependence on the angle disappears. In addition, after  $\theta=60^\circ$  for the bottom illumination and  $\theta=80^\circ$  for the top illumination, there was a serious increase in the reflection spectrum of the SC, especially in the visible region, and there was a deterioration in  $J_{ph}$ .

#### 4. CONCLUSION

In this paper, we examined the interaction of the structure formed by the integration of the MgF<sub>2</sub>/MoO<sub>3</sub> 1D-PC system with PBG, which is designed with a central wavelength at 850 nm to improve photon harvesting in the CdTe/CdS heterojunction SC system, which can already be achieved with high efficiency, with the electromagnetic wave depending on the angle. We evaluated the optical properties by calculating the reflection, transmittance and absorption spectra theoretically with TMM. We presented and discussed all optical spectra for bifacial working conditions depending on the angle under both top and bottom illumination.

It was aimed to increase photon harvesting in the region where the absorption of CdTe, which is the absorber layer, is weak with PBG with a central wavelength at 850 nm, and we determined that the characteristic of PBG significantly changes the optical spectrum of the entire SC structure, especially under top illumination, depending on the angle. For  $\theta=0^\circ$ , under top illumination, wavelengths longer than 700 nm are directly reflected from the surface, thus preventing sufficient photon harvesting of the SC, causing a serious decrease in photovoltaic performance. For top illumination, the reflection intensity drops drastically at incidence angles greater than  $\theta=30^\circ$ . As the most important feature, as a typical PC feature, the increase of  $\theta$  shifts the center wavelength of PBG to shorter wavelengths. Increasing the incidence angle of the electromagnetic wave increases the transmittance and especially the absorption intensity of the SC in the designed PBG. In PBG, for  $\theta>45^\circ$ , the probability of absorption increases significantly with the introduction of more electromagnetic waves into the SC.

For bottom illumination, the PBG effect is not as effective as for top illumination and there is no serious dependence on the angle of incidence of the electromagnetic wave. For  $\theta=75^\circ$ , an increase in reflection for all wavelengths and thus a decrease in absorption is observed. In addition, a critical angle occurs, especially for angles greater than  $60^\circ$ . The PBG effect designed at  $\lambda_B=850$  nm is effective in the absorption spectrum for all angles and the weak absorption property of the CdTe absorber layer can be improved with MgF<sub>2</sub>/MoO<sub>3</sub>.

For  $J_{ph}$ , sufficient photon harvesting can not be achieved in the SC, since the electromagnetic wave is directly reflected from the surface in the top interaction, and  $J_{ph}$  is significantly less than in the case of bottom illumination. In top illumination, there is a deterioration in  $J_{ph}$  for angles greater than  $\theta=30^\circ$  and there is no drastic change in  $J_{ph}$  directly due to a specific angle. In addition, after  $\theta=60^\circ$  for bottom illumination and  $\theta=80^\circ$  for top illumination, a significant increase occurred in the reflection spectrum of SC, especially in the visible region, and weakening of  $J_{ph}$  values was observed.

#### CONFLICT OF INTEREST

The authors declare no conflict of interest.

## REFERENCES

- Çetinkaya, Ç., Çokduygulular, E., Kınacı, B., Güzelçimen, F., Candan, İ., Efkere, H. İ., Özen, Y., & Özçelik, S. (2021a). Evaluation on output parameters of the inverted organic solar cells depending on transition-metal-oxide based hole-transporting materials. *Optical Materials*, 120, 111457. doi:[10.1016/j.optmat.2021.111457](https://doi.org/10.1016/j.optmat.2021.111457)
- Çetinkaya, Ç., Çokduygulular, E., Kınacı, B., Güzelçimen, F., Özen, Y., Efkere, H. İ., Candan, İ., Emik, S., & Özçelik, S. (2021b). Design and fabrication of a semi-transparent solar cell considering the effect of the layer thickness of MoO<sub>3</sub>/Ag/MoO<sub>3</sub> transparent top contact on optical and electrical properties. *Scientific Reports*, 11(1), 1-17. doi:[10.1038/s41598-021-92539-8](https://doi.org/10.1038/s41598-021-92539-8)
- Çetinkaya, Ç., Çokduygulular, E., Güzelçimen, F., & Kınacı, B. (2022). Functional optical design of thickness-optimized transparent conductive dielectric-metal-dielectric plasmonic structure. *Scientific Reports*, 12(1), 8822. doi:[10.1038/s41598-022-13038-y](https://doi.org/10.1038/s41598-022-13038-y)
- Green, M. A., Dunlop, E. D., Hohl-Ebinger, J., Yoshita, M., Kopidakis, N., & Ho-Baillie, A. W. Y. (2020). Solar cell efficiency tables (Version 55). *Progress in Photovoltaics: Research and Applications*, 28(1), 3-15. doi:[10.1002/ppp.3228](https://doi.org/10.1002/ppp.3228)
- He, F., Yin, X., Li, J., Lin, S., Wu, L., Hao, X., Zhang, J., & Feng, L. (2020). Characterization of sputtered MoO<sub>x</sub> thin films with different oxygen content and their application as back contact in CdTe solar cells. *Vacuum*, 176, 109337. doi:[10.1016/j.vacuum.2020.109337](https://doi.org/10.1016/j.vacuum.2020.109337)
- Hu, Z., Zhang, F., An, Q., Zhang, M., Ma, X., Wang, J., Zhang, J., & Wang, J. (2018). Ternary Nonfullerene Polymer Solar Cells with a Power Conversion Efficiency of 11.6% by Inheriting the Advantages of Binary Cells. *ACS Energy Letters*, 3(3), 555-561. doi:[10.1021/acsenergylett.8b00100](https://doi.org/10.1021/acsenergylett.8b00100)
- Li, F., Chen, C., Tan, F., Li, C., Yue, G., Shen, L., & Zhang, W. (2014). Semitransparent inverted polymer solar cells employing a sol-gel-derived TiO<sub>2</sub> electron-selective layer on FTO and MoO<sub>3</sub>/Ag/MoO<sub>3</sub> transparent electrode. *Nanoscale Research Letters*, 9(1), 579. doi:[10.1186/1556-276X-9-579](https://doi.org/10.1186/1556-276X-9-579)
- Lin, H., Xia, W., Wu, H. N., & Tang, C. W. (2010). CdS/CdTe solar cells with MoO<sub>x</sub> as back contact buffers. *Applied Physics Letters*, 97(12), 123504. doi:[10.1063/1.3489414](https://doi.org/10.1063/1.3489414)
- Liu, W., Ma, H., & Walsh, A. (2019). Advance in photonic crystal solar cells. *Renewable and Sustainable Energy Reviews*, 116, 109436. doi:[10.1016/j.rser.2019.109436](https://doi.org/10.1016/j.rser.2019.109436)
- Lova, P., Manfredi, G., & Comoretto, D. (2018). Advances in Functional Solution Processed Planar 1D Photonic Crystals. *Advanced Optical Materials*, 6(24), 1800730. doi:[10.1002/adom.201800730](https://doi.org/10.1002/adom.201800730)
- Nguyen, D.-T., Vedraïne, S., Cattin, L., Torchio, P., Morsli, M., Flory, F., & Bernède, J. C. (2012). Effect of the thickness of the MoO<sub>3</sub> layers on optical properties of MoO<sub>3</sub>/Ag/MoO<sub>3</sub> multilayer structures. *Journal of Applied Physics*, 112(6), 063505. doi:[10.1063/1.4751334](https://doi.org/10.1063/1.4751334)
- Wang, Z., Zhang, C., Gao, R., Chen, D., Tang, S., Zhang, J., Wang, D., Lu, X., & Hao, Y. (2014). Improvement of transparent silver thin film anodes for organic solar cells with a decreased percolation threshold of silver. *Solar Energy Materials and Solar Cells*, 127, 193-200. doi:[10.1016/j.solmat.2014.04.024](https://doi.org/10.1016/j.solmat.2014.04.024)
- Xiong, L., Guo, Y., Wen, J., Liu, H., Yang, G., Qin, P., & Fang, G. (2018). Review on the Application of SnO<sub>2</sub> in Perovskite Solar Cells. *Advanced Functional Materials*, 28(35), 1802757. doi:[10.1002/adfm.201802757](https://doi.org/10.1002/adfm.201802757)
- Yablonovitch, E., Gmitter, T. J., & Leung, K.-M. (1991). Photonic band structure: The face-centered-cubic case employing nonspherical atoms. *Physical Review Letters*, 67(17), 2295-2298. doi:[10.1103/PhysRevLett.67.2295](https://doi.org/10.1103/PhysRevLett.67.2295)
- Zhang, J., Xu, G., Tao, F., Zeng, G., Zhang, M., Yang, Y. M., Li, Y., & Li, Y. (2019). Highly Efficient Semitransparent Organic Solar Cells with Color Rendering Index Approaching 100. *Advanced Materials*, 31(10), 1807159. doi:[10.1002/adma.201807159](https://doi.org/10.1002/adma.201807159)



Gazi University

**Journal of Science**

PART A: ENGINEERING AND INNOVATION

<http://dergipark.org.tr/gujsa>

# On Approximation Properties of Stancu Type Post-Widder Operators Preserving Exponential Functions

Gülten TORUN<sup>1\*</sup> <sup>1</sup> Kastamonu University, Faculty of Education, Mathematics and Science Education, Kastamonu, TURKEY

Keywords	Abstract
Post-Widder Operators Stancu Type Post-Widder Operators Modulus of Continuity Voronovskaja Type Theorem	In this article, Stancu type Post-Widder operators are introduced, which are a modification of the Post-Widder operators that preserve the functions constant and $e^{2ax}$ for fixed $a > 0$ . The uniform convergence of these modified operators for the function $f$ on $[0, \infty)$ is examined and then the convergence rate is investigated with the help of the continuity module. The Voronovskaja type asymptotic formula is obtained to examine the asymptotic behavior of these operators. Finally, numerical examples and graphs are given to show the convergence of Stancu type Post-Widder operators and compared with Post Widder operators.

## Cite

Torun, G. (2022). On Approximation Properties of Stancu Type Post-Widder Operators Preserving Exponential Functions. *GU J Sci, Part A, 9(2)*, 173-186.

Author ID (ORCID Number)	Article Process
G. Torun, 0000-0002-1897-0174	<b>Submission Date</b> 07.05.2022 <b>Revision Date</b> 25.05.2022 <b>Accepted Date</b> 27.06.2022 <b>Published Date</b> 29.06.2022

## 1. INTRODUCTION

Linear positive operators take an important place in approximation theory. These operators are monotonous operators since they convert positive functions to positive functions. This property allows to proving inequalities for positive operators (Hacısalıhoğlu & Hacıyev, 1995).

For  $n \in \mathbb{N} = \{1, 2, \dots\}$  and  $f \in C(0, \infty)$ , Widder (1941) examined the Post-Widder operators is defined by

$$P_n(f; x) := \frac{1}{n!} \left(\frac{n}{x}\right)^{n+1} \int_0^\infty t^n e^{-\frac{nt}{x}} f(t) dt, \quad (1)$$

where  $x \in (0, \infty)$ , and these operators protect only fixed functions. After Widder (1941), Rathore and Sing (1980) defined the operators in the following way

$$P_n^p(f; x) := \frac{1}{(n+p)!} \left(\frac{n}{x}\right)^{n+p+1} \int_0^\infty t^{n+p} e^{-\frac{nt}{x}} f(t) dt, \quad (2)$$

where  $p$  be a fixed integer. They created the simultaneous approximation property of the operators (2) and obtained an asymptotic formula. In the case of  $p = 0$ , the operators (2) reduce to the operators (1). In addition for the  $p = -1$  case, the operators (2) was handled by May (1976).

Rempulska and Skorupka (2009) introduced the Post-Widder and Stancu operators preserving test function  $x^2$  in polynomial weighted space. They showed that these operators had better approximation properties than classical Post-Widder and Stancu operators.

\*Corresponding Author, e-mail: [gtorun@kastamonu.edu.tr](mailto:gtorun@kastamonu.edu.tr)

In recent years, the Post-Widder operators preserving test functions  $x^r$  for  $r \in \mathbb{N}$  have been appropriately modified to get a better approximation. The approximation properties of the modified form of the Post-Widder operators have been studied by [Gupta and Agrawal \(2019\)](#), [Gupta and Tachev \(2022\)](#). In addition, the several linear operators preserving the functions constantly and  $e^{2ax}$  for fixed  $a > 0$ , such as Szász-Mirakyan, Baskakov, Baskakov-Schurer-Szász, Baskakov-Szász-Stancu, Baskakov-Schurer-Szász-Stancu, Post-Widder and Stancu type Szász-Mirakyan-Durrmeyer operators were studied by [Acar et al. \(2017\)](#), [Gürel-Yılmaz et al. \(2017; 2018\)](#), [Bodur et al. \(2018\)](#), [Aral et al. \(2019\)](#), [Sofyaloğlu and Kanat \(2019; 2020\)](#), [Gupta and Maheshwari \(2019\)](#), [Kanat & Sofyaloğlu \(2021\)](#), and they examined the approximation properties of these operators. [Gupta and Maheshwari \(2019\)](#) considered a modification of Post-Widder operators preserving the exponential functions. They made a direct estimate and proved the quantitative asymptotic formula for these modified operators. The case  $p = -1$  of Post-Widder operators (2) preserving constant and  $e^{-2ax}$  for fixed  $a > 0$  has been handled by [Sofyaloğlu and Kanat \(2020\)](#). They investigated the convergence behavior of modified Post-Widder operators and the convergence ratio using different module types. Finally, they compared their newly established operators with the Post-Widder operators which preserve  $x^r$  for  $r \in \mathbb{N}$ .

In this article, the approximation properties of the Stancu type Post-Widder operators that preserve the functions constant and  $e^{2ax}$  for fixed  $a > 0$  are examined and the Voronovskaja type approximation theorem is given for the asymptotic behavior of these operators.

Several studies were conducted on Voronovskaja type approximation for some operators by [Dinlemez Kantar and Ergelen \(2019\)](#), [Cai et al. \(2020; 2021a, 2021b\)](#), [Sofyaloğlu et al. \(2021\)](#), [Dinlemez Kantar and Yüksel \(2022\)](#), [Torun et al. \(2022\)](#).

Let be defined the Stancu type Post-Widder operators for  $n \in \mathbb{N}$  and  $x \in [0, \infty)$  as

$$P_{n,p,\Psi}^{\alpha,\beta}(f; x) = \frac{1}{(n+p)!} \left(\frac{n}{\Psi_n(x)}\right)^{n+p+1} \int_0^\infty t^{n+p} e^{-\frac{nt}{\Psi_n(x)}} f\left(\frac{nt+\alpha}{n+\beta}\right) dt, \tag{3}$$

where the real-valued function  $f$  is a bounded function over the interval  $[0, \infty)$ ,  $\alpha$  and  $\beta$  positive real numbers satisfying  $0 \leq \alpha \leq \beta$ , and  $p$  is a constant integer such that  $p < n$ . For  $a > 0$ , assume that operators (3) preserve the function  $e^{2ax}$ . It can be easily seen that the conditions

$$P_{n,p,\Psi}^{\alpha,\beta}(e^{2at}; x) = e^{2ax}$$

are satisfied. In this case, it would be

$$\begin{aligned} P_{n,p,\Psi}^{\alpha,\beta}(e^{2at}; x) &= e^{2ax} = \frac{1}{(n+p)!} \left(\frac{n}{\Psi_n(x)}\right)^{n+p+1} \int_0^\infty t^{n+p} e^{-\frac{nt}{\Psi_n(x)}} e^{2a\frac{nt+\alpha}{n+\beta}} dt \\ &= \frac{e^{\frac{2a\alpha}{n+\beta}}}{(n+p)!} \left(\frac{n}{\Psi_n(x)}\right)^{n+p+1} \int_0^\infty t^{n+p} e^{-\frac{(n+\beta)-2a\Psi_n(x)}{(n+\beta)\Psi_n(x)}nt} dt \\ &= e^{\frac{2a\alpha}{n+\beta}} \left(\frac{n+\beta}{n+\beta-2a\Psi_n(x)}\right)^{n+p+1}, \end{aligned}$$

where  $\frac{n+\beta}{\Psi_n(x)} > 2a$ . With a simple calculation, the function  $\Psi_n(x)$  is obtained as follows:

$$\Psi_n(x) = \frac{n+\beta}{2a} \left( 1 - \left( e^{\frac{2a(x(n+\beta)-\alpha)}{n+\beta}} \right)^{\frac{-1}{n+p+1}} \right). \tag{4}$$

And it can be easily shown that  $\lim_{n \rightarrow \infty} \Psi_n(x) = x$ .

If the function  $\Psi_n(x)$  given in (4) is replaced in (3), the Stancu type Post-Widder operators take the form

$$\begin{aligned}
 P_{n,p}^{\alpha,\beta}(f;x) &:= P_{n,p,\Psi}^{\alpha,\beta}(f;x) \\
 &= \frac{1}{(n+p)!} \left( \frac{2an}{(n+\beta) \left( 1 - e^{\frac{-2a(x(n+\beta)-\alpha)}{(n+\beta)(n+p+1)}} \right)} \right)^{n+p+1} \int_0^\infty t^{n+p} e^{\frac{-2ant}{(n+\beta) \left( 1 - e^{\frac{-2a(x(n+\beta)-\alpha)}{(n+\beta)(n+p+1)}} \right)}} f\left(\frac{nt+\alpha}{n+\beta}\right) dt. \quad (5)
 \end{aligned}$$

**2. SOME PRELIMINARY RESULTS**

In this section, several lemmas and their results necessary to prove the main theorem are given.

**Lemma 2.1** Let  $\Psi_n(x)$  be function given in (4). The Stancu type Post-Widder operators (3) give the following equations:

$$P_{n,p,\Psi}^{\alpha,\beta}(e^{\phi t}; x) = e^{\frac{\phi\alpha}{n+\beta}} \left( 1 - \frac{\phi\Psi_n(x)}{n+\beta} \right)^{-(n+p+1)}, \quad \phi \in \mathbb{R}. \quad (6)$$

**Proof:** Let  $f(t) = e^{\phi t}$ ,  $\phi \in \mathbb{R}$ . From the operators (3), the following equation is given by

$$\begin{aligned}
 P_{n,p,\Psi}^{\alpha,\beta}(e^{\phi t}; x) &= \frac{1}{(n+p)!} \left( \frac{n}{\Psi_n(x)} \right)^{n+p+1} \int_0^\infty t^{n+p} e^{-\frac{nt}{\Psi_n(x)}} e^{\phi \frac{nt+\alpha}{n+\beta}} dt \\
 &= \frac{1}{(n+p)!} \left( \frac{n}{\Psi_n(x)} \right)^{n+p+1} e^{\frac{\phi\alpha}{n+\beta}} \int_0^\infty t^{n+p} e^{-\left(\frac{1}{\Psi_n(x)} - \frac{\phi}{n+\beta}\right)nt} dt.
 \end{aligned}$$

By substituting the variable  $\left(\frac{1}{\Psi_n(x)} - \frac{\phi}{n+\beta}\right)nt = u$  in the above integral and then using the gamma function,

$$\begin{aligned}
 P_{n,p,\Psi}^{\alpha,\beta}(e^{\phi t}; x) &= \frac{e^{\frac{\phi\alpha}{n+\beta}}}{(n+p)!} \left( \frac{n}{\Psi_n(x)} \left( \frac{n+\beta-\phi\Psi_n(x)}{\Psi_n(x)(n+\beta)} n \right)^{-1} \right)^{n+p+1} \int_0^\infty u^{n+p} e^{-u} du \\
 &= \frac{e^{\frac{\phi\alpha}{n+\beta}}}{(n+p)!} \left( \frac{n+\beta-\phi\Psi_n(x)}{n+\beta} \right)^{-(n+p+1)} \Gamma(n+p+1) = e^{\frac{\phi\alpha}{n+\beta}} \left( 1 - \frac{\phi\Psi_n(x)}{n+\beta} \right)^{-(n+p+1)}
 \end{aligned}$$

is obtained.

**Lemma 2.2** Let  $e_j(t) = t^j$ ,  $j = 0,1,2,3,4$ . The moments of the Stancu type Post-Widder operators (3) are obtained as follows:

- (i)  $P_{n,p,\Psi}^{\alpha,\beta}(e_0(t); x) = 1,$
- (ii)  $P_{n,p,\Psi}^{\alpha,\beta}(e_1(t); x) = \frac{n+p+1}{n+\beta} \Psi_n(x) + \frac{\alpha}{n+\beta},$
- (iii)  $P_{n,p,\Psi}^{\alpha,\beta}(e_2(t); x) = \frac{(n+p+2)(n+p+1)}{(n+\beta)^2} \Psi_n^2(x) + \frac{2\alpha(n+p+1)}{(n+\beta)^2} \Psi_n(x) + \frac{\alpha^2}{(n+\beta)^2},$
- (iv)  $P_{n,p,\Psi}^{\alpha,\beta}(e_3(t); x) = \frac{(n+p+3)(n+p+2)(n+p+1)}{(n+\beta)^3} \Psi_n^3(x) + \frac{3\alpha(n+p+2)(n+p+1)}{(n+\beta)^3} \Psi_n^2(x) + \frac{3\alpha^2(n+p+1)}{(n+\beta)^3} \Psi_n(x) + \frac{\alpha^3}{(n+\beta)^3},$
- (v)  $P_{n,p,\Psi}^{\alpha,\beta}(e_4(t); x) = \frac{(n+p+4)(n+p+3)(n+p+2)(n+p+1)}{(n+\beta)^4} \Psi_n^4(x) + \frac{4\alpha(n+p+3)(n+p+2)(n+p+1)}{(n+\beta)^4} \Psi_n^3(x)$



$$+ \frac{6\alpha^2(n+p+2)(n+p+1)}{(n+\beta)^4} \Psi_n^2(x) + \frac{4\alpha^3(n+p+1)}{(n+\beta)^4} \Psi_n(x) + \frac{\alpha^4}{(n+\beta)^4}.$$

**Proof: (i)** Taking  $e_j(t) = t^j, j = 0$  in operators  $P_{n,p,\Psi}^{\alpha,\beta}(e_j(t); x)$ , the following equation can be obtained by

$$P_{n,p,\Psi}^{\alpha,\beta}(e_0(t); x) = \frac{1}{(n+p)!} \left(\frac{n}{\Psi_n(x)}\right)^{n+p+1} \int_0^\infty t^{n+p} e^{-\frac{nt}{\Psi_n(x)}} dt.$$

Substituting  $\frac{n}{\Psi_n(x)} t = u$  and then from the gamma function, it is easily found that

$$P_{n,p,\Psi}^{\alpha,\beta}(e_0(t); x) = \frac{1}{(n+p)!} \left(\frac{n}{\Psi_n(x)}\right)^{n+p+1} \left(\frac{\Psi_n(x)}{n}\right)^{n+p+1} \int_0^\infty u^{n+p} e^{-u} du = \frac{1}{(n+p)!} \Gamma(n+p+1) = 1$$

**(ii)** The operators  $P_{n,p,\Psi}^{\alpha,\beta}(e_j(t); x)$  for  $j = 1$  are yielded as follows:

$$\begin{aligned} P_{n,p,\Psi}^{\alpha,\beta}(e_1(t); x) &= \frac{1}{(n+p)!} \left(\frac{n}{\Psi_n(x)}\right)^{n+p+1} \int_0^\infty t^{n+p} e^{-\frac{nt}{\Psi_n(x)}} \left(\frac{nt+\alpha}{n+\beta}\right) dt \\ &= \frac{n}{(n+p)!(n+\beta)} \left(\frac{n}{\Psi_n(x)}\right)^{n+p+1} \int_0^\infty t^{n+p+1} e^{-\frac{nt}{\Psi_n(x)}} dt + \frac{\alpha}{(n+p)!(n+\beta)} \left(\frac{n}{\Psi_n(x)}\right)^{n+p+1} \int_0^\infty t^{n+p} e^{-\frac{nt}{\Psi_n(x)}} dt. \end{aligned}$$

From (i), the value of the second sum on the right side of the above equation is  $\frac{\alpha}{n+\beta}$ . In the first integral on the right side of the above equation, the variable  $\frac{n}{\Psi_n(x)} t = u$  is changed. And then using the gamma function, the following equation is obtained:

$$P_{n,p,\Psi}^{\alpha,\beta}(e_1(t); x) = \frac{n+p+1}{n+\beta} \Psi_n(x) + \frac{\alpha}{n+\beta}.$$

**(iii)** For  $j = 2$ , the operators  $P_{n,p,\Psi}^{\alpha,\beta}(e_j(t); x)$  are written as follows:

$$\begin{aligned} P_{n,p,\Psi}^{\alpha,\beta}(e_2(t); x) &= \frac{1}{(n+p)!} \left(\frac{n}{\Psi_n(x)}\right)^{n+p+1} \int_0^\infty t^{n+p} e^{-\frac{nt}{\Psi_n(x)}} \left(\frac{nt+\alpha}{n+\beta}\right)^2 dt \\ &= \frac{n^2}{(n+p)!(n+\beta)^2} \left(\frac{n}{\Psi_n(x)}\right)^{n+p+1} \int_0^\infty t^{n+p+2} e^{-\frac{nt}{\Psi_n(x)}} dt + \frac{2n\alpha}{(n+p)!(n+\beta)^2} \left(\frac{n}{\Psi_n(x)}\right)^{n+p+1} \int_0^\infty t^{n+p+1} e^{-\frac{nt}{\Psi_n(x)}} dt \\ &\quad + \frac{\alpha^2}{(n+p)!(n+\beta)^2} \left(\frac{n}{\Psi_n(x)}\right)^{n+p+1} \int_0^\infty t^{n+p} e^{-\frac{nt}{\Psi_n(x)}} dt. \end{aligned}$$

In the first integral on the right side of the above equation, the variable  $\frac{n}{\Psi_n(x)} t = u$  is changed and then the gamma function is used. From (i) and (ii),

$$P_{n,p,\Psi}^{\alpha,\beta}(e_2(t); x) = \frac{(n+p+2)(n+p+1)}{(n+\beta)^2} \Psi_n^2(x) + \frac{2\alpha(n+p+1)}{(n+\beta)^2} \Psi_n(x) + \frac{\alpha^2}{(n+\beta)^2}.$$

Similarly, the equations (iv) and (v) are proved.

**Corollary 2.3** Let  $\varphi_x^j(t) = (t-x)^j, j = 0,1,2,4$ . The central moments of Stancu type Post-Widder operators (3) are bellowed

$$P_{n,p,\Psi}^{\alpha,\beta}(\varphi_x^0(t); x) = 1,$$

$$\begin{aligned}
 P_{n,p,\Psi}^{\alpha,\beta}(\varphi_x^1(t); x) &= \frac{(n+p+1)\Psi_n(x)+\alpha}{n+\beta} - x, \\
 P_{n,p,\Psi}^{\alpha,\beta}(\varphi_x^2(t); x) &= \frac{(n+p+2)(n+p+1)\Psi_n^2(x)+2\alpha(n+p+1)\Psi_n(x)+\alpha^2}{(n+\beta)^2} - 2x \frac{(n+p+1)\Psi_n(x)+\alpha}{n+\beta} + x^2, \\
 P_{n,p,\Psi}^{\alpha,\beta}(\varphi_x^4(t); x) &= \frac{(n+p+4)(n+p+3)(n+p+2)(n+p+1)\Psi_n^4(x)+4\alpha(n+p+3)(n+p+2)(n+p+1)\Psi_n^3(x)}{(n+\beta)^4} \\
 &\quad + \frac{6\alpha^2(n+p+2)(n+p+1)\Psi_n^2(x)+4\alpha^3(n+p+1)\Psi_n(x)+\alpha^4}{(n+\beta)^4} \\
 &\quad - 4x \left( \frac{(n+p+3)(n+p+2)(n+p+1)\Psi_n^3(x)+3\alpha(n+p+2)(n+p+1)\Psi_n^2(x)+3\alpha^2(n+p+1)\Psi_n(x)+\alpha^3}{(n+\beta)^3} \right) \\
 &\quad + 6x^2 \left( \frac{(n+p+2)(n+p+1)\Psi_n^2(x)+2\alpha(n+p+1)\Psi_n(x)+\alpha^2}{(n+\beta)^2} \right) - 4x^3 \left( \frac{(n+p+1)\Psi_n(x)+\alpha}{n+\beta} \right) + x^4.
 \end{aligned}$$

In addition, considering the equation  $\Psi_n(x)$  defined in (4), the following limits are obtained:

$$(i) \quad \lim_{n \rightarrow \infty} n P_{n,p,\Psi}^{\alpha,\beta}(t-x; x) = -ax^2 \tag{7}$$

$$(ii) \quad \lim_{n \rightarrow \infty} n P_{n,p,\Psi}^{\alpha,\beta}((t-x)^2; x) = x^2 \tag{8}$$

$$(iii) \quad \lim_{n \rightarrow \infty} n^2 P_{n,p,\Psi}^{\alpha,\beta}((t-x)^4; x) = 3x^4 \tag{9}$$

### 3. THE UNIFORM CONVERGENCE OF THE OPERATORS $P_{n,p,\Psi}^{\alpha,\beta}$

Boyanov and Veselinov (1970) showed uniform convergence of the sequence of linear positive operators. In the following theorem, the uniform convergence of the Stancu type Post-Widder operators (3) for the function  $f$  on  $[0, \infty)$  is investigated. Let the subspace of all continuous and real-valued functions on  $[0, \infty)$  be denoted by  $C^*[0, \infty)$  with the property that  $\lim_{x \rightarrow \infty} f(x)$  exists and finite, given with the uniform norm.

**Theorem 3.1** If the sequence of the Stancu type Post-Widder operators (3) satisfy

$$\lim_{n \rightarrow \infty} P_{n,p,\Psi}^{\alpha,\beta}(e^{-vt}; x) = e^{-vx}, \quad v = 0,1,2 \tag{10}$$

uniformly in  $[0, \infty)$ , then for each  $f \in C^*[0, \infty)$

$$\lim_{n \rightarrow \infty} P_{n,p,\Psi}^{\alpha,\beta}(f; x) = f(x) \tag{11}$$

uniformly in  $[0, \infty)$ .

**Proof:** For  $v = 0$ , it becomes that  $\lim_{n \rightarrow \infty} P_{n,p,\Psi}^{\alpha,\beta}(1; x) = 1$  from (i) of Lemma 2.2. Now the equation (6), and  $\Psi_n(x)$  defined with (4) will be used to prove the images of  $f(t) = e^{-vt}$  for  $v = 1,2$  respectively,

$$P_{n,p,\Psi}^{\alpha,\beta}(e^{-t}; x) = e^{-\frac{\alpha}{n+\beta}} \left( 1 + \frac{1}{2\alpha} \left( 1 - e^{\frac{-2\alpha(x(n+\beta)-\alpha)}{(n+\beta)(n+p+1)}} \right) \right)^{-(n+p+1)} \tag{12}$$

and

$$P_{n,p,\Psi}^{\alpha,\beta}(e^{-2t}; x) = e^{-\frac{2\alpha}{n+\beta}} \left( 1 + \frac{1}{a} \left( 1 - e^{\frac{-2a(x(n+\beta)-\alpha)}{(n+\beta)(n+p+1)}} \right) \right)^{-(n+p+1)}. \tag{13}$$

Using the software Maple to calculate the right side of the equation (12), the following equation is obtained:

$$P_{n,p,\Psi}^{\alpha,\beta}(e^{-t}; x) = e^{-x} + \frac{(2a+1)e^{-x}x^2}{2n} + \frac{(2a+1)(3(2a+1)e^{-x}x^4 - 8(a+1)e^{-x}x^3 - 12(p+1)e^{-x}x^2 - 24\alpha e^{-x}x)}{24n^2} + O\left(\frac{1}{n^3}\right). \tag{14}$$

Similarly, again using Maple to calculate the right side of the equation (13),

$$P_{n,p,\Psi}^{\alpha,\beta}(e^{-2t}; x) = e^{-2x} + \frac{2(a+1)e^{-2x}x^2}{n} + \frac{(a+1)(6(a+1)e^{-2x}x^4 - 4(a+2)e^{-2x}x^3 - 6(p+1)e^{-2x}x^2 - 12\alpha e^{-2x}x)}{3n^2} + O\left(\frac{1}{n^3}\right) \tag{15}$$

is found. Thus,  $\lim_{n \rightarrow \infty} P_{n,p,\Psi}^{\alpha,\beta}(e^{-vt}; x) = e^{-vx}$ ,  $v = 0,1,2$  in the interval  $[0; \infty)$ . That is,

$$\lim_{n \rightarrow \infty} P_{n,p,\Psi}^{\alpha,\beta}(f; x) = f$$

for any  $f \in C^*[0; \infty)$ . This indicates that the sequence  $\{P_{n,p,\Psi}^{\alpha,\beta} f\}$  uniformly converges in the interval  $[0, \infty)$  for any  $f \in C^*[0, \infty)$ .

After [Boyanov and Veselinov \(1970\)](#), [Holhoş \(2010\)](#) studied the uniform convergence of a sequence of linear positive operators and obtained the following theorem.

**Theorem 3.2** If  $\{P_n\}$  is a sequence of linear positive operators from  $C^*[0, \infty)$ , to  $C^*[0, \infty)$ , then for each  $f \in C^*[0, \infty)$ , the following inequality is satisfied:

$$\|P_n(f; x) - f(x)\|_{[0,\infty)} \leq \|f\|_{[0,\infty)} a_n + (2 + a_n) \omega^*(f, \sqrt{a_n + 2b_n + c_n}),$$

where  $a_n, b_n$  and  $c_n$  are defined as follows:

$$\|P_n(1; x) - 1\|_{[0,\infty)} = a_n,$$

$$\|P_n(e^{-t}; x) - e^{-x}\|_{[0,\infty)} = b_n,$$

$$\|P_n(e^{-2t}; x) - e^{-2x}\|_{[0,\infty)} = c_n$$

and they approach zero as  $n$  goes to infinity. In addition, the modulus of continuity is expressed by

$$\omega^*(f, \gamma) = \sup_{|e^{-t} - e^{-x}| \leq \gamma; x, t \geq 0} |f(t) - f(x)| \tag{16}$$

and this modulus has to property:

$$|f(t) - f(x)| \leq \left( 1 + \frac{1}{\gamma^2} (e^{-t} - e^{-x})^2 \right) \omega^*(f, \gamma), \quad \gamma > 0 \tag{17}$$

The main result of the uniform convergence of a sequence of linear positive operators is given by the following theorem.

**Theorem 3.3** Let  $\{P_{n,p,\Psi}^{\alpha,\beta} f\}$  be a sequence of linear positive operators  $P_{n,p,\Psi}^{\alpha,\beta}: C^*[0, \infty) \rightarrow C^*[0, \infty)$ . For every function  $f \in C^*[0, \infty)$ , the following inequality is satisfied:

$$\|P_{n,p,\Psi}^{\alpha,\beta}(f; x) - f(x)\|_{[0,\infty)} \leq 2\omega^*(f, \sqrt{2\sigma_n + \mu_n}), \tag{18}$$

where the modulus of continuity  $\omega^*$  which is defined in (16) and

$$\|P_{n,p,\Psi}^{\alpha,\beta}(e^{-t}; x) - e^{-x}\|_{[0,\infty)} = \sigma_n,$$

$$\|P_{n,p,\Psi}^{\alpha,\beta}(e^{-2t}; x) - e^{-2x}\|_{[0,\infty)} = \mu_n,$$

Here  $\sigma_n$  and  $\mu_n$  tend to zero as  $n$  goes to infinity and the sequence  $\{P_{n,p,\Psi}^{\alpha,\beta} f\}$  uniformly converges to  $f$ .

**Proof:** From (i) of Lemma 2.2,

$$\rho_n = \|P_{n,p,\Psi}^{\alpha,\beta}(1; x) - 1\|_{[0,\infty)} = 0$$

is obtained. To calculate  $\sigma_n$  and  $\mu_n$ , the equalities (14) and (15) are taken respectively

$$\begin{aligned} \sigma_n &= \|P_{n,p,\Psi}^{\alpha,\beta}(e^{-t}; x) - e^{-x}\|_{[0,\infty)} = \sup_{x \in [0,\infty)} |P_{n,p,\Psi}^{\alpha,\beta}(e^{-t}; x) - e^{-x}| \\ &= \sup_{x \in [0,\infty)} \left| \frac{(2a+1)e^{-x}x^2}{2n} + \frac{(2a+1)(3(2a+1)e^{-x}x^4 - 8(a+1)e^{-x}x^3 - 12(p+1)e^{-x}x^2 - 24ae^{-x}x)}{24n^2} + O\left(\frac{1}{n^3}\right) \right| \\ &\leq \frac{2(2a+1)}{ne^2} + \frac{2a+1}{n^2} \left( \frac{32(2a+1)}{e^4} - \frac{9(a+1)}{e^3} - \frac{p+1}{e^2} - \frac{\alpha}{e} \right) + O\left(\frac{1}{n^3}\right), \end{aligned}$$

$$\begin{aligned} \mu_n &= \|P_{n,p,\Psi}^{\alpha,\beta}(e^{-2t}; x) - e^{-2x}\|_{[0,\infty)} = \sup_{x \in [0,\infty)} |P_{n,p,\Psi}^{\alpha,\beta}(e^{-2t}; x) - e^{-2x}| \\ &= \sup_{x \in [0,\infty)} \left| \frac{2(a+1)e^{-2x}x^2}{n} + \frac{(a+1)(6(a+1)e^{-2x}x^4 - 4(a+2)e^{-2x}x^3 - 6(p+1)e^{-2x}x^2 - 12ae^{-2x}x)}{3n^2} + O\left(\frac{1}{n^3}\right) \right| \\ &\leq \frac{2(a+1)}{ne^2} + \frac{a+1}{n^2} \left( \frac{32(a+1)}{e^4} - \frac{9(a+2)}{e^3} - \frac{2(p+1)}{e^2} - \frac{2\alpha}{e} \right) + O\left(\frac{1}{n^3}\right) \end{aligned}$$

As a consequence,  $\sigma_n$  and  $\mu_n$  tend to zero as  $n$  goes to infinity. Thus, the Theorem is proved.

#### 4. APPROXIMATION PROPERTIES OF THE OPERATORS $P_{n,p,\Psi}^{\alpha,\beta}$

In this section, firstly, the convergence rate is examined with the help of the continuity module.

Let  $C_B[0, \infty)$  be the class of all bounded and uniform continuous functions  $f$  on  $[0, \infty)$  with the norm

$\|f\|_{C_B} = \sup_{x \in [0,\infty)} |f(x)|$ . For  $\varepsilon > 0$ , the Peetre K-functional is defined as

$$K_2(f, \varepsilon) := \inf_{g \in C_B^2[0,\infty)} [\|f - g\| + \varepsilon\|g''\|],$$

where  $C_B^2[0, \infty) := \{g \in C_B[0, \infty) : g', g'' \in C_B[0, \infty)\}$ .

The first-order modulus of continuity of  $f \in C_B[0, \infty)$  is defined as follows:

$$\omega(f, \varepsilon) := \sup_{0 < h \leq \varepsilon} \sup_{x, x+h \in [0, \infty)} |f(x+h) - f(x)|.$$

The second-order modulus of continuity of  $f \in C_B[0, \infty)$  is given by

$$\omega_2(f, \sqrt{\varepsilon}) := \sup_{0 < h \leq \sqrt{\varepsilon}} \sup_{x, x+h, x+2h \in [0, \infty)} |f(x+2h) - 2f(x+h) + f(x)|.$$

In Theorem 2.4 given by DeVore and Lorentz (1993) is proved that there exists an absolute constant  $C > 0$  such that

$$K_2(f, \varepsilon) \leq C \omega_2(f, \sqrt{\varepsilon}). \tag{19}$$

**Lemma 4.1** For  $f \in C_B[0, \infty)$ , the following inequality is obtained:

$$|P_{n,p,\Psi}^{\alpha,\beta}(f; x)| \leq \|f\|. \tag{20}$$

**Proof:**

$$\begin{aligned} |P_{n,p,\Psi}^{\alpha,\beta}(f; x)| &= |P_{n,p}^{\alpha,\beta}(f; x)| \\ &\leq \frac{1}{(n+p)!} \left( \frac{2an}{(n+\beta) \left(1 - e^{\frac{-2a(x(n+\beta)-\alpha)}{(n+\beta)(n+p+1)}}\right)} \right)^{n+p+1} \int_0^\infty t^{n+p} e^{\frac{-2ant}{(n+\beta) \left(1 - e^{\frac{-2a(x(n+\beta)-\alpha)}{(n+\beta)(n+p+1)}}\right)}} \left| f\left(\frac{nt+\alpha}{n+\beta}\right) \right| dt. \\ &\leq \|f\| P_{n,p,\Psi}^{\alpha,\beta}(1; x) = \|f\|. \end{aligned}$$

**Theorem 4.2** For  $f \in C_B[0, \infty)$ , there exists a positive constant  $L$ , such that

$$\left| P_{n,p,\Psi}^{\alpha,\beta}(f; x) - f(x) \right| \leq L \omega_2 \left( f, \sqrt{\frac{\xi_{n,p,\Psi}^{\alpha,\beta}}{8}} \right) + \omega \left( f, \left| \frac{n+p+1}{2a} \left( 1 - e^{\frac{-2a(x(n+\beta)-\alpha)}{(n+\beta)(n+p+1)}} \right) + \frac{\alpha}{n+\beta} - x \right| \right),$$

where

$$\xi_{n,p,\Psi}^{\alpha,\beta} = \frac{(n+p+1)(2n+2p+3)}{(n+\beta)^2} \Psi_n^2(x) + 4 \left( \frac{\alpha(n+p+1)}{(n+\beta)^2} - \frac{x(n+p+1)}{n+\beta} \right) \Psi_n(x) + \frac{2\alpha^2}{(n+\beta)^2} - \frac{4x\alpha}{n+\beta} + 2x^2.$$

**Proof:** Let the auxiliary operators  $\tilde{P}_{n,p,\Psi}^{\alpha,\beta}$  from  $C_B[0, \infty)$  to  $C_B[0, \infty)$  be defined as

$$\tilde{P}_{n,p,\Psi}^{\alpha,\beta}(g; x) = P_{n,p,\Psi}^{\alpha,\beta}(g; x) + g(x) - g \left( \frac{n+p+1}{2a} \left( 1 - e^{\frac{-2a(x(n+\beta)-\alpha)}{(n+\beta)(n+p+1)}} \right) + \frac{\alpha}{n+\beta} \right). \tag{21}$$

Using the equalities (i) and (ii) of Lemma 2.2 and the linearity of the operators  $\tilde{P}_{n,p,\Psi}^{\alpha,\beta}(g; x)$ ,

$$\tilde{P}_{n,p,\Psi}^{\alpha,\beta}(t-x; x) = 0 \tag{22}$$

is obtained. Using Taylor expansion for  $g \in C_B^2[0, \infty)$ , it can be written as

$$g(t) = g(x) + g'(x)(t-x) + \int_x^t (t-u)g''(u)du. \tag{23}$$

Applying the auxiliary operators (21) to both sides of equation (23) and using (22), it is obtained

$$\tilde{P}_{n,p,\Psi}^{\alpha,\beta}(g; x) = g(x) + \tilde{P}_{n,p,\Psi}^{\alpha,\beta} \left( \int_x^t (t-u)g''(u)du; x \right).$$

$$\begin{aligned} \left| \tilde{P}_{n,p,\Psi}^{\alpha,\beta}(g; x) - g(x) \right| &\leq \left| P_{n,p,\Psi}^{\alpha,\beta} \left( \int_x^t (t-u)g''(u)du; x \right) \right| + \left| \int_x^{P_{n,p,\Psi}^{\alpha,\beta}(e_1;x)} \left( P_{n,p,\Psi}^{\alpha,\beta}(e_1; x) - u \right) g''(u)du \right| \\ &\leq \frac{\|g''\|}{2} P_{n,p,\Psi}^{\alpha,\beta}((t-x)^2; x) + \frac{\|g''\|}{2} \left( \frac{n+p+1}{2a} \left( 1 - e^{\frac{-2a(x(n+\beta)-\alpha)}{(n+\beta)(n+p+1)}} \right) + \frac{\alpha}{n+\beta} - x \right)^2 \\ &\leq \frac{\|g''\|}{2} \left( \left( P_{n,p,\Psi}^{\alpha,\beta}((t-x)^2; x) \right) + \left( P_{n,p,\Psi}^{\alpha,\beta}(t-x; x) \right)^2 \right) = \frac{\|g''\|}{2} \xi_{n,p,\Psi}^{\alpha,\beta}, \end{aligned} \tag{24}$$

where

$$\xi_{n,p,\Psi}^{\alpha,\beta} = \frac{(n+p+1)(2n+2p+3)}{(n+\beta)^2} \Psi_n^2(x) + 4 \left( \frac{\alpha(n+p+1)}{(n+\beta)^2} - \frac{x(n+p+1)}{n+\beta} \right) \Psi_n(x) + \frac{2\alpha^2}{(n+\beta)^2} - \frac{4x\alpha}{n+\beta} + 2x^2.$$

Taking the norm of the auxiliary operators (21) and using Lemma (4.1), the following inequality is obtained:

$$\left\| \tilde{P}_{n,p,\Psi}^{\alpha,\beta}(f; x) \right\| \leq 3 \|f\|, \quad f \in C_B[0, \infty). \tag{25}$$

Using the operators (21) and the inequalities (24) and (25), for every  $g \in C_B^2[0, \infty)$ , it can be written as

$$\begin{aligned} \left| P_{n,p,\Psi}^{\alpha,\beta}(f; x) - f(x) \right| &\leq \left| \tilde{P}_{n,p,\Psi}^{\alpha,\beta}(f-g; x) - (f-g)(x) \right| \\ &\quad + \left| f \left( \frac{n+p+1}{2a} \left( 1 - e^{\frac{-2a(x(n+\beta)-\alpha)}{(n+\beta)(n+p+1)}} \right) + \frac{\alpha}{n+\beta} \right) - f(x) \right| + \left| \tilde{P}_{n,p,\Psi}^{\alpha,\beta}(g; x) - g(x) \right| \\ &\leq 4 \|f-g\| + \frac{\|g''\|}{2} \xi_{n,p,\Psi}^{\alpha,\beta} + \left| f \left( \frac{n+p+1}{2a} \left( 1 - e^{\frac{-2a(x(n+\beta)-\alpha)}{(n+\beta)(n+p+1)}} \right) + \frac{\alpha}{n+\beta} \right) - f(x) \right|. \end{aligned} \tag{26}$$

If the infimum on the right side of (26) over all the function  $g \in C_B^2[0, \infty)$  is taken, then

$$\begin{aligned} \left| P_{n,p,\Psi}^{\alpha,\beta}(f; x) - f(x) \right| &\leq 4K_2 \left( f, \frac{\xi_{n,p,\Psi}^{\alpha,\beta}}{8} \right) + \omega \left( f, \left| \frac{n+p+1}{2a} \left( 1 - e^{\frac{-2a(x(n+\beta)-\alpha)}{(n+\beta)(n+p+1)}} \right) + \frac{\alpha}{n+\beta} - x \right| \right) \\ &\leq L\omega_2 \left( f, \sqrt{\frac{\xi_{n,p,\Psi}^{\alpha,\beta}}{8}} \right) + \omega \left( f, \left| \frac{n+p+1}{2a} \left( 1 - e^{\frac{-2a(x(n+\beta)-\alpha)}{(n+\beta)(n+p+1)}} \right) + \frac{\alpha}{n+\beta} - x \right| \right), \end{aligned}$$

where L is a positive constant. Thus, the Theorem is proved.

**Remark 4.3** Since  $\lim_{n \rightarrow \infty} \xi_{n,p,\Psi}^{\alpha,\beta} = 0$  and  $\lim_{n \rightarrow \infty} \left( \frac{n+p+1}{2a} \left( 1 - e^{\frac{-2a(x(n+\beta)-\alpha)}{(n+\beta)(n+p+1)}} \right) + \frac{\alpha}{n+\beta} - x \right) = 0$ , these limits guarantees a rate of pointwise convergence of the operators  $P_{n,p,\Psi}^{\alpha,\beta}(f; x)$  to  $f(x)$ .

Finally, the Voronovskaja-type theorem is given to examine the asymptotic behavior of the Stancu type Post-Widder operators (3).

**Theorem 4.4** For each  $f \in C^*[0, \infty)$  and  $x \in [0, \infty)$ , the following inequality holds:

$$\left| n \left( P_{n,p,\Psi}^{\alpha,\beta}(f; x) - f(x) \right) + ax^2 f'(x) - \frac{x^2}{2} f''(x) \right| \leq |u_n(x)| |f'(x)| + \frac{1}{2} |v_n(x)| |f''(x)|$$

$$+2(v_n(x) + x^2 + w_n(x))\omega^*(f'', n^{-\frac{1}{2}}),$$

where  $f', f''$  exists in  $C^*[0, \infty)$ , and

$$u_n(x) = nP_{n,p,\Psi}^{\alpha,\beta}(t - x; x) + ax^2,$$

$$v_n(x) = nP_{n,p,\Psi}^{\alpha,\beta}((t - x)^2; x) - x^2,$$

$$w_n(x) = \left(n^2 P_{n,p,\Psi}^{\alpha,\beta}((e^{-t} - e^{-x})^4; x)\right)^{\frac{1}{2}} \left(n^2 P_{n,p,\Psi}^{\alpha,\beta}((t - x)^4; x)\right)^{\frac{1}{2}}.$$

**Proof:** By Taylor's formula for a function  $f$ , the following equation can be written:

$$f(t) = f(x) + f'(x)(t - x) + \frac{f''(x)}{2}(t - x)^2 + r(t, x)(t - x)^2, \tag{27}$$

where Peano form of the remainder  $r(t, x)$  is defined by

$$r(t, x) := \frac{f''(\tau) - f''(x)}{2}, \quad x < \tau < t$$

and the limit value of the remainder term  $r(t, x)$  is 0 as  $t$  approaches  $x$ . By applying the operators  $P_{n,p,\Psi}^{\alpha,\beta}(f; x)$  on both sides of the equation in (27), the following equality is obtained:

$$P_{n,p,\Psi}^{\alpha,\beta}(f; x) - f(x) = f'(x)P_{n,p,\Psi}^{\alpha,\beta}(t - x; x) + \frac{f''(x)}{2}P_{n,p,\Psi}^{\alpha,\beta}((t - x)^2; x) + P_{n,p,\Psi}^{\alpha,\beta}(r(t, x)(t - x)^2; x).$$

Taking into account the Corollary (2.3), the following inequality can be written:

$$\begin{aligned} \left|n \left(P_{n,p,\Psi}^{\alpha,\beta}(f; x) - f(x)\right) + ax^2 f'(x) - \frac{x^2}{2} f''(x)\right| &\leq \left|nP_{n,p,\Psi}^{\alpha,\beta}(t - x; x) + ax^2\right| |f'(x)| \\ &+ \frac{1}{2} \left|nP_{n,p,\Psi}^{\alpha,\beta}((t - x)^2; x) - x^2\right| |f''(x)| + \left|nP_{n,p,\Psi}^{\alpha,\beta}(r(t, x)(t - x)^2; x)\right|. \end{aligned}$$

Let  $u_n(x) = nP_{n,p,\Psi}^{\alpha,\beta}(t - x; x) + ax^2$ , and  $v_n(x) = nP_{n,p,\Psi}^{\alpha,\beta}((t - x)^2; x) - x^2$ . Then

$$\begin{aligned} \left|n \left(P_{n,p,\Psi}^{\alpha,\beta}(f; x) - f(x)\right) + ax^2 f'(x) - \frac{x^2}{2} f''(x)\right| \\ \leq |u_n(x)| |f'(x)| + \frac{1}{2} |v_n(x)| |f''(x)| + nP_{n,p,\Psi}^{\alpha,\beta}(|r(t, x)|(t - x)^2; x). \end{aligned} \tag{28}$$

From (7) and (8),  $u_n(x)$  and  $v_n(x)$  approach zero, as  $n$  goes to infinity at any point  $x \in [0, \infty)$ . To calculate the term  $|r(t, x)|$  in the inequality (28), from (17),

$$|r(t, x)| \leq \left(1 + \frac{(e^{-t} - e^{-x})^2}{\gamma^2}\right) \omega^*(f'', \gamma), \quad \gamma > 0$$

can be written and here the modulus of continuity  $\omega^*(f, \gamma)$  is defined in (16). Moreover,

$$|r(t, x)| \leq \begin{cases} 2\omega^*(f'', \gamma) & , \quad |e^{-t} - e^{-x}| \leq \gamma \\ 2\frac{(e^{-t} - e^{-x})^2}{\gamma^2} \omega^*(f'', \gamma) & , \quad |e^{-t} - e^{-x}| > \gamma \end{cases}$$

and thus  $|r(t, x)| \leq 2 \left(1 + \frac{(e^{-t}-e^{-x})^2}{\gamma^2}\right) \omega^*(f'', \gamma)$ .

The Cauchy Schwartz inequality is applied to the last term of the sum on the right side of (28) and  $\gamma^2 = n^{-1}$  is chosen.

$$\begin{aligned} & nP_{n,p,\Psi}^{\alpha,\beta}(|r(t, x)|(t-x)^2; x) \\ & \leq 2n\omega^*\left(f'', n^{-\frac{1}{2}}\right)\left(P_{n,p,\Psi}^{\alpha,\beta}((t-x)^2; x) + nP_{n,p,\Psi}^{\alpha,\beta}((e^{-t}-e^{-x})^2(t-x)^2; x)\right) \\ & \leq 2\omega^*\left(f'', n^{-\frac{1}{2}}\right)\left(nP_{n,p,\Psi}^{\alpha,\beta}((t-x)^2; x) + \left(n^2P_{n,p,\Psi}^{\alpha,\beta}((e^{-t}-e^{-x})^4; x)\right)^{\frac{1}{2}}\left(n^2P_{n,p,\Psi}^{\alpha,\beta}((t-x)^4; x)\right)^{\frac{1}{2}}\right) \\ & \leq 2(v_n(x) + x^2 + w_n(x))\omega^*\left(f'', n^{-\frac{1}{2}}\right), \end{aligned}$$

where  $w_n(x) = \left(n^2P_{n,p,\Psi}^{\alpha,\beta}((e^{-t}-e^{-x})^4; x)\right)^{\frac{1}{2}}\left(n^2P_{n,p,\Psi}^{\alpha,\beta}((t-x)^4; x)\right)^{\frac{1}{2}}$ .

Thus, the Voronovskaja type asymptotic formula is obtained.

**Remark 4.5** Using the software Maple, the following equation is obtained:

$$\lim_{n \rightarrow \infty} n^2 P_{n,p,\Psi}^{\alpha,\beta}((e^{-t}-e^{-x})^4; x) = 3e^{-4x}x^4.$$

A result of Theorem 4.4, from the equation (9) and Remark 4.5 can be given as follows :

**Corollary 4.6** Let  $f, f'' \in C^*[0, \infty)$ . Thus

$$\lim_{n \rightarrow \infty} n \left(P_{n,p,\Psi}^{\alpha,\beta}(f; x) - f(x)\right) = -ax^2 f'(x) + \frac{x^2}{2} f''(x)$$

holds for any  $x \in [0, \infty)$ .

### 5. SOME GRAPHICAL ANALYSIS

In this section, the graphs below show the convergence of the Stancu type Post-Widder operators to the considered function  $f(x) = x^3 e^{-3x}$  for different values of  $n, p, a, \alpha$  and  $\beta$  (Figure 1).



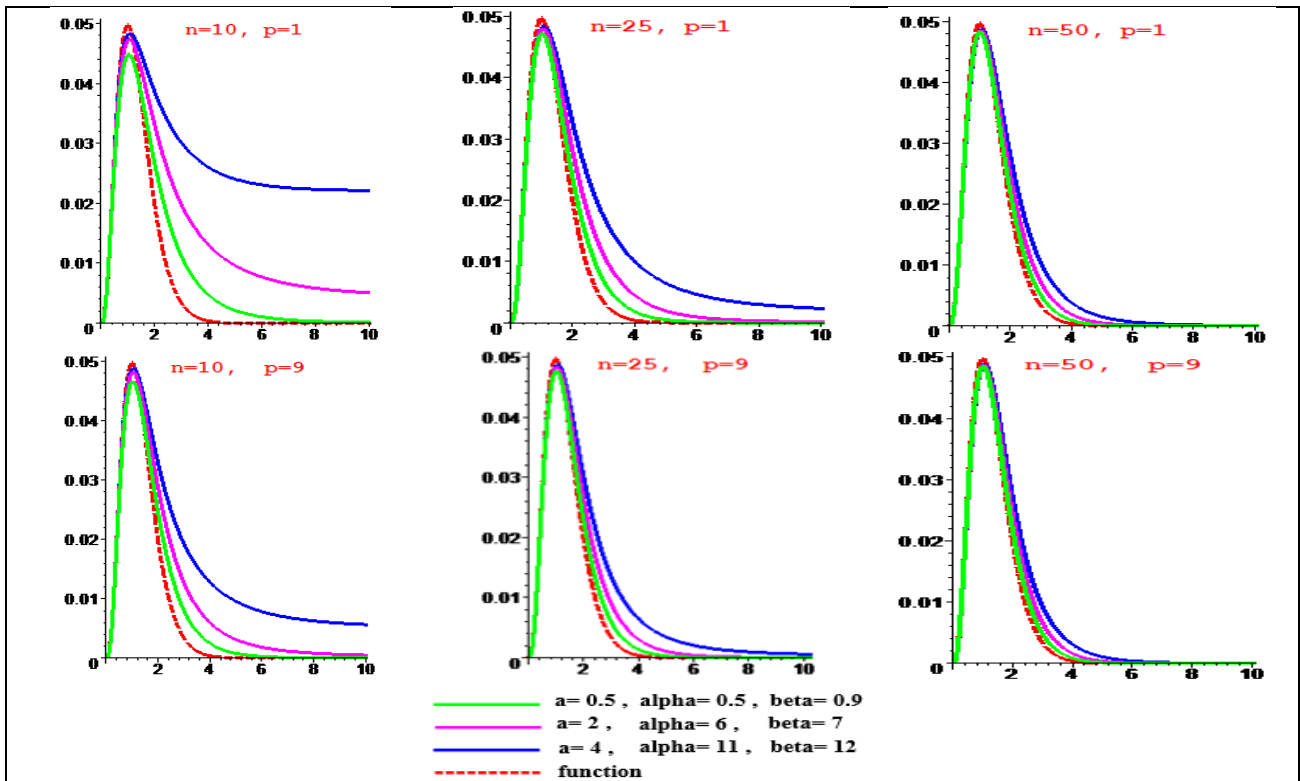


Figure 1. Convergence of  $P_{n,p}^{\alpha,\beta}(f; x)$  for different values of  $n, p, a, \alpha$  and  $\beta$

The graph below shows the convergence of the Post-Widder Operators  $P_{n,\theta}^*(f; x)$  and the Stancu type Post-Widder Operators  $P_{n,p,\psi}^{\alpha,\beta}(f; x)$  to the function  $f(x) = x^3 e^{-3x}$  for  $n = 50, a = 4$ , and different values of  $p, \alpha$  and  $\beta$  (Figure 2).

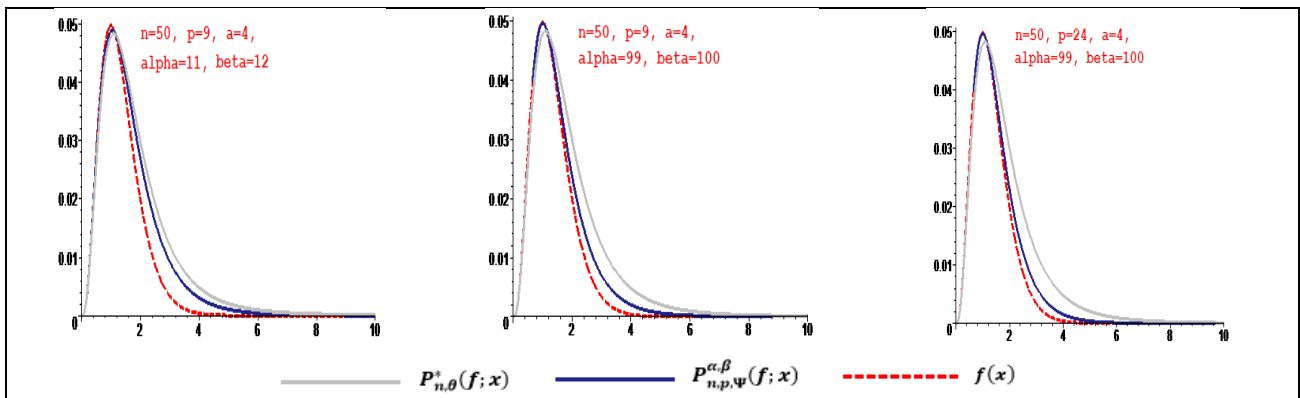


Figure 2. Convergence of  $P_{n,\theta}^*(f; x)$  and  $P_{n,p,\psi}^{\alpha,\beta}(f; x)$  to  $f(x)$  for  $n = 50$  and  $a = 4$

**ACKNOWLEDGMENT**

The author would like to thank the referee for the careful reading of this paper.

**CONFLICTS OF INTEREST**

The author declares no conflict of interest.

## REFERENCES

- Acar, T., Aral, A., & Gonska, H. (2017). On Szász-Mirakyan operators preserving  $e^{2ax}$ ,  $a > 0$ . *Mediterranean Journal of Mathematics*, 14(6), 1-14. doi:[10.1007/s00009-016-0804-7](https://doi.org/10.1007/s00009-016-0804-7)
- Aral, A., Inoan, D., & Raşa, I. (2019). Approximation properties of Szász-Mirakyan operators preserving exponential functions. *Positivity*, 23, 233-246. doi:[10.1007/s11117-018-0604-3](https://doi.org/10.1007/s11117-018-0604-3)
- Bodur, M., Gürel-Yılmaz, Ö., & Aral, A. (2018). Approximation by Baskakov-Szász-Stancu operators preserving exponential functions. *Constructive Mathematical Analysis*, 1(1), 1-8. doi:[10.33205/cma.450708](https://doi.org/10.33205/cma.450708)
- Boyanov, B. D., & Veselinov, V. M. (1970). A note on the approximation of functions in an infinite interval by linear positive operators. *Bull Math Soc Sci Math Roum*, 14(62), 9-13.
- Cai, Q.-B., Dinlemez Kantar, Ü., & Çekim, B. (2020). Approximation properties for the genuine modified Bernstein-Durrmeyer-Stancu operators. *Applied Mathematics-A Journal of Chinese Universities*, 35(4), 468-478. doi:[10.1007/s11766-020-3918-y](https://doi.org/10.1007/s11766-020-3918-y)
- Cai, Q.-B., Sofyalıoğlu, M., Kanat, K., & Çekim, B. (2021a). Some approximation results for the new modification of Bernstein-Beta operators. *AIMS Mathematics*, 7(2): 1831-1844. doi:[10.3934/math.2022105](https://doi.org/10.3934/math.2022105)
- Cai, Q.-B., Torun, G., & Dinlemez Kantar, Ü. (2021b). Approximation properties of generalized  $\lambda$ -Bernstein-Stancu-type operators. *Journal of Mathematics*, 2021, 5590439. doi:[10.1155/2021/5590439](https://doi.org/10.1155/2021/5590439)
- DeVore, R. A., & Lorentz, G. G. (1993). *Constructive Approximation*. (Grundlehren der mathematischen Wissenschaften, Vol. 303) Springer, Berlin.
- Dinlemez Kantar, Ü., & Ergelen, G. (2019). A voronovskaja-type theorem for a kind of Durrmeyer-Bernstein-Stancu operators. *Gazi University Journal of Science*, 32(4), 1228-1236. doi:[10.35378/gujs.513478](https://doi.org/10.35378/gujs.513478)
- Dinlemez Kantar, Ü., & Yüksel, İ. (2022). Investigating (p, q)-hybrid Durrmeyer-type operators in terms of their approximation properties. *Gazi University Journal of Science Part A: Engineering and Innovation*, 9(1), 1-11. doi:[10.54287/gujsa.1029633](https://doi.org/10.54287/gujsa.1029633)
- Gupta, V., & Agrawal, D. (2019). Convergence by modified Post-Widder operators. *RACSAM*, 113(2), 1475-1486. doi:[10.1007/s13398-018-0562-4](https://doi.org/10.1007/s13398-018-0562-4)
- Gupta, V., & Maheshwari, P. (2019). Approximation with certain Post-Widder operators. *Publications de L'Institut Mathématique*, 105(119), 131-136. doi:[10.2298/PIM1919131G](https://doi.org/10.2298/PIM1919131G)
- Gupta, V., & Tachev, G. (2022). Some results on Post-Widder operators preserving test function  $x^r$ . *Kragujevac Journal of Mathematics*, 46(1), 149-165. doi:[10.46793/KgJMat2201.149G](https://doi.org/10.46793/KgJMat2201.149G)
- Gürel-Yılmaz, Ö., Gupta, V., & Aral, A. (2017). On Baskakov operators preserving the exponential function. *Journal of Numerical Analysis and Approximation Theory*, 46(2), 150-161.
- Gürel-Yılmaz, Ö., Bodur, M., & Aral, A. (2018). On approximation properties of Baskakov-Schurer-Szász operators preserving exponential functions. *Filomat*, 32(15), 5433-5440. doi:[10.2298/FIL1815433Y](https://doi.org/10.2298/FIL1815433Y)
- Hacısalıhoğlu, H., & Hacıyev, A. (1995). *Lineer Pozitif Operatör Dizilerin Yakınsaklığı*. Ankara University F.F., Ankara.
- Holhoş, A. (2010). The rate of approximation of functions in an infinite interval by positive linear operators. *Stud Univ Babeş-Bolyai Math.*, 55(2). 133-142.
- Kanat, K., & Sofyalıoğlu, M. (2021). On Stancu type Szász-Mirakyan-Durrmeyer operators preserving  $e^{2ax}$ ,  $a > 0$ . *Gazi University Journal of Science*, 34(1), 196-209. doi:[10.35378/gujs.691419](https://doi.org/10.35378/gujs.691419)
- May, C. P. (1976). Saturation and inverse theorems for combinations of a class of exponential type operators. *Canadian Journal of Mathematics*, 28(6), 1224-1250. doi:[10.4153/CJM-1976-123-8](https://doi.org/10.4153/CJM-1976-123-8)
- Rathore, R. K. S., & Singh, O. P. (1980). On convergence of derivatives of Post-Widder operators. *Indian J. Pure Appl. Math.*, 11(5), 547-561.
- Rempulska, L., & Skorupka, M. (2009). On approximation by Post-Widder and Stancu operators preserving  $x^2$ . *Kyungpook Mathematical Journal*, 49(1), 57-65. doi:[10.5666/KMJ.2009.49.1.057](https://doi.org/10.5666/KMJ.2009.49.1.057)

- Sofyalıođlu, M., & Kanat, K. (2019). Approximation properties of generalized Baskakov–Schurer–Szász–Stancu operators preserving  $e^{2ax}$ ,  $a > 0$ . *Journal of Inequalities and Applications and Applications*, 2019(1), 112. doi:[10.1186/s13660-019-2062-2](https://doi.org/10.1186/s13660-019-2062-2)
- Sofyalıođlu, M., & Kanat, K. (2020). Approximation properties of the Post-Widder operators preserving  $e^{2ax}$ ,  $a > 0$ . *Mathematical Methods in the Applied Sciences*, 43(7), 4272-4285. doi:[10.1002/mma.6192](https://doi.org/10.1002/mma.6192)
- Sofyalıođlu, M., Kanat, K., & ekim, B. (2021). Parametric generalization of the Meyer–König–Zeller operators. *Chaos, Solitons & Fractals*, 152, 111417. doi:[10.1016/j.chaos.2021.111417](https://doi.org/10.1016/j.chaos.2021.111417)
- Torun, G., Mercan Boyraz, M., & Dinlemez Kantar, Ü. (2022). Investigation of the Asymptotic Behavior of Generalized Baskakov–Durrmeyer–Stancu Type Operators. *Cumhuriyet Science Journal*, 43(1), 98-104. doi:[10.17776/csj.1030637](https://doi.org/10.17776/csj.1030637)
- Widder, D. V. (1941). *The Laplace Transform*. (Princeton Mathematical Series, 6) Princeton University Press, Princeton, New Jersey.

# JOURNAL OF SCIENCE

PART A: ENGINEERING AND INNOVATION



## Correspondence Address

Gazi University  
Graduate School of Natural and Applied Sciences  
Emniyet Neighborhood, Bandırma Avenue  
No:6/20B, 06560, Yenimahalle - ANKARA  
B Block, Auxiliary Building

## Yazışma Adresi

Gazi Üniversitesi  
Fen Bilimleri Enstitüsü  
Emniyet Mahallesi, Bandırma Caddesi  
No:6/20B, 06560, Yenimahalle - ANKARA  
B Blok, Ek Bina

**e-mail | e-posta**  
gujsa06@gmail.com

**web page | web sayfası**  
<https://dergipark.org.tr/tr/pub/gujisa>

e-ISSN 2147-9542